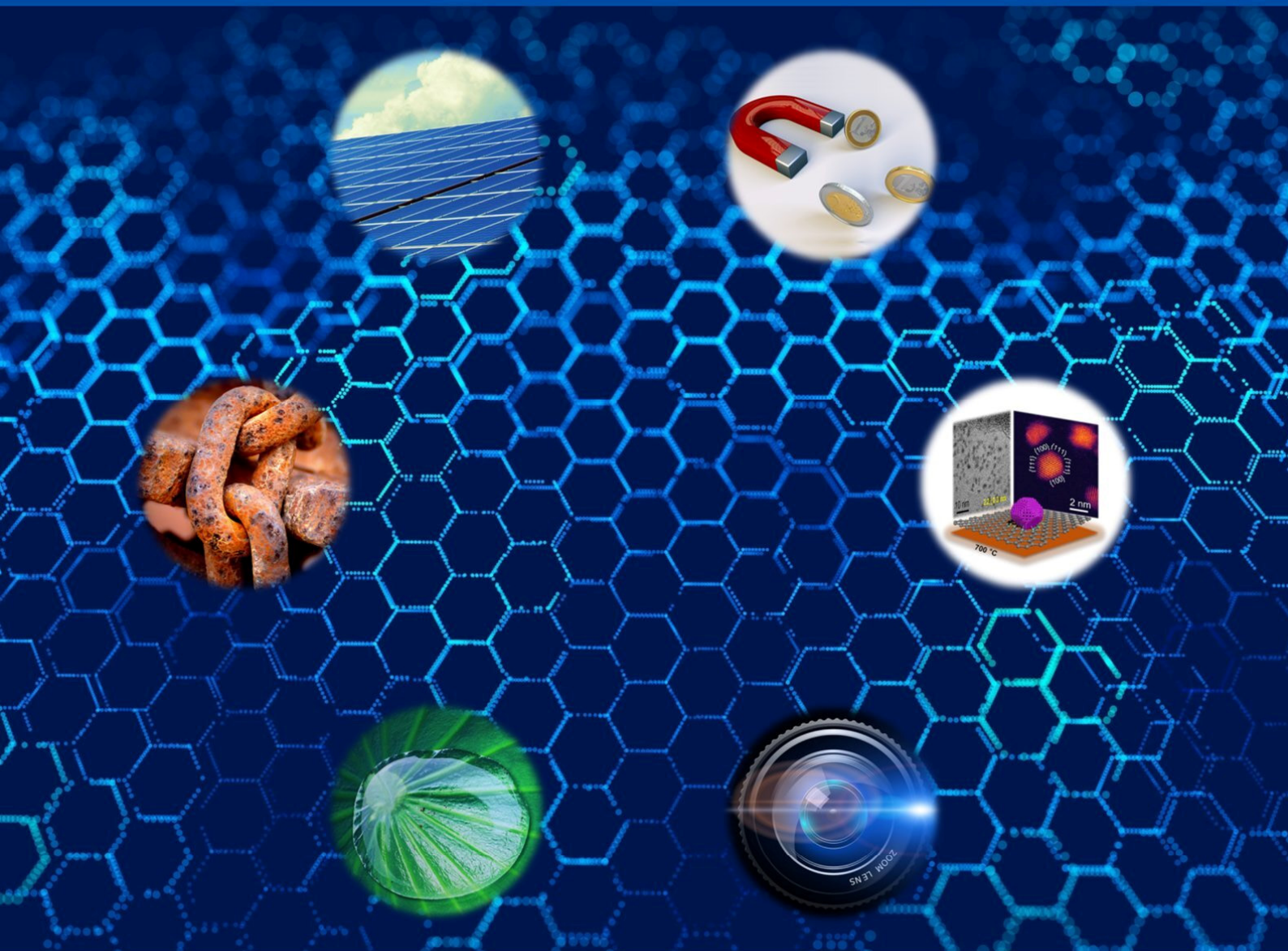


Materials and Interfaces

<https://www.sciltp.com/journals/mi>

Online ISSN: 2982-2394

Volume 1, Issue 1, 2024



Contents

Vol. 1 No. 1 December 2024

Welcome to Materials and Interfaces	1
Younan Xia	
On the Surface Compositions of Molybdenum Carbide Nanoparticles for Electrocatalytic Applications	3
Siying Yu and Hong Yang *	
Emerging Piezoelectric Metamaterials for Biomedical Applications	13
Zishuo Yan, Huy Tran, Dezun Ma, and Jingwei Xie *	
A Novel Bi-Directional and Bi-Temporal Delivery System for Enhancing Intrasyovial Tendon Repair	35
Yidan Chen, Seth Kinoshita, Emily Yan, Min Hao, Hua Shen, Richard Gelberman, Stavros Thomopoulos, and Younan Xia *	
Effect of Protein Loading Density on the Structure and Biopreservation Efficacy of Metal-Organic Frameworks	47
Yixuan Wang, Sirimuvva Tadepalli, Harsh Baldi, Jeremiah J. Morrissey, and Srikanth Singamaneni *	
Silver-Platinum Hollow Nanoparticles as Labels for Colorimetric Lateral Flow Assay	58
Jinfeng Zhou, Shikuan Shao, Zhiyuan Wei, and Xiaohu Xia *	
Piezocatalytic ZnS: Mn²⁺ Nanocrystals for Enhanced Organic Dye Degradation	68
Zhongxiang Wang, Elizaveta Tiukalova, Youyi Tai, Miaofang Chi, Jin Nam *, and Yadong Yin *	
Cathodic Corrosion-Induced Structural Evolution of CuNi Electrocatalysts for Enhanced CO₂ Reduction	79
Wenjin Sun, Bokki Min, Maoyu Wang, Xue Han, Qiang Gao, Sooyeon Hwang, Hua Zhou, and Huiyuan Zhu *	
Controlled Polymerization of Aniline against Templating Oxide Nanostructures	89
Matas Simukaitis, Grace Purnell, Zachary Zander, Danielle Kuhn, and Yugang Sun *	

Editorial

Welcome to *Materials and Interfaces*

Younan Xia^{1,2}¹ The Wallace H. Coulter Department of Biomedical Engineering, Georgia Institute of Technology and Emory University, Atlanta, GA 30332, USA; younan.xia@bme.gatech.edu² School of Chemistry and Biochemistry, Georgia Institute of Technology, Atlanta, GA 30332, USA

Received: 16 December 2024; Accepted: 17 December 2024; Published: 20 December 2024

After six months of preparation, it gives me the greatest satisfaction to announce the debut of a new journal that aims to become one of the world's premier journals for disseminating cutting-edge research related to two important subjects: **Materials** and **Interfaces**. It is not an overstatement that everything tangible in the universe is built upon materials unless it exists in the form of atoms or molecules. In essence, a material can be characterized as an assembly of atomic, ionic, and/or molecular building blocks. In addition to the nature of the building blocks, the interactions among them also play a critical role in determining the properties of a material. An interface is the boundary between two spatial regions occupied by different materials, or by the same material in different physical states. Sometimes, the materials involved in such a situation are referred to as different phases. When a material is surrounded by a gaseous environment or vacuum, the interface is often called a surface, a subject that has been extensively explored for centuries in the context of surface science. The journal will cover the design, synthesis, and characterization of materials and interfaces, as well as their applications across a diverse spectrum of fields that may include catalysis, energy conversion/harvesting/storage, electronics, photonics, sensing, diagnostics, and biomedicine. It will serve as the hub for sharing knowledge among materials scientists, chemists, physicists, and engineers, as well as health and life scientists.

The inaugural issue contains contributions from eight research groups, including one perspective article, one review article, and six original articles. In their perspective article, Hong Yang and a coworker discuss the importance to control the surface composition of molybdenum carbide (MoC_x) nanoparticles in optimizing their electrocatalytic performance. After reviewing the surface components and nanostructures favored by thermodynamics for partially-oxidized MoC_x nanoparticles, they highlight the capability of an electrochemical oxidation method in engineering the surface composition. They use a set of examples to illustrate the structure-property relationship, with a focus on the phase dependency of the adsorption energy of reaction intermediates. In their review article, Jingwei Xie and coworkers offer a comprehensive overview of various types of piezoelectric materials, including molecular crystals, ceramics, and polymers, with remarkable piezoelectric performance and biocompatibility. They highlight a number of advanced engineering approaches to the customization of piezoelectric properties for an array of biomedical applications, including tissue engineering, drug delivery, wound healing, and biosensing.

In terms of original research articles, Younan Xia and coworkers report the design and fabrication of a bi-directional and bi-temporal drug delivery system to improve the outcome of a flexor tendon repair by targeting both the initial inflammatory phase and the subsequent proliferative and remodeling phases of healing. The system features a multi-layered structure, with the anti-adhesion and pro-matrix factors encapsulated in separate layers of hyaluronate films crosslinked to different degrees to help control their direction and kinetics of release. Srikanth Singamaneni and coworkers systematically evaluated the structure and properties of metal-organic frameworks (MOFs) as a function of protein loading density using a model system based upon zeolitic imidazolate framework crystals and bovine/human serum albumin. As expected, the concentration of protein in the MOF growth solution significantly affects the morphology, degree of crystallinity, and biopreservation efficacy of the resultant MOF crystals. Within an optimal protein concentration range of 0.1–1 mg/mL, both the structure integrity of the MOF and the immunologic functionality of albumin can be preserved. Xiaohu Xia and coworkers report the development of a unique colorimetric label based on silver-platinum hollow nanoparticles (Ag-Pt HNPs) for colorimetric lateral flow assay (CLFA). The intrinsic enzyme-like catalytic activity of Ag-Pt HNPs enables CLFA with a strong color signal and thereby high sensitivity. Meanwhile, their interior and the involvement of silver make the Ag-Pt HNP-based CLFA cost-effective. Using prostate-specific antigen as a model disease biomarker, they demonstrated a



detection limit as low as picogram-per-milliliter. Yadong Yin and coworkers report the synthesis and characterization of Mn^{2+} -doped ZnS nanocrystals with improved piezocatalytic properties to drive chemical reactions by harnessing mechanical energy. By controlling the doping level of Mn^{2+} , the nanocrystals show enhanced piezocatalytic activity toward the degradation of organic dyes under ultrasonic vibration. Significantly, pre-irradiation of the catalytic material with an ultraviolet light further boosted the efficiency by filling the electron trap states. Huiyuan Zhu and coworkers synthesized a series of $\text{Cu}_x\text{Ni}_{1-x}$ nanoparticles and then investigated their structural evolution during the electrochemical CO_2 reduction reaction (CO2RR). Due to the higher oxophilicity of Ni relative to Cu, the nanoparticles became Ni-enriched at the surface upon exposure to air, promoting the competing hydrogen evolution reaction (HER). With the use of both in situ and ex situ techniques, cathodic corrosion was observed in $\text{Cu}_x\text{Ni}_{1-x}$ nanoparticles at negative activation potentials, leading to the significant loss of Ni and thereby the formation of irregularly shaped Cu nanoparticles with increased defects. The structural evolution shifted the electrolysis from HER to CO2RR, enhancing the Faradaic efficiency of multi-carbon products (C_2^+). Yugang Sun and coworkers report the synthesis of polyaniline (PANI) nanotubes with a strong broadband optical absorption by leveraging the power of single-crystalline MnO_2 nanotubes as a solid-state oxidant to induce polymerization in an acidic solution. The high crystallinity and smooth surface of the MnO_2 nanotubes provide an ideal solid/liquid interface for templating the formation of PANI nanotubes. The template-directed synthesis was also extended to silica-coated MnO_2 nanotubes for the fabrication of silica-coated PANI nanotubes with versatile chemistry for convenient grafting of other interesting motifs.

The articles published in the inaugural issue cover a range of representative and exciting snapshots regarding recent progress in the context of materials and interfaces. It is hoped that the readers will enjoy the mix of topics presented in this issue and, most importantly, find the inspiration to push these research fronts to the next level of success. Personally, I want this journal to be broad in outlook and inclusive. I especially welcome contributions from colleagues in all disciplines, including chemistry, physics, biology, chemical engineering, materials science and engineering, biomedical engineering, mechanical engineering, electrical engineering, biological engineering, and even geology. I want to thank the members of advisory board and the authors, as well as the remarkable staff in the journal office for their help in putting this first issue together, and I look forward to receiving feedback and contributions from the community.

Conflicts of Interest: The author declares no conflict of interest.

Perspective

On the Surface Compositions of Molybdenum Carbide Nanoparticles for Electrocatalytic Applications

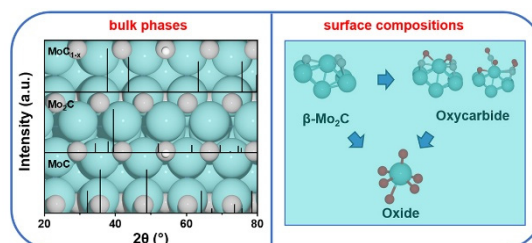
Siying Yu and Hong Yang *

Department of Chemical and Biomolecular Engineering, University of Illinois Urbana-Champaign, 600 S. Mathews, Urbana, IL 61801, USA

* Correspondence: hy66@illinois.edu

Received: 28 November 2024; Accepted: 2 December 2024; Published: 6 December 2024

Abstract: Molybdenum carbide has attracted much research attention for its precious metal-like catalytic properties, especially in hydrogen-involved reactions. It possesses rich crystal and surface structures leading to different activity and product selectivity. With advances in nanoengineering and new understanding of their surfaces and interfaces, one can control the transition between different phases and surface structures for molybdenum carbide nanoparticles. In this context, it is essential to understand their surface compositions and structures under operating conditions in addition to their intrinsic ones under ambient conditions without external cues. The necessity of surface study also comes from the mild oxidation brought by passivation in carbide nanoparticles. made using the bottom-up synthesis or solid-gas phase temperature-programmed reduction. In this perspective, we first introduce the relevant crystal structures of molybdenum carbides and highlight the features of the three types of chemical bonding within. We then briefly review the studies of thermodynamically favored surface components and nanostructures for partially oxidized molybdenum carbide nanoparticles based on both experimental and theoretical data. An electrochemical oxidation method is used to illustrate the feasibility in controlling and understanding the surface oxidation. Finally, structure-property relationship is discussed with several recent examples, focusing on the effect of phase dependency on the adsorption energy of reaction intermediates.



Keywords: molybdenum carbide; surface composition; oxycarbide; electrocatalysis; hydrogen evolution reaction; density functional theory

1. Introduction

Renewable energy such as hydropower, wind, solar, and biofuel occupies a growing share of global energy consumption, playing an important role in steadily reducing the dominant status of fossil fuels. Sustainable electrochemical technologies focusing on fuel cells, electrolyzers for water splitting, and batteries have been intensively studied for their large-scale commercialization [1,2]. Design of electrocatalysts and electrode materials is crucial to bring out the maximum activity and durability of the energy devices, achieving both energy- and cost-efficiency. Noble metals such as platinum and palladium are conventional electrocatalysts but less favorable due to their high cost [3,4]. As potential substitutions for precious metals, molybdenum carbide (Mo_xC) materials have been widely studied for their application in electrochemical catalysis, especially for hydrogen evolution reaction (HER) [5,6] oxygen evolution reaction (OER) [7], nitrogen reduction reaction (NRR) [8], and carbon dioxide reduction reaction (CO_2RR) [9]. While the mechanisms for their Pt-like properties are still under investigation, it has been reported that the (111) surface of $\beta\text{-Mo}_2\text{C}$ exhibits comparable Gibbs free energy to that of Pt (111) plane [10]. After modification of surface components of carbide materials, a balanced adsorption/desorption of reacting species, intermediates, and products on catalyst surface can be achieved, which is beneficial to facilitate the kinetics of a target reaction [11,12]. Considerable approaches have been examined, such as exposing active sites by nanoengineering [13,14], surface modification using heteroatom doping [12,15], interface engineering by incorporation of catalyst supports [16,17], and structural design using porous and hierarchical materials [18,19].



Copyright: © 2024 by the authors. This is an open access article under the terms and conditions of the Creative Commons Attribution (CC BY) license (<https://creativecommons.org/licenses/by/4.0/>).

Publisher's Note: Scilight stays neutral with regard to jurisdictional claims in published maps and institutional affiliations

All strategies require a comprehensive understanding of surface compositions of Mo_xC and how these compositions may modify the interaction between surface sites and reactants.

The necessity to understand surface components also arises from the synthetic conditions of Mo_xC materials. Using $\beta\text{-Mo}_2\text{C}$ as an example, it can be made in three major approaches: solid-solid, solid-liquid, and solid-gas methods [20,21]. In a solid-solid phase method, carbon is used as support in the process of carburization of Mo precursors. The synthesis is carried out at high temperatures ($>1500^\circ\text{C}$) to overcome the energy barrier of carbon diffusion into Mo lattice, resulting in large particle size, low specific surface area, and inferior catalytic properties [18,22]. The solid-liquid phase method, which usually uses urea glass, alcohol, and phenolic resin as the carbon source, can reduce the reaction temperature to $600\sim 900^\circ\text{C}$ [20,21].

An effective, current synthesis is based on solid-gas phase temperature programmed reduction (TPR) method. In this approach, hydrocarbon gases such as methane may be reduced by hydrogen gas to produce the carbon in metal carbides, which greatly lowers the synthetic temperature to make nanometer (nm)-sized carbide particles [23,24]. The benefit of using gaseous carbon sources includes flexibility in the choice of catalyst support, especially allowing for a delicate size and morphology control of carbide nanoparticles. The choice of carbon-containing gas is also reported to affect the structure of the obtained carbide [20,25]. Using solid-gas synthesis may have its challenges as well. The incomplete combustion of excess carbon-containing gases may result in the formation of carbon residue on carbide surface [26]. The carbon residue not only complicates the microscopic study of carbide nanomaterials but also deactivates the surface. As Mo_xC nanoparticles are pyrophoric due to their highly reactive surfaces, post-treatment, such as mild passivation, may also be needed for their safe use under ambient conditions [27], resulting in surface oxidation [23]. The partially oxidized surface, known as oxycarbide, can be either carbidic or oxidic based on oxygen coverage [28]. There is much research interest in characterizing the surface of oxidized molybdenum carbide [29,30] and studying the impact of controlled oxidation on catalytic properties [23,31,32], because surface composition often determines catalytic activity.

In this Perspective, we highlight the understanding of surface compositions of Mo_xC nanoparticles and their effects on electrochemical catalysis. We first present the crystal structures and summarize the key relevant features of chemical bonding in Mo_xC . We then discuss the thermodynamically favored surface components and nanostructures of partially oxidized Mo_xC nanoparticles based on both experimental and theoretical data. Relationship between catalytic properties and compositional and structural parameters of Mo_xC nanocatalysts is explained based on adsorption energy of reaction intermediates. The effects of phase dependency on catalytic applications are highlighted using selected recent examples.

2. Structure of Molybdenum Carbides and Key Features of Chemical Bonding

Molybdenum carbides can be regarded as interstitial compounds, where large transition Mo atoms serve as the host lattice, and small carbon atoms occupy the interstitial vacancies. Experimentally, X-ray diffraction (XRD) is a common technique to study the crystal structure of Mo_xC . There are mainly three types of packing structures for interstitial carbides, i.e., face-centered cubic (*fcc*), hexagonal closed packed (*hcp*), and simple hexagonal (*hex*) structures. Their corresponding standard XRD patterns are illustrated in Figure 1. In a cubic structure, each Mo atom is surrounded by six C atoms. The hexagonal Mo_xC forms a structure with alternating Mo and C layers [33].

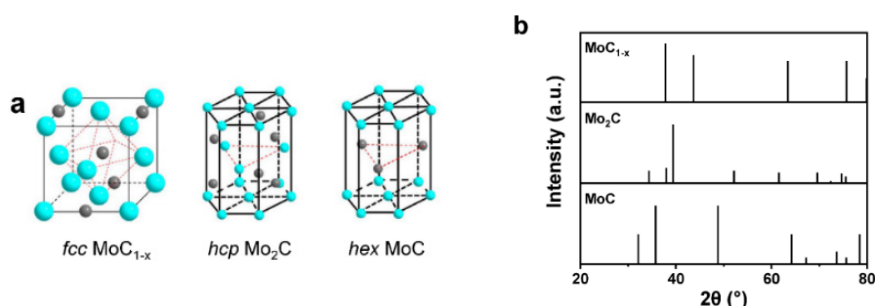


Figure 1. (a) Illustration of the three common Mo_xC crystal structures. Reprinted with permission from Ref. [34]. (b) The corresponding standard XRD patterns of MoC_{1-x} , Mo_2C , and MoC .

There are three kinds of bonding in the Mo_xC materials, i.e., metallic bond between Mo atoms, covalent bond between Mo and C, and ionic bond caused by charge transfer between Mo and C. The electron localization function (ELF) topological analysis was applied to study the chemical bonding in molybdenum carbide nanoparticles [35].

A detailed electronic structure calculation shows the local maxima of electron density are contained in a basin as illustrated in the isosurfaces of each configuration (Figure 2a–c). The core basin (i.e., $C(X)$, $X = \text{Mo}$ or C) contains a nucleus meanwhile the valence basin (i.e., $V(mX, nY)$, $X, Y = \text{Mo}$ or C , m and n are integers) includes a number of core basins. For Mo_1C_1 configuration, the electron density maximum is found 0.624 Å from Mo and 1.067 Å from C, with a low basin population of 0.2e. This calculation implies the ionic character of the Mo–C bonding (Figure 2a). In contrast, two bonding basins of Mo–C (i.e., $V(\text{C}, \text{Mo})$) in the Mo_2C_1 configuration have 1.8e, indicating a significant change to a more covalent character (Figure 2b). The ELF method was further applied to a more complex $\text{Mo}_{28}\text{C}_{14}$ configuration regarding its Mo-terminated surface. Three-center basins $V(3\text{Mo})$ and four-center basins $V(\text{C}, 3\text{Mo})$ are observed and reported to related to the three kinds of three-fold hollow sites (V_C , H_M , H_C) for surface adsorption [36].

Analysis of density of states (DOS) is another method to investigate the electronic structure of Mo_xC [33]. Different phases of Mo_xC have different C 2s bands in shape and energy between -10.5 and -13.5 eV (Figure 2d). For δ -MoC and α -MoC, the bands around the Fermi energy (E_F) have a narrow close-to-zero region, which separates the whole band into the covalent bonding and antibonding areas (Figure 2d,e). These two regions are composed of C 2p and Mo 5d electrons, though the metallic nature of carbide mainly comes from Mo. The DOS of δ -MoC has the sharpest peaks, indicating the most localized distribution of electrons and mixed ionic-covalent bonding. For β - Mo_2C , however, it has the most metallic character because E_F is within the electronic bands. Due to the strong interaction between carbon and metal atoms, Mo_xC (e.g., Mo_2C) possesses a high melting point (2520°C) with its electric and thermal conductivity similar to ceramics [34]. These properties make them attractive functional materials, especially after they were found to exhibit catalytic activity in electrochemical reactions [5,37,38].

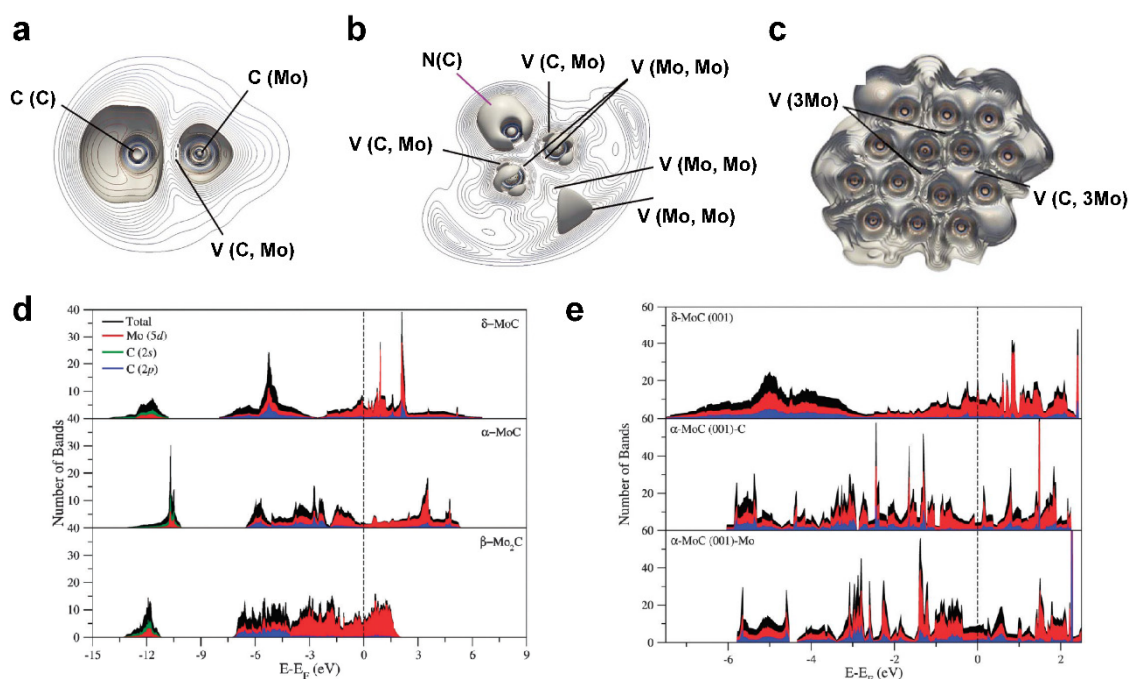


Figure 2. ELF isosurfaces of (a) Mo_1C_1 , (b) Mo_2C_1 , and (c) $\text{Mo}_{28}\text{C}_{14}$ complexes. $V(X, Y)$ indicates the valence basin between two centers ($X, Y = \text{C}$ or Mo), and $C(\text{C})$ and $C(\text{Mo})$ indicate a carbon and molybdenum core basin, respectively. Reprinted with permission from Ref. [35]. (d) Total and projected DOS for Mo_xC with different bulk structures. (e) Projected DOS for the most stable low Miller-index surfaces of δ -MoC and α -MoC phases. Reprinted with permission from Ref. [33].

3. Surface Composition: Experimental and Quantum Simulation Studies

3.1. Phase Behaviors of Mo_xC Nanomaterials

Size and composition control is crucial in synthesizing Mo_xC nanomaterials to bring out their precious metal-like catalytic properties. Molybdenum carbides have been reported to exhibit multiple crystal structures (Figure 3a) and reactions conditions can be modified to prepare different targeted products. The transition between different carbide structures becomes easier when the particle size is reduced to nm-sized scale. The large surface

area-to-volume ratio means contribution of surface energy to the total energy becomes significant, making those metastable phases with low surface energy becomes thermodynamically preferable at small sizes (Figure 3b–d) [14]. In another word, nanosized carbide particles may have different phases from those suggested by the conventional phase diagram (Figure 3b). To obtain this size-dependent phase diagram, the bulk free energy values ($\Delta\Omega_{\text{bulk}}$) of different Mo_xC were estimated as a function of the chemical potential of carbon ($\Delta\mu_{\text{C}}$) (Figure 3c). Surface energies were incorporated into the calculation of size-dependent free energy based on the Gibbs-Thomson equation. It is also necessary to optimize the computed Wulff constructions based on equilibrium particle morphologies of different carbide phases to address the relationship between surface energy and Miller index (Figure 3d). Combining both bulk phase and surface energy terms, δ -MoC phase dominates in the size regime of <3.3 nm and α - Mo_2C phase is the preferable product in the range of 3.3–40 nm. When the resulting nanoparticle is larger than 40 nm, γ -MoC and β - Mo_2C are expected to form (Figure 3b).

Other than thermodynamic considerations, the structural transformation can also be realized through formation of energetically favored interface [39]. Density functional theory (DFT) calculations suggest the feasibility of Zn-facilitated phase transformation. The adhesion energy of $\text{MoC}(101)\|\text{Mo}_2\text{C}(101)$ interface is found to be smaller than the sum of surface energy of $\text{MoC}(101)$ and $\text{Mo}_2\text{C}(101)$. Thus, the epitaxial growth of MoC from Mo_2C should be thermodynamically favored. A Zn-modified $\text{MoC}(101)/\text{Mo}_2\text{C}(101)$ interface is calculated to be more stable than a Zn-free interface, further benefiting the formation of MoC/ Mo_2C interface. This structural transformation can be demonstrated by the XRD patterns of carbide samples with different Zn/Mo ratios (Figure 3e). The characteristic peaks of MoC (101) and Mo_2C (101) are located at 36.3° and 39.6° , respectively. With a higher Zn/Mo feeding ratio, the peak intensity ratio between MoC (101) and Mo_2C (101) also increases. With bulky phase information characterized by XRD, researchers rely on X-ray photoelectron spectroscopy (XPS) to study the surface chemical constituents. Figure 3f shows the Mo 3d spectrum for Zn-MoC/ Mo_2C -0.5. Peak deconvolution was performed to assign each XPS peak to the four oxidation states of Mo, i.e., Mo(II), Mo(III), Mo(IV), and Mo(VI). Peaks around 228.6 eV and 231.8 eV refer to Mo(II) $3d_{3/2}$ and $3d_{5/2}$ of Mo_2C , which have comparable peak intensity to those for Mo(III) of MoC. The co-existence of MoC and Mo_2C in the surface region is consistent with the XRD results as shown in Figure 3e. It should be noted that Mo(IV) and Mo(VI) are commonly observed in Mo carbide nanosized samples unless they are prepared and characterized in situ without exposure to air. These oxides are a result of surface oxidation of Mo_xC nanoparticles under ambient conditions.

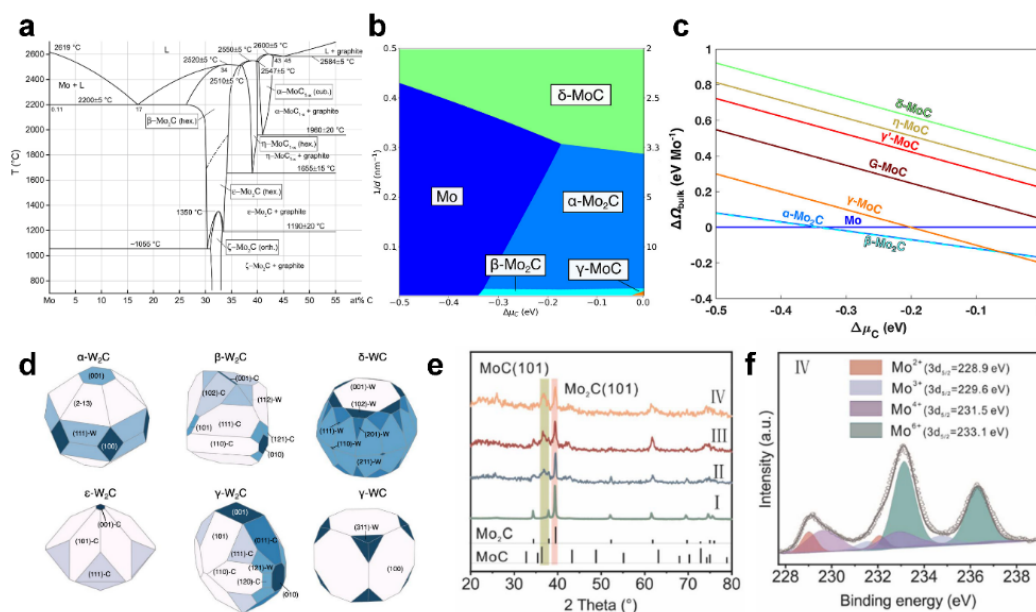


Figure 3. (a) Binary phase diagram of Mo and C. Reprinted with permission from Ref. [22]. (b) Lowest energy 2-D phase diagram by projecting 3-D diagram onto $\Delta\mu_{\text{C}}-1/d$ axis. (c) Free energy of Mo_xC at different chemical potentials of carbon ($\Delta\mu_{\text{C}}$). (d) Computed Wulff constructions of the equilibrium particle morphologies of different carbide phases at $\Delta\mu_{\text{C}} = -0.15$ eV. This value of $\Delta\mu_{\text{C}}$ was chosen because it roughly corresponds to common composition and temperature synthesis conditions. Reprinted with permission from Ref. [14]. (e) XRD patterns of the Zn-MoC/ Mo_2C catalysts with different Zn/Mo feeding ratio (I: 0, II: 0.1, III:0.2, IV: 0.5). (f) High resolution XPS spectrum of Mo 3d for the Zn-MoC/ Mo_2C -0.5 catalyst. Reprinted with permission from Ref. [39]. Copyright 2021 American Chemical Society.

3.2. Controlled Surface Oxidation by an Electrochemical Approach

While there is a great incentive to control the surface chemistry of metal carbide to optimize their catalytic properties, it is non-trivial to develop a proper synthetic approach with the precision that is needed. Surface oxidation can be best controlled with those Mo_xC nanomaterials made using the solid-gas synthesis [23]. This method significantly reduces the reaction temperature of Mo_xC nanomaterials, preventing severe overgrowth of carbide while enabling the exposure of active surfaces using the bottom-up synthesis. In a typical synthesis, a mixed forming gas consisting of a short-chain hydrocarbon (e.g., methane) and hydrogen is often used. Heat treatment of metal precursors in such a reducing atmosphere gives rise to the formation of highly reactive carbide nanoparticles, whose surface can be partially oxidized to result in metallic-like H-adsorption sites and Brønsted acid hydroxyl sites [40]. Catalytic properties of Mo_xC nanoparticles thus are readily tunable by the surface oxidation [41]. Controlled treatment through oxidation of surface sites was reported to help adjust the acidic site density of 2–5 nm Mo_2C nanoparticles [42]. Product selectivity could also be affected by the oxygen coverage on carbide surface [30,43].

While the solid-gas phase synthesized Mo_xC can be oxidized readily, the approach is lacking the control in the degree of oxidation. Electrochemical oxidation appears to be an ideally suited approach to making partially and fully oxidized Mo_xC nanoparticles, meeting the technical challenge on quantitatively control over the degree of oxidation. In our recent study, different degrees of surface oxidation were achieved by applying predetermined upper limit of oxidation potential in an aqueous electrolyte, shown in cyclic voltammetry (CV) (Figure 4a) [23]. In this synthesis, electrooxidation of $\beta\text{-Mo}_2\text{C}$ could occur at an onset potential of around 0.6 V (vs. RHE) and the peak current density was achieved at ~0.8 V. When the upper limit was raised to 1.2 V, the oxidation current density was close to zero, suggesting a complete surface oxidation. X-ray photoelectron spectroscopy (XPS) study indicates the complete surface oxidation started at a high potential, ranging from 0.975 V and 1.2 V. Our XPS study indicates the carbidic peaks appearing between 0.4 V and 0.85 V in Mo spectra can be assigned to (Mo) oxycarbides.

Our density functional theory (DFT) simulations further catch this change from carbides, to oxycarbides, and ultimately to oxides in detail, providing strong atomic analysis of relationship between surface structure and degree of oxidation (Figure 4c–f). Oxygen-covered surface configurations are thermodynamically more stable than those of oxygen-free configurations across the potential range from 0 to 0.6 V (Figure 4d). In the range of 0 to 0.28 V, 1/3 of Mo sites and all C sites are covered with oxygen ((Mo-O)₁(C-O)₆). The DFT simulation also reveals that, on a carbon-terminated facet, surface carbon is more sensitive to oxidation than surface Mo, which is consistent with our spectroscopic data. When the oxidation potential increases, the surface oxycarbide structure transforms into more oxidized configurations, i.e., (Mo-O)₃(C-O)₆ and (Mo-O)₄(C-O)₆. Our quantum simulation results further indicate a fully oxygen-covered carbide surface may be on a nanoparticle that is not fully oxidized. With an oxidation potential higher than 0.6 V, a substitutional oxidation pathway may occur, where oxygen-covered surface carbons further react to form CO and CO₂ species. These carbon derivatives subsequently desorb from the surface, exposing carbide subsurfaces, allowing oxidization of sublayer Mo and C sites, and triggering the structural transformation from oxycarbide to oxide (Figure 4e). The DFT simulation suggests such a process is thermodynamically favorable at a wide range up to an oxidative potential of 1.2 V and explains the experimentally observed peak current density around 0.8 V in CV scans (Figure 4a).

The DFT and experimental studies developed for $\beta\text{-Mo}_2\text{C}$ nanoparticles were applicable to analyze the surface composition of $\alpha\text{-MoC}$ [44]. Both computational and experimental data indicate that $\alpha\text{-MoC}$ is more resistant to electrochemical oxidation than $\beta\text{-Mo}_2\text{C}$, i.e., the surface structural transformation of $\alpha\text{-MoC}$ to oxycarbide and oxide is more difficult (Figure 5a–c). This resistance to oxidation is attributed to the unfavored substitutional oxidation. The ab initio thermodynamics calculation suggests $\alpha\text{-MoC}(311)\text{-Mo}$ and $\beta\text{-Mo}_2\text{C}(011)\text{-C}$ surfaces as the most dominant facets under synthetic conditions. Considering the adsorption of O*/OH*/H*, the pH-dependent surface Pourbaix diagram for $\alpha\text{-MoC}(311)\text{-Mo}$ facet was obtained (Figure 5a). At pH = 1, the oxidized surface, with all Mo_{fcc} sites and half of C_{top} sites covered with oxygen, is stable up to 0.71 V. A structural transformation from (Mo-O)₈(C-O)₄ to (Mo-O)₈(C-O)₅ configuration happens in the potential range from 0.71 to 0.84 V. This conversion is limited by H₂O dissociation and is thus considered as a slow oxidation. After reaching 0.84 V, the product, (Mo-O)₈(C-O)₅, becomes thermodynamically favorable, thus promoting the reaction rate of surface oxidation. Further oxidation is expected if the oxidative potential is above 0.84 V at pH = 1. For $\beta\text{-Mo}_2\text{C}$, however, the slow and fast oxidation steps happen at the potential of 0.23 and 0.46 V, respectively (at pH = 1 in Figure 5b). This stability analysis is based on the thermodynamically stable (311)-Mo facet of $\alpha\text{-MoC}$. It appears the metal-terminated surface adds to the difficulty of oxidation and retards the oxidation of C atoms to CO and CO₂ species. In contrast, the carbon-terminated $\beta\text{-Mo}_2\text{C}(011)\text{-C}$ facet may react with O* and form mobile CO*

species. The experimental results show a more pronounced and broader oxidation peak for β -Mo₂C than α -MoC (Figure 5c), which is consistent with the theoretical predictions.

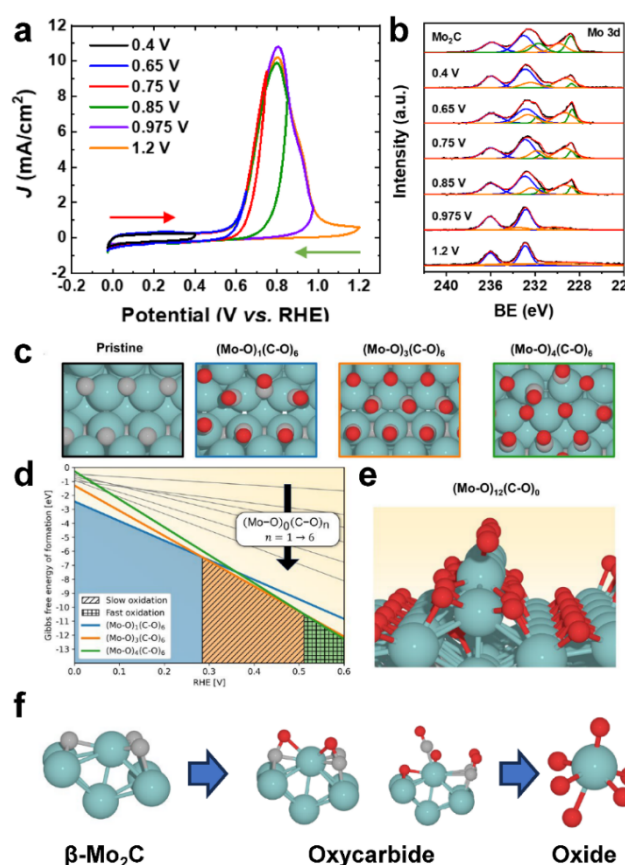


Figure 4. (a) CV curves for the electrochemical surface oxidation (red arrow: direction of the forward scan; green arrow: direction of the back scan). (b) XPS of Mo 3d regions (blue: VI; orange: IV; green: II), showing the evolution of surface compositions as a function of the upper limit of potential used in the electrochemical oxidation process. The black lines are obtained XPS curves, and the red lines are fitting envelopes. (c) Models of top view of thermodynamically stable β -Mo₂C(011) carbon-terminated surfaces. The pristine surface is included for reference. (d) Gibbs free energy of formation as a function of applied potential computed by the DFT simulation. (e) Proposed surface oxide structure formed after the complete oxidation in hatched regions at a high potential (cyan: Mo; grey: C; red: O). (f) Illustrations of nearest neighboring atoms for a given Mo at different surface coverages. Reprinted with permission from Ref. [23].

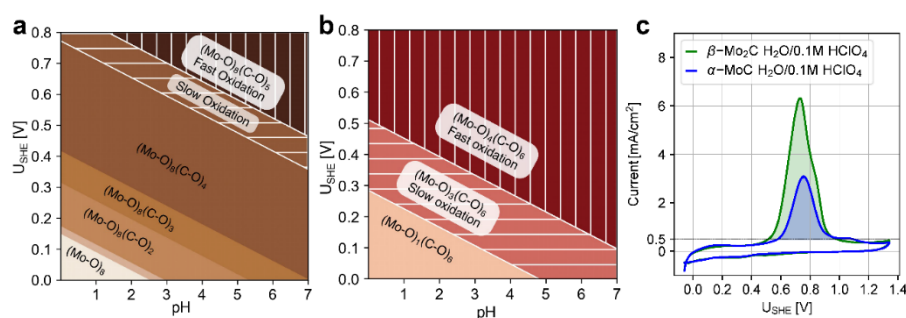


Figure 5. (a) Surface Pourbaix diagram for α -MoC considering the adsorption of O*/OH*/H*. Horizontal hatches show slow oxidation, and the vertical hatch corresponds to facile fast oxidation through CO desorption. At pH = 1, the onset potentials for each region starting with (Mo-O)₈(C-O)₁ are 0.09, 0.11, 0.25, 0.34, and 0.84 V, respectively. (b) Surface Pourbaix diagram for β -Mo₂C(011) considering only O* coverage. (c) CV for α -MoC and β -Mo₂C in an aqueous solution (pH = 1). The shaded area corresponds to the region of the CV curve considered for the charge transfer calculation. The threshold current used is 0.5 mA/cm². Reprinted with permission from Ref. [44].

4. Electrocatalysis of Molybdenum Carbide Nanoparticles

Properties of electrocatalysts are closely related to the adsorption/desorption of reactants, their intermediates and final products. Catalytic performance of Mo_xC is often dependent on different structural factors, including crystal phase, metal dopant, and Mo valence. Dependency of performance on surface structures can be illustrated through hydrogen evolution reaction (HER) by Mo_xC electrocatalysts. Figure 6 shows the results of a theoretical study of the effects of twenty-nine atomic configurations of seven different surfaces on HER [11], including their atomic configuration, stability, and adsorption of O^* and HO^* . Figure 6a shows the free-energy change of hydrogen (ΔG_{H}) at different hydrogen coverages on the bare, oxygenated, hydroxylated, or oxygenated/hydroxylated surfaces. The exchange current densities for each surface were derived to reflect their predicted HER activities (Figure 6b). An absolute value of 0.20 eV of ΔG_{H} is regarded as too large for a favorable adsorption/desorption. Based on this criterion, the sites on top of O of oxide δ -(111)-Mo, on top of C of hydroxyl G-(110), and hcp site of oxide η -(001)-Mo are regarded to be catalytically favorable. The values of ΔG_{H} were further optimized by considerations of different hydrogen coverages. Based on the hydrogen coverage determined by hydrogen adsorption ability on each surface, the calculated exchange current densities for every potential facet were combined into a volcano plot (Figure 6b). Nine surfaces were found to exhibit an exchange current density larger than 0.1 mA/cm^2 . It is interesting that most of them are terminated with carbon atoms and not covered by either oxygen or hydroxyl. This result suggests positive effects from surface carbon sites and inferior adsorption of water on Mo_xC surfaces for HER.

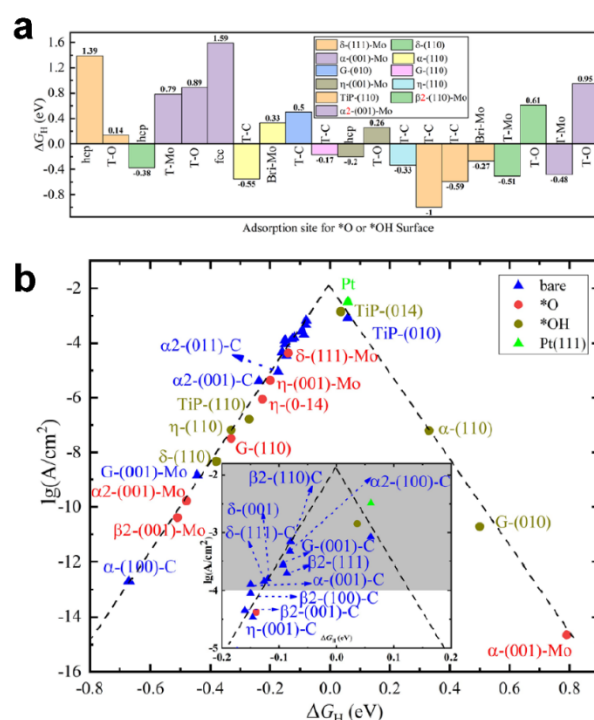


Figure 6. (a) Free-energy change of adsorbed H (ΔG_{H}) on different sites of O^* and HO^* surfaces. δ , α , G, η , TiP refer to different Mo_xC crystal phases and structures. (b) Exchange current densities as a function of hydrogen adsorbed free energy for MoC and Mo₂C surfaces. The grey area indicates the corresponding surfaces which exhibit an exchange current density larger than 0.1 mA/cm^2 . α 2 and β 2 represents α -MoC and β -Mo₂C, respectively. Reprinted with permission from Ref. [11].

The above simulation data highlights the effect of surface composition on catalytic properties and the potential applications to different reactions catalyzed by Mo_xC such as carbon dioxide utilization, biomass upgrading conversions, and electrochemical hydrogen generation. We examined electrocatalysis of surface oxidized Mo_xC catalysts towards HER, as this reaction is well studied and could be a good model reaction to evaluate the reactive sensitivity of catalyst surface or interface structures (Figure 7a) [45]. We performed controlled oxidation of Mo_2C nanoparticles and studied the effects of different surface compositions on HER activities (Figure 7b) [23]. The partially oxidized Mo_2C electrodes were tested for HER activity by linear scanning voltammetry (LSV). The HER polarization curves overlapped with each other for Mo_2C electrocatalysts formed under oxidative potentials up to 0.4 V (Mo_2C -0.4) and 0.6 V (Mo_2C -0.65), respectively, suggesting similar HER

catalytic properties. Based on XPS data, both carbides were partially oxidized to produce Mo oxycarbide surfaces under relatively mild oxidation conditions. For further oxidized $\text{Mo}_2\text{C}-x$ (x represents the upper limit of oxidative potentials and is equal to 0.75, 0.85, 0.975, and 1.2 V), the HER current densities decreased continuously with the increase of value x , indicating that a reduced HER activity due to the surface oxidation of Mo_2C catalysts (Figure 4).

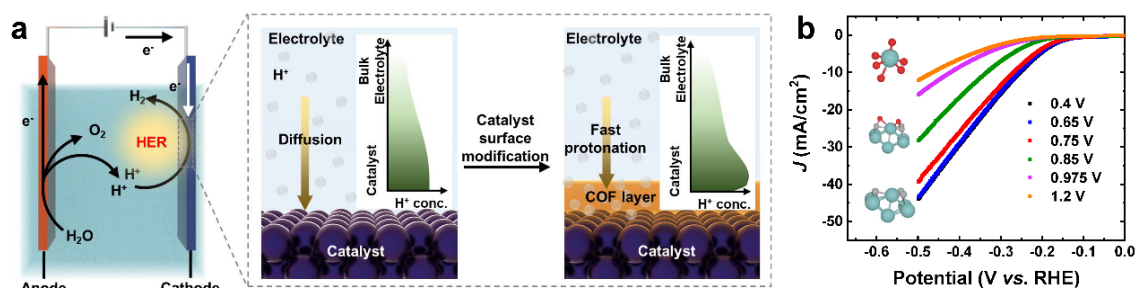


Figure 7. (a) Schematic illustration of electrode chemical reactions in water electrolyzer and the control of HER reactants (protons) at unmodified (left) and covalent organic framework-modified (right) electrode surfaces. Reprinted with permission from Ref. [45]. (b) Polarization curves of surface oxidized $\beta\text{-Mo}_2\text{C}$ electrocatalysts for the HER. Insets are the corresponding illustrations of nearest neighboring atoms for a given Mo with different oxidative states formed under different upper oxidation potentials. Reprinted with permission from Ref. [23].

5. Summary

Molybdenum carbide nanomaterials are promising electrocatalysts in multiple sustainable electrochemical conversion technologies, such as hydrogen production. Unlike noble metal catalysts, metal carbides are opted to surface oxidation, especially for those highly active nm-sized particles that are favored for catalysis. Controlled surface modification could be a powerful and feasible way to affect their electrochemical applications. Precision engineering of surface compositions and structures often require a better understanding of conversion processes. We recently showed electrooxidation can be an effective method for the control of surface compositions of Mo_xC catalysts, especially those made by solid-gas phase synthesis, in which case the pristine surface with no surfactant or other capping agents can be exposed. When properly excused, different degrees of surface oxidation are readily achievable by applying predetermined oxidative potentials. In the case of nm-sized $\beta\text{-Mo}_2\text{C}$ nm-sized catalysts, carbide, oxycarbide and oxide surfaces could all be controllable formed electrochemically. Quantum simulations suggest the above compositions are feasible as computational data matched well with the experimental observations. Interestingly, DFT calculation suggests imbedded carbon could also be selectively oxidized.

Experimentally, the surface oxidized $\beta\text{-Mo}_2\text{C}$ electrocatalysts indeed exhibited a great deal of sensitivity to surface composition or oxidation, as being demonstrated in HER. As Mo_xC can possess different bonds with metallic, covalent, and ionic features, which result in a vastly different adsorption/desorption of reactive agents and intermediates, it is no surprise that further controlling surface composition though precision electrooxidation could be a very useful tool for post-synthesis treatment of metal carbide electrocatalysts. It is anticipated electrooxidation should be applicable to change structural parameters of transition metal carbide nanocatalysts in different phases with (or without) heteroatom dopants and varied Mo valences, opening new avenues of developing non-precious metal catalysts for scalable chemical production processes.

Author Contributions: S.Y.: Conceptualization, Writing—original draft, Writing—review & editing. H.Y.: Conceptualization, Writing—review & editing, Supervision, Resources, Funding acquisition. All authors have read and agreed to the published version of the manuscript.

Funding: This work is supported in part by the National Science Foundation (CBET-2055734) and University of Illinois Urbana-Champaign (UIUC).

Data Availability Statement: Not applicable.

Conflicts of Interest: The authors declare no conflict of interest.

References

1. Huang, L.; Zheng, X.; Gao, G.; Zhang, H.; Rong, K.; Chen, J.; Liu, Y.; Zhu, X.; Wu, W.; Wang, Y.; et al. Interfacial electron engineering of palladium and molybdenum carbide for highly efficient oxygen reduction. *J. Am. Chem. Soc.* **2021**, *143*, 6933–6941.

2. Ge, R.; Huo, J.; Sun, M.; Zhu, M.; Li, Y.; Chou, S.; Li, W. Surface and interface engineering: Molybdenum carbide-based nanomaterials for electrochemical energy conversion. *Small* **2021**, *17*, 1903380.
3. Wu, J.; Yang, H. Platinum-based oxygen reduction electrocatalysts. *Acc. Chem. Res.* **2013**, *46*, 1848–1857.
4. Yu, S.; Yang, H. Design principles for the synthesis of platinum–cobalt intermetallic nanoparticles for electrocatalytic applications. *Chem. Comm.* **2023**, *59*, 4852–4871.
5. Tong, Y.; Zhang, Z.; Hou, Y.; Yan, L.; Chen, X.; Zhang, H.; Wang, X.; Li, Y. Recent progress of molybdenum carbide based electrocatalysts for electrocatalytic hydrogen evolution reaction. *Nanoscale* **2023**, *15*, 14717–14736.
6. Zhang, X.; Shi, C.; Chen, B.; Kuhn, A.N.; Ma, D.; Yang, H. Progress in hydrogen production over transition metal carbide catalysts: challenges and opportunities. *Curr. Opin. Chem. Eng.* **2018**, *20*, 68–77.
7. Liu, S.; Lin, Z.; Wan, R.; Liu, Y.; Liu, Z.; Zhang, S.; Zhang, X.; Tang, Z.; Lu, X.; Tian, Y. Cobalt phosphide supported by two-dimensional molybdenum carbide (MXene) for the hydrogen evolution reaction, oxygen evolution reaction, and overall water splitting. *J. Mater. Chem. A* **2021**, *9*, 21259–21269.
8. Zhang, B.; Zhou, J.; Elliott, S.R.; Sun, Z. Two-dimensional molybdenum carbides: Active electrocatalysts for the nitrogen reduction reaction. *J. Mater. Chem. A* **2020**, *8*, 23947–23954.
9. Li, Z.; Attanayake, N.H.; Blackburn, J.L.; Miller, E.M. Carbon dioxide and nitrogen reduction reactions using 2D transition metal dichalcogenide (TMDC) and carbide/nitride (MXene) catalysts. *Energy Environ. Sci.* **2021**, *14*, 6242–6286.
10. Wan, J.; Liu, Q.; Wang, T.; Yuan, H.; Zhang, P.; Gu, X. Theoretical investigation of platinum-like catalysts of molybdenum carbides for hydrogen evolution reaction. *Solid State Commun.* **2018**, *284–286*, 25–30.
11. Yu, G.-Q.; Huang, B.-Y.; Chen, X.; Wang, D.; Zheng, F.; Li, X.-B. Uncovering the surface and phase effect of molybdenum carbides on hydrogen evolution: A first-principles study. *J. Phys. Chem. C* **2019**, *123*, 21878–21887.
12. Wang, W.; Geng, W.; Zhang, L.; Zhao, Z.; Zhang, Z.; Ma, T.; Cheng, C.; Liu, X.; Zhang, Y.; Li, S. Molybdenum oxycarbide supported Rh-clusters with modulated interstitial C–O microenvironments for promoting hydrogen evolution. *Small* **2023**, *19*, 2206808.
13. Deng, B.; Wang, Z.; Chen, W.; Li, J.T.; Luong, D.X.; Carter, R.A.; Gao, G.; Jakobson, B.I.; Zhao, Y.; Tour, J.M. Phase controlled synthesis of transition metal carbide nanocrystals by ultrafast flash Joule heating. *Nat. Comm.* **2022**, *13*, 262.
14. Shrestha, A.; Gao, X.; Hicks, J.C.; Paolucci, C. Nanoparticle size effects on phase stability for molybdenum and tungsten carbides. *Chem. Mater.* **2021**, *33*, 4606–4620.
15. Hu, Z.; Zhang, L.; Huang, J.; Feng, Z.; Xiong, Q.; Ye, Z.; Chen, Z.; Li, X.; Yu, Z. Self-supported nickel-doped molybdenum carbide nanoflower clusters on carbon fiber paper for an efficient hydrogen evolution reaction. *Nanoscale* **2021**, *13*, 8264–8274.
16. Kuhn, A.N.; Park, R.C.; Yu, S.; Gao, D.; Zhang, C.; Zhang, Y.; Yang, H. Valorization of carbon dioxide into C1 product via reverse water gas shift reaction using oxide-supported molybdenum carbides. *Carbon Future* **2024**, *1*, 9200011.
17. Li, J.-S.; Wang, Y.; Liu, C.-H.; Li, S.-L.; Wang, Y.-G.; Dong, L.-Z.; Dai, Z.-H.; Li, Y.-F.; Lan, Y.-Q. Coupled molybdenum carbide and reduced graphene oxide electrocatalysts for efficient hydrogen evolution. *Nat. Commun.* **2016**, *7*, 11204.
18. Zhao, T.; Lan, D.; Jia, Z.; Gao, Z.; Wu, G. Hierarchical porous molybdenum carbide synergic morphological engineering towards broad multi-band tunable microwave absorption. *Nano Res.* **2024**, *17*, 9845–9856.
19. Baek, D.S.; Lee, J.; Kim, J.; Joo, S.H. Metastable phase-controlled synthesis of mesoporous molybdenum carbides for efficient alkaline hydrogen evolution. *ACS Catal.* **2022**, *12*, 7415–7426.
20. Wang, H.; Diao, Y.; Gao, Z.; Smith, K.J.; Guo, X.; Ma, D.; Shi, C. H₂ production from methane reforming over molybdenum carbide catalysts: From surface properties and reaction mechanism to catalyst development. *ACS Catal.* **2022**, *12*, 15501–15528.
21. Upadhyay, S.; Pandey, O.P. Synthesis and electrochemical applications of molybdenum carbide: Recent progress and perspectives. *J. Electrochem. Soc.* **2022**, *169*, 016511.
22. Guardia-Valenzuela, J.; Bertarelli, A.; Carra, F.; Mariani, N.; Bizzaro, S.; Arenal, R. Development and properties of high thermal conductivity molybdenum carbide–graphite composites. *Carbon* **2018**, *135*, 72–84.
23. Yu, S.; Gautam, A.K.; Gao, D.; Kuhn, A.N.; He, H.; Mironenko, A.V.; Yang, H. Implication of surface oxidation of nanoscale molybdenum carbide on electrocatalytic activity. *J. Mater. Chem. A* **2024**, *12*, 15163–15176.
24. Yang, Q.; Sun, K.; Xu, Y.; Ding, Z.; Hou, R. Tuning crystal phase of molybdenum carbide catalyst to induce the different selective hydrogenation performance. *Appl. Catal. A* **2022**, *630*, 118455.
25. Xiao, T.-c.; York, A.P.E.; Williams, V.C.; Al-Megren, H.; Hanif, A.; Zhou, X.-y.; Green, M.L.H. Preparation of molybdenum carbides using butane and their catalytic performance. *Chem. Mater.* **2000**, *12*, 3896–3905.
26. Tacey, S.A.; Jankousky, M.; Farberow, C.A. Assessing the role of surface carbon on the surface stability and reactivity of β -Mo₂C catalysts. *Appl. Surf. Sci.* **2022**, *593*, 153415.
27. Wyvrat, B.M.; Gaudet, J.R.; Thompson, L.T. Effects of passivation on synthesis, structure and composition of molybdenum carbide supported platinum water–gas shift catalysts. *J. Catal.* **2015**, *330*, 280–287.
28. Likith, S.R.J.; Farberow, C.A.; Manna, S.; Abdulsalam, A.; Stevanović, V.; Ruddy, D.A.; Schaidle, J.A.; Robichaud, D.J.; Ciobanu, C.V. Thermodynamic stability of molybdenum oxycarbides formed from orthorhombic Mo₂C in oxygen-rich environments. *J. Phys. Chem. C* **2018**, *122*, 1223–1233.

29. Yu, W.; Saliccioli, M.; Xiong, K.; Barteau, M.A.; Vlachos, D.G.; Chen, J.G. Theoretical and experimental studies of C–C versus C–O bond scission of ethylene glycol reaction pathways via metal-modified molybdenum carbides. *ACS Catal.* **2014**, *4*, 1409–1418.
30. Murugappan, K.; Anderson, E.M.; Teschner, D.; Jones, T.E.; Skorupska, K.; Román-Leshkov, Y. Operando NAP-XPS unveils differences in MoO₃ and Mo₂C during hydrodeoxygenation. *Nat. Catal.* **2018**, *1*, 960–967.
31. Kumar, A.; Bhan, A. Oxygen content as a variable to control product selectivity in hydrodeoxygenation reactions on molybdenum carbide catalysts. *Chem. Eng. Sci.* **2019**, *197*, 371–378.
32. Ammal, S.C.; Heyden, A. Active site identification for glycerol hydrodeoxygenation over the oxygen modified molybdenum carbide surface. *ACS Catal.* **2023**, *13*, 7499–7513.
33. Politi, J.R. d. S.; Viñes, F.; Rodriguez, J.A.; Illas, F. Atomic and electronic structure of molybdenum carbide phases: bulk and low Miller-index surfaces. *Phys. Chem. Chem. Phys.* **2013**, *15*, 12617–12625.
34. Ma, Y.; Guan, G.; Hao, X.; Cao, J.; Abudula, A. Molybdenum carbide as alternative catalyst for hydrogen production—A review. *Renewable Sustainable Energy Rev.* **2017**, *75*, 1101–1129.
35. Liu, X.; Salahub, D.R. Application of topological analysis of the electron localization function to the complexes of molybdenum carbide nanoparticles with unsaturated hydrocarbons. *Can. J. Chem.* **2016**, *94*, 282–292.
36. Ren, J.; Huo, C.-F.; Wang, J.; Cao, Z.; Li, Y.-W.; Jiao, H. Density functional theory study into the adsorption of CO₂, H and CH_x (x = 0–3) as well as C₂H₄ on α -Mo₂C(0001). *Surf. Sci.* **2006**, *600*, 2329–2337.
37. Zhao, L.; Yuan, H.; Sun, D.; Jia, J.; Yu, J.; Zhang, X.; Liu, X.; Liu, H.; Zhou, W. Active facet regulation of highly aligned molybdenum carbide porous octahedrons via crystal engineering for hydrogen evolution reaction. *Nano Energy* **2020**, *77*, 105056.
38. Wu, N.; Liu, J.; Zhao, W.; Du, J.; Zhong, W. Molybdenum carbide MXene embedded with nickel sulfide clusters as an efficient electrocatalyst for hydrogen evolution reaction. *Int. J. Hydrogen Energy* **2023**, *48*, 17526–17535.
39. Yang, C.; Zhao, R.; Xiang, H.; Wu, J.; Zhong, W.; Li, X.; Zhang, Q. Structural transformation of molybdenum carbide with extensive active centers for superior hydrogen evolution. *Nano Energy* **2022**, *98*, 107232.
40. Sullivan, M.M.; Bhan, A. Acid site densities and reactivity of oxygen-modified transition metal carbide catalysts. *J. Catal.* **2016**, *344*, 53–58.
41. Yao, S.; Yan, B.; Jiang, Z.; Liu, Z.; Wu, Q.; Lee, J.H.; Chen, J.G. Combining CO₂ reduction with ethane oxidative dehydrogenation by oxygen-modification of molybdenum carbide. *ACS Catal.* **2018**, *8*, 5374–5381.
42. Sullivan, M.M.; Held, J.T.; Bhan, A. Structure and site evolution of molybdenum carbide catalysts upon exposure to oxygen. *J. Catal.* **2015**, *326*, 82–91.
43. Sullivan, M.M.; Bhan, A. Effects of oxygen coverage on rates and selectivity of propane-CO₂ reactions on molybdenum carbide. *J. Catal.* **2018**, *357*, 195–205.
44. Gautam, A.K.; Yu, S.; He, H.; Yang, H.; Mironenko, A.V. Role of surface oxygen in α -MoC catalyst stability and activity under electrooxidation conditions. *ChemRxiv* **2024**. <https://doi.org/10.26434/chemrxiv-2024-xwh17>.
45. Park, J.H.; Lee, C.H.; Yu, S.; Kharel, P.; Choi, R.; Zhang, C.; Huang, P.Y.; Kwon, J.S.-I.; Yang, H. Effects of amine-based covalent organic framework on platinum electrocatalyst performance towards hydrogen evolution reaction. *Nano Energy* **2024**, *128*, 109947.

Review

Emerging Piezoelectric Metamaterials for Biomedical Applications

Zishuo Yan ¹, Huy Tran ¹, Dezun Ma ¹, and Jingwei Xie ^{1,2,*}

¹ Department of Surgery-Transplant and Mary & Dick Holland Regenerative Medicine Program, University of Nebraska Medical Center, Omaha, NE, 68198, USA

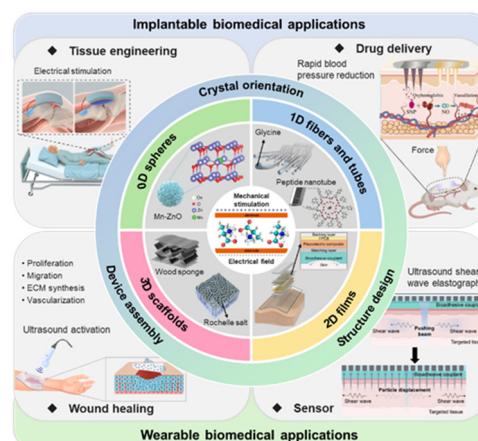
² Department of Mechanical and Materials Engineering, University of Nebraska Lincoln, Lincoln, NE, 68588, USA

* Correspondence: jingwei.xie@unmc.edu

Received: 30 September 2024; Revised: 18 November 2024; Accepted: 20 November 2024; Published: 21 November 2024

Abstract: Emerging piezoelectric metamaterials hold immense promise for biomedical applications by merging the intrinsic electrical properties of piezoelectricity with the precise architecture of metamaterials. This review provides a comprehensive overview of various piezoelectric materials—such as molecular crystals, ceramics, and polymers—known for their exceptional piezoelectric performance and biocompatibility. We explore the advanced engineering approaches, including molecular design, supramolecular packing, and 3D assembly, which enable the customization of piezoelectric properties for targeted biomedical applications. Particular attention is given to the pivotal role of metamaterial structuring in the development of 0D spheres, 1D fibers and tubes, 2D films, and 3D scaffolds. Key biomedical applications, including tissue engineering, drug delivery, wound healing, and biosensing, are discussed through illustrative examples. Finally, the article addresses critical challenges and future directions, aiming to drive further innovations in piezoelectric biomaterials for next-generation healthcare technologies.

Keywords: piezoelectric metamaterials, molecular design, supramolecular packing, 3D assembly, biomedical applications



1. Introduction

As public focus and demand for health management continue to grow, the intersection of advanced materials science and biomedical engineering has given rise to a transformative field [1–3]. This development redefines the boundaries of medical science, aiming to address medical challenges and enhance patient care through innovative materials. One of the most promising engineered biomedical materials is piezoelectric metamaterials, which combine the electrically stimulating functional properties of piezoelectricity with the complex structural design possibilities of metamaterials [4,5]. Piezoelectric materials have the capacity to convert mechanical stress into electrical energy, a phenomenon arising from the intrinsic structural asymmetry of the material [6–8]. In piezoelectric materials, the non-centrosymmetric crystal structure induces the formation of electric dipoles. When mechanical stress is applied, the internal polarization of the material alters and results in a surface voltage. This capability has been utilized to stimulate cellular growth and repair in tissue regeneration, enhance controlled drug delivery through electrically regulated release mechanisms, accelerate wound healing by providing electrical stimulation to promote cellular migration and proliferation at the wound site and enable precise sensing of physiological and environmental changes by translating mechanical signals into electrical responses [9–13]. Piezoelectric materials are often oriented to enhance their performance and functionality, as the direction of their response is highly dependent on the alignment of their internal crystal structures [14–16].

Metamaterials, defined by their engineered structural properties, have evolved from their foundational applications in electromagnetism to a wide range of materials science fields, including energy harvesting, acoustic



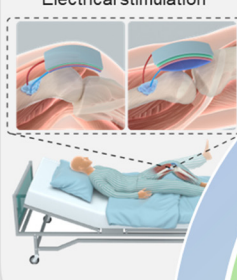
Copyright: © 2024 by the authors. This is an open access article under the terms and conditions of the Creative Commons Attribution (CC BY) license (<https://creativecommons.org/licenses/by/4.0/>).

Publisher's Note: Scilight stays neutral with regard to jurisdictional claims in published maps and institutional affiliations

Implantable biomedical applications


◆ Tissue engineering

Electrical stimulation



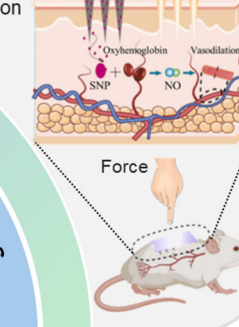
• Proliferation
• Migration
• ECM synthesis
• Vascularization

Ultrasound activation

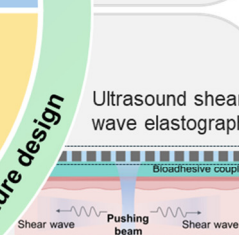


◆ Drug delivery

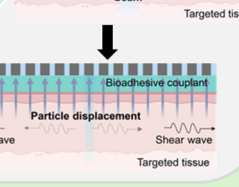
Rapid blood pressure reduction



Force



Ultrasound shear wave elastography



◆ Wound healing

◆ Sensor

Crystal orientation

0D spheres

1D fibers and tubes

2D films

3D scaffolds

Device assembly

Structure design

Electrical stimulation

Electrical field

Mn-ZnO

Glycine

Peptide nanotube

Wood sponge

Rochelle salt

Backing layer (PCP)

Piezoelectric composite

Matching layer

Bioadhesive couplant

Skin

Particle displacement

Targeted tissue

Wearable biomedical applications

14

and biosensing. Tissue engineering: Reproduced with permission [39]. Copyright 2024, The American Association for the Advancement of Science. Drug delivery: Reproduced with permission [40]. Copyright 2024, Elsevier. Wound healing: Reproduced with permission [41]. Copyright 2023, Elsevier. Sensor and 2D films: Reproduced with permission [42]. Copyright 2024, The American Association for the Advancement of Science. 0D spheres: Reproduced with permission [43]. Copyright 2023, Wiley. 1D fibers: Reproduced with permission [44]. Copyright 2023, The American Association for the Advancement of Science. 1D tubes: Reproduced under the terms of the CC BY license [45]. Copyright 2019, Authors, published by AIP Publishing. Wood sponge: Reproduced with permission [46]. Copyright 2020, American Chemical Society. 3D scaffolds with Rochelle salt: Reproduced with permission [47]. Copyright 2023, Springer Nature. Piezoelectric effect: Reproduced with permission [48]. Copyright 2018, American Chemical Society.

2. Piezoelectric Materials

To meet the stringent requirements of biomedical applications, piezoelectric materials should demonstrate both high piezoelectric coefficients and excellent biocompatibility. Since the piezoelectric effect arises in noncentrosymmetric crystals, this section provides a detailed overview of key piezoelectric materials, categorized into three major groups: (1) molecular crystals, (2) ceramics, and (3) polymers.

2.1. Molecular Crystals

Previous studies have demonstrated that various biological materials, both in the human body and nature, such as collagen, viruses, amino acids, cellulose, chitin, and silk, exhibit piezoelectric properties [49–54]. Among these, glycine, a simple and biocompatible amino acid, stands out due to its piezoelectricity in two of its crystalline forms: the β and γ -phases, while its α -phase is non-piezoelectric [55]. Yang et al. employed electrohydrodynamic spraying to fabricate piezoelectric β -glycine films, which resemble the polycrystalline morphology found in inorganic materials [56]. Their approach combined nanoconfinement and in situ electric fields during glycine nucleation and self-assembly, simulating the sintering and polarization steps used piezoelectric ceramic fabrication. Similarly, Wang et al. prepared wafer-scale heterostructured piezoelectric glycine films using a direct solidification process [57]. The hydrogen bonding between glycine and polyvinyl alcohol (PVA) at the interface facilitated the formation of self-aligned γ -glycine crystals with enhanced piezoelectricity. Building on this, Wu et al. focused on optimizing glycine's piezoelectric potential by refining its crystal orientation [58]. Their study, employing density functional theory (DFT), examined γ -glycine's crystal structure and the origin of its piezoelectric properties. Figure 2a,b depict the charge density distribution, highlighting the high charge densities of O and N atoms, with N atoms extending to H3, suggesting the formation of hydrogen bonds with surrounding molecules. Among the piezoelectric coefficients, the d_{33} was identified as the most significant, with a value of 9.53 pC N^{-1} (Figure 2c). Further analysis revealed that optimal piezoelectric performance of γ -glycine is achieved when the crystals are oriented at the smallest possible angle on the substrate (Figure 2d). Additionally, when glycine crystals are stretched, the increased intermolecular distance weakens hydrogen bonds, causing molecular contraction and a corresponding reduction in polarization (Figure 2e). This highlights the sensitivity of glycine's piezoelectric properties to molecular interactions and mechanical strain.

To advance the development and application of γ -glycine in biomedical applications, self-assembled γ -glycine/PVA films were synthesized using an ultrasonic-assisted mixing-solidification technique (Figure 2f,g). The output voltages of these films increased proportionally with trigger voltages, reaching approximately 220 mV at 110 Vpp (Figure 2h). In addition to direct solidification, Nguyen et al. used electrospinning to fabricate glycine-poly(ϵ -caprolactone) (PCL) nanofibers with highly oriented glycine crystals [44]. This hybrid electrospinning technique, which involves high voltage and rapid collector speeds, stretches and aligns the nanofibers, resulting in enhanced piezoelectric properties in glycine-PCL nanofibrous membranes [59]. The applied electric field during electrospinning improves the polarization of glycine within the fibers by reorienting the crystalline dipoles. Scanning electron microscopy (SEM) images of PCL and glycine-PCL nanofibers revealed their surface morphology and the incorporation of glycine crystals within individual nanofibers (Figure 2i). The aligned electrospun membranes demonstrated a displacement of approximately $12 \mu\text{m}$, in contrast to solvent-cast and randomly oriented samples, which showed no measurable displacement (Figure 2j). These results suggest that aligned glycine-PCL nanofibrous membranes hold significant potential as actuators for ultrasonic applications under applied voltage. However, most glycine-based materials are currently limited to out-of-plane piezoelectric responses, which correspond to longitudinal and transverse piezoelectric coefficients. This leaves the full potential of shear piezoelectricity yet to be explored. Notably, β -glycine exhibits piezoelectric responses as high as 180 pC N^{-1} [60]. Future research should focus on optimizing the spatial arrangement of these materials to create

stress distributions dominated by shear forces, enabling more effective utilization of shear piezoelectricity in integrated devices.

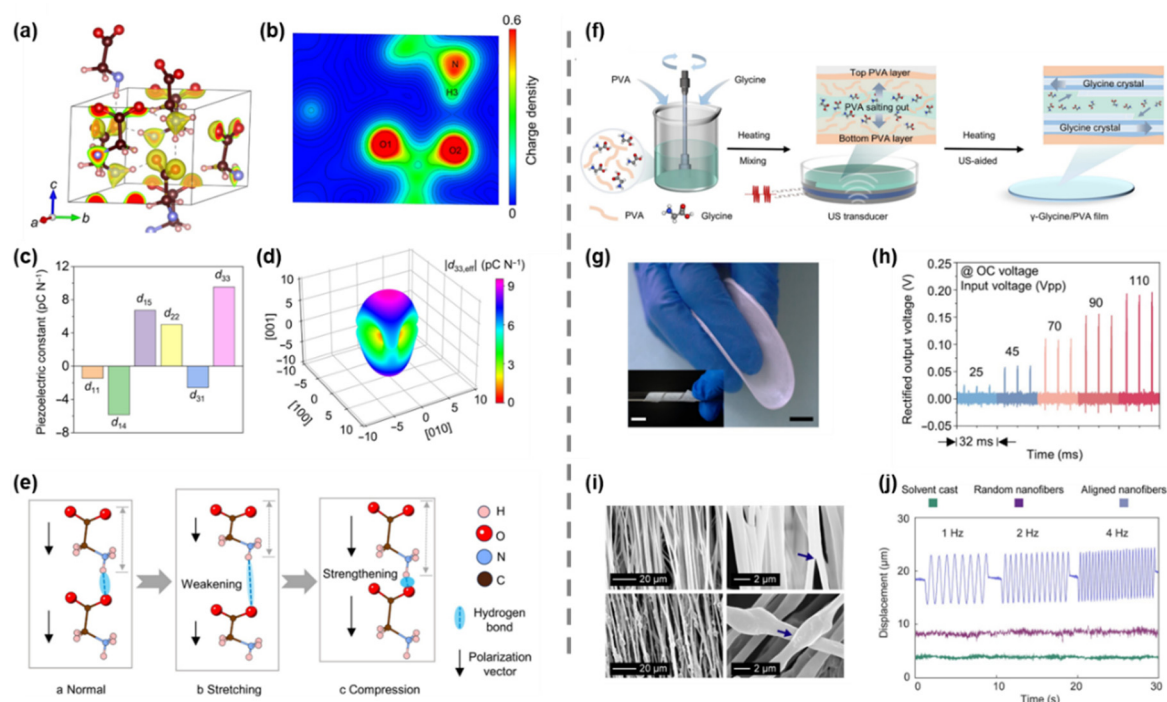


Figure 2. Glycine-based piezoelectric materials. (a) Schematic diagram and (b) contour plot of charge density distribution of γ -glycine molecules. (c) Piezoelectric constants of γ -glycine. (d) Orientation dependence of $d_{33,\text{eff}}$. (e) The piezoelectric effect of γ -glycine induced by the hydrogen bonding interactions. (f) The fabrication process of γ -glycine/PVA films. (g) Optical photographs of the flexible γ -glycine/PVA films. The inset shows the twisted films. Scale bars, 10 mm. (h) Voltage output of glycine/PVA films. (a–h) Reproduced with permission [58]. Copyright 2024, The American Association for the Advancement of Science. (i) SEM images of PCL (top) and glycine-PCL (bottom) fibers. (j) Displacement of solvent-casting, random electrospinning, and aligned electrospinning films. (i–j) Reproduced with permission [44]. Copyright 2023, The American Association for the Advancement of Science.

2.2. Ceramics

Some of the earliest piezoelectric materials identified, such as quartz and Rochelle salt, were utilized in ultrasound technologies throughout the 20th century [61,62]. In recent years, ceramics with excellent piezoelectric properties and chemical stability, such as biocompatible zinc oxide (ZnO) and zinc stannate, have been applied in biomedical applications [63–65]. Cauda et al. investigated the effectiveness of piezoelectric ZnO micro- and nanoparticles in ultrasound-assisted sonodynamic therapy for cancer treatment [66]. Their research demonstrated that the combined ZnO-ultrasound treatment exhibited remarkable efficacy against osteosarcoma and glioblastoma cell lines in vitro. ZnO's role as a catalyst for reactive oxygen species (ROS) production under ultrasound underscores its therapeutic potential. However, the intrinsic rigidity and brittleness of ceramic materials limit their mechanical tolerance to defects and external strains [67–69]. To address these limitations, bio-piezoelectric ceramics have been incorporated into flexible films and fibers to enhance mechanical robustness. For example, Zhu et al. developed a Janus nanofibrous scaffold with piezoelectric properties designed to promote tendon-to-bone healing [70]. The scaffold was prepared by electrospinning poly (*L*-lactic acid) (PLLA)/ZnO (OPZ) and PLLA/barium titanate (RBP), with fiber alignment varying between the layers by manipulating the rotating speed of the roller (Figure 3a). The OPZ layer featured aligned fibers, while the RBP layer contained randomly oriented fibers, mimicking the natural structural of collagen fibers in tendons and bones. This specific configuration was aimed at promoting topographical effects that support tendon-to-bone healing. The OPZ/RBP scaffold possessed remarkable structural integrity and flexibility. The OPZ layer's fibers had an average diameter of 756.84 nm, while the RBP layer's fibers measured 986.52 nm in diameter (Figure 3b,c). As illustrated in Figure 3d, the scaffold's piezoelectric performance significantly outperformed pure PLLA scaffolds, with a 110.78% increase in voltage output compared to a bilayered oriented PLLA/random PLLA (OP/RP) scaffold. Furthermore, the OPZ/RBP scaffold was able to generate real-time electrical signals in response to subtle body movements (Figure 3e). The

durability of the biocompatible scaffold was evidenced by maintaining over 80% of its piezoelectric output even after four weeks of immersion in a PBS solution, highlighting its exceptional capacity for providing electrical stimulation (Figure 3f). In addition, the OPZ/RPB scaffold has outstanding mechanical properties, making it highly suitable for rotator cuff repair (Figure 3g). While combining ceramic crystals with polymer matrices in flexible composites enhances performances, it is crucial to address a commonly overlooked issue the viscoelastic properties of the polymer matrix. Over time, polymer creep can occur under load, reducing stress transfer efficiency and ultimately affecting the piezoelectric performance of the device. This issue must be a focus of future research and development to further optimize the long-term functionality of these flexible piezoelectric composites.

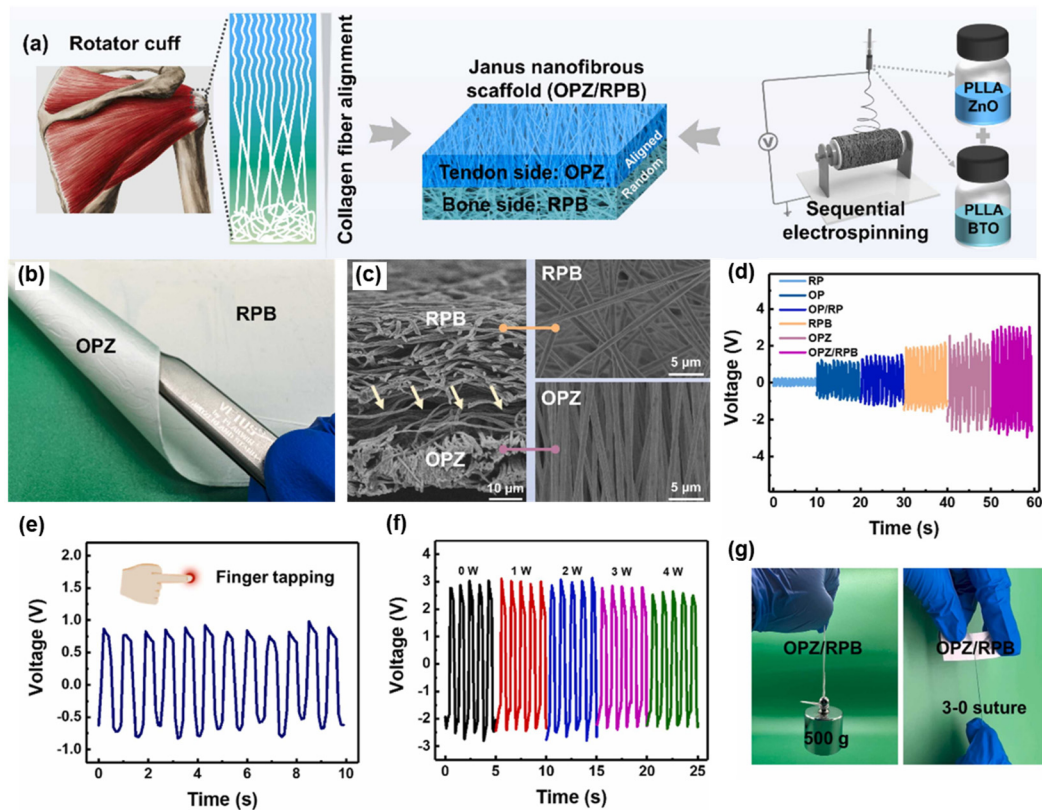


Figure 3. Ceramic-based piezoelectric materials. (a) The fabrication process of the Janus piezoelectric nanofibrous scaffolds. (b) The optical photographs of the OPZ/RPB scaffold. (c) The SEM images of the OPZ/RPB scaffold. (d) Voltage output of the scaffolds under an external periodic impact force (20 kPa, 1 Hz). (e) Voltage output of the OPZ/RPB scaffold under slight finger tapping. (f) The maintenance of the piezoelectric output during the degradation period. (g) The mechanical performances of the OPZ/RPB scaffold. Reproduced with permission [70]. Copyright 2024, Elsevier.

2.3. Polymers

Polymers with asymmetrical molecular structures and orientations are highly attractive as piezoelectric materials due to their superior mechanical flexibility, ease of low-temperature processing, and design versatility compared to inorganic alternatives. In particular, biodegradable and biocompatible polymers like PLLA and its composites are widely employed in implantable and wearable biomedical applications [71–73]. Wang et al. developed a core-shell structure of PLLA/glycine nanofibers using an electrospinning technique through an interfacial anchoring strategy [74]. These nanofibers exhibit a high proportion of piezoelectric β -phase and excellent alignment. The self-assembled core-shell architecture promoted strong intermolecular interactions between the hydroxyl groups of glycine and the carbonyl groups of PLLA, facilitating the formation and alignment of β -phase in PLLA. Piezoresponse force microscopy (PFM) which was used to characterize the piezoelectric properties revealed a d^{eff} value of 2.21 pm V⁻¹ for individual fibers. A stable voltage output with a peak-to-peak voltage of 1.2 V is achieved under repetitive pressure applied over a vertical distance of 8 mm at a frequency of 4 Hz. In addition to nanofibers, Tang et al. utilized microinjection molding to fabricate hybrid PLLA/polyvinylidene fluoride (PLLA/PVDF) micro bone screws with enhanced toughness for bone repair [75]. SEM images of the screws showed high-quality fabrication with smooth surfaces and no visible defects (Figure 4a,b). After bending tests, digital images confirmed the improved mechanical properties of the screws,

attributed to the incorporation of PVDF (Figure 4c). During microinjection molding, the shear stress field induced the in-situ formation of highly oriented PVDF fiber arrays (Figure 4d–g). These aligned PVDF fibers significantly enhanced both the toughness and strength of the micro bone screws. Piezoelectric testing demonstrated that these screws could generate an open-circuit voltage of up to 2 V (Figure 4h). Although multiple physical field methods including electric field and directional shear force field could induce phase transitions or orientation alignment in polymer crystals, the piezoelectric performance of polymer-based materials remains significantly lower than that of piezoelectric ceramics and single crystals. To meet higher performance demands, future research should focus on constructing porous structures to enhance polarization efficiency and improve the piezoelectric properties of polymer-based materials.

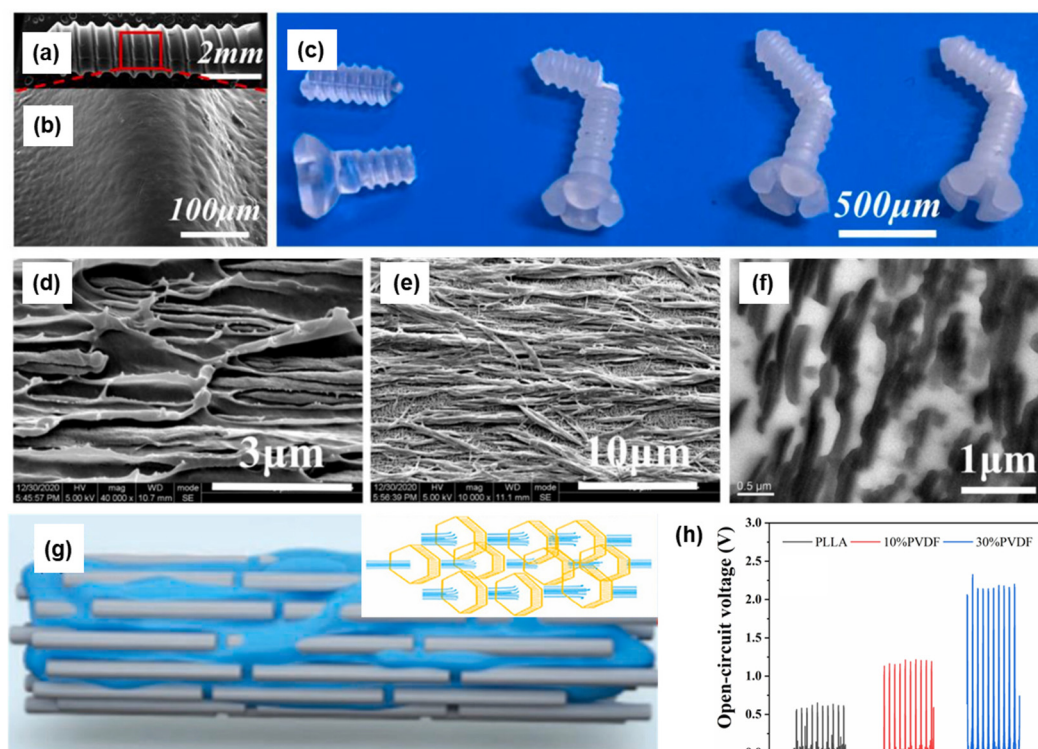


Figure 4. Polymer-based piezoelectric materials. (a,b) The SEM images of micro bone screw. (c) Optical photographs of the micro bone screw after three-point bending test (from left to right: 0 wt%, 10 wt%, 20 wt%, and 30 wt% PVDF, respectively). The morphology characterization of PVDF dispersed phase fibers: (d) SEM images of cryo-fracture surface, (e) after etching PLLA matrix and (f) transmission electron microscopy image. (g) The formation of the submicron PVDF fibers. (h) The piezoelectric performances of micro bone screws. Reproduced with permission [75]. Copyright 2024, Elsevier.

Table 1 summarizes the piezoelectric properties of various biomaterials, including their composition, fabrication methods, structures, piezoelectric performances, and applications. In brief, piezoelectric ceramic materials are renowned for their high piezoelectric performance, making them valuable for a wide range of applications. However, their inherent rigidity and brittleness limit their integration into flexible or dynamic systems. Furthermore, many piezoelectric ceramics lack biodegradability and biocompatibility, necessitating restrictions of their use in medical devices. In contrast, piezoelectric polymers are flexible, lightweight, and easily deployable. However, repeated mechanical stress and strain could induce changes in their internal structures through mechanisms such as creep. The accumulation of such changes ultimately leads to a gradual decline in their piezoelectric performance of the polymers. Molecular crystals, such as amino acids, exhibit excellent biocompatibility and biodegradability. Despite these advantages, their piezoelectric performance is relatively low, often relegating them to roles as fillers in polymer matrices.

Table 1. Summary of piezoelectric properties of biomaterials.

	Piezoelectric Composition	Fabrication Method	Morphology	Piezoelectric Performance	Application	Refs.
0D	Amide-functionalized sulfonic acid bioorganic monomers	Hydrothermal method	Crystals	$d_{11} = 15.9 \text{ pm V}^{-1}$	/	[76]
	Mn–Ti bimetallic organic framework	Hydrothermal method	Particles	$d_{33} = 151 \text{ pm V}^{-1}$	Tumor therapy	[77]
	MoS ₂	Hydrothermal method	Nanoflowers	99 mV (measured by PFM under an applied voltage of 3 V)	Drug delivery	[78]
1D	Barium titanate (BTO)/PLLA BTO	Electrospinning	Nanofibers	1.25 V (under the strain of 6 %)	Wound healing dressings	[79]
	nanowires/polyvinylidene fluoride-trifluoroethylene P(VDF-TrFE)	Electrospinning	Coaxial nanofibers	18.2 V (under an impact force of 5 N)	Physiological multimodal sensing	[80]
	Al ion doped strontium titanate/titanium dioxide	Anodic oxidation, annealing, and hydrothermal reaction	Nanotubes	$d_{33} = 13.8 \text{ pm V}^{-1}$	Antibacterial Therapy	[81]
2D	PVA/Glycine/PVA	Electric field-assisted water evaporation	Film	$d_{33} = 6.6 \text{ pC N}^{-1}$	Nanogenerator	[82]
	β -glycine/alginate/glycerol	Solvent-casting method	Film	$d_{33} = 7.2 \text{ pC N}^{-1}$	Sensor in artificial cochlea	[83]
	DL-alanine	Solution-Phase Self-Assembly	Biocrystal network	150 mV (under an impact force of 6 N)	Tactile sensor	[84]
3D	BTO/bioactive glasses	3D printing	Scaffold	$d_{33} = 1.1 \text{ pC N}^{-1}$	Bone regeneration	[85]
	BTO/P(VDF-TrFE)	Electrospinning and cross-linking polymerization with poly(N-isopropylacrylamide)	Nanofibrous hydrogel conduit	1.69 V (under US stimulation with 0.75 W cm^{-2})	Nerve regeneration	[15]
	1,3-propanediol, 2,3-butanediol, sebacic acid, succinic acid, and itaconic acid	Random copolymerization and hot press molding	Elastomer scaffold	0.9 V (50% horizontal elongation)	Repairing of skeletal muscles loss	[86]

3. Multi-Level Structural Construction Strategies

Recent advancements in mechanical engineering and material fabrication technologies have paved the way for high-performance piezoelectric devices, unlocking new possibilities for biomedical applications. This section highlights key strategies to enhance piezoelectric performance, while also improving structural stability and durability through innovations in molecular design, supramolecular packing, and 3D assembly techniques.

3.1. Molecular Design

Although biodegradable materials such as collagen, cellulose, and PLLA have been investigated for biomedical applications, there remains a need for biomaterials with superior piezoelectric properties [22]. In this context, Xiong et al. pioneered the development of a molecular crystal $\text{HOCH}_2(\text{CF}_2)_3\text{CH}_2\text{OH}$ [2,2,3,3,4,4-hexafluoropentane-1,5-diol (HFPD)], exhibiting a remarkable piezoelectric response of 138 pC N^{-1} , which is more than 13 times higher than glycine [87,88]. HFPD molecules form a 2D hydrogen-bonded layer through $\text{O}-\text{H}\cdots\text{O}$ interactions, while the asymmetric distribution of C-F bonds creates non-zero molecular dipole moments, aligned by the hydrogen-bonded structure (Figure 5a,b). The mechanical properties of HFPD crystals revealed significant anisotropy in the directional Young's modulus, with two maximum values aligned on an elliptical plane. This anisotropy stems from the 2D hydrogen-bonding network and the ordered arrangement of F atoms (Figure 5c). The spatial dependence of the shear modulus also displays a shell-like structure, where the MIN surface is nested within the MAX surface, contributing to the high piezoelectric coefficient (Figure 5d,e). The piezoelectric performance of HFPD was characterized using PFM (Figure 5f,g), showing a much higher response peak compared to PVDF. The estimated piezoelectric coefficient for HFPD is 119.3 pm/V , significantly outperforming PVDF's 18.8 pm/V . These findings suggest that HFPD molecular crystals could be developed into flexible piezoelectric films suitable for drug delivery, energy-harvesting devices, and tissue engineering scaffolds. In parallel, Ji et al. investigated how molecular design could enhance the piezoelectricity of amino acid-based materials [89]. They found that chemically modifying amino acid side chains through acetylation could increase molecular polarization, significantly enhancing the piezoelectric response. For example, acetylated tryptophan was predicted to have a piezoelectric strain constant of 47 pm V^{-1} , comparable to that of bismuth triboride. These results emphasize the critical role of molecular design in optimizing the piezoelectric properties of biomolecular crystals.

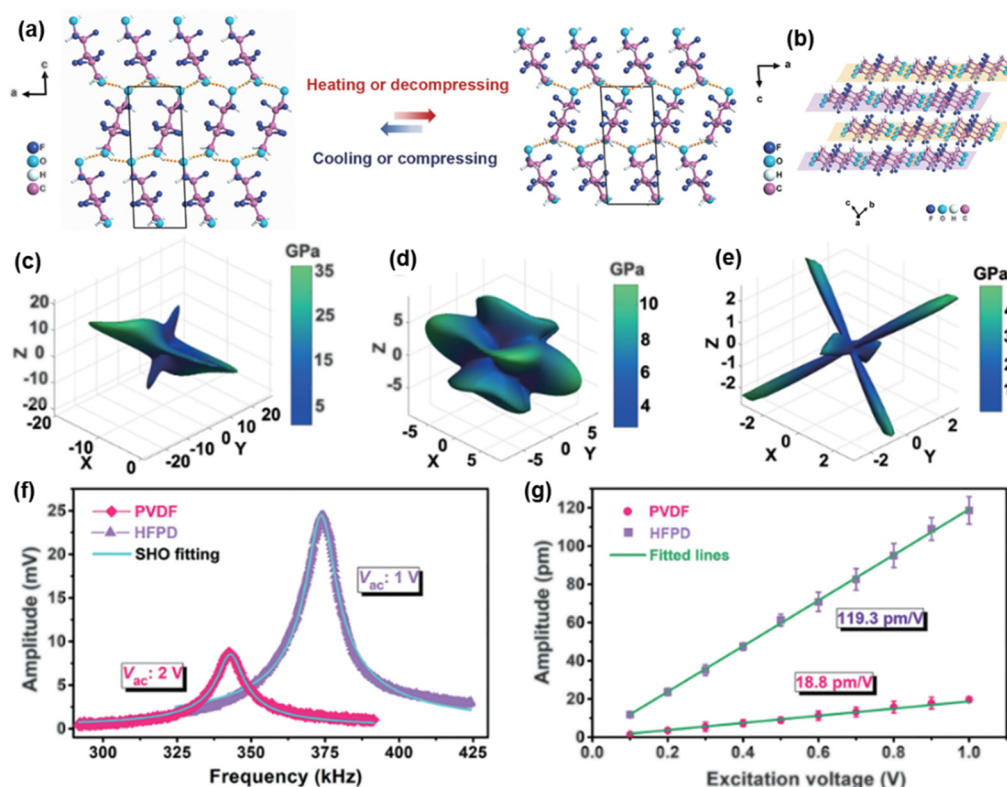


Figure 5. Molecular design for enhancing piezoelectric properties. (a) The transition of 2D monolayer formed through O–H···O interactions. (b) Packing view of 2D hydrogen bond layers. 3D plots of elastic modulus of HFPD crystals: (c) Young’s modulus, (d) shear modulus MAX, and (e) shear modulus MIN. (f) Piezoelectric response of HFPD and PVDF films versus excitation frequency measured with PFM. (g) The derived amplitude curve for HFPD and PVDF films. Reproduced with permission [87]. Copyright 2024, The American Association for the Advancement of Science.

3.2. Supramolecular Packing

Supramolecular packing involves the organized assembly of molecules through non-covalent interactions, such as hydrogen bonding, van der Waals forces, and π - π stacking. Researchers have employed various strategies, including template-assisted methods, dynamic self-assembly, and the use of external electrostatic and magnetic fields, to align molecules along specific crystallographic planes and directions, thereby affecting the overall dipole moment and enhancing piezoelectric properties [90–92]. For instance, Thompson et al. demonstrated how co-crystallization can enhance the piezoelectric properties of materials by using glycine and sulfamic acid as examples [60]. While these co-formers typically crystallize in centrosymmetric space groups when grown independently, co-crystallization leads to the formation of non-centrosymmetric, piezoelectrically active ionic co-crystals. In a related study, Feng et al. engineered flexible β -glycine/Nb₂CT_x piezoelectric nanofibers using a nanoconfinement self-assembly approach, which locked aligned crystal domains through interfacial polarization (Figure 6a) [93]. Nb₂CT_x nanosheets acted as nucleating agents, guiding the crystallization of glycine from the edges to the surfaces along its 2D crystal plane. This spontaneous kinetic crystallization process allowed precise control over the orientation of the glycine crystals. To elucidate the mechanism of the polarization templating, the interaction between glycine and the nanosheets was explored through DFT (Figure 6b,c). The alignment orientations and the electronic charge density difference map indicate the formation of weak ionic bonds between glycine and Nb₂CT_x nanosheets, facilitating preferential crystallization of glycine on the nanosheet surfaces. After the co-crystallization process, glycine crystallizes into β -phase, optimally oriented on the Nb₂CT_x nanosheets, forming an interfacial polarization lock. This configuration maintained a non-zero net polarization in the glycine crystals, yielding piezoelectric coefficients d_{16} and d_{22} (Figure 6d,e). Experimental results demonstrated that these glycine/Nb₂CT_x co-crystals grew uniformly on aligned nanofiber substrates, generating a stable output voltage of 4.3 V under a stress of 10 N (Figure 6f,g).

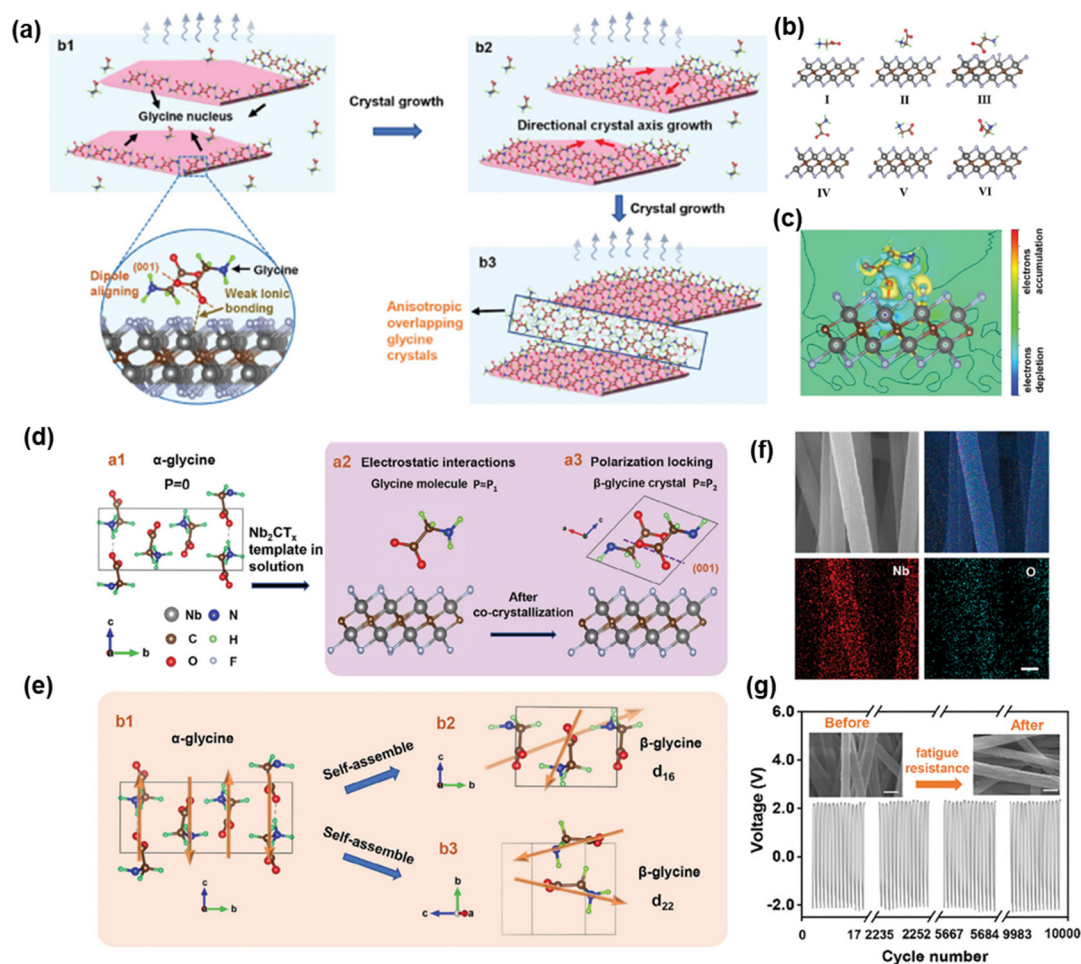


Figure 6. Supramolecular packing for enhancing piezoelectric properties. (a) The growth mechanism of glycine on Nb₂CT_x nanosheets. (b) Adsorption configurations of glycine-Nb₂CT_x nanosheets. (c) Difference of charge density contour on adsorption plane. (d) Formation of piezoelectric glycine induced by Nb₂CT_x nanosheets. (e) Piezoelectric response in glycine crystals with molecular dipoles. (f) SEM image of obtained nanofibers and corresponding EDS map of O and Nb elements. Scale bar = 400 nm. (g) Stability of the piezoelectric output. The inset shows the SEM image before and after fatigue resistance. Scale bar = 400 nm. Reproduced with permission [93]. Copyright 2024, Wiley.

3.3. Three-Dimensional Assembly

3D piezoelectric materials, known for their complex structures, superior mechanical properties, lightweight nature, and enhanced surface activity, hold significant promise for applications in biomedical sensors, tissue engineering scaffolds, and wearable devices [94–97]. Inspired by the unique chambered wall-septa microstructure of cuttlebone, Yang et al. developed a biomimetic 3D piezoelectric composite with enhanced mechanical and electrical properties [47]. They utilized stereolithography to create a photocurable resin model mimicking the cuttlebone structure, then grew recyclable piezoelectric Rochelle salt crystals within the resin framework (Figure 7a). When compared to other conventional structures with the same dimensions (e.g., cubic, honeycomb, and triangular), the cuttlebone-inspired composite exhibited the least deformation and most uniform stress distribution under compressive loads (Figure 7b). As shown in Figure 7c, the composite was integrated into devices with silver electrodes to evaluate its piezoelectric properties, showing a robust response to varying force levels and producing significant voltage outputs. Moreover, the composite exhibited excellent durability, maintaining stable voltage output over 6800 shock cycles (Figure 7d,e). These biomimetic 3D piezoelectric composites offer both exceptional mechanical protection and impressive sensing capabilities, making them ideal for applications such as smart knee pads. These pads can deliver integrated mechanical protection, act as fall detection alarms, and collect data for medical evaluation. In addition to biomimetic design, advanced technologies such as 3D printing and 3D weaving have been employed to assemble complex piezoelectric materials [98,99]. These fabrication methods enable the creation of complex, customized structures that enhance the functionality and performance of

piezoelectric composites, paving the way for innovative applications and improved integration into various smart devices.

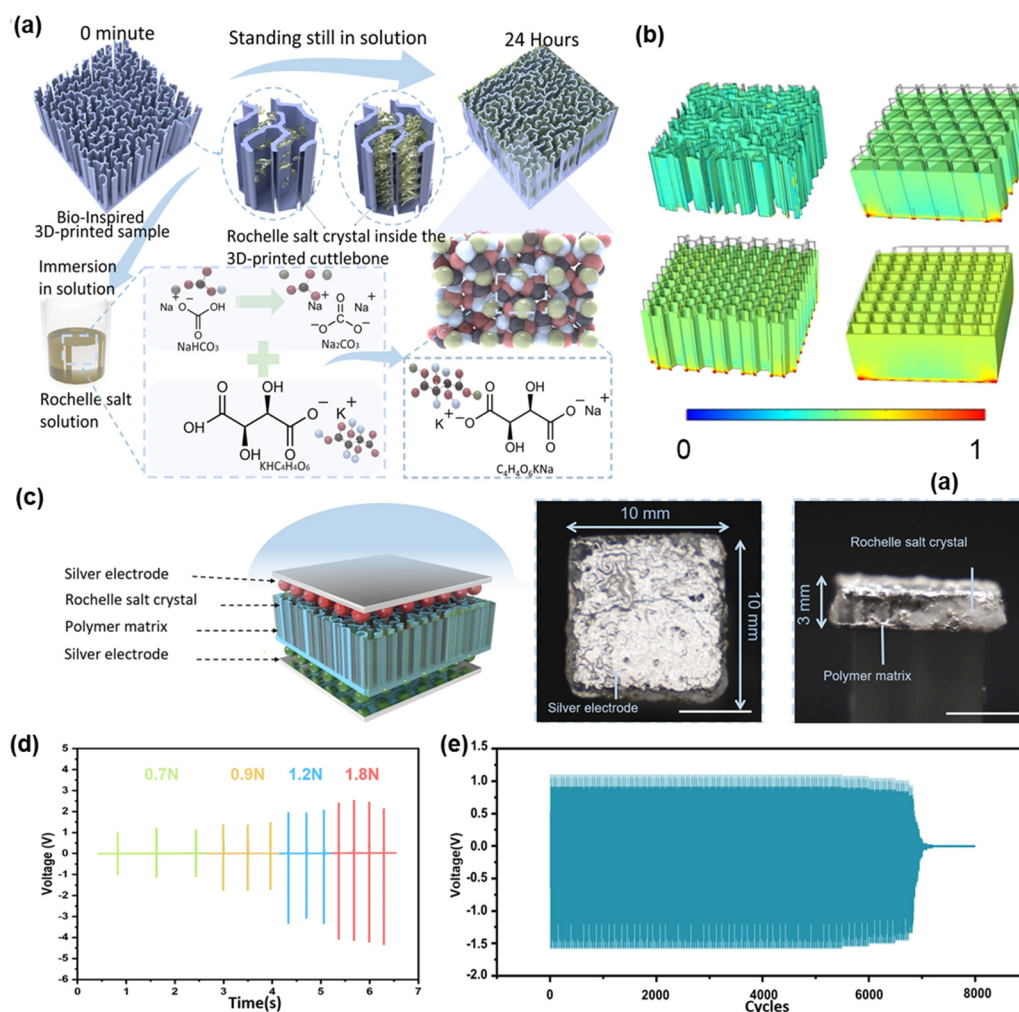


Figure 7. 3D assembly for enhancing piezoelectric properties. (a) Fabrication process of bio-inspired 3D-printed cuttlefish bone structure and Rochelle salt crystal. (b) Simulation results of the stress distribution under compressive loading. (c) Schematic of 3D printed sample for piezoelectric performance testing. Scale bar = 5 mm. (d) Voltage output at different frequencies. (e) Voltage output over 8000 cycles cyclic impact test (2 Hz). Reproduced with permission [47]. Copyright 2023, Springer Nature.

4. Biomedical Applications

The electromechanical conversion capabilities of piezoelectric bio-systems allow them to convert external stimuli into electrical energy, making them ideal for a wide range of biomedical applications. In recent years, significant advancements have been made in both implantable and wearable devices leveraging this technology [100–104]. Research has primarily focused on four key areas: (i) Stimulating cellular growth and tissue repair and regeneration; (ii) Enhancing drug delivery by improving molecular release and permeability; (iii) Directing and accelerating cell migration to promote wound healing; and (iv) Capturing multimodal physiological signals for non-invasive diagnostic purposes.

4.1. Tissue Regeneration

Over the past decades, piezoelectric biomaterials have shown great potential in tissue healing and the restoration of cellular functions. Biomedical engineers have used dynamic electric stimulation on these materials to activate, proliferate, and differentiate cells, aiding the repair of various tissues including nerves, muscles, skin, and bone [105–108]. For example, Wang et al. fabricated electrospun fibers composed of PCL embedded with piezoelectric tetragonal-SrTiO₃ to mimic the native tendon structure for tendon injury repair [109]. The tetragonal-SrTiO₃ enhanced the expression of tendon-related genes, and promoted collagen deposition, and reduced

inflammation. Similarly, Liu et al. created a conductive piezoelectric BaTiO₃/perampanel silk fibroin hydrogel capable of wireless electrical stimulation triggered by ultrasound [110]. This hydrogel not only showed excellent electrical conductivity but also anti-glutamate excitotoxicity, enhanced motor function recovery, and promoted spinal cord regeneration in a spinal cord injury rat model. During bone regeneration, electrical stimulation enhances Ca²⁺ influx by activating voltage-gated calcium channels (VGCCs) and triggering the Ca²⁺ signaling pathway, thereby promoting osteogenic differentiation [111,112]. In nerve regeneration, an increase in intracellular calcium concentration can induce actin depolymerization and contraction of this side of the cell, directing the cell's movement toward the cathode [113,114]. Similarly, in neural stem cell differentiation, applying an electric field modulates calcium signaling at the early stage, effectively steering differentiation toward neuronal lineages [115].

4.1.1. Bone Regeneration

Zheng et al. developed a fully implantable bone defect electrical stimulation (BD-ES) device, which integrates a hybrid tribo-/piezoelectric nanogenerator (HTP-NG) to generate electric pulses in response to rehabilitation movements [39]. This system was coupled with a conductive bioactive hydrogel made from ECM/alginate methacryloyl/polydopamine modified black phosphorus nanosheets (EABP) (Figure 8a). The BD-ES system facilitated the creation of an osteogenic microenvironment at the defect site by triggering biological processes, including calcium ion influx, cell proliferation and migration, and osteogenic differentiation. The piezoelectric materials used in the device consisted of commercial poled PVDF films with silver electrodes on both sides. In vivo studies on the osteogenic properties of the BD-ES system involved placing the HTP-NG near the knee joint and drilling a 3-mm-diameter cylindrical defect in the medial femur condyle. The HTP-NG was connected to the defect site via subcutaneously implanted platinum wires. The device efficiently harvested energy from rat knee joint's movements, generating electric pulses. Micro-CT scans demonstrated that the group treated with EABP and ES showed enhanced osteogenic induction compared to the control groups (ECM/alginate methacryloyl hydrogel (EA) and EABP without stimulation) (Figure 8b). Morphological parameters such as bone mineral density (BMD), bone volume (BV)/total volume (TV), trabecular number (Tb. N), and trabecular thickness (Tb. Th) were also assessed, with the EABP + ES group exhibiting significantly improved bone regeneration (Figure 8c). The BV/TV ratio was 1.4 times greater in the EABP + ES group than in the EABP group (Figure 8d), and Tb. N and Tb. Th also showed significant differences (Figure 8e,f). Additionally, histological analyses using hematoxylin and eosin (H&E) and Masson trichrome staining demonstrated a marked increase in newly formed bone and collagen in the EABP + ES group (Figure 8g). The BD-ES system demonstrates the potential for integrating rehabilitation exercise with electrical stimulation to enhance bone regeneration, offering new insights for the design of self-responsive devices for intelligent healthcare. This innovation holds promise for improving the treatment of clinical BD.

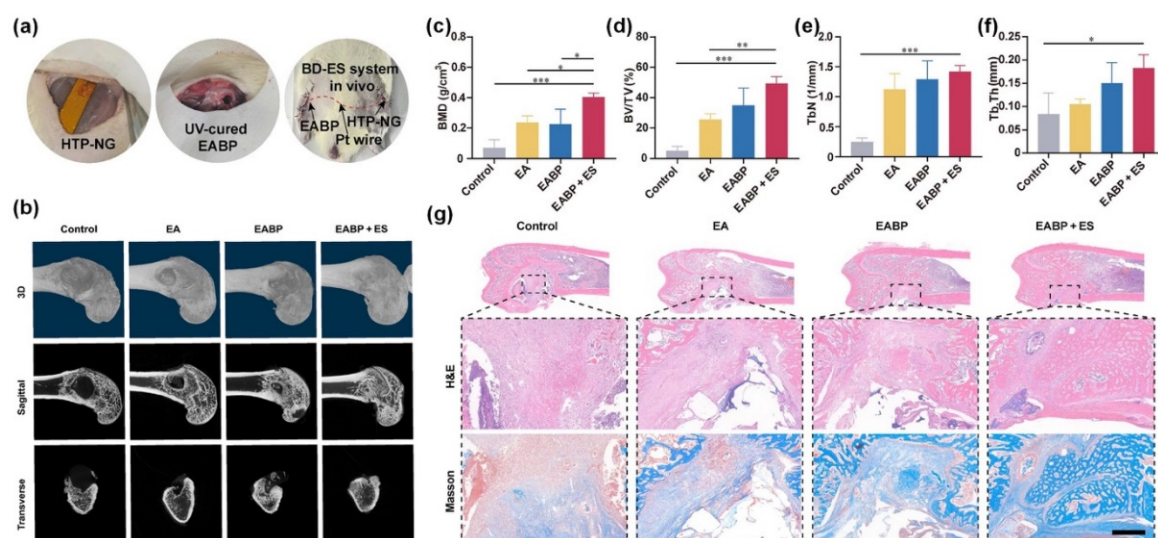


Figure 8. Implantable electrical stimulation device made of tribo- and piezoelectric nanogenerators for enhancing bone regeneration. (a) Surgical images of the implanted system. (b) 3D reconstruction images and sagittal and transverse view images of the distal femur by micro-CT. (c–f) Micro-CT quantitative evaluation of BMD, BV/TV, Tb. n, and Tb. Th in defect areas. Data are expressed as means ± SD. One-way ANOVA with Tukey's multiple comparisons test, *** $p < 0.001$ and * $p < 0.05$, $n = 3$. (g) H&E and Masson's trichrome staining images of the rat

femurs. Scale bar = 500 μm . Reproduced with permission [39]. Copyright 2024, The American Association for the Advancement of Science.

4.1.2. Wound Healing

Wound healing is crucial for maintaining the integrity of multicellular organisms. Numerous studies have demonstrated that disruption of the epithelial layer generates endogenous electric fields (EF) that play a key role in directing and accelerating cell migration [116,117]. However, the clinical application of exogenous EF to promote wound healing is often hindered by the need for cumbersome and complex ES devices at the injury site. To address this challenge, Sun et al. developed a flexible sono-piezo patch comprised of multifunctional fibers embedded with piezoelectric ZnO nanoparticles [118]. This patch leveraged low-intensity pulsed ultrasound to activate ES in the target tissues, which enhanced pro-regenerative behaviors in surrounding tissues and cells. Similarly, bio-piezoelectric materials, which convert motion-induced mechanical energy into electricity, show promise in actively accelerating the wound healing process. In this context, Wu et al. designed a self-aligned piezoelectric γ -glycine/PVA biofilm, optimized for use as a bioresorbable ultrasonic wireless electrotherapy device (b-WPUE) [58]. With concentric electrode devices spaced 1 mm apart, the system produced an electric field strength of approximately 220 mV mm^{-1} , sufficient for effective wound electrotherapy. In a rodent model with artificial surgical wounds, the functionality of the b-WPUE was evaluated. Figure 9a illustrates the healing progress across four different treatment groups, where the wounds treated with b-WPUE and ultrasound exhibited significantly faster healing ($\sim 40\%$ acceleration) compared to the control group. Notably the b-WPUE device alone did not alter the rate of healing, and while all wounds healed by day 15, the stimulated group achieved nearly complete recovery by day 10 (Figure 9b,c). No significant changes in weight were observed during treatment (Figure 9d). Histology analysis using H&E staining on tissue samples collected on days 6 and 12 further confirmed accelerated wound healing in the stimulated group (Figure 9e). These findings suggest that piezoelectric biofilms with excellent acoustic-electric conversion can be successfully integrated into b-WPUE device, offering an effective wireless electrotherapy approach that promotes wound healing rates in preclinical models.

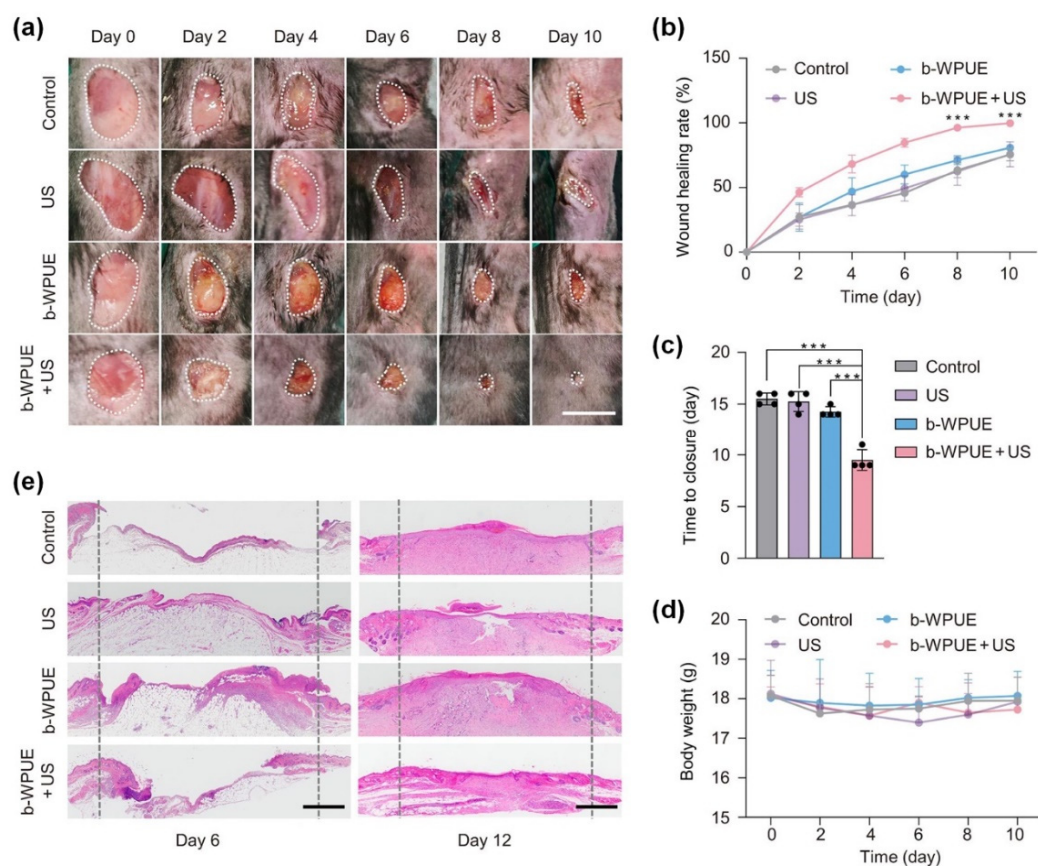


Figure 9. Bioresorbable ultrasonic wireless electrotherapy device made of piezoelectric γ -glycine/PVA biofilm for enhancing wound healing. (a) Optical photographs of wound healing in mice with different treatments. Scale bar = 6 mm. (b) Quantitative analysis of wound healing from 0 to 10 days ($n = 4$; *** $p < 0.001$). (c) Summary of the complete wound closure times ($n = 4$; *** $p < 0.001$). (d) Mice weight changes during wound treatments ($n = 4$).

(e) H&E staining images of wound sections at days 6 and 12 after wounding. Scale bar = 1 mm. Reproduced with permission [58]. Copyright 2024, The American Association for the Advancement of Science.

4.1.3. Nerve Regeneration

Peripheral nerve injuries are common in clinical settings and often involve severe long-gap interruptions, significantly impacting patients' daily lives and social activities [119,120]. For large-diameter peripheral nerve injuries (greater than 2 mm), researchers typically use biocompatible conduits to encase the damaged sciatic nerve, creating an artificial guiding channel to promote nerve regeneration. For example, Chai et al. developed a nerve guidance conduit composed of BTO nanoparticles-doped P(VDF-TrFE) aligned piezoelectric nanofibers, capable of repairing peripheral nerve injuries through ultrasound-triggered electrical stimulation [15]. These piezoelectric nanofibers achieved an open-circuit voltage of about 1.69 V under ultrasound stimulation at 0.75 W cm^{-2} . To evaluate their clinical potential, conduits with varying treatments were implanted into 10 mm sciatic nerve defects in Sprague-Dawley (SD) rats (Figure 10a). Immunostaining of regenerated nerve tissue for S-100 β (a Schwann cell marker) and NF200 (a neurofilament marker) confirmed nerve regeneration. Figure 10b,c demonstrate the presence of S-100 β -positive cells and NF200-positive cells in the transversal nerves of experimental groups. Importantly, conduits subjected to ultrasound stimulation (BPN US(+)) exhibited higher expression of S-100 β and NF200 compared to those without stimulation (BPN US(-)), demonstrating the enhanced nerve regeneration achieved through ultrasound-triggered wireless electrical stimulation. For smaller-diameter nerves (less than 1 mm) located in deeper anatomical sites and in contact with surrounding tissues, a nanopatch offers a promising alternative for nerve repair. Liu et al. introduced a band-aid-like nanopatch made of BTO@PCL/graphene oxide@gelatin methacryloyl for peripheral nerve repair using wireless ultrasound-electrical stimulation [121]. In a rat model of erectile dysfunction caused by peripheral nerve injury, the nanopatch adhered seamlessly to the damaged nerve, functioning like a band-aid (Figure 10d–f). This approach significantly improved corpus cavernosum nerve regeneration, enhancing tissue structure, erectile function, and a higher conception rate in female rats.

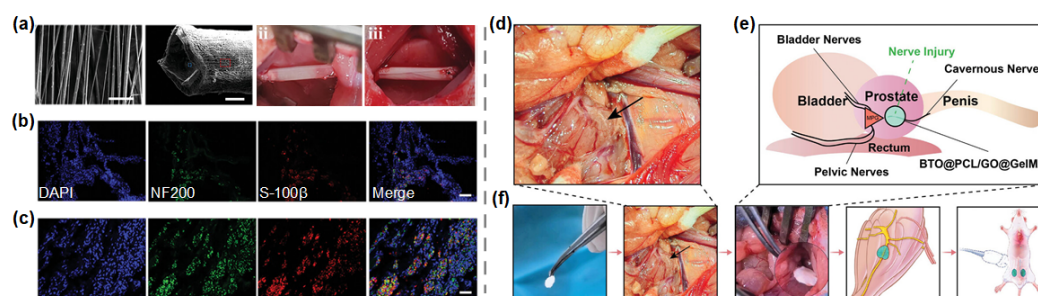


Figure 10. Piezoelectric conduits and nanopatches for the repair of peripheral nerve injuries. (a) SEM images of the aligned electrospun nanofibers and conduit; Photographs of implantation of (BPN US(-)) and (BPN US(+)). Scale bars are 5 μm in the first SEM image, 500 μm in the second SEM image. (b,c) Immunofluorescent staining of DAPI, NF200, and S-100 β of (BPN US(-)) and (BPN US(+)) at eight weeks postoperatively. Scar bar is 20 μm . (a–c) Reproduced with permission [15]. Copyright 2024, Wiley. (d) Anatomical location diagram of cavernous nerve in rats. (e,f) Diagram of a band-aid-like nanopatch acting on neurologic erectile dysfunction rats. (d,e) Reproduced with permission [121]. Copyright 2024, Wiley.

4.2. Drug Delivery

Precise drug delivery is essential for the treatment of various diseases, including cancer, tissue damage, and degenerative diseases. Recent research highlights the potential of piezoelectric materials in enhancing drug delivery systems by providing electrical stimulation, which can significantly improve the release and permeability of therapeutic molecules [122–124]. For instance, Lin et al. developed a controlled drug delivery system using piezocatalytic molybdenum disulfide nanoflowers as carriers for indomethacin, which can be activated by ultrasound to generate reactive oxygen species, facilitating targeted drug release for acute inflammation therapy [78]. In a paw edema model, a commercially available dressing functionalized with MoS₂ containing indomethacin showed effective in vivo drug release, reducing paw swelling by up to 56% within 6 h. In another study, Nguyen et al. designed biodegradable, flexible piezoelectric glycine-PCL nanofiber membranes, which served as the core of an implantable ultrasonic transducer. This device, implanted into the brain, enhanced drug delivery across the blood-brain barrier (BBB), offering a novel approach for treating brain cancers [i.e.,

glioblastoma (GBM)] (Figure 11a) [44]. In an orthotopic U87MG-Luc GBM mouse model, the combination of paclitaxel (PTX) and ultrasound stimulation from the piezoelectric glycine-PCL transducer significantly improved anti-tumor efficacy (Figure 11b,c). Bioluminescence imaging revealed that mice treated with ultrasound-assisted PTX had the smallest tumors compared to other treatment groups (Figure 11d). Furthermore, the Kaplan-Meier survival analysis demonstrated that mice receiving the combined treatment had a prolonged median survival time of 65 days, with some surviving up to 72 days, which was significantly longer than those in other groups (Figure 11e). Furthermore, the corresponding images of the bioluminescence intensity of GBM cell at day 26, collected brain ex vivo imaging of the entire brain (Figure 11f) confirm that, in comparison to all other treatment groups, mice treated with glycine-PCL ultrasound-assisted PTX possessed the smallest tumor. All these findings indicate that biodegradable ultrasonic transducers based on piezoelectric glycine-PCL present a reliable and efficient option for future GBM treatments. These technologies have the potential to significantly advance biomedicine by overcoming the limitations of conventional external focused ultrasound, particularly in opening the BBB. Traditional methods face challenges such as significant attenuation of sound waves when passing through thick skulls and the difficulty of inducing effects repeatedly at precise locations. Piezoelectric systems offer a more targeted and reliable alternative.

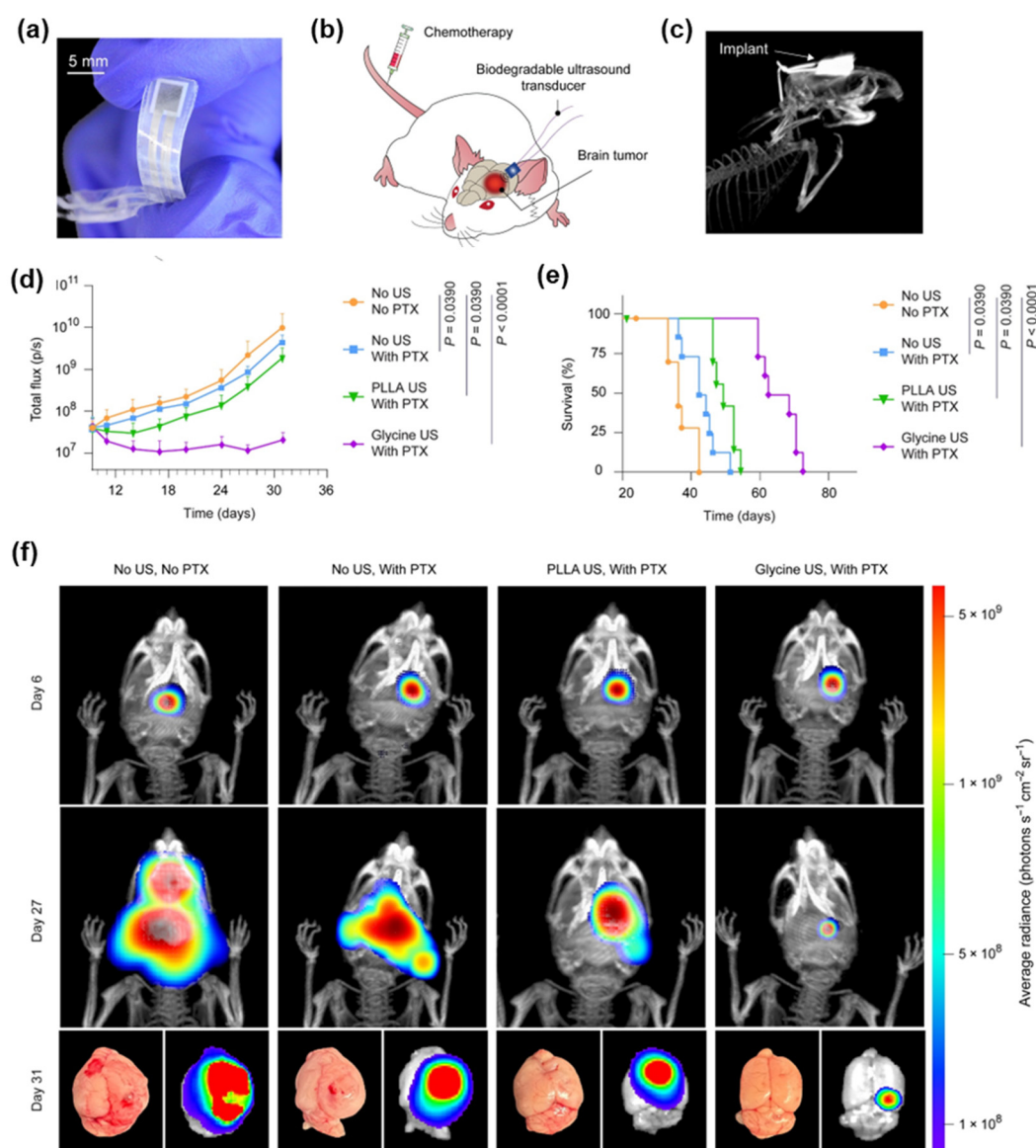


Figure 11. Implantable device made of glycine-PCL nanofiber membranes for facilitated delivery of chemotherapeutic drugs to brain tissue. **(a)** Optical photograph of a biodegradable glycine-PCL ultrasonic transducer. **(b)** Model of the glycine-PCL ultrasonic transducer in enhancing the delivery of chemotherapeutic drug to the brain for the treatment of GBM tumor. **(c)** Micro-CT image revealing the position of the implant in the animal. **(d)** Mean GBM tumor luminescence intensity levels of mice receiving different treatments. Data are means \pm SD ($n = 8$, one-way ANOVA and Tukey multiple comparisons tests at day 31). **(e)** Kaplan-Meier survival of animals

receiving different treatments ($n = 8$, log-rank test). (f) Bioluminescence images of GBM tumor growth in live animals and ex vivo images of GBM-bearing brains. Reproduced with permission [44]. Copyright 2023, The American Association for the Advancement of Science.

4.3. Biosensors

As digital healthcare technology continues to advance, wearable biosensors are being increasingly utilized to monitor multimodal physiological signals for various biomedical applications such as mental stress analysis, bladder volume monitoring, and blood pressure measurement [125–129]. A recent study introduced a wearable bio-adhesive ultrasound elastography (BAUS-E) device, featuring a piezoelectric lead zirconate titanate (PZT) layer. This device generated acoustic radiation force impulses to create shear waves, enabling the continuous evaluation of liver stiffness. Such measurements can serve as valuable biomarkers for tracking the progression of acute liver failure (ALF) through rapid, real-time changes in tissue elasticity. Figure 12a depicts the procedure for monitoring liver stiffness using a pharmacologically induced ALF animal model. Shear wave elastography (SWEs) data were collected over a 48-h period to evaluate the elasticity of rat livers using BAUS-E. The shear wave velocity (group velocity, C_g) values for the rat livers at four distinct time points—0, 12, 30, and 48 h—were recorded as 1.23, 1.53, 1.80, and 2.42 m/s, respectively, indicating a clear progression of liver injury (Figure 12b). A significant difference in liver stiffness was observed between normal livers and those affected by ALF at every time point (Figure 12c,d). Both BAUS-E and histological staining confirmed a strong positive correlation between liver stiffness and the severity of ALF. These findings suggest that BAUS-E could have extensive clinical applications, particularly for the non-invasive and continuous monitoring of internal organ changes in rapidly progressing conditions like ALF. The device's potential for real-time tracking could be especially valuable in intensive care units and clinical settings where timely diagnosis and monitoring are critical.

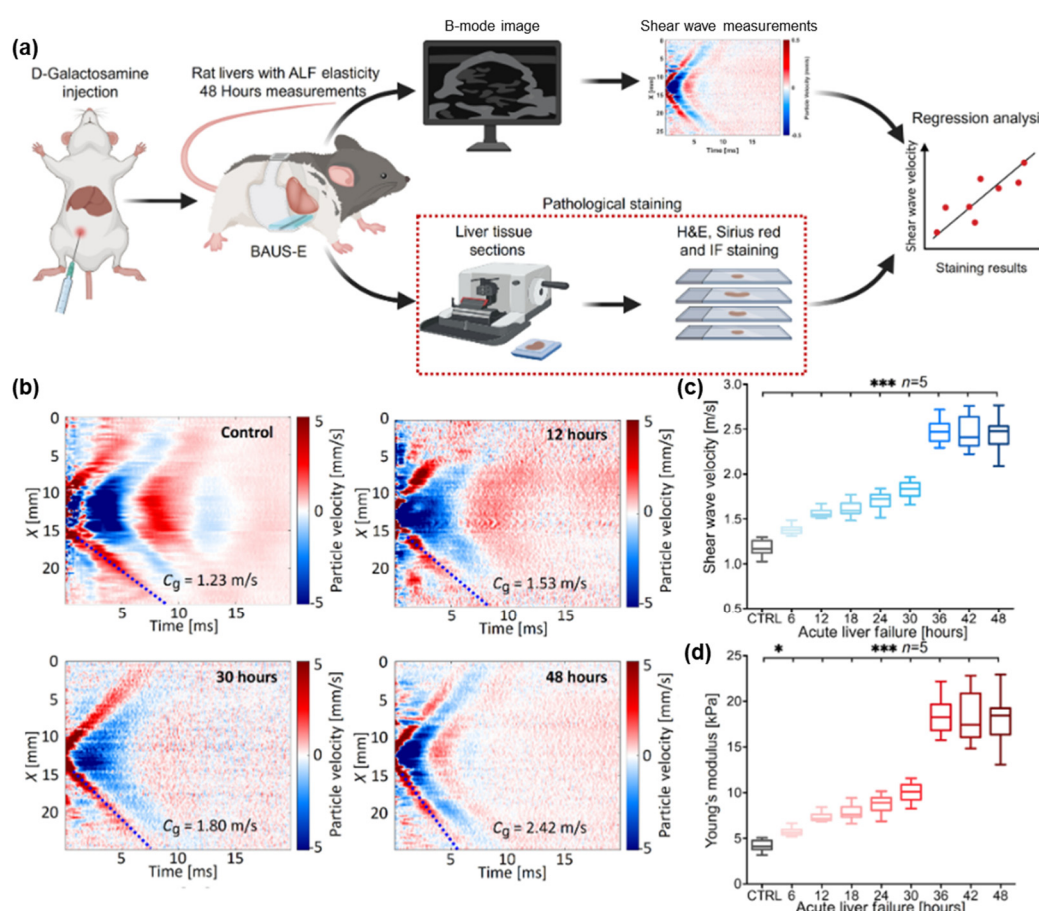


Figure 12. Wearable bio-adhesive ultrasound elastography based on a piezoelectric PZT layer for monitoring liver elasticity. (a) Schematic diagram of the procedure for assessing elasticity changes in rats with ALF. (b) Spatiotemporal maps of shear wave velocities. (c) Shear wave velocities were observed from 0 to 48 h using BAUS-E. (d) Trend of Young's modulus changes in relation to the severity of rats with ALF over 48 h. IF, immunofluorescence. $* p < 0.05$, $** p \leq 0.01$, and $*** p \leq 0.001$. Reproduced with permission [42]. Copyright 2024, The American Association for the Advancement of Science.

In addition to these specialized applications, the use of piezoelectric materials in integrated diagnostic and treatment systems is propelling the development of innovative, non-invasive, and personalized medical technologies. These materials have been employed in efforts to achieve simultaneous visualization and treatment of malignant tissues. For instance, Shung et al. designed an integrated multifunctional confocal phased zirconate titanate array for noninvasive prostate tissue surgery, combining diagnosis and therapy capabilities [130]. The device features a triple row phased arrays: a 6-MHz array in the center row for imaging and two 4-MHz arrays in the outer rows for therapy. The 6-MHz imaging array consists of 128 elements with a $0.73\lambda = 188\ \mu\text{m}$ pitch, 25 μm kerf, and 8 mm height, while each 4-MHz therapy array also has 128 elements with a $0.5\lambda = 188\ \mu\text{m}$ pitch, 25 μm kerf, and 14 mm height. Both simulation and experimental results confirmed the device's ability to provide real-time imaging during treatment. Similarly, Shrestha et al. developed a dual-mode piezo-composite transducer array integrating the therapeutic and diagnostic functions for image guided surgery [131,132]. This system offers immediate, spatially accurate lesion imaging and real-time feedback on tissue response to high-intensity focused ultrasound beams. As research advances, the application of piezoelectric materials in such integrated systems is expected to grow, enhancing the efficiency, accessibility, and effectiveness of healthcare delivery.

5. Conclusions and Outlook

Engineered piezoelectric metamaterials have emerged as an important innovation in biomedical applications, offering promising capabilities in addressing complex medical challenges and enhancing patient care. By integrating piezoelectric materials with metamaterial structures, researchers have developed highly specialized devices and systems that enhance both performance and functionality. The ability of these materials to efficiently convert mechanical stress into electrical energy has driven substantial progress in areas such as tissue regeneration, drug delivery, wound healing, and biosensing.

However, despite these advancements, a considerable gap remains between laboratory-scale demonstrations and practical clinical applications. As an emerging field, the development and deployment of piezoelectric metamaterials face several challenges. While many piezoelectric biomaterials exhibit excellent biocompatibility, their lack of biodegradability often requires secondary surgical procedures to remove them once they have served their purpose. To address this, there is increasing focus on developing naturally biodegradable piezoelectric materials. Modified proteins, for instance, are being explored as potential candidates to reduce the need for additional surgeries, thereby improving patient outcomes [89,133,134]. The degradation rates of biodegradable materials are often either too rapid or too slow for clinical needs. Many biomedical implants require functionality for several months to even years. Therefore, it is crucial to develop safe encapsulation materials or integrate degradation catalysts into piezoelectric devices to ensure they remain functional for the desired period and degrade predictably thereafter. For wearable biomedical devices, ensuring breathability and moisture management is crucial for user comfort and device reliability. Piezoelectric materials used in wearables must allow sufficient airflow and manage moisture effectively to prevent skin irritation [135–137]. Balancing piezoelectric functionality with user comfort is critical to the successful adoption of these devices in practical, long-term applications.

Moreover, the piezoelectric properties of materials can be significantly enhanced by subjecting them to high electric fields through polarization [71]. In their natural state, the dipoles within a material are randomly oriented, canceling each other out and resulting in minimal or no piezoelectric response. When an electric field greater than the saturation field but below the breakdown field is applied, the dipoles align, creating directional polarization [138]. Two commonly poling methods are direct current poling (DCP) and alternating current poling (ACP). DCP, a traditional technique, involves applying a DC voltage for a specific duration, allowing complete domain motion or switching during the poling process. In contrast, ACP is a dynamic approach that cyclically changes the polarization direction, offering significant potential for industrial applications. However, ACP does not allow sufficient time for internal stress relaxation, making it more difficult to achieve saturated poling compared to DCP [139,140]. To address this limitation, some researchers have combined the two methods, using ACP to change domain configuration initially, followed by DCP to ensure full domain reorientation [141]. Developing optimized polarization processes remains a key focus for advancing the fabrication of biological piezoelectric materials, paving the way for enhanced performance and broader applications. In summary, while piezoelectric metamaterials hold great promise in advancing biomedical technologies, overcoming these challenges will be essential for their widespread clinical adoption and sustained success.

Author Contributions: Z.Y.: conceptualization, writing-original draft preparation; H.T., D.M., and J.X.: writing-review and editing. All authors have read and agreed to the published version of the manuscript.

Funding: This work was partially supported by startup funds from the University of Nebraska Medical Center (UNMC), National Institute of Dental and Craniofacial Research (NIDCR) of the National Institutes of Health under Award Number R01DE031272 (JX), NE LB606 (JX), and Nebraska Research Initiative grant (JX).

Institutional Review Board Statement: Not applicable.

Informed Consent Statement: Not applicable.

Data Availability Statement: Not applicable.

Conflicts of Interest: The authors declare no competing financial interest.

References

1. Evangel Chinyere, A.; Femi, O.; Opeoluwa Oluwanifemi, A.; Jane Osareme, O.; Tolulope, O.; Ebere Rosita, D. Biomedical engineering advances: A review of innovations in healthcare and patient outcomes. *Int. J. Sci. Res. Arch.* **2024**, *11*, 870–882.
2. Yi, J.; Zou, G.; Huang, J.; Ren, X.; Tian, Q.; Yu, Q.; Wang, P.; Yuan, Y.; Tang, W.; Wang, C.; et al. Water-responsive supercontractile polymer films for bioelectronic interfaces. *Nature* **2023**, *624*, 295–302.
3. Chen, S.; Tong, X.; Huo, Y.; Liu, S.; Yin, Y.; Tan, M.L.; Cai, K.; Ji, W. Piezoelectric biomaterials inspired by nature for applications in biomedicine and nanotechnology. *Adv. Mater.* **2024**, *36*, e2406192.
4. Yang, J.; Li, Z.; Xin, X.; Gao, X.; Yuan, X.; Wang, Z.; Yu, Z.; Wang, X.; Zhou, J.; Dong, S. Designing electromechanical metamaterial with full nonzero piezoelectric coefficients. *Sci. Adv.* **2019**, *5*, eaax1782.
5. Qiao, L.; Gao, X.; Ren, K.; Qiu, C.; Liu, J.; Jin, H.; Dong, S.; Xu, Z.; Li, F. Designing transparent piezoelectric metasurfaces for adaptive optics. *Nat. Commun.* **2024**, *15*, 805.
6. Lin, B.; Ong, K.P.; Yang, T.; Zeng, Q.; Hui, H.K.; Ye, Z.; Sim, C.; Yen, Z.; Yang, P.; Dou, Y.; et al. Ultrahigh electromechanical response from competing ferroic orders. *Nature* **2024**, *633*, 798–803.
7. Kim, Y.; Suh, J.; Shin, J.; Liu, Y.; Yeon, H.; Qiao, K.; Kum, H.; Kim, C.; Lee, H.; Choi, C.; et al. Chip-less wireless electronic skins by remote epitaxial freestanding compound semiconductors. *Science* **2022**, *377*, 859–864.
8. Yang, M.M.; Zhu, T.Y.; Renz, A.B.; Sun, H.M.; Liu, S.; Gammon, P.M.; Alexe, M. Auxetic piezoelectric effect in heterostructures. *Nat. Mater.* **2024**, *23*, 95–100.
9. Mac, C.H.; Tai, H.M.; Huang, S.M.; Peng, H.H.; Sharma, A.K.; Nguyen, G.L.T.; Chang, P.J.; Wang, J.T.; Chang, Y.; Lin, Y.J.; et al. Orally ingested self-powered stimulators for targeted gut-brain axis electrostimulation to treat obesity and metabolic disorders. *Adv. Mater.* **2024**, *36*, e2310351.
10. Li, J.; Zhao, X.; Xia, Y.; Qi, X.; Jiang, C.; Xiao, Y.; Jiang, F.; Jiang, X.; Yuan, G. Strontium-containing piezoelectric biofilm promotes dentin tissue regeneration. *Adv. Mater.* **2024**, *36*, e2313419.
11. You, Y.; Jiang, J.; Zheng, G.; Chen, Z.; Zhu, Y.X.; Ma, H.; Lin, H.; Guo, X.; Shi, J. In situ piezoelectric-catalytic anti-inflammation promotes the rehabilitation of acute spinal cord injury in synergy. *Adv. Mater.* **2024**, *36*, e2311429.
12. Fernandez-Yague, M.A.; Trotier, A.; Demir, S.; Abbah, S.A.; Larranaga, A.; Thirumaran, A.; Stapleton, A.; Tofail, S.A.M.; Palma, M.; Kilcoyne, M.; et al. A self-powered piezo-bioelectric device regulates tendon repair-associated signaling pathways through modulation of mechanosensitive ion channels. *Adv. Mater.* **2021**, *33*, e2008788.
13. Li, T.; Qu, M.; Carlos, C.; Gu, L.; Jin, F.; Yuan, T.; Wu, X.; Xiao, J.; Wang, T.; Dong, W.; et al. High-performance poly(vinylidene difluoride)/dopamine core/shell piezoelectric nanofiber and its application for biomedical sensors. *Adv. Mater.* **2021**, *33*, e2006093.
14. Cui, H.; Hensleigh, R.; Yao, D.; Maurya, D.; Kumar, P.; Kang, M.G.; Priya, S.; Zheng, X.R. Three-dimensional printing of piezoelectric materials with designed anisotropy and directional response. *Nat. Mater.* **2019**, *18*, 234–241.
15. Xu, D.; Fu, S.; Zhang, H.; Lu, W.; Xie, J.; Li, J.; Wang, H.; Zhao, Y.; Chai, R. Ultrasound-responsive aligned piezoelectric nanofibers derived hydrogel conduits for peripheral nerve regeneration. *Adv. Mater.* **2024**, *36*, e2307896.
16. Tian, G.; Deng, W.; Yang, T.; Zhang, J.; Xu, T.; Xiong, D.; Lan, B.; Wang, S.; Sun, Y.; Ao, Y.; et al. Hierarchical piezoelectric composites for noninvasive continuous cardiovascular monitoring. *Adv. Mater.* **2024**, *36*, e2313612.
17. Imani, I.M.; Kim, H.S.; Shin, J.; Lee, D.G.; Park, J.; Vaidya, A.; Kim, C.; Baik, J.M.; Zhang, Y.S.; Kang, H.; et al. Advanced ultrasound energy transfer technologies using metamaterial structures. *Adv. Sci.* **2024**, *11*, e2401494.
18. Chen, J.C.; Bhave, G.; Alrashdan, F.; Dhuliyawalla, A.; Hogan, K.J.; Mikos, A.G.; Robinson, J.T. Self-rectifying magnetoelectric metamaterials for remote neural stimulation and motor function restoration. *Nat. Mater.* **2024**, *23*, 139–146.
19. Yan, Z.; Liu, X.; Ding, B.; Yu, J.; Si, Y. Interfacial engineered superelastic metal-organic framework aerogels with van-der-Waals barrier channels for nerve agents decomposition. *Nat. Commun.* **2023**, *14*, 2116.
20. Zhu, L.; Ding, X.; Wu, X.; Yan, Z.; Lei, S.; Si, Y. Innovative and sustainable multifunctional finishing method for textile materials by applying engineered water nanostructures. *ACS Sustain. Chem. Eng.* **2020**, *8*, 14833–14844.
21. Ma, K.; Chen, H.; Wu, Z.; Hao, X.; Yan, G.; Li, W.; Shao, L.; Meng, G.; Zhang, W. A wave-confining metasphere beamforming acoustic sensor for superior human-machine voice interaction. *Sci. Adv.* **2022**, *8*, eadc9230.
22. Petroff, C.A.; Cassone, G.; Sponer, J.; Hutchison, G.R. Intrinsically polar piezoelectric self-assembled oligopeptide monolayers. *Adv. Mater.* **2021**, *33*, e2007486.
23. Liu, Y.; He, H.; Cao, Y.; Liang, Y.; Huang, J. Inverse design of TPMS piezoelectric metamaterial based on deep learning. *Mech. Mater.* **2024**, *198*, 105109.
24. Cai, J.; Yan, L.; Seyedkanani, A.; Orsat, V.; Akbarzadeh, A. Nano-architected GaN metamaterials with notable topology-dependent enhancement of piezoelectric energy harvesting. *Nano Energy* **2024**, *129*, 109990.

25. Shi, J.; Ju, K.; Chen, H.; Mirabolghasemi, A.; Akhtar, S.; Sasmito, A.; Akbarzadeh, A. 3D printed architected shell-based ferroelectric metamaterials with programmable piezoelectric and pyroelectric properties. *Nano Energy* **2024**, *123*, 109385.
26. Li, Z.; Yi, X.; Yang, J.; Bian, L.; Yu, Z.; Dong, S. Designing artificial vibration modes of piezoelectric devices using programmable, 3d ordered structure with piezoceramic strain units. *Adv. Mater.* **2022**, *34*, e2107236.
27. Wang, X.; Sun, K.; Wang, C.; Yang, M.; Qian, K.; Ye, B.; Guo, X.; Shao, Y.; Chu, C.; Xue, F.; et al. Ultrasound-responsive microfibers promoted infected wound healing with neuro-vascularization by segmented sonodynamic therapy and electrical stimulation. *Biomaterials* **2025**, *313*, 122803.
28. Priangga Perdana, P.; Akasaka, S.; Konosu, Y.; Zhang, S.; Tanioka, A.; Matsumoto, H. Structure-piezoelectric property relationships of thin films composed of electrospun aligned poly(vinylidene fluoride) nanofibers. *Nanomaterials* **2024**, *14*, 491.
29. Kowalchik, T.; Khan, F.; Le, K.; Leland, P.; Roundy, S.; Warren, R. Effect of pore structure on the piezoelectric properties of barium titanate-polyvinylidene fluoride composite films. *Nano Energy* **2023**, *109*, 108276.
30. Lu, H.; Cui, H.; Lu, G.; Jiang, L.; Hensleigh, R.; Zeng, Y.; Rayes, A.; Panduranga, M.K.; Acharya, M.; Wang, Z.; et al. 3D Printing and processing of miniaturized transducers with near-pristine piezoelectric ceramics for localized cavitation. *Nat. Commun.* **2023**, *14*, 2418.
31. Li, X.; Zhang, Z.; Peng, Z.; Yan, X.; Hong, Y.; Liu, S.; Lin, W.; Shan, Y.; Wang, Y.; Yang, Z. Fast and versatile electrostatic disc microprinting for piezoelectric elements. *Nat. Commun.* **2023**, *14*, 6488.
32. Wu, J.; Jiao, C.; Yu, H.; Naqvi, S.M.R.; Ge, M.; Cai, K.; Liang, H.; Liu, J.; Zhao, J.; Tian, Z.; et al. 3D Printed barium titanate/calcium silicate composite biological scaffold combined with structural and material properties. *Biomater. Adv.* **2024**, *158*, 213783.
33. Lee, J.E.; Sun, Y.-C.; Lees, I.; Naguib, H.E. Additive manufacturing of hybrid piezoelectric/magnetic self-sensing actuator using pellet extrusion and immersion precipitation with statistical modelling optimization. *Compos. Sci. Technol.* **2024**, *247*, 110393.
34. Mirjalali, S.; Bagherzadeh, R.; Mahdavi Varposhti, A.; Asadnia, M.; Huang, S.; Chang, W.; Peng, S.; Wang, C.H.; Wu, S. Enhanced piezoelectricity of PVDF-TrFE nanofibers by intercalating with electrospayed BaTiO₃. *ACS Appl. Mater. Interfaces* **2023**, *15*, 41806–41816.
35. Hong, Y.; Liu, S.; Yang, X.; Hong, W.; Shan, Y.; Wang, B.; Zhang, Z.; Yan, X.; Lin, W.; Li, X.; et al. A bioinspired surface tension-driven route toward programmed cellular ceramics. *Nat. Commun.* **2024**, *15*, 5030.
36. Yan, Z.; Liu, X.; Si, Y.; Dai, Z.; Yu, J.; Ding, B. Ternary-porous conjugated N-halamine nanofibers/graphene aerogels for rechargeable degradation of mustard gas. *Adv. Funct. Mater.* **2022**, *32*, 2206018.
37. Zhang, J.; Yang, T.; Tian, G.; Lan, B.; Deng, W.; Tang, L.; Ao, Y.; Sun, Y.; Zeng, W.; Ren, X.; et al. Spatially confined MXene/PVDF nanofiber piezoelectric electronics. *Adv. Fiber Mater.* **2023**, *6*, 133–144.
38. Tran, H.Q.; Shreem Polavaram, N.; Yan, Z.; Lee, D.; Xiao, Y.; Shahriar, S.M.S.; Yan, Z.; Xie, J. Enoki-inspired microfibers and extracellular matrix enhance biaxially interlocking interfaces. *Small Struct.* **2024**, *5*, 2400193.
39. Wang, T.; Ouyang, H.; Luo, Y.; Xue, J.; Wang, E.; Zhang, L.; Zhou, Z.; Liu, Z.; Li, X.; Tan, S.; et al. Rehabilitation exercise-driven symbiotic electrical stimulation system accelerating bone regeneration. *Sci. Adv.* **2024**, *10*, eadi6799.
40. Chen, Z.; Lai, Y.; Xu, S.; Zhu, M.; Sun, Y.; Cheng, Y.; Zhao, G. A self-powered controllable microneedle drug delivery system for rapid blood pressure reduction. *Nano Energy* **2024**, *123*, 109344.
41. Das, R.; Le, T.T.; Schiff, B.; Chorsi, M.T.; Park, J.; Lam, P.; Kemerley, A.; Supran, A.M.; Eshed, A.; Luu, N.; et al. Thirunavukkarasu, M.; Maulik, N.; Nguyen, T.D. In vitro-biodegradable piezoelectric skin-wound scaffold. *Biomaterials* **2023**, *301*, 122270.
42. Liu, H.; Zeng, Y.; Gong, C.; Chen, X.; Kijanka, P.; Zhang, J.; Genyk, Y.; Tchelepi, H.; Wang, C.; Zhou, Q.; et al. Wearable bioadhesive ultrasound shear wave elastography. *Sci. Adv.* **2024**, *10*, eadk8426.
43. Tian, B.; Tian, R.; Liu, S.; Wang, Y.; Gai, S.; Xie, Y.; Yang, D.; He, F.; Yang, P.; Lin, J. Doping engineering to modulate lattice and electronic structure for enhanced piezocatalytic therapy and ferroptosis. *Adv. Mater.* **2023**, *35*, 2304262.
44. Chorsi, M.; Le, T.; Lin, F.; Vinikoor, T.; Das, R.; Stevens, J.; Mundrane, C.; Park, J.; Tran, K.; Liu, Y.; et al. Highly piezoelectric, biodegradable, and flexible amino acid nanofibers for medical applications. *Sci. Adv.* **2023**, *9*, eadg6075.
45. Khanra, S.; Vassiliades, S.V.; Alves, W.A.; Yang, K.; Glaser, R.; Ghosh, K.; Bhattacharya, P.; Yu, P.; Guha, S. Enhanced piezoresponse and nonlinear optical properties of fluorinated self-assembled peptide nanotubes. *AIP Adv.* **2019**, *9*, 115202.
46. Sun, J.; Guo, H.; Ribera, J.; Wu, C.; Tu, K.; Binelli, M.; Panzarasa, G.; Schwarze, F.; Wang, Z.L.; Burgert, I. Sustainable and biodegradable wood sponge piezoelectric nanogenerator for sensing and energy harvesting applications. *ACS Nano* **2020**, *14*, 14665–14674.
47. He, Q.; Zeng, Y.; Jiang, L.; Wang, Z.; Lu, G.; Kang, H.; Li, P.; Bethers, B.; Feng, S.; Sun, L.; et al. Growing recyclable and healable piezoelectric composites in 3D printed bioinspired structure for protective wearable sensor. *Nat. Commun.* **2023**, *14*, 6477.
48. Guerin, S.; Tofail, S.A.M.; Thompson, D. Longitudinal piezoelectricity in orthorhombic amino acid crystal films. *Cryst. Growth Des.* **2018**, *18*, 4844–4848.
49. Dolai, J.; Maity, A.; Mukherjee, B.; Ray, R.; Jana, N.R. Piezoelectric amyloid fibril for energy harvesting, reactive oxygen species generation, and wireless cell therapy. *ACS Appl. Mater. Interfaces* **2024**, *16*, 217–227.
50. Kim, H.; Lee, S.W. Molecular mechanisms and enhancement of piezoelectricity in the M13 virus. *Adv. Funct. Mater.* **2024**, *34*, 2407462.

51. Son, H.; Park, S. Collagen-based biopiezoelectric nanogenerator prepared from pollack skin. *Mater. Today Sustain.* **2024**, *25*, 100689.
52. Zhu, Q.; Chen, X.; Li, D.; Xiao, L.; Chen, J.; Zhou, L.; Chen, J.; Yuan, Q. Large enhancement on performance of flexible cellulose-based piezoelectric composite film by welding CNF and MXene via growing ZnO to construct a “brick-rebar-mortar” structure. *Adv. Funct. Mater.* **2024**, 2408588. <https://doi.org/10.1002/adfm.202408588>.
53. Barlemont, S.; Burg, A.; Serghei, A.; Capsal, J.F.; Fumagalli, M. Macroscopic tensile piezoelectricity characterization of β -chitin in tubeworm tissues. *Cellulose* **2023**, *30*, 8451–8458.
54. Niu, Q.; Chen, J.; Fan, S.; Yao, X.; Gu, Y.; Hsiao, B.S.; Wei, H.; Zhang, Y. Silk nanoribbon films with enriched silk II structure and enhanced piezoelectricity for self-powered implantable and wearable devices. *Nano Today* **2024**, *56*, 102228.
55. Yu, Q.; Bai, Y.; Li, Z.; Jiang, F.; Luo, R.; Gai, Y.; Liu, Z.; Zhou, L.; Wang, Y.; Li, C.; et al. Interface-induced high piezoelectric γ -glycine-based flexible biodegradable films. *Nano Energy* **2024**, *121*, 109196.
56. Zhang, Z.; Li, X.; Peng, Z.; Yan, X.; Liu, S.; Hong, Y.; Shan, Y.; Xu, X.; Jin, L.; Liu, B.; et al. Active self-assembly of piezoelectric biomolecular films via synergistic nanoconfinement and in-situ poling. *Nat. Commun.* **2023**, *14*, 4094.
57. Yang, F.; Li, J.; Long, Y.; Zhang, Z.; Wang, L.; Sui, J.; Dong, Y.; Wang, Y.; Taylor, R.; Ni, D.; et al. Wafer-scale heterostructured piezoelectric bio-organic thin films. *Science* **2021**, *373*, 337–342.
58. Xue, H.; Jin, J.; Tan, Z.; Chen, K.; Lu, G.; Zeng, Y.; Hu, X.; Peng, X.; Jiang, L.; Wu, J. Flexible, biodegradable ultrasonic wireless electrotherapy device based on highly self-aligned piezoelectric biofilms. *Sci. Adv.* **2024**, *10*, eadn0260.
59. Liu, X.; Zhang, M.; Jiang, B.; Zhang, Q.; Chen, H.; Shen, Y.; Wang, Z.; Yin, X. Process investigation on robust electrospinning of non-aligned and aligned polyvinylidene fluoride nanofiber mats for flexible piezoelectric sensors. *Polymers* **2024**, *16*, 816.
60. Guerin, S.; Khorasani, S.; Gleeson, M.; O'Donnell, J.; Sanii, R.; Zwane, R.; Reilly, A.M.; Silien, C.; Tofail, S.A.M.; Liu, N.; et al. A piezoelectric ionic cocrystal of glycine and sulfamic acid. *Cryst. Growth Des.* **2021**, *21*, 5818–5827.
61. Fox, G.; Fink, G. The piezoelectric properties of quartz and tourmaline. *Physics* **1934**, *5*, 302–306.
62. Sawyer, C.; Tower, C. Rochelle salt as a dielectric. *Phys. Rev.* **1930**, *35*, 269–273.
63. Zhang, R.; Yang, D.; Zang, P.; He, F.; Gai, S.; Kuang, Y.; Yang, G.; Yang, P. Structure engineered high piezo-photoelectronic performance for boosted sono-photodynamic therapy. *Adv. Mater.* **2024**, *36*, e2308355.
64. Zhang, X.; Qiao, Z.; Lian, M.; Han, Y.; Lin, J.; Yu, B.; Peng, L.; Wang, H.; Dai, K. In-situ electret scaffolds with controllable electric fields printed by MEW for bone tissue regeneration. *Chem. Eng. J.* **2024**, *496*, 154330.
65. Wang, A.; Ma, X.; Yang, Y.; Shi, G.; Han, L.; Hu, X.; Shi, R.; Yan, J.; Guo, Q.; Zhao, Y. Biophysical-driven piezoelectric and aligned nanofibrous scaffold promotes bone regeneration by re-establishing physiological electrical microenvironment. *Nano Res.* **2024**, *17*, 7376–7393.
66. Carofiglio, M.; Percivalle, N.M.; Hernandez, S.; Laurenti, M.; Canavese, G.; Matos, J.C.; Goncalves, M.C.; Cauda, V. Ultrasound-assisted water oxidation: Unveiling the role of piezoelectric metal-oxide sonocatalysts for cancer treatment. *Biomed. Microdevices* **2024**, *26*, 37.
67. Xu, L.; Lv, J.; Yu, S. Piezoelectric properties of as-spun poly(vinylidene fluoride)/multi-walled carbon nanotube/zinc oxide nanoparticle (PVDF/MWCNT/ZnO) nanofibrous films. *Polymers* **2024**, *16*, 2483.
68. Qiu, Y.; Bao, C.; Gou, M.; Zhao, J.; Yang, D. Fabrication and piezoelectric analysis based on nanogrid architecture composed of ZnO ultrathin nanosheets grown on fiber paper substrates for wearable energy harvesting. *Mater. Today Commun.* **2024**, *39*, 108598.
69. Chang, G.; Pan, X.; Hao, Y.; Du, W.; Wang, S.; Zhou, Y.; Yang, J.; He, Y. PVDF/ZnO piezoelectric nanofibers designed for monitoring of internal micro-pressure. *RSC Adv.* **2024**, *14*, 11775–11783.
70. Zhang, Q.; Zhu, J.; Fei, X.; Zhu, M. A Janus nanofibrous scaffold integrated with exercise-driven electrical stimulation and nanotopological effect enabling the promotion of tendon-to-bone healing. *Nano Today* **2024**, *55*, 102208.
71. Shan, Y.; Wang, E.; Cui, X.; Xi, Y.; Ji, J.; Yuan, J.; Xu, L.; Liu, Z.; Li, Z. A biodegradable piezoelectric sensor for real-time evaluation of the motor function recovery after nerve injury. *Adv. Funct. Mater.* **2024**, *34*, 2400295.
72. Schönlein, R.; Larrañaga, X.; Azkune, M.; Li, Y.; Liu, G.; Müller, A.J.; Aguirresarobe, R.; Ugartemendia, J.M. The combined effects of optical purity, chain orientation, crystallinity, and dynamic mechanical activation as means to obtain highly piezoelectric polylactide materials. *ACS Appl. Mater. Interfaces* **2024**, *6*, 7561–7571.
73. Cui, X.; Shan, Y.; Li, J.; Xiao, M.; Xi, Y.; Ji, J.; Wang, E.; Zhang, B.; Xu, L.; Zhang, M.; et al. Bifunctional piezo-enhanced PLLA/ZA coating prevents aseptic loosening of bone implants. *Adv. Funct. Mater.* **2024**, *34*, 2403759.
74. Li, T.; Yuan, Y.; Gu, L.; Li, J.; Shao, Y.; Yan, S.; Zhao, Y.; Carlos, C.; Dong, Y.; Qian, H. et al. Ultrastable piezoelectric biomaterial nanofibers and fabrics as an implantable and conformal electromechanical sensor patch. *Sci. Adv.* **2024**, *10*, eadn8706.
75. Tan, J.; Li, T.; Xie, Y.; Chen, M.; Li, L.; Zhang, C.; Chen, Y.; Pang, L.; Zhang, C.; Li, Y.; et al. Fabricating high-performance biomedical PLLA/PVDF blend micro bone screws through in situ structuring of oriented PVDF submicron fibers in microinjection molding. *Compos. Part. B Eng.* **2024**, *281*, 111567.
76. Yuan, H.; Cazade, P.A.; Zhou, S.; Shimon, L.J.W.; Yuan, C.; Tan, D.; Liu, C.; Fan, W.; Thangavel, V.; Cao, Y.; et al. Molecular engineering of ordered piezoelectric sulfonic acid-containing assemblies. *Small* **2024**, *20*, e2309493.
77. Wang, Q.; Tian, Y.; Yao, M.; Fu, J.; Wang, L.; Zhu, Y. Bimetallic organic frameworks of high piezovoltage for sono-piezo dynamic therapy. *Adv. Mater.* **2023**, *35*, e2301784.
78. Lin, S.C.; Joshi, R.; Ganguly, A.; Barman, S.R.; Pal, A.; Kaswan, K.; Liu, K.L.; Nain, A.; Kao, F.C.; Lin, Z.H. Ultrasound-

- guided drug delivery system utilizing piezocatalytic MoS₂ nanomaterials for anti-inflammatory therapy. *Nano Energy* **2024**, *127*, 109732.
79. Liu, Q.; Liu, L.; Fan, D.; Xie, S.; Wang, C.; Gou, X.; Li, X. Self-powered biodegradable piezoelectric fibrous composites as antibacterial and wound healing dressings. *Appl. Mater. Today* **2024**, *37*, 102120.
80. Wan, X.; Wang, Z.; Zhao, X.; Hu, Q.; Li, Z.; Lin Wang, Z.; Li, L. Flexible and highly piezoelectric nanofibers with organic–inorganic coaxial structure for self-powered physiological multimodal sensing. *Chem. Eng. J.* **2023**, *451*, 139077.
81. Pan, Q.; Zheng, Y.; Zhou, Y.; Zhang, X.; Yuan, M.; Guo, J.; Xu, C.; Cheng, Z.; Kheraif, A.A.A.; Liu, M.; et al. Doping engineering of piezo-sonocatalytic nanocoating confer dental implants with enhanced antibacterial performances and osteogenic activity. *Adv. Funct. Mater.* **2024**, *34*, 2313553.
82. Liu, J.; Li, S.; Zhou, S.; Chen, Z.; Xu, J.; Cui, N.; Yuan, M.; Li, B.; Gu, L. A high-performance, biocompatible, and fully biodegradable piezo-triboelectric hybrid nanogenerator based on PVA/Glycine/PVA heterostructured piezoelectric film. *Nano Energy* **2024**, *122*, 109310.
83. Lin, Q.; Zhang, Y.; Chen, L.; Zhang, H.; An, C.; Li, C.; Wang, Q.; Song, J.; He, W.; Wang, H. Glycine/alginate-based piezoelectric film consisting of a single, monolithic beta-glycine spherulite towards flexible and biodegradable force sensor. *Regen. Biomater.* **2024**, *11*, rbac047.
84. Li, J.; Carlos, C.; Zhou, H.; Sui, J.; Wang, Y.; Silva-Pedraza, Z.; Yang, F.; Dong, Y.; Zhang, Z.; Hacker, T.A.; et al. Stretchable piezoelectric biocrystal thin films. *Nat. Commun.* **2023**, *14*, 6562.
85. Yang, Z.; He, X.; Chen, Y.; Zhu, M.; Xu, P. 3D-printed piezoelectric scaffolds composed of uniform core-shell structured BaTiO₃@ bioactive glasses particles for bone regeneration. *Ceram. Int.* **2024**, *50*, 18303–18311.
86. Fang, Q.; Wang, D.; Lin, W.; Ge, Z.; Deng, X.; Zhao, R.; Tang, Y.; Liu, W.; Xiong, Z.; Duan, A.; et al. Highly stretchable piezoelectric elastomer for accelerated repairing of skeletal muscles loss. *Adv. Funct. Mater.* **2024**, *34*, 2313055.
87. Zhang, H.; Tang, Y.; Gu, Z.; Wang, P.; Chen, X.; Lv, H.; Li, P.; Jiang, Q.; Gu, N.; Ren, S.; et al. Biodegradable ferroelectric molecular crystal with large piezoelectric response. *Science* **2024**, *383*, 1492–1498.
88. Wang, L.; Li, R. A more biofriendly piezoelectric material. *Science* **2024**, *383*, 1416.
89. Wang, Y.; Liu, S.; Li, L.; Li, H.; Yin, Y.; Rencus-Lazar, S.; Guerin, S.; Ouyang, W.; Thompson, D.; Yang, R.; et al. Manipulating the piezoelectric response of amino acid-based assemblies by supramolecular engineering. *J. Am. Chem. Soc.* **2023**, *145*, 15331–15342.
90. Guerin, S.; Stapleton, A.; Chovan, D.; Mouras, R.; Gleeson, M.; McKeown, C.; Noor, M.R.; Silien, C.; Rhen, F.M.F.; Kholkin, A.L.; et al. Control of piezoelectricity in amino acids by supramolecular packing. *Nat. Mater.* **2018**, *17*, 180–186.
91. Sharafkhani, S. Highly aligned thin PVDF/Cloisite 30B nanofibers as a piezoelectric sensor. *Mater. Res. Bull.* **2024**, *180*, 113060.
92. Wang, S.; Tang, C.-Y.; Jia, J.; Zha, X.-J.; Liu, J.-H.; Zhao, X.; Ke, K.; Wang, Y.; Yang, W. Liquid electrolyte-assisted electrospinning for boosting piezoelectricity of poly (vinylidene fluoride) fiber mats. *Macromolecules* **2023**, *56*, 7479–7489.
93. Zheng, W.; Li, T.; Jin, F.; Qian, L.; Ma, J.; Wei, Z.; Ma, X.; Wang, F.; Sun, J.; Yuan, T.; et al. Interfacial polarization locked flexible beta-phase glycine/Nb₂CT_x piezoelectric nanofibers. *Small* **2024**, *20*, 2308715.
94. Hou, L.; Huan, Y.; Zheng, M.; Liu, Y.; Wang, C.; Wang, X.; Li, C.; Wang, Z.; Wei, T. 3D vertically aligned microchannel structure to enhance piezoelectric energy harvesting performance of PZT/PVDF&CNTs piezoelectric composites. *J. Mater.* **2024**, *10*, 1063–1070.
95. Wei, X.; Xu, K.; Wang, Y.; Zhang, Z.; Chen, Z. 3D Printing of flexible BaTiO₃/polydimethylsiloxane piezocomposite with aligned particles for enhanced energy harvesting. *ACS Appl. Mater. Interfaces* **2024**, *16*, 11740–11748.
96. Pawar, O.Y.; Lim, S. 3D-Printed piezoelectric nanogenerator with aligned graphitic carbon nitrate nanosheets for enhancing piezoelectric performance. *J. Colloid. Interface Sci.* **2024**, *654*, 868–877.
97. Tavares, C.; Vieira, T.; Silva, J.C.; Borges, J.; Lanca, M.C. Bioactive hydroxyapatite aerogels with piezoelectric particles. *Biomimetics* **2024**, *9*, 143.
98. Fan, W.; Lei, R.; Dou, H.; Wu, Z.; Lu, L.; Wang, S.; Liu, X.; Chen, W.; Rezakazemi, M.; Aminabhavi, T.M.; et al. Sweat permeable and ultrahigh strength 3D PVDF piezoelectric nanoyarn fabric strain sensor. *Nat. Commun.* **2024**, *15*, 3509.
99. Chen, K.; Qin, Z.; Zhang, M.; Wang, L.; Zheng, S.; Wang, Y.; Chen, C.; Tang, H.; Zhong, Y.; Yang, H.; et al. The electrical properties and in vitro osteogenic properties of 3D-printed MgO@BT/HA piezoelectric ceramic disk. *J. Am. Ceram. Soc.* **2024**, *107*, 7441–7451.
100. Zhang, W.; Peng, Z.; Xia, H.; Ma, L.; Qiu, L.; Yan, X.; Gao, Y.; Yang, X.; Yang, Z. Long-lifespan and sterilizable face masks leveraging the power of light and electricity. *Sep. Purif. Technol.* **2025**, *354*, 128697.
101. Kaarthik, J.; Ram, N.; Pabba, D.P.; Reddy, S.G.; Venkateswarlu, A. Optimization of structural, dielectric, and electrical properties in lead-free Ba_{0.85}Ca_{0.15}Zr_{0.1}Ti_{0.9}O₃ through site engineering for biocompatible energy harvesting. *Mater. Today Commun.* **2024**, *41*, 110441.
102. Zhang, S.; Chen, D.; Gu, Z.; Luo, H.; Chen, X.; Fu, Q. Ultrasound-triggered piezocatalytic conductive Guar gum/PEDOT: PSS/BTO composite hydrogels for bacterial-infected skin wound healing. *Nano TransMed* **2024**, *3*, 100035.
103. Li, Y.; Fan, Y.; Zhao, S.; Cheng, B. Ultrasound-triggered piezoelectric polyetheretherketone with boosted osteogenesis via regulating Akt/GSK3β/β-catenin pathway. *J. Nanobiotechnology* **2024**, *22*, 539.
104. Chen, Y.; Guan, H.; Wang, X.; Wen, Y.; He, Q.; Lin, R.; Yang, Z.; Wang, S.; Zhu, X.; Zhong, T.; et al. Implantable and

- wireless-controlled antibacterial patch for deep abscess eradication and therapeutic efficacy monitoring. *Nano Energy* **2024**, *131*, 110193.
105. Hu, C.; Liu, B.; Huang, X.; Wang, Z.; Qin, K.; Sun, L.; Fan, Z. Sea cucumber-inspired microneedle nerve guidance conduit for synergistically inhibiting muscle atrophy and promoting nerve regeneration. *ACS Nano* **2024**, *18*, 14427–14440.
106. Zhang, M.; Yang, G.; Long, Z.; Tang, Y.; Li, D.; Liang, S.; Lin, R.; Yang, Z.; Bao, H.; Xing, L.; et al. Wireless battery-free peripheral nerve stimulation conch for remote muscle activation. *Adv. Mater. Technol.* **2024**, *9*, 2301458.
107. Liu, H.; Ding, S.; Lin, X.; Wang, S.; Wang, Y.; Feng, Z.; Song, J. Bone fracture healing under the intervention of a stretchable ultrasound array. *ACS Nano* **2024**, *18*, 19549–19560.
108. Chen, Y.; An, Q.; Hu, X.; Zhao, R.; Teng, K.; Zhang, Y.; Zhao, Y. Effective scald wound functional recovery patch achieved by molecularly intertwined electrical and chemical message in self-adhesive assemblies. *ACS Appl. Mater. Interfaces* **2023**, *15*, 38346–38356.
109. Wang, W.; Wang, P.; Li, Q.; Dai, W.; Yi, B.; Gao, Z.; Liu, W.; Wang, X. Piezoelectrically-enhanced composite membranes mimicking the tendinous electrical microenvironment for advanced tendon repair. *Nano Today* **2024**, *57*, 102381.
110. Li, Z.; Wang, X.; Zhao, Z.; Liu, Y. A conductive piezoelectric hydrogel combined with peramp panel and wireless electrical stimulation for spinal cord injury repair. *Chem. Eng. J.* **2024**, *493*, 152238.
111. Li, Z.; He, D.; Guo, B.; Wang, Z.; Yu, H.; Wang, Y.; Jin, S.; Yu, M.; Zhu, L.; Chen, L.; et al. Self-promoted electroactive biomimetic mineralized scaffolds for bacteria-infected bone regeneration. *Nat. Commun.* **2023**, *14*, 6963.
112. George, L.; Bates, E. Mechanisms underlying influence of bioelectricity in development. *Front. Cell Dev. Biol.* **2022**, *10*, 772230.
113. Mycielska, M.; Djamgoz, M. Cellular mechanisms of direct-current electric field effects: Galvanotaxis and metastatic disease. *J. Cell Sci.* **2004**, *117*, 1631–1639.
114. Wehrle-Haller, B.; Imhof, B. Actin, microtubules and focal adhesion dynamics during cell migration. *Int. J. Biochem. Cell Biol.* **2003**, *35*, 39–50.
115. Zhao, H.; Steiger, A.; Nohner, M.; Ye, H. Specific intensity direct current (DC) electric field improves neural stem cell migration and enhances differentiation towards β III-tubulin+ neurons. *PLoS ONE* **2015**, *10*, e0129625.
116. Xu, Q.; Dai, W.; Li, P.; Li, Q.; Gao, Z.; Wu, X.; Liu, W.; Wang, W. Piezoelectric film promotes skin wound healing with enhanced collagen deposition and vessels regeneration via upregulation of PI3K/AKT. *Nano Res.* **2024**, *17*, 7461–7478.
117. Ke, Q.; Zhang, X.; Yang, Y.; Chen, Q.; Su, J.; Tang, Y.; Fang, L. Wearable magnetoelectric stimulation for chronic wound healing by electrospun CoFe_2O_4 @CTAB/PVDF dressings. *ACS Appl. Mater. Interfaces* **2024**, *16*, 9839–9853.
118. Pi, W.; Chen, H.; Liu, Y.; Xiang, J.; Zhang, H.; Yang, X.; Zhang, M.; Cao, J.; Chang, T.; Zheng, Y.; et al. Flexible sonopiezo patch for functional sweat gland repair through endogenous microenvironmental remodeling. *ACS Nano* **2024**, *18*, 20283–20295.
119. Jin, F.; Li, T.; Yuan, T.; Du, L.; Lai, C.; Wu, Q.; Zhao, Y.; Sun, F.; Gu, L.; Wang, T.; et al. Physiologically self-regulated, fully implantable, battery-free system for peripheral nerve restoration. *Adv. Mater.* **2021**, *33*, 2104175.
120. Wang, Q.; Wei, Y.; Yin, X.; Zhan, G.; Cao, X.; Gao, H. Engineered PVDF/PLCL/PEDOT dual electroactive nerve conduit to mediate peripheral nerve regeneration by modulating the immune microenvironment. *Adv. Funct. Mater.* **2024**, *34*, 2400217.
121. Liu, Y.; Zhang, Z.; Zhao, Z.; Xu, Y.; Duan, X.; Zhao, Y.; Ma, W.; Yang, Y.; Yang, Y.; Liu, Z. An easy nanopatch promotes peripheral nerve repair through wireless ultrasound-electrical stimulation in a band-aid-like way. *Adv. Funct. Mater.* **2024**, *34*, 2407411.
122. Yu, C.C.; Shah, A.; Amiri, N.; Marcus, C.; Nayeem, M.O.G.; Bhayadia, A.K.; Karami, A.; Dagdeviren, C. A conformable ultrasound patch for cavitation-enhanced transdermal cosmeceutical delivery. *Adv. Mater.* **2023**, *35*, e2300066.
123. Huang, R.; Lin, C.; Jiang, G.; Zhang, M.; Gao, W.; Aihemaiti, K.; Liu, Q.; Shi, J.; Shi, W.; Huang, R. BBB-penetrating magnetoelectric nanoparticles with sustainable Gel formulation for enhanced chemotherapy and reduced postoperative glioma recurrence. *Chem. Eng. J.* **2024**, *496*, 154208.
124. Wang, Y.; Tang, Q.; Wu, R.; Sun, S.; Zhang, J.; Chen, J.; Gong, M.; Chen, C.; Liang, X. Ultrasound-triggered piezocatalysis for selectively controlled no gas and chemodrug release to enhance drug penetration in pancreatic cancer. *ACS Nano* **2023**, *17*, 3557–3573.
125. Van Neer, P.; Peters, L.; Verbeek, R.; Peeters, B.; de Haas, G.; Horchens, L.; Fillinger, L.; Schrama, T.; Merks-Swolfs, E.J.W.; Gijbsbertse, K.; et al. Flexible large-area ultrasound arrays for medical applications made using embossed polymer structures. *Nat. Commun.* **2024**, *15*, 2802.
126. Chen, J.X.; Li, J.W.; Jiang, Z.J.; Chiu, C.W. Polymer-assisted dispersion of reduced graphene oxide in electrospun polyvinylidene fluoride nanofibers for enhanced piezoelectric monitoring of human body movement. *Chem. Eng. J.* **2024**, *498*, 155244.
127. Das, T.; Kumar Yadav, M.; Dev, A.; Kar, M. Double perovskite-based wearable ternary nanocomposite piezoelectric nanogenerator for self-charging, human health monitoring and temperature sensor. *Chem. Eng. J.* **2024**, *496*, 153926.
128. Zhang, L.; Marcus, C.; Lin, D.; Mejorado, D.; Schoen, S.J.; Pierce, T.; Kumar, V.; Fernandez, S.; Hunt, D.; Li, Q.; et al. A conformable phased-array ultrasound patch for bladder volume monitoring. *Nat. Electron.* **2024**, *7*, 77–90.
129. Kim, M.; Joe, D.J.; Doh, I.; Cho, Y.H. Piezoelectric nanocomposite-based multifunctional wearable bioelectronics for mental stress analysis utilizing physiological signals. *Adv. Mater. Technol.* **2024**, *9*, 2301610.
130. Jeong, J.S.; Chang, J.H.; Shung, K.K. Ultrasound transducer and system for real-time simultaneous therapy and diagnosis

- for noninvasive surgery of prostate tissue. *IEEE Trans. Ultrason. Ferroelectr. Freq. Control* **2009**, *9*, 1913–1922.
131. Wan, Y.; Ebbini, E.S. Imaging with concave large-aperture therapeutic ultrasound arrays using conventional synthetic-aperture beamforming. *IEEE Trans. Ultrason. Ferroelectr. Freq. Control* **2008**, *8*, 1705–1718.
132. Ebbini, E.S.; Yao, H.; Shrestha, A. Dual-mode ultrasound phased arrays for image-guided surgery. *Ultrason. Imaging* **2006**, *28*, 65–82.
133. Voignac, D.; Belsey, S.; Wermter, E.; Paltiel, Y.; Shoseyov, O. Biobased electronics: Tunable dielectric and piezoelectric cellulose nanocrystal-protein films. *Nanomaterials* **2023**, *13*, 2258.
134. Zhang, Y.; Li, Q.; Wu, H.; Wang, Y.; Wang, Y.; Rencus-Lazar, S.; Zhao, Y.; Wang, J.; Mei, D.; Xu, H.; et al. Racemic amino acid assembly enables supramolecular beta-sheet transition with property modulations. *ACS Nano* **2023**, *17*, 2737–2744.
135. Ding, C.; Lin, Y.; Cheng, N.; Meng, N.; Wang, X.; Yin, X.; Yu, J.; Ding, B. Dual-cooling textile enables vertical heat dissipation and sweat evaporation for thermal and moisture regulation. *Adv. Funct. Mater.* **2024**, *34*, 2400987.
136. Fan, W.; Zhang, C.; Liu, Y.; Wang, S.; Dong, K.; Li, Y.; Wu, F.; Liang, J.; Wang, C.; Zhang, Y. An ultra-thin piezoelectric nanogenerator with breathable, superhydrophobic, and antibacterial properties for human motion monitoring. *Nano Res.* **2023**, *16*, 11612–11620.
137. Kwon, S.H.; Zhang, C.; Jiang, Z.; Dong, L. Textured nanofibers inspired by nature for harvesting biomechanical energy and sensing biophysiological signals. *Nano Energy* **2024**, *122*, 109334.
138. Habib, M.; Lantgios, I.; Hornbostel, K. A review of ceramic, polymer and composite piezoelectric materials. *J. Phys. D: Appl. Phys.* **2022**, *55*, 423002.
139. Zhao, K.; Zheng, M.; Yan, X.; Zhu, M.; Hou, Y. Effect of direct current and alternating current poling on the piezoelectric properties of $\text{Ba}_{0.85}\text{Ca}_{0.15}\text{Ti}_{0.9}\text{Zr}_{0.1}\text{O}_3$ ceramics. *J. Mater. Sci: Mater. Electron.* **2021**, *32*, 27815–27822.
140. Kim, H.; Wan, H.; Luo, C.; Sun, Y.; Yamashita, Y.; Karaki, T.; Lee, H.; Jiang, X. A review on alternating current poling for perovskite relaxor- PbTiO_3 single crystals. *IEEE Trans. Ultrason. Ferroelectr. Freq. Control* **2022**, *69*, 3037–3047.
141. Hong, C.; Wang, Z.; Su, B.; Guo, L.; Yang, X.; Long, X.; He, C. Enhanced piezoelectric and dielectric properties of $\text{Pb}(\text{Yb}_{1/2}\text{Nb}_{1/2})\text{O}_3$ - $\text{Pb}(\text{Mg}_{1/3}\text{Nb}_{2/3})\text{O}_3$ - PbTiO_3 crystals by combining alternating and direct current poling. *J. Appl. Phys.* **2021**, *129*, 124101.

Article

A Novel Bi-Directional and Bi-Temporal Delivery System for Enhancing Intrasyovial Tendon Repair

Yidan Chen¹, Seth Kinoshita², Emily Yan³, Min Hao³, Hua Shen⁴,
Richard Gelberman⁴, Stavros Thomopoulos⁵, and Younan Xia^{2,3,*}

¹ School of Materials Science and Engineering, Georgia Institute of Technology, Atlanta, GA 30332, USA

² School of Chemistry and Biochemistry, Georgia Institute of Technology, Atlanta, GA 30332, USA

³ The Wallace H. Coulter Department of Biomedical Engineering, Georgia Institute of Technology and Emory University, Atlanta, GA 30332, USA

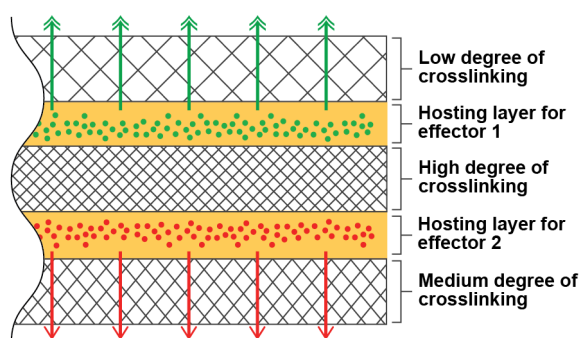
⁴ Department of Orthopedic Surgery, Washington University School of Medicine, St. Louis, MO 63110, USA

⁵ Department of Orthopedic Surgery, Department of Biomedical Engineering, Columbia University, New York, NY 10032, USA

* Correspondence: younan.xia@bme.gatech.edu

Received: 24 September 2024; Revised: 8 October 2024; Accepted: 14 October 2024; Published: 18 October 2024

Abstract: Flexor tendon injuries are common and often require surgical repair and prolonged rehabilitation. Successful clinical outcomes depend on the concurrent suppression of adhesions (caused by inflammation) at the tendon surface and promotion of matrix synthesis inside the tendon. Herein, we report a bi-directional and bi-temporal drug delivery system designed to target both the initial inflammatory phase and the subsequent proliferative and remodeling phases of healing to improve outcomes after flexor tendon repair. The system features a multi-layered design with anti-adhesion and pro-matrix factors encapsulated in separate layers of hyaluronate films crosslinked to different degrees to control their direction and rate of release. After validating drug delivery under controlled release, cell culture experiments involving tendon fibroblasts and a Transwell system are conducted to demonstrate the system's efficacy in modulating local cellular responses. The promising results from this study lay the groundwork for moving this system toward in vivo testing and clinical translation.



Keywords: flexor tendon repair; sodium hyaluronate; drug delivery; controlled release; Transwell cell culture

1. Introduction

The flexor tendons of the hand facilitate movements necessary for daily activities such as gripping and manipulating objects. Intrasyovial flexor tendon injuries, including lacerations and ruptures, are common and they result in significant pain and disability. Treatment of these injuries typically requires surgical repair and prolonged rehabilitation to regain function. Unfortunately, current approaches often fail to return full function to the hand due to poor healing that leads to gapping or repair-site-failure, and adhesion formation that limits motion. To improve the outcome of the repair of an intrasyovial flexor tendon injury, it is necessary to concurrently suppress the adhesion between the tendon and the surrounding sheath while accelerating the regeneration of the tendon at the repair site [1].

Recent research efforts have focused on applying stem cells, growth factors, and/or small molecule drugs to the tendon injury site following surgical repair to improve the outcome [2–5]. However, most delivery systems are designed to release a single factor at the target site, making them inadequate for flexor tendon repair, which requires simultaneous prevention of adhesion at the tendon surface and promotion of matrix synthesis inside the tendon. Herein, we report a novel bi-directional and bi-temporal controlled release system that can be wrapped around the intrasyovial tendon repair site to address this need. Specifically, this system delivers an anti-adhesion factor toward the tendon sheath during the early inflammatory period and a pro-matrix factor toward the tendon



Copyright: © 2024 by the authors. This is an open access article under the terms and conditions of the Creative Commons Attribution (CC BY) license (<https://creativecommons.org/licenses/by/4.0/>).

Publisher's Note: Scilight stays neutral with regard to jurisdictional claims in published maps and institutional affiliations

repair site in the subsequent proliferative and remodeling phases, effectively addressing both requirements for successful healing.

Our controlled release system is based on sodium hyaluronate (NaHA), a major lubricating component of the synovial fluid that has been extensively used in flexor tendon repairs [6,7]. Prior studies suggested that NaHA can prevent adhesion formation and reduce gliding resistance both *in vitro* and *in vivo* [8,9]. Therefore, NaHA is considered an excellent carrier material for delivering biological effectors in intrasynovial tendon repair. However, the half-life of NaHA in the physiological environment is very short (several hours to 1.5 days [10]) due to the presence of enzymes, such as hyaluronidase (HAase), capable of rapidly breaking down NaHA-based carriers once implanted. To increase the tissue residence time of a NaHA-based delivery system while enhancing its mechanical properties, here we use (1-ethyl-3-(3-dimethylaminopropyl) carbodiimide (EDC) to help crosslink the NaHA matrix into a network. By controlling the duration of crosslinking, we obtain NaHA films with different degrees of crosslinking under a condition compatible with the physiological system. The crosslinked NaHA films are fully characterized, and their drug delivery capabilities are examined, including the degradation rates and cumulative drug release profiles. To achieve bi-directional and bi-temporal release, the delivery system is designed to adopt a multi-layered structure, in which the payloads are encapsulated in two separate hosting layers between NaHA films crosslinked to different degrees (Figure 1). While the two sides of the system are capped by NaHA films (i.e., the permeable layers) crosslinked to different degrees to achieve bi-temporal release, a middle film made of the most heavily crosslinked NaHA serves as a blocking layer to prevent the inter-diffusion between the two drug-loaded layers, realizing bi-directional delivery. We explore two small molecule drugs, the IKK β inhibitor 2-amino-6-(2-(cyclopropylmethoxy)-6-hydroxyphenyl)-4-(piperidin-4-yl)nicotinonitrile hydrochloride (ACHP hydrochloride, C₂₁H₂₅ClN₄O₂) (to control inflammation) and sodium dichloroacetate (DCA) (to control metabolism), in this study. To avert a potential detrimental burst release effect, the small molecule drugs are pre-loaded in nanoparticles made of natural fatty acids and then encapsulated in a hosting layer comprised of physically-crosslinked poly(vinyl alcohol) (PVA) and NaHA. The bi-directional and bi-temporal release is visualized and validated by replacing the small molecule drugs with fluorescent model compounds. A series of tendon fibroblast Transwell culture experiments are conducted to demonstrate the efficacy of the bi-directional and bi-temporal delivery system in modulating cellular responses. By establishing the biological effectiveness of the bi-directional delivery of ACHP and DCA *in vitro*, the current study poses a strong foundation for exploring the opportunity to concurrently prevent adhesion formation through IKK β inhibition and enhance tendon strength through modulation of metabolism.

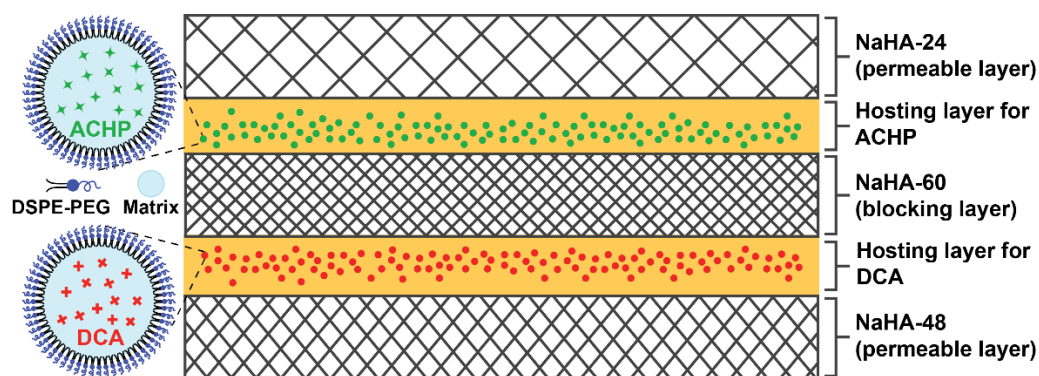


Figure 1. Schematic of the bi-directional and bi-temporal release system, which adopts a multi-layered structure, with two hosting layers containing fatty acid nanoparticles pre-loaded with the small molecule drugs, ACHP and DCA, respectively, and stabilized by DSPE-PEG surfactant. The hosting layers are comprised of a physically-crosslinked PVA-NaHA matrix. The two hosting layers are separated by a blocking layer made of NaHA-60. Two permeable layers, made of NaHA-24 and NaHA-48, respectively, help control the release kinetics of the ACHP- and DCA-loaded nanoparticles. NaHA-24, NaHA-48, and NaHA-60 correspond to NaHA films crosslinked for 24, 48, and 60 h in the presence of (1-ethyl-3-(3-dimethylaminopropyl) carbodiimide, respectively.

2. Experimental Section

2.1. Chemicals and Materials

Lauric acid (>98%), stearic acid (95%), ethanol (EtOH, HPLC grade), PVA (M_w ≈ 89,000–98,000), thiazolyl blue tetrazolium bromide (MTT), dimethyl sulfoxide (DMSO), rhodamine B (RhB), indocyanine green (ICG), DCA, hyaluronidase (from bovine testes, 400–1000 units/mg solid), and glass microcapillary tube (Ace Glass) were all obtained from Sigma-Aldrich (St. Louis, MO, USA). Fetal bovine serum (FBS), EDC hydrochloride,

Dulbecco's modified Eagle medium (DMEM) with a high glucose content (4.5 g/L), DMEM with a low glucose content (1 g/L) and sodium pyruvate (110 mg/L), antibiotic-antimycotic, phosphate-buffered saline (PBS, pH = 7.4), calcein-AM, ethidium homodimer-1 (EthD-1), TRIzol reagent, and PVC tubes were ordered from Thermo Fisher (Waltham, MA, USA). ACHP hydrochloride was obtained from MedChemExpress (Monmouth Junction, NJ, USA); 1,2-distearoyl-sn-glycero-3-phosphoethanolamine-N-[methoxy (polyethylene glycol)-5000] (Mw \approx 5000, DSPE-PEG 5000) was purchased from Laysan Bio Inc (Arab, AL, USA); NaHA (Mw \approx 200 k) was ordered from Lifecore Biomedical (Chaska, MN, USA); syringe needles (18 G and 26 G) were ordered from BD (Franklin Lakes, NJ, USA); and epoxy adhesive was obtained from Devcon. All chemicals and materials were used as received. The deionized (DI) water used in all experiments was obtained by filtering through a Millipore ultrapure water system (Billerica, MA, USA).

2.2. Fabrication of Fatty Acid Nanoparticles and Encapsulation of Payloads

Fatty acid nanoparticles were prepared through hydrodynamic focusing in a homemade fluidic device by following a published protocol [11]. Briefly, the fluidic device was fabricated by inserting a 26 G needle into a PVC tube (inner diameter: 1/16 inch) and connecting it with a microcapillary tube (550 μ m inner diameter), followed by fixing and sealing with epoxy adhesive. The focused phase, a solution of fatty acids, was prepared by dissolving lauric acid and stearic acid at a 4:1 mass ratio in EtOH with a total concentration of 6 mg/mL. The focusing phase was prepared by dissolving the surfactant DSPE-PEG in water at a concentration of 0.2 mg/mL. The fatty acid and surfactant solutions were introduced using two syringe pumps (KD100, KD Scientific, Holliston, MA, USA) with independently controlled flow rates. The flow rates of the focused phase and focusing phase were set to 14 and 700 μ L/min, respectively. The encapsulation of the fluorescent molecules (RhB and ICG), DCA, and ACHP in the fatty acid nanoparticles was achieved by directly adding them into the fatty acid solution. For molecules that are scarcely soluble in EtOH, including ICG and ACHP, they were dissolved in DMSO at specific concentrations (10 mg/mL for ICG and 25 mg/mL for ACHP), followed by mixing with the fatty acid solution in ethanol at a 5:95 (v/v) ratio. For compounds highly soluble in EtOH (e.g., RhB and DCA), the powders were directly dissolved in the fatty acid solution in EtOH at a concentration of 20 mg/mL for RhB and 30 mg/mL for DCA at 50 °C, respectively. The nanoparticles were collected and kept in an ice bath, except for washing. The nanoparticles were washed with water containing DSPE-PEG (0.5 mg/mL) three times at 16,600 g rcf for 8 min using a centrifuge (5471C and 5810, Eppendorf, Hamburg, Germany) to remove the free drug molecules. The nanoparticles were finally resuspended in water containing DSPE-PEG (1 mg/mL) for further use.

2.3. Preparation and Characterization of the Crosslinked NaHA Films

The NaHA films were prepared through solution casting, followed by crosslinking in a 50 mM EDC solution in an EtOH/water mixture (8:2, v/v) for different periods of time. The polymer solution was prepared by dissolving NaHA in water at a concentration of 1 wt.% under stirring overnight on an orbital shaker (Apollo Digital Orbital Shaker, CLP) at 300 rpm and room temperature. In a typical process, 5 mL of 1 wt.% NaHA was cast in a glass petri dish (VWR, Radnor, PA, USA) with a diameter of 50 mm. The dish was placed in a fume hood with a laminar flow for 20 h to allow the solvent to evaporate. The dried NaHA film was peeled off and then cut into smaller pieces of the desired size (circles with a diameter of 1 inch). The crosslinking solution was prepared by dissolving EDC in the EtOH/water mixture and shaking at 300 rpm for 1 h to obtain a homogeneous mixture. To achieve varying degrees of crosslinking, the NaHA films were immersed in the crosslinking solution for 24, 48, and 60 h at room temperature. The resultant films are denoted NaHA-24, NaHA-48, and NaHA-60, respectively, according to the duration of crosslinking. After crosslinking, the films were washed with the EtOH/water mixture for 3 min, followed by rinsing with 50% EtOH and H₂O and finally drying at room temperature in a fume hood with laminar flow. Infrared (IR) spectra of the non-crosslinked NaHA, NaHA-24, NaHA-48, and NaHA-60 films were recorded using a Fourier Transform Infrared (FT-IR) Spectrometer (Shimadzu IRAffinity-1, Shimadzu, Kyoto, Kyoto, Japan) under attenuated total reflection mode.

2.4. Degradation of the Crosslinked NaHA Films

The degradation of the NaHA films with different degrees of crosslinking was evaluated in vitro by immersing the NaHA-24, NaHA-48, and NaHA-60 films in 1 mL of PBS containing 20 U HAase and incubating at 37 °C [12]. The medium was changed every day. For each type of film, multiple (N = 3) pieces were used for mass loss measurement at each time point. Briefly, the medium was removed, and the films were then freeze-dried for 5 h to remove any remaining liquid before being weighed on a balance. The percentage mass remaining for each group was calculated by normalizing the value against the starting mass of the respective group.

2.5. Monitoring the Release of Fatty Acid Nanoparticles from the Crosslinked NaHA Films

Fluorescently-labeled fatty acid nanoparticles were prepared by encapsulating RhB and ICG using the antisolvent precipitation method described above. A mixture of PVA (7.5 wt.%) and NaHA (0.5 wt.%) was prepared by mixing 15 wt.% PVA and 1 wt.% NaHA at 1:1 (v/v) ratio and vortexing for 1 min on a Vortex-Genie 2 vortex mixer (Scientific Industries, Bohemia, NY, USA) to obtain a homogeneous solution. This mixture was used both as the hosting layer for the drug-loaded fatty acid nanoparticles and as a glue during the layer-by-layer assembly process. The fluorescently labeled nanoparticles were loaded between NaHA films with different degrees of crosslinking. Release from NaHA-24 and NaHA-48 were monitored using the structure in Figure S1A, and that from NaHA-60 was monitored using the structure in Figure S1B. After the assembling process, the structure went through three freeze-thawing cycles for the PVA in the PVA-NaHA mixture to form hydrogen bonds. One freeze-thawing cycle involved freezing at $-80\text{ }^{\circ}\text{C}$ for 3 h and thawing at $4\text{ }^{\circ}\text{C}$ for 1 h. The structure was subsequently incubated in 150 μL of PBS, or PBS containing 10 U or 20 U HAase at $37\text{ }^{\circ}\text{C}$ [12,13]. For each sample, the incubation solution was removed every 24 h and 150 μL of fresh solution of the corresponding type was supplemented back. The amount of nanoparticles released was correlated with the reduction of fluorescence intensity within the system. Fluorescence images were recorded using a confocal fluorescence microscope (Zeiss LSM 900, Zeiss, Oberkochen, Germany) every 24 h for the first 5 days and every 48 h for the remaining period. The beam intensity, exposure time, and digital gain were fixed for each sample. At each time point, images were taken at 10 random spots on a single sample and the average fluorescence intensity of these spots was recorded. The release for each sample was normalized against the fluorescence intensity recorded at the beginning of the experiment ($t = 0\text{ h}$). Three technical replicates with the same degree of crosslinking and the same incubation condition were performed for each group ($N = 3$).

2.6. Fabrication of the Bi-Directional and Bi-Temporal Delivery System

We fabricated the delivery system by assembling the NaHA films in a layer-by-layer manner. In a typical process, a NaHA-48 film was placed at the bottom and then a thin layer of the PVA-NaHA mixture was applied by brush coating. Afterward, 50 μL of the suspension of DCA-loaded fatty acid nanoparticles containing a total dose of 1.483 mg (9.83 μmol) DCA was dropped on the top. The PVA-NaHA mixture was evenly applied to the bottom of a NaHA-60 film and the film was attached to the previous structure, with the PVA-NaHA side facing down. The same procedure was repeated for the top layers containing the ACHP-loaded nanoparticles: a 10 μL suspension of ACHP-loaded fatty acid nanoparticles containing a total dose of 22.3 μg (56 nmol) ACHP was sandwiched between the middle layer of NaHA-60 and the topmost layer of NaHA-24. After the assembly process, the delivery system went through three freeze-thawing cycles. The thickness of the dried construct was around 46.0 μm .

2.7. Visualization of the Bi-Directional Release

The bi-directional release from the multi-layered NaHA construct was visualized using fatty acid nanoparticles pre-loaded with fluorescent model compounds. Specifically, ICG and RhB were selected to represent ACHP and DCA, respectively. The construct was incubated in 200 μL of 20 U HAase-supplemented PBS solution at $37\text{ }^{\circ}\text{C}$ in a 12-well plate for up to 6 days [12]. Z-stack confocal fluorescence micrographs were captured every day using a confocal fluorescence microscope (Zeiss LSM 900). Cross-sectional images were reconstructed from the z-stack ones using the Zen (blue) software from Zeiss.

2.8. Fabrication of a Unidirectional Delivery System for the Cell Culture Experiment

A simplified unidirectional delivery system was used in the in vitro experiment (Figure S2). The system was fabricated and attached to the Transwell insert in a similar manner to the bi-directional and bi-temporal delivery system, except that only two layers of NaHA films were involved. The system was attached to the bottom of a Transwell insert (6-well insert, 0.4 μm , PET translucent, cellQART, SABEU, Northeim, Germany) with the same PVA-NaHA mixture as described above, covering the Transwell membrane entirely from the bottom. The PVA-NaHA mixture was carefully applied to the peripheral region of the film only. Three freeze-thawing cycles were carried out to securely bond the delivery system to the Transwell membrane. For the DCA experiment, DCA-loaded fatty acid nanoparticles were hosted in a PVA-NaHA mixture layer sandwiched between a NaHA-48 film and a NaHA-60 film. The system was attached to the bottom of the Transwell insert with the NaHA-60 film facing the membrane. For the ACHP experiment, ACHP-loaded fatty acid nanoparticles were hosted in a PVA-NaHA

mixture layer sandwiched between a NaHA-60 film and a NaHA-24 film. The system was attached to the bottom of the Transwell insert with the NaHA-24 film facing the membrane.

2.9. Isolation, Culture, and Seeding of Tendon Fibroblasts

Primary rat tail tendon fibroblasts were received from Columbia University. After being recovered from cryopreservation, the cells were cultured until the fourth generation in a DMEM medium supplemented with 10% FBS and 1% antibiotics (containing penicillin and streptomycin) prior to seeding. Tendon fibroblasts were seeded in both the upper and lower chambers at a density of 0.021×10^6 cells/cm². A total of 1.2 mL and 3 mL of the medium were added to the upper and lower chambers of the Transwell, respectively. For the ACHP experiment, a normal DMEM medium with a high glucose content (4.5 g/L) was used, whereas for the DCA experiment, DMEM with a low glucose content (1 g/L) and sodium pyruvate (110 mg/L) was used to amplify the cellular response to DCA. After adding the cell suspension, the system was shaken on a 3D shaker platform (Corning GyroTwister S1000-40, Corning Life Sciences, Durham, NC, USA) at 30 rpm for 5 min, followed by incubation at 37 °C in a humidified chamber containing 5% CO₂ for 12 h to allow the cells to sediment and adhere to the Transwell membrane in the upper chamber and the bottom of the lower chamber.

2.10. Evaluation of the Biocompatibility of the Delivery System

Live/dead staining and MTT assay were used to evaluate the biocompatibility of the delivery system. Calcein-AM and EthD-1 were used to stain the live and dead cells, respectively. After 24 h of culture, cells were incubated with serum-free DMEM containing 5 mM calcein-AM and 4 µM EthD-1 at 37 °C for 30 min. After washing with PBS three times, the samples were observed under a confocal fluorescence microscope (Zeiss LSM 900). For the MTT assay, the upper and lower chambers of the Transwell system were rinsed three times with PBS and then 500 µL of serum-free DMEM containing 0.5 mg/mL MTT was added into both chambers. After incubation at 37 °C in a humidified chamber containing 5% CO₂ for 4 h, the MTT solution was removed and 500 µL of DMSO was added to dissolve the formazan produced. The DMSO solution was then transferred to a 24-well plate and its absorbance at 570 nm was read with a microplate reader (Infinite 200, Tecan, Männedorf, Switzerland). Five technical replicates were performed for each group (N = 5).

2.11. In Vitro Transwell Cell Culture Experiment for Directional Delivery of ACHP.

After tendon fibroblasts had adhered for 12 h, both the upper and lower chambers of the ACHP-treated and control group received 20 ng/mL Interleukin-1β (IL-1β) (R&D Systems, Minneapolis, MN, USA) for 48 h to stimulate inflammatory conditions. At the end of the culture period, the supernatants of all chambers were separately collected to evaluate inflammatory cytokine production (Interleukin 6, IL-6). The concentration of IL-6 was measured using a commercial IL-6 ELISA kit (Aviva Systems Biology, San Diego, CA, USA). The values obtained were subsequently used to calculate the total amount of IL-6 produced in each chamber by multiplying the concentration with a known total volume of the medium. The total IL-6 was normalized against the number of cells seeded in the respective chamber. RNA samples of the cells in both chambers were isolated to evaluate inflammatory-related gene expressions. 500 µL TRIzol was added to each chamber and RNA samples were isolated following the manufacturer's protocol. Total RNA yield and sample purity were determined using a spectrophotometer (Nanodrop, Thermo Fisher, Waltham, MA, USA). 100 ng of total RNA was reverse transcribed to complementary DNA (reverse transcription kit, QIAGEN, Hilden, Germany) using a dry bath (myBlock, Benchmark Scientific, Sayreville, NJ, USA). Quantitative real-time polymerase chain reaction (PCR) was performed using TB Green and a real-time PCR System (StepOnePlus, Applied Biosystems, Waltham, MA, USA). Primers were designed using PrimerQuest (Integrated DNA Technologies, Coralville, IA, USA) and were commercially obtained from ThermoFisher Scientific. The sequences for the primers followed those published in our prior work [14]. Analysis was performed using the $\Delta\Delta C_t$ method with *Rplp1* as the housekeeping gene.

2.12. In Vitro Transwell Cell Culture Experiment for Directional Delivery of DCA

After 60 h of culture, tendon fibroblasts in both the upper and lower chambers of the DCA-treated and control groups were trypsinized, snap-frozen with liquid N₂, and pulverized by quick sonication (10 s). Acetyl-CoA concentrations in the sample extracts were determined with an acetyl-coenzyme A assay kit (Sigma-Aldrich) according to the manufacturer's instructions. Since different numbers of cells were seeded in the upper and lower chambers of the Transwell culture system, the results were normalized against the number of cells seeded.

2.13. Statistical Analysis

Data are presented as mean \pm standard deviation and “N” indicates the number of samples per group. One-way analysis of variance (one-way ANOVA) was performed to evaluate the generation of acetyl-CoA and the level of IL-6 production in the experiment (DCA- and ACHP-treated) and control groups; two-way analysis of variance (two-way ANOVA) was performed to evaluate the expression of inflammatory-related genes in these groups (GraphPad Prism). A significant difference was represented by a bar (** $p < 0.01$, *** $p < 0.001$, **** $p < 0.0001$).

3. Results and Discussion

3.1. Design and Characterizations of the Bi-Directional and Bi-Temporal Release System

The release system was fabricated using NaHA thin films with different degrees of crosslinking. Instead of using classic crosslinking agents such as glutaraldehyde and epoxy [15,16], we chose to focus on the use of EDC for its water solubility and thus high biocompatibility of the crosslinking process. Following the protocol developed by Tomihata and Ikada [17], small pieces of NaHA thin films were immersed in an aqueous solution containing EDC and EtOH for 24, 48, and 60 h at 25 °C to achieve different degrees of crosslinking. It is worth noting that the entire process occurred under close-to-physiological pH at room temperature and did not involve any harmful organic solvents. After crosslinking, FT-IR spectra were recorded from the films, including the pristine sample, to gain a quantitative measure of the degree of crosslinking. As shown in Figures 2A and S3, the most notable difference between the spectra occurred around 1700 cm^{-1} , which can be assigned to the carbonyl group (C=O stretching) associated with the new C=O bond formed during the crosslinking process. In the crosslinking process, EDC did not directly serve as a crosslinker but as an activator for the carboxylate group of the polysaccharide NaHA (Figure S4) [18]. Eventually, intermolecular ester bonds were formed between the hydroxyl and carboxyl groups of NaHA to achieve crosslinking. Compared to the initial pristine sample, the by-product of the crosslinking reaction, which was supposed to be trapped within the crosslinked polymer network, contains an additional C=O bond, contributing to the rise of the C=O stretching peak in the FT-IR spectra. Using the peak intensity around 2925 cm^{-1} for the $-\text{CH}_2$ group, which did not participate in the crosslinking reaction, as a reference, the relative intensity of the C=O stretching peak increased with the duration of crosslinking (Table S1), indicating a higher degree of crosslinking.

Subsequently, we monitored the degradation of the crosslinked NaHA films in PBS supplemented with 20 units of HAase (in vivo mimicry [12]) over a period of two weeks. As shown in Figure 2B, the NaHA-60 films exhibited the slowest degradation rate, with over 60% of their original mass remaining by the end of the experimental period. In contrast, both NaHA-48 and NaHA-24 films degraded more rapidly. Specifically, NaHA-24 films lost over 50% of their original mass within the first 24 h of incubation. The cumulative release of fatty acid nanoparticles pre-loaded with a fluorescent model drug from the three types of NaHA thin films showed a trend similar to that of the degradation profile (Figure S5). Considering the presence of HAase in the in vivo environment, we monitored the release under three different conditions, with the construct being incubated in pure PBS, PBS with 10 units of HAase, and PBS with 20 units of HAase, respectively [12,13]. To quantify the release behavior, we assumed that the release process follows the first order kinetics and calculated the half-life for each type of NaHA film (Figure 2C, Table 1). As expected, increasing the concentration of HAase from 0 to 20 units significantly shortened the half-life for all three types of crosslinked HA films. At a moderate concentration of 10 units, NaHA-24 had a short half-life of around 1 day, while those of NaHA-48 and NaHA-60 were over 3 days and up to 2 weeks, respectively. These half-life values match the required time scales for inflammatory suppression in the early phase of healing and for metabolism regulation during the later proliferative and remodeling phases of healing for the in vivo repair model.

Table 1. Half-life of the crosslinked NaHA films as a function of HAase concentration.

HAase Concentration (U)	NaHA-24 (Day)	NaHA-48 (Day)	NaHA-60 (Day)
0	1.5	4.9	37.9
10	0.9	3.4	16.3
20	0.8	1.9	8.8

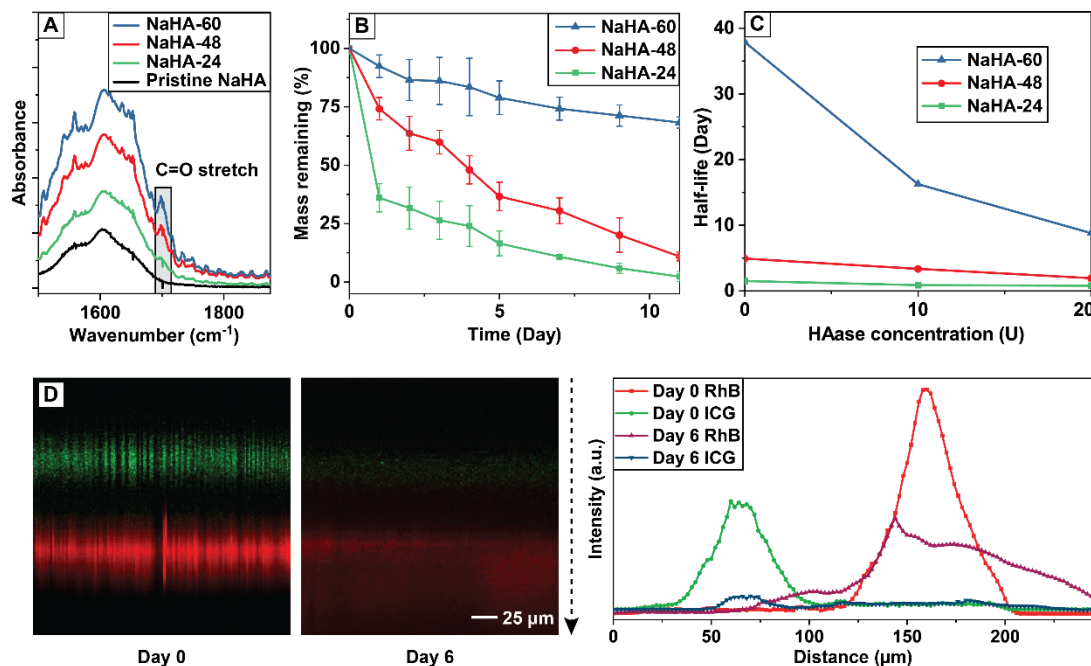


Figure 2. Characterizations of pristine NaHA films and those crosslinked to different degrees. (A) FT-IR spectra recorded from the films. (B) Degradation profiles of the films (N = 3 for each data point). (C) Half-life of the films when incubated in PBS containing different amounts of HAase (N = 3 for each data point). (D) Bi-directional release of fatty acid nanoparticles pre-loaded with fluorescent model compounds, ICG (green color) and RhB (red color), respectively, from the construct when incubated in enzyme-supplemented PBS at 37 °C and a quantitative analysis of the distribution of ICG and RhB following the direction of the dashed arrow (Day 0 and Day 6).

In practice, water infiltrates the looser network of the lightly-crosslinked NaHA barrier layer (NaHA-24) more rapidly when compared to the heavily-crosslinked NaHA-48 layer, leading to its disintegration within the first three days of implementation. Upon exposure to an aqueous environment, the hosting layer will swell to swiftly release the embedded fatty acid nanoparticles. While a small number of the nanoparticles may start to release their payloads (the small molecule drugs) at this stage, the major release should not occur until the nanoparticles have escaped from the crosslinked NaHA layer. When the nanoparticles are internalized by cells *in vitro* or come into contact with plasma albumin in body fluid *in vivo*, the fatty acids will be quickly dissolved or degraded, releasing the payloads [19]. Throughout this process, the most heavily-crosslinked NaHA-60 layer can prevent the inter-diffusion of nanoparticles between the two hosting layers, achieving bi-directional release.

To visualize and qualitatively analyze the release kinetics, two fluorescent compounds, ICG (green fluorescence) and RhB (red fluorescence), were selected as model compounds for ACHP and DCA, respectively. We recorded confocal fluorescence micrographs (cross-sectional view) from the construct after incubation in the enzyme-supplemented PBS at 37 °C for up to 6 days (Figure 2D, Figure S6). Due to the presence of the NaHA-60 blocking layer, the nanoparticles pre-loaded with the model compounds were released in two opposite directions with minimum inter-mixing. On day six, the signal from ICG, which represented ACHP that was supposed to be released in the early stage to combat inflammatory response, was mostly diminished. In contrast, the signal from RhB was still visible at this time point, confirming the more sustained release from this side of the construct.

In principle, NaHA films with varying degrees of crosslinking could be produced by controlling the duration of crosslinking until the maximum level is reached. As demonstrated above, the water infiltration rate is expected to be inversely correlated with the degree of NaHA crosslinking. While NaHA-24, -48, and -60 were selected based on the specific cumulative drug release requirements for the flexor tendon repair *in vitro* model, they can be substituted by films with other degrees of crosslinking and/or different thicknesses to achieve alternative release profiles. Furthermore, the fatty acid matrix that encapsulates the small molecule drugs could also be modified by crosslinking to offer another layer of control over the temporal release profile. The modular design grants a high level of flexibility, allowing for a broader spectrum of applications for the proposed system.

3.2. *In Vitro* Transwell Cell Culture Experiments

To demonstrate the bi-directional release capability of the delivery system in modulating cellular behavior *in vitro*, we adopted a Transwell culture system that allowed for the segregation of the environments. Specifically,

ACHP (an IKK β inhibitor) and DCA (a pyruvate dehydrogenase kinase 1 [PDK1] inhibitor) were delivered into the upper and lower chambers of the Transwell system. Rat tail tendon fibroblasts were seeded into both chambers, allowing us to analyze the biological effects of the directional delivery of these two effectors.

We first assessed the biocompatibility of the delivery system by incubating it with tendon fibroblasts under normal growth conditions in the Transwell system. Specifically, the delivery construct was attached to the polyethylene terephthalate (PET) membrane at the bottom of the Transwell insert using the same PVA-NaHA mixture used for the hosting layer. Through freeze-thawing cycles, physical crosslinking was established between PET, PVA, and NaHA to firmly attach the construct to the Transwell membrane throughout the cell culture experiment. Live/dead staining and MTT assay were performed for cells seeded in both the upper and lower chambers of the Transwell system. The cells showed good viability in all groups, with negligible differences between the construct-treated and control groups (Figure S7). These results indicate that the delivery system has excellent biocompatibility, which is vital to the proposed application.

Since ACHP and DCA are known to have contrasting effects on the tendon fibroblast cells, two simplified versions of the construct (Figure S8) were designed to deliver a single type of effector at a time and thereby isolate the cellular responses in one culture system. The construct, which contained either drug-loaded or plain (control group) fatty acid nanoparticles encapsulated between one barrier layer and one blocking layer of NaHA films, was attached to the Transwell insert in the same manner as described above. To better demonstrate the directionality of the delivery system, we purposely covered the entire permeable Transwell membrane with the construct to reduce the medium exchange and thereby enhance the segregation between the upper and lower chambers.

Cell culture experiments were conducted using the ACHP-loaded constructs to demonstrate the directional release of ACHP toward the upper chamber (Figure 3A). The early inflammatory phase of healing of an intrasynovial flexor tendon is dominated by high levels of proinflammatory cytokine production and the activation of the NF- κ B pathway [20]. Our previous work showed that the IKK β inhibitor ACHP is effective in modulating inflammatory response in tendon fibroblasts in vitro and in vivo by suppressing the NF- κ B pathway (Figure 3B) [14]. As a result, ACHP was designed to be released toward the tendon sheath to subdue the early inflammation and thus prevent adhesion or scar tissue formation. To model the inflammatory environment in the in vitro culture system, the tendon fibroblasts in both chambers were treated with 20 ng/mL IL-1 β for 48 h after they had been seeded for 12 h. Afterward, the biological effectiveness of the directional delivery of IKK β inhibitor ACHP was evaluated for both the ACHP delivery and control groups. Since the activation of the NF- κ B pathway by IL-1 β would lead to a dramatic increase in IL-6 cytokine production, we compared the concentrations of IL-6 in the ACHP upper and lower chambers with the control upper chamber. As shown in Figure 3C, the IL-6 level was significantly lower in the ACHP upper chamber ($p < 0.01$), suggesting that ACHP was predominantly released into the upper chamber, thereby effectively inhibiting the generation of IL-6. The gene expression analysis corroborated the IL-6 production result (Figure 3D,E). In the ACHP upper chamber, the expressions of NF- κ B target genes (*IL-1 β* , *IL-6*, and *Cox2*) were reduced significantly compared to the ACHP lower chamber and control upper chamber ($p < 0.0001$). In addition, the expressions of other inflammatory-related genes, such as *Ccl2*, which is involved in the recruitment of immune cells [21], and *Mmp3*, which encodes a common inflammation-promoting factor [22], were also reduced ($p < 0.001$ for comparing *Ccl2* between the ACHP and control upper chamber; $p < 0.0001$ for all other comparisons). This downregulation of inflammation-related gene expression was consistent with what was observed following systemic treatment with ACHP [14]. In contrast, there was no significant difference between the upper and lower chambers of the control group (Figure S9A,B). Collectively, it can be concluded that ACHP was successfully delivered to the upper chamber only, suppressing the NF- κ B pathway and modulating inflammation.

In the DCA cell culture experiment, the effector was designed to be released toward the lower chamber, mimicking its desired release direction toward the intrasynovial tendon in an in vivo application scenario (Figure 4A). In one of our prior studies, we reported that DCA is effective in shifting the metabolism of tendon fibroblasts from glycolysis to oxidative phosphorylation (Figure 4B) by inhibiting PDK1 [23]. Since PDK prevents pyruvate from being converted to acetyl-CoA, an inhibition of this enzyme would essentially increase the production of acetyl-CoA. To amplify the in vitro effect of DCA, we cultured the tendon fibroblasts in a pyruvate-enhanced environment. After 60 h of culture, the tendon fibroblasts were collected and pulverized. Acetyl-CoA concentrations in the sample extracts were determined. As shown in Figure 4C, within the same culture system, there was a significant increase in acetyl-CoA production in the lower chamber compared to the upper chamber as DCA was predominantly released toward the lower chamber ($p < 0.001$). Concurrently, the acetyl-CoA level in the lower chamber was also significantly higher than that in the lower chamber of the control group, where a construct loaded with plain fatty acid nanoparticles was used ($p < 0.001$). Notably, there was no significant difference between the upper chamber of the DCA release group and the lower chamber of the control group, nor

between the upper and lower chambers of the control group (Figure S9C). This trend further indicates the effectiveness of the blocking layer (NaHA-60) in controlling the directionality of DCA release.

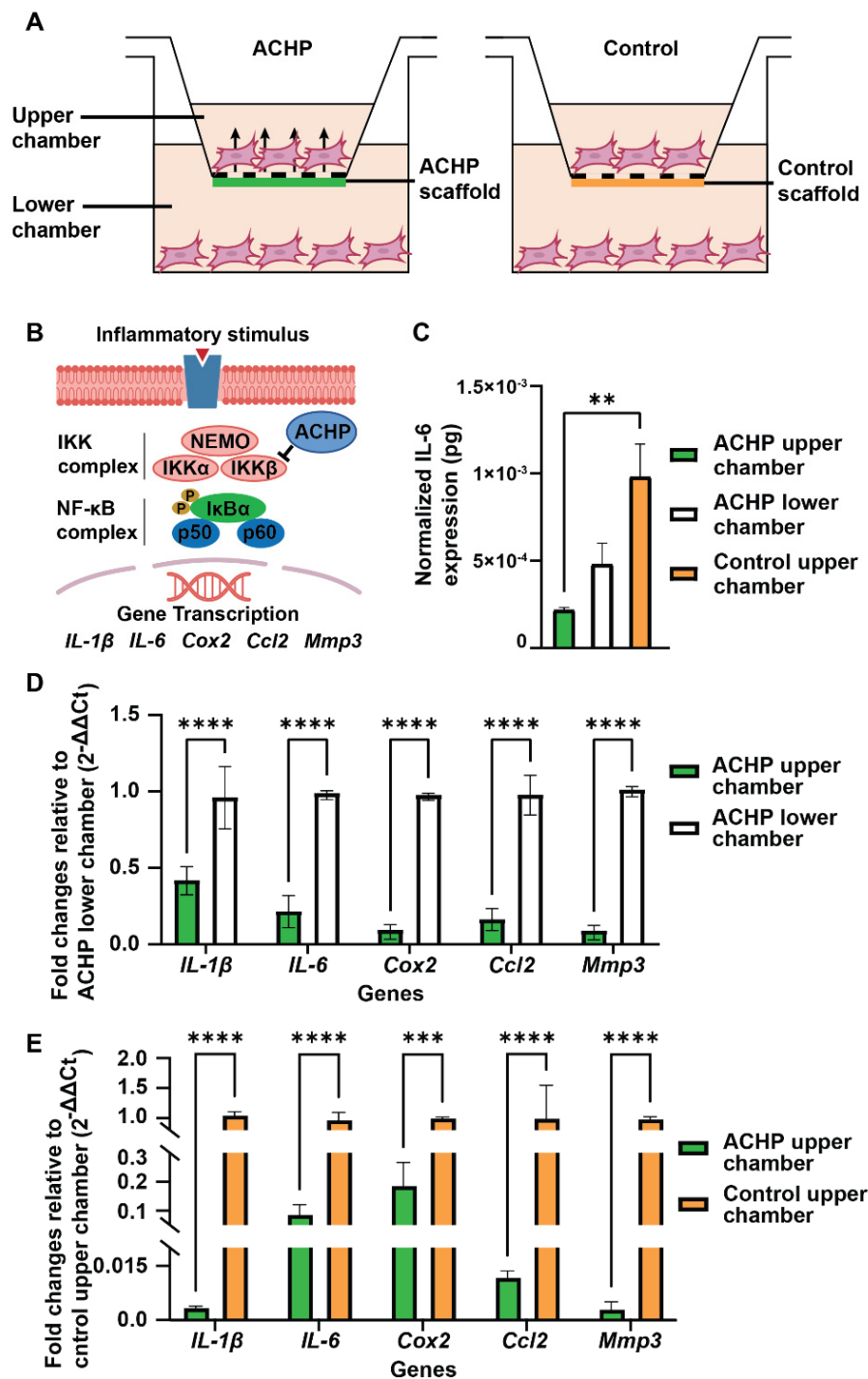


Figure 3. In vitro Transwell culture experiment demonstrating the directional release of ACHP. (A) Schematic of the experimental setup. (B) Schematic of the modulation of NF- κ B signaling pathways by ACHP. Adapted from ref. [14]. (C–E) The biological effect of the directional release of ACHP as demonstrated by (C) reduced production of inflammatory cytokine IL-6 in the ACHP upper chamber. The value was normalized to the number of cells seeded into the upper or lower chamber of the Transwell system, respectively. (D) Fold changes in gene expression for the cells from the ACHP upper chamber relative to those from the ACHP lower chamber. (E) Fold changes in gene expression for the cells from the ACHP upper chamber relative to those from the control upper chamber. A significant difference was represented by a bar (** $p < 0.01$, *** $p < 0.001$, **** $p < 0.0001$). N = 3 for the ACHP-treated group and N = 2 for the control group.

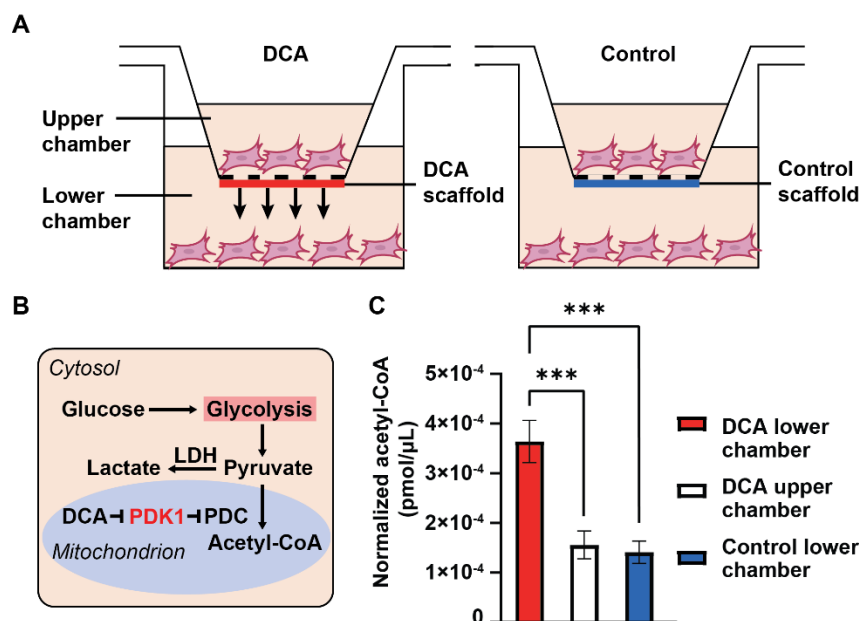


Figure 4. In vitro Transwell culture experiment demonstrating the directional release of DCA. (A) Schematic of the experimental setup. (B) Schematic of the primary pathways and regulation of glucose metabolism by DCA in tendon fibroblast cells. LDH, lactate dehydrogenase; PDK1, pyruvate dehydrogenase kinase 1; PDC, pyruvate dehydrogenase complex. Adapted from ref. [23]. (C) The biological effect of DCA as demonstrated by the increased generation of acetyl-CoA in the DCA lower chamber. The value was normalized to the number of cells seeded into the upper or lower chamber of the Transwell system, respectively. A significant difference was represented by a bar (***) ($p < 0.001$). N = 4 for the DCA-treated group and N = 2 for the control group.

Taking together the results from the two stand-alone in vitro Transwell studies, we have demonstrated that ACHP and DCA can be effectively delivered to their targeted chambers, with minimum release toward the other side of the construct. Moreover, the biological effects of the two small molecule drugs were retained and both drugs were potent enough to induce major biological responses. This work serves as a sound basis for more comprehensive studies combining the delivery of ACHP and DCA in a single cell culture system, which would in turn serve as a strong foundation for future in vivo experiments.

4. Conclusions

Using NaHA, a naturally derived polymer, we have developed a bi-directional and bi-temporal controlled release system to concurrently deliver two therapeutics to address the contrasting goals of suppressing adhesion at the tendon surface and promoting tendon matrix formation within the repair site. Leveraging the distinct drug delivery capabilities of NaHA films with different degrees of crosslinking, we designed a multi-layered construct capable of releasing two payloads in opposite directions at different rates. Following validation and visualization of the delivery system, we conducted a set of Transwell cell culture experiments with tendon fibroblasts to demonstrate the system's potential in flexor tendon repair. Two small molecule drugs, anti-adhesion ACHP and pro-matrix factor DCA, were delivered to their targeted locations to effectively modulate the cellular behaviors. The success of the in vitro study laid the groundwork for future in vivo inquiries and potential clinical translation. In principle, this delivery system can also be readily extended to deliver other combinations of therapeutics, such as cells, growth factors, and cytokines, expanding its application in tendon injury repair.

Supplementary Materials: The following supporting information can be downloaded at: <https://www.sciltp.com/journals/mi/2024/1/519/s1>, Figure S1: Schematic of the construct used for monitoring the release; Figure S2: Digital photos of the bi-directional and bi-temporal delivery system; Figure S3: FT-IR spectra recorded from the NaHA films crosslinked for different periods of time; Figure S4: Schematic of the crosslinking reaction between two HA chains in the presence of EDC as an activator; Table S1: Ratio between the absorbance of C=O stretching ($A_{C=O}$) and the absorbance of -CH₂ stretching (A_{CH_2}) for the crosslinked NaHA films; Figure S5: Cumulative release of fatty acid nanoparticles pre-loaded with fluorescent model compounds from the NaHA films with different degrees of crosslinking; Figure S6: Bi-directional release of fatty acid nanoparticles pre-loaded with fluorescent model compounds, ICG (green color) and RhB (red color), respectively, from the construct when incubated in the enzyme-supplemented PBS at 37 °C; Figure S7: Biocompatibility of the delivery system; Figure S8: Schematic of the delivery systems used in the Transwell cell culture experiments; Figure S9: Comparison between the cellular response in the two chambers of the control group, where a construct loaded with plain fatty acid nanoparticles was used.

Author Contributions: Y.C.: conceptualization, methodology, investigation, data curation, validation, visualization, writing—original draft, writing—reviewing and editing; S.K.: investigation, data curation, writing—reviewing and editing; E.Y.: investigation, data curation, writing—reviewing and editing; M.H.: methodology, visualization; H.S.: conceptualization, methodology, writing—reviewing and editing; R.G.: conceptualization, methodology, writing—reviewing and editing; S.T.: conceptualization, methodology, resources, supervision, writing—reviewing and editing; Y.X.: conceptualization, methodology, resources, supervision, writing—reviewing and editing. All authors have read and agreed to the published version of the manuscript.

Funding: This research was funded in part by a research grant from the NIH (R01 AR080924) and startup funds from the Georgia Institute of Technology.

Data Availability Statement: The data that support the findings of this study are available from the corresponding author, Y. Xia, upon reasonable request.

Conflicts of Interest: The authors declare no conflict of interest.

References

- Griffin, M.; Hindocha, S.; Jordan, D.; Saleh, M.; Khan, W. An Overview of the Management of Flexor Tendon Injuries. *Open J. Orthop.* **2012**, *6*, 28–35. <https://doi.org/10.2174/1874325001206010028>.
- Thomopoulos, S.; Das, R.; Silva, M.J.; Sakiyama-Elbert, S.; Harwood, F.L.; Zampiakakis, E.; Kim, H.M.; Amiel, D.; Gelberman, R.H. Enhanced Flexor Tendon Healing through Controlled Delivery of PDGF-BB. *J. Orthop. Res.* **2009**, *27*, 1209–1215. <https://doi.org/10.1002/jor.20875>.
- Shen, H.; Gelberman, R.H.; Silva, M.J.; Sakiyama-Elbert, S.E.; Thomopoulos, S. BMP12 Induces Tenogenic Differentiation of Adipose-Derived Stromal Cells. *PLoS ONE* **2013**, *8*, e77613. <https://doi.org/10.1371/journal.pone.0077613>.
- Hayashi, M.; Zhao, C.; Thoreson, A.R.; Chikenji, T.; Jay, G.D.; An, K.-N.; Amadio, P.C. The Effect of Lubricin on the Gliding Resistance of Mouse Intrasyneovial Tendon. *PLoS ONE* **2013**, *8*, e83836. <https://doi.org/10.1371/journal.pone.0083836>.
- Zhao, C.; Ozasa, Y.; Reisdorf, R.L.; Thoreson, A.R.; Jay, G.D.; An, K.-N.; Amadio, P.C. Engineering Flexor Tendon Repair with Lubricant, Cells, and Cytokines in a Canine Model. *Clin. Orthop. Relat. Res.* **2014**, *472*, 2569–2578. <https://doi.org/10.1007/s11999-014-3690-y>.
- Abate, M.; Pulcini, D.; Di Iorio, A.; Schiavone, C. Viscosupplementation with Intra-Articular Hyaluronic Acid for Treatment of Osteoarthritis in the Elderly. *Curr. Pharm. Des.* **2010**, *16*, 631–640. <https://doi.org/10.2174/138161210790883859>.
- Zhao, C.; Sun, Y.-L.; Amadio, P.C.; Tanaka, T.; Ettema, A.M.; An, K.-N. Surface Treatment of Flexor Tendon Autografts with Carbodiimide-Derivatized Hyaluronic Acid. An in Vivo Canine Model. *J. Bone Jt. Surg.* **2006**, *88*, 2181–2191. <https://doi.org/10.2106/JBJS.E.00871>.
- Liu, Y.; Skardal, A.; Shu, X.Z.; Prestwich, G.D. Prevention of Peritendinous Adhesions Using a Hyaluronan-Derived Hydrogel Film Following Partial Thickness Flexor Tendon Injury. *J. Orthop. Res.* **2008**, *26*, 562–569. <https://doi.org/10.1002/jor.20499>.
- Taguchi, M.; Zhao, C.; Sun, Y.-L.; Jay, G.D.; An, K.-N.; Amadio, P.C. The Effect of Surface Treatment Using Hyaluronic Acid and Lubricin on the Gliding Resistance of Human Extrasynovial Tendons In vitro. *J. Hand Surg.* **2009**, *34*, 1276–1281. <https://doi.org/10.1016/j.jhsa.2009.04.011>.
- Felson, D.T.; Anderson, J.J. Hyaluronate Sodium Injections for Osteoarthritis: Hope, Hype, and Hard Truths. *Arch. Intern. Med.* **2002**, *162*, 245–247. <https://doi.org/10.1001/archinte.162.3.245>.
- Chen, Q.; Zhu, C.; Huo, D.; Xue, J.; Cheng, H.; Guan, B.; Xia, Y. Continuous Processing of Phase-Change Materials into Uniform Nanoparticles for Near-Infrared-Triggered Drug Release. *Nanoscale* **2018**, *10*, 22312–22318. <https://doi.org/10.1039/c8nr07027j>.
- Vartanian, A.J.; Frankel, A.S.; Rubin, M.G. Injected Hyaluronidase Reduces Restylane-Mediated Cutaneous Augmentation. *JAMA Facial Plast. Surg.* **2005**, *7*, 231–237. <https://doi.org/10.1001/archfaci.7.4.231>.
- Ryu, C.; Lu, J.E.; Zhang-Nunes, S. Response of Twelve Different Hyaluronic Acid Gels to Varying Doses of Recombinant Human Hyaluronidase. *J. Plast. Reconstr. Aesthet. Surg.* **2021**, *74*, 881–889. <https://doi.org/10.1016/j.bjps.2020.10.051>.
- Golman, M.; Li, X.; Skouteris, D.; Abraham, A.A.; Song, L.; Abu-Amer, Y.; Thomopoulos, S. Enhanced Tendon-to-Bone Healing via IKK β Inhibition in a Rat Rotator Cuff Model. *Am. J. Sports Med.* **2021**, *49*, 780–789. <https://doi.org/10.1177/0363546520985203>.
- Hu, M.; Sabelman, E.E.; Tsai, C.; Tan, J.; Hentz, V.R. Improvement of Schwann Cell Attachment and Proliferation on Modified Hyaluronic Acid Strands by Polylysine. *Tissue Eng.* **2000**, *6*, 585–593. <https://doi.org/10.1089/10763270050199532>.
- Zhao, X. Synthesis and Characterization of a Novel Hyaluronic Acid Hydrogel. *J. Biomater. Sci. Polym. Ed.* **2006**, *17*, 419–433. <https://doi.org/10.1163/156856206776374115>.
- Tomihata, K.; Ikada, Y. Crosslinking of Hyaluronic Acid with Water-Soluble Carbodiimide. *J. Biomed. Mater. Res.* **1997**, *37*, 243–251. [https://doi.org/10.1002/\(sici\)1097-4636\(199711\)37:2<243::aid-jbm14>3.0.co;2-f](https://doi.org/10.1002/(sici)1097-4636(199711)37:2<243::aid-jbm14>3.0.co;2-f).
- Lu, P.-L.; Lai, J.-Y.; Ma, D.H.-K.; Hsiue, G.-H. Carbodiimide Cross-Linked Hyaluronic Acid Hydrogels as Cell Sheet Delivery Vehicles: Characterization and Interaction with Corneal Endothelial Cells. *J. Biomater. Sci. Polym. Ed.* **2008**, *19*, 1–18. <https://doi.org/10.1163/156856208783227695>.
- van der Vusse, G.J. Albumin as Fatty Acid Transporter. *Drug Metab. Pharmacokinet.* **2009**, *24*, 300–307. <https://doi.org/10.2133/dmpk.24.300>.
- Manning, C.N.; Havlioglu, N.; Knutsen, E.; Sakiyama-Elbert, S.E.; Silva, M.J.; Thomopoulos, S.; Gelberman, R.H. The Early Inflammatory Response after Flexor Tendon Healing: A Gene Expression and Histological Analysis. *J. Orthop. Res.* **2014**, *32*, 645–652. <https://doi.org/10.1002/jor.22575>.

21. Ajuebor, M.N.; Flower, R.J.; Hannon, R.; Christie, M.; Bowers, K.; Verity, A.; Perretti, M. Endogenous Monocyte Chemoattractant Protein-1 Recruits Monocytes in the Zymosan Peritonitis Model. *J. Leukocyte Biol.* **1998**, *63*, 108–116. <https://doi.org/10.1002/jlb.63.1.108>.
22. Fingleton, B. Matrix Metalloproteinases as Regulators of Inflammatory Processes. *Biochim. Biophys. Acta Mol. Cell Res.* **2017**, *1864*, 2036–2042. <https://doi.org/10.1016/j.bbamcr.2017.05.010>.
23. Gelberman, R.H.; Lane, R.A.; Sakiyama-Elbert, S.E.; Thomopoulos, S.; Shen, H. Metabolic Regulation of Intrasynovial Flexor Tendon Repair: The Effects of Dichloroacetate Administration on Early Tendon Healing in a Canine Model. *J. Orthop. Res.* **2023**, *41*, 278–289. <https://doi.org/10.1002/jor.25354>.

Article

Effect of Protein Loading Density on the Structure and Biopreservation Efficacy of Metal-Organic Frameworks

Yixuan Wang^{1,2}, Sirimuvva Tadeipalli^{3,†}, Harsh Baldi^{1,2}, Jeremiah J. Morrissey^{1,4}, and Srikanth Singamaneni^{1,2,4,*}

¹ Department of Mechanical Engineering and Materials Science, Washington University in St. Louis, St. Louis, MO 63130, USA

² Institute of Materials Science and Engineering, Washington University in St. Louis, St. Louis, MO 63130, USA

³ Radiation Oncology-Radiation Physics, Stanford School of Medicine, Stanford, CA 94305, USA

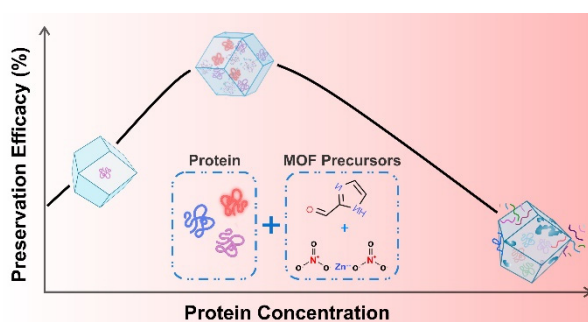
⁴ Siteman Cancer Center, Barnes-Jewish Hospital, and Washington University School of Medicine in St. Louis, St. Louis, MO 63130, USA

* Correspondence: singamaneni@wustl.edu

† Present Affiliation: Department of Immunology, School of Medicine, Stanford University, Stanford, CA 94305, USA

Received: 9 September 2024; Revised: 31 October 2024; Accepted: 5 November 2024; Published: 20 November 2024

Abstract: Metal-organic frameworks (MOFs) have emerged as attractive bioencapsulants for preserving the structure and function of various biomolecules against harsh environmental conditions. However, the effect of the loading density of the biomolecules on the structure, physical properties, and biopreservation efficacy of MOF crystals remains elusive. We investigated the structure and properties of zeolitic imidazolate framework (ZIF)-90 crystals as a function of the loading density of a model protein, bovine/human serum albumin (BSA/HSA). We show that the total protein concentration in the MOF growth reaction solution significantly affects the morphology, degree of crystallinity, and biopreservation efficacy of the MOF crystals. The structure integrity and immunologic functionality of albumin remained well-preserved within an optimal protein concentration range of 0.1–1 mg/mL. The proposed optimal range of biomolecule concentration during in situ MOF growth is critical for guiding future research and design endeavors within the rapidly evolving field of MOF-biomedical applications, offering exciting possibilities for biopreservation, drug delivery, and diagnostics.



Keywords: metal-organic framework; biopreservation; protein loading density; MOF biocomposites

1. Introduction

The stability and functionality of biomolecules in various biofluids and biospecimens are critical considerations in biomedical research and clinical diagnosis [1–3]. The accuracy of diagnostic information obtained from analyzing biofluids heavily depends on the stability and functionality of the biomolecules [2]. Unfortunately, many molecular biomarkers, particularly proteins, are prone to losing their structure and biofunctionality due to poor stability under ambient and elevated temperatures [4,5]. To accurately measure biomolecules in clinical labs, an extensive ‘cold chain’ distribution network is required [6], which is often impractical and unaffordable in resource-limited settings, especially given the existential threat of climate change. To address this challenge, extensive efforts have been dedicated to developing refrigeration-free techniques for preserving biospecimens and other biological entities [6–12].

Metal-organic frameworks (MOF) are crystalline [13,14], nanoporous materials comprised of metal clusters and bridged by organic ligands. A subclass of MOFs, zeolitic imidazolate frameworks (ZIFs), are comprised of metal nodes and imidazolate linkers held together by metal-coordination bonds. Over the past decade, ZIFs have emerged as highly promising encapsulants for a diverse range of biomolecules, including DNA [8], peptides [15],



Copyright: © 2024 by the authors. This is an open access article under the terms and conditions of the Creative Commons Attribution (CC BY) license (<https://creativecommons.org/licenses/by/4.0/>).

Publisher's Note: Scilight stays neutral with regard to jurisdictional claims in published maps and institutional affiliations

therapeutic proteins [16,17], enzymes [15,18,19], vaccines [20–22], living cells [23], and immobilized antibodies in biodiagnostic devices [24]. ZIFs are particularly attractive as encapsulants and preservatives due to their remarkable properties, which include high thermal and chemical stability, tunable pore size, high loading capacity, biocompatibility, and mild synthesis conditions and on-demand dissociation. ZIF crystals can be formed under mild aqueous conditions (i.e., at room temperature and physiological pH), readily encapsulating biomolecules and effectively preserving their structural and functional integrity against denaturation and degradation under harsh conditions.

Encapsulation of various biological entities within MOFs has been achieved through two primary pathways: molecular infiltration and biomineralization [11,25]. Molecular diffusion involves the passive transport of biomolecules into pre-synthesized MOFs [26], but this method is limited by the stringent requirements of guest size and surface chemistry of MOFs, potentially denaturing biomolecules during the formation of MOF-protein inclusion complexes. ZIF-90 possesses a aperture size of approximately 0.35 nm [14], which is significantly smaller than the dimensions of most proteins. As a result, the encapsulation and preservation of proteins within ZIF-90 using diffusion-based methods are inherently challenging. The limited pore size restricts the diffusion of larger biomolecules into the internal cavities of the ZIF-90 crystals, thereby hindering effective protein loading and storage. The second method involves the in situ growth of MOF crystals in the presence of the biological species [7], offering a unique opportunity to create precisely tailored MOF-biomolecule composites with enhanced stability of the encapsulated biomolecules [10,27–29]. This interest in utilizing MOFs for hosting and delivering biological guest materials has prompted investigations into the interaction between MOFs and biomolecules through experimental and computational methods [25–28,30–40]. However, the structure and properties of MOFs, biomolecules, and their interfaces in MOF-based biocomposites remain elusive: (i) what is the effect of the loading density of the proteins on the structure and properties of MOF crystals? (ii) how does the biopreservation efficacy of MOF crystals vary with the loading density of the proteins? (iii) what are the optimal conditions for protein encapsulation and preservation within MOF crystals?

In this study, we reveal how the total protein concentration in the reaction solution governs the morphology, crystallinity, thermal stability, and preservation efficacy of the in situ-synthesized ZIF-90 crystals. The morphological and structural evolution of protein-encapsulated ZIF-90 crystals were explored with environmental scanning electron microscope (ESEM), transmission electron Microscope (TEM), Brunauer-Emmett-Teller (BET), X-ray diffraction (XRD), and differential scanning calorimetry (DSC). The structure and functionality of protein were evaluated by using a plasmonic-fluor-linked enzyme-linked immunosorbent assay (p-FLISA) and Fourier transform infrared (FTIR) spectroscopy. The crystallinity and thermal stability of MOF crystals progressively decreased with an increase in the protein loading. The biopreservation efficacy of the MOF crystals was maximum at an intermediate protein concentration, determined by the tradeoff between efficient loading/recovery of the protein and optimal encapsulation under harsh environmental conditions.

2. Materials and Methods

2.1. Materials

Human serum albumin (HSA) (H6914), and bovine serum albumin (BSA) (A7030) were purchased from Millipore Sigma (St. Louis, MO, USA), human serum albumin ELISA kits (DY 1455) from R&D Systems (Minneapolis, MN, USA). Plasmonic-fluor-800 was purchased from Auragent Biosciences (St. Louis, MO, USA), while zinc nitrate, 2-imidazolecarboxaldehyde (ICA), ethylenediaminetetraacetic acid (EDTA), polyvinylpyrrolidone (PVP), tween-20, sodium phosphate monobasic, and sodium phosphate dibasic, were purchased from Millipore Sigma (St. Louis, MO, USA). All chemicals were used as received without further purification.

2.2. Methods

2.2.1. Encapsulation of HSA/BSA Proteins with ZIF-90 Crystals

HSA/BSA were diluted 10 times and 30 times with nanopure water. Then each diluted sample was mixed with ICA (320 μ L) and 80 μ L of zinc nitrate solution, the final concentration of HSA/BSA in each samples are 0, 0.01, 0.05, 0.1, 0.32, 0.5, 0.64, 1, 1.2, 5, 10 and 20 mg/mL. 0.2 wt% PVP were mixed well with ICA before reacting with zinc nitrate solution. The final concentration of ICA was 160 mM and the molar ratio of ICA and zinc nitrate was controlled to be 4:1. After 4 h of incubation at room temperature (20–23 °C), the mixture solution was

centrifuged at 8000 rpm for 15 min. The resultant particles were then rinsed with slightly alkaline nanopure water three times. Finally, the particles were stored at 55 °C for various lengths of time up to 2 weeks.

2.2.2. Protein Recovery

To recover embedded proteins from ZIF-90 crystals, MOF dissociation buffer (0.1 M phosphate buffer with 100 mM EDTA and 0.05% Tween-20 at pH 5.1) was added to each of the tubes and subjected to gentle orbital mixing for 25 min. After protein released from the crystals, the suspension turned from white to clear. To quantify the protein recovery after storage, HSA p-FLISA were performed. The preservation efficacy was calculated by comparing the amount of HSA released from ZIF crystals to the amount of HSA stored at −20° C, a standard cold chain condition, which represents 100%.

2.2.3. Plasmonic-Fluor-Linked Immunosorbent Assay of HSA

Human HSA DuoSet ELISA kit (R&D DY1455) was employed in the study. Specifically, 96-well plates were first incubated with capture antibodies (2 µg/mL in phosphate buffered saline (PBS) overnight at room temperature, followed by blocking with 3% BSA in 1X PBS for 2 h at room temperature. After 3 times washing with PBS containing 0.5% Tween 20 (PBST), 100 µL of serially diluted standard as well as samples (e.g., eluted protein solution) were added into different wells, and the plate was incubated at room temperature for two hours. The plate was washed subsequently and incubated with biotinylated detection antibodies for 2 h, followed by washing and the addition of 100 µL of plasmonic-fluors [3]. Plasmonic-fluors were incubated for 30 min, and the plate was washed three times with PBST. The fluorescence image of the microtiter plate was obtained using a LI-COR CLx fluorescence scanner. The concentration of the protein in unknown samples was determined using standard curve fit with a 4-parameter logistic model.

2.2.4. Statistics

For analyzing the statistical difference between two groups, an unpaired two-tailed t-test with Welch's correction was used. For analyzing the statistical difference between more than two groups, one-way analysis of variance (ANOVA) with a post-hoc Dunnett's significance test was used. Statistical significance of the data was calculated at 95% ($p < 0.05$) confidence intervals. All values are expressed as mean \pm s.d.

2.2.5. Material Characterization

X-ray diffraction (XRD) measurements of the samples were performed on a Bruker D8-Advance X-ray powder diffractometer (Madison, WI, USA) using Cu K α radiation ($\lambda = 1.5406$ Å) with scattering angles (2θ) of 5–25°. SEM images were obtained using Thermo Scientific Quattro S Environmental Scanning Electron Microscope (ESEM, Waltham, MA, USA). Transmission electron microscopy images were obtained using a JEOL JEM-2100F field emission instrument (TEM, Akishima, Japan). The surface area was calculated with the Brunauer–Emmett–Teller (BET) equation, and the pore size distribution was calculated by the Barrett–Joyner–Halenda (BJH) method. Attenuated total reflection Fourier transform infrared spectra (ATR-FTIR, Waltham, MA, USA) were obtained using a Nicolet iS10 spectrometer in the range of 400–4000 cm^{−1} at a resolution of 0.48 cm^{−1}, averaging 100 scans. Differential scanning calorimetry (DSC, Greifensee, Switzerland) measurements were performed on a Mettler Toledo STARE DSC1 with a heating rate of 20 K/min.

3. Results and Discussion

We have investigated the influence of protein concentration on the structure and properties of biomineralized ZIF-90 crystals, using BSA as a model protein. We synthesized biocomposite samples by varying the concentration of BSA with fixed concentrations of zinc nitrate (100 mM) and 2-imidazolecarboxaldehyde (ICA, 25 mM). The final concentrations of BSA in ZIF-90 precursor solution ranged from 0 to 20 mg/mL. All reactions were conducted in water with a Zn/ICA molar ratio of 1:4. After mixing BSA and precursors, the solutions with different compositions were kept at room temperature (22–25 °C) for 4 h. The resultant particles were collected by centrifugation and washed with slightly alkaline water (pH > 7.2) three times.

It has been suggested that proteins serve as pre-nucleation sites and facilitate the nucleation and crystallization of ZIF crystals [10,19,39]. At low BSA concentration (0.1–0.5 mg/mL), the reaction solution turns turbid rapidly upon the addition and redispersion of BSA (Supplementary Video S1). The MOF crystals grow and precipitate within 40 min after the BSA addition. For BSA concentrations exceeding 1.2 mg/mL, the solution turned cloudy upon the addition of BSA and resulted in the formation of a much denser white precipitate. At the

highest BSA concentration studied here (20 mg/mL), the solution became cloudy initially, and with further mixing, it transitioned to a semi-transparent state (Supplementary Video S2). Without the addition of BSA, the rate of ZIF-90 formation is slower compared to when BSA is present, and the reaction solution did not turn turbid during the first 20 mins. The visual observation of the reaction solutions suggests that when BSA concentration is within 0.1–1 mg/mL, the rate of BSA-ZIF-90 crystal formation increases as the BSA concentration increases. At higher BSA concentrations, the excess BSA possibly disrupts the formation of well-defined BSA-ZIF-90 crystals.

To further probe the structural variations of BSA-embedded ZIF-90 crystals with varying BSA concentrations, we examined selected samples using high-angle annular dark-field scanning transmission electron microscopy (HAADF-HRSTEM), ESEM, XRD, and DSC. First, we investigated the particle size and morphology of different samples by BET, ESEM and HR-STEM (Figures 1 and 2). MOF crystals formed under various reaction conditions exhibited a tendency to adopt a rhombic dodecahedral structure (Figure 1), which corresponds to the stable structure of ZIF-90. With a BSA concentration of 0.1 mg/mL in the reaction solution, we found the average crystal size to be 1.0–1.5 μm from ESEM and HR-STEM images (Figures 1 and 2b). At this concentration, the BSA-ZIF-90 crystals exhibit a well-defined rhombic dodecahedral shape and are of similar size to pristine ZIF-90 crystals (Figure 1a), but the surface of BSA-ZIF-90 crystals was not as smooth as that of pristine ZIF-90 crystals. In the presence of BSA concentrations ranging from 0.5 to 1.2 mg/mL, the particles have an average size of 1.2–2.0 μm and maintain the rhombic dodecahedra structure but exhibit a rough and grainy surface (Figures 1c,d and 2c,d). The specific surface area and pore volume of the MOF crystals decreased upon loading the crystals with BSA. (Figure S1 and Table S1). The grainy surface and the presence of defects indicate that the encapsulation of higher concentrations of protein is beginning to disrupt the formation of the ZIF matrix, albeit not catastrophically. At BSA concentrations around 5 mg/mL, the estimated average size ranged from 2 to 5 μm , displaying a less well-defined rhombic dodecahedral morphology (Figures 1e and 2e). The pronounced granularity of particle surface and increased occurrence of defects in BSA-embedded ZIF-90 particles indicate reduced crystallinity at very high BSA concentrations. At a BSA concentration of 20 mg/mL, particle size decreased to approximately 500 nm, accompanied by an extremely rough surface (Figures 1f and 2f). At this concentration, the particles lack well-defined facets and appear to be surrounded by aggregated BSA-precursor complexes, suggesting that the excess biomolecules in the reaction solution hinder the growth of the nuclei into well-defined crystals.

Next, to further explore the effect of the concentration of encapsulated biomolecule on ZIF-90 crystals, we investigated the thermal properties and crystallinity of BSA-ZIF crystals using DSC and XRD. DSC revealed the progressive decay in the thermal stability of ZIF-based biocomposites with different BSA concentrations (Figure 3A,B). We observed that as the BSA concentration increased, the exothermic peak in the DSC curves of all seven samples consistently shifted to lower temperatures. Specifically, the exothermic peak shifted from 320 $^{\circ}\text{C}$ in pristine ZIF-90 to 270 $^{\circ}\text{C}$ in the ZIF-based biocomposites with a BSA concentration of 20 mg/mL. These shifts indicate a lower decomposition temperature during the pyrolysis process as the BSA content increases. High BSA loading within the ZIF-90 crystals partially disrupts the coordination between metal ions and organic linkers, lowering the thermal stability of the crystals.

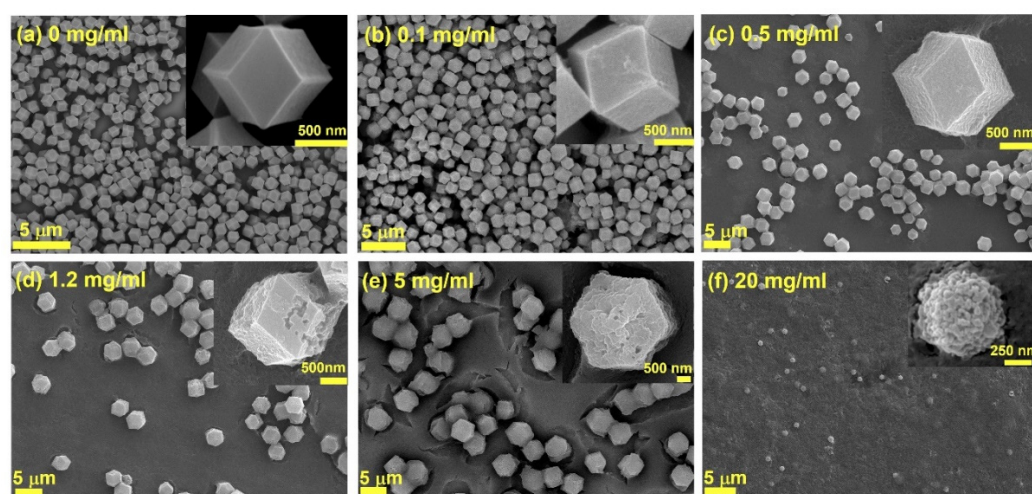


Figure 1. ESEM images of BSA-embedded ZIF-90 crystals with BSA concentrations of (a) 0 mg/mL, (b) 0.1 mg/mL, (c) 0.5 mg/mL, (d) 1.2 mg/mL, (e) 5 mg/mL, (f) 20 mg/mL.

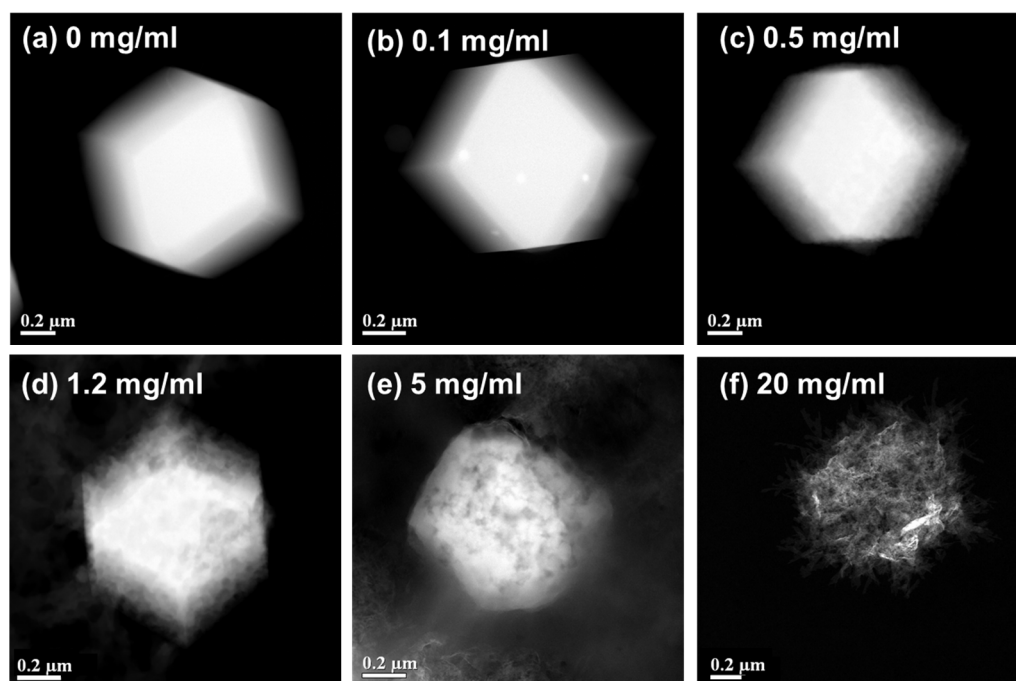


Figure 2. HAADF-HRSTEM images of BSA-embedded ZIF-90 crystals with BSA concentrations of (a) 0 mg/mL, (b) 0.1 mg/mL, (c) 0.5 mg/mL, (d) 1.2 mg/mL, (e) 5 mg/mL, (f) 20 mg/mL.

XRD is routinely employed to probe the crystal structure of pristine MOFs grown in solution and on surfaces. We determined the degree of crystallinity of pristine and protein-embedded ZIF-90 crystals by calculating the ratio of the areas of crystalline peaks to the total area of XRD peaks of each sample [41]. Crystallite size was determined by using the Bruker Topas software and Scherrer equation [41]. The predominant peaks of the pristine ZIF-90 sample (S0) at (110), (200), (211), (220), (310) and (222) are in good agreement with the literature, confirming the typical sodalite structure of ZIF-90 (Figure 3C), consistent with our ESEM and HR-STEM results (Figures 1A and 2A). From samples S0 to S6, which correspond to increasing BSA concentrations ranging from 0 mg/mL to 20 mg/mL, we observed a progressive broadening of the XRD peaks. This observation suggests a correlation between BSA concentration and crystallinity (Figure 3D). The crystallite size and crystallinity were found to decrease gradually with an increase in BSA concentrations encapsulated in ZIF-90 crystals (Figure 3D–F). The variations in particle size and morphology can be ascribed to the partial disruption in the crystalline framework in the presence of BSA. In the range of BSA concentrations from 0 to 1.2 mg/mL, the samples exhibit strong agreement with simulated ZIF-90 patterns, indicating that the incorporation of BSA did not significantly disrupt the long-range order and general morphology of the host MOF material. At BSA concentrations higher than 5 mg/mL, biocomposites show a significant decrease in crystallinity and an associated reduction in thermal stability (Figure 3B). This observation suggests that an increase in the amount of BSA embedded in the ZIF-90 crystals increases the defects in the crystals by disrupting the tight and extended metal-organic ligand coordination network observed in pristine crystals.

To explore the effect of increasing encapsulated biomolecule concentrations on the structure of biomolecules within BSA-ZIF-90 biocomposites, we obtained ATR-FTIR spectra of lyophilized biocomposite samples. This technique enables us to investigate the conformational changes of BSA embedded in the microcrystals [37,42–44]. Pristine ZIF-90 crystals exhibited absorption peaks at 1402–1467 cm^{-1} and 1680–1700 cm^{-1} , while pristine BSA exhibited absorption peaks at 1600–1700 cm^{-1} , 1500–1560 cm^{-1} , corresponding to amide I and amide II bonds of BSA [43], respectively (Figure 4A). FTIR spectra of BSA-ZIF-90 biocomposites shared the characteristic peaks of both ZIF-90 and BSA, suggesting the successful incorporation of BSA within ZIF-90 crystals [35,37,44,45]. Amide I involves the C=O stretching of CONH groups in proteins [37] and encompasses the major elements of proteins secondary structure, including α -helix, β -sheet/ β -turn, random coils and extended chains [37,43,46,47]. Amide II primarily involves N-H bending and C-N stretching, which is less affected by the changes in the protein structure. Therefore, to decipher the interaction between BSA and ZIF-90 in the biocomposites, we analyzed the Amide I peak (1600–1700 cm^{-1}) with quantitative Voigt peak fitting to determine the secondary structure of BSA (Figure 4B–G). The FTIR vibrational frequency assignments are summarized in Table 1. To quantify the secondary structures, the percentage of each structure is calculated by measuring the area of the corresponding absorption band to the total area of all assigned bands in the FTIR spectrum. Among all the possible secondary structures of

lyophilized free BSA, α -helix is the dominant conformation with an estimated contribution of 46% (Figure 4H), which agrees with previous studies [42,43,46,48]. With an increase in the BSA concentration from 0.1 mg/mL to 2.5 mg/mL in the MOF crystals, there was a reduction in the contribution of MOF ($1700\text{--}1680\text{ cm}^{-1}$) (Figure 4C–F). Correspondingly, there was increased loss of α -helix ($1655\text{--}1648\text{ cm}^{-1}$), increase in β -turns ($1684\text{--}1662\text{ cm}^{-1}$), and extended chains ($1620\text{--}1639\text{ cm}^{-1}$), indicating that higher concentrations of encapsulated proteins lead to a higher possibility of unfolded protein structure. Additionally, there are increased contributions from short segment chains connecting α -helix segments and aggregated strands ($1620\text{--}1630\text{ cm}^{-1}$), alongside the presence of intermolecular β -sheet ($1600\text{--}1616\text{ cm}^{-1}$) at elevated BSA concentration. These changes indicate the partial denaturation/aggregation of BSA at high encapsulation concentrations during the formation of BSA-ZIF-90 microcrystals [46].

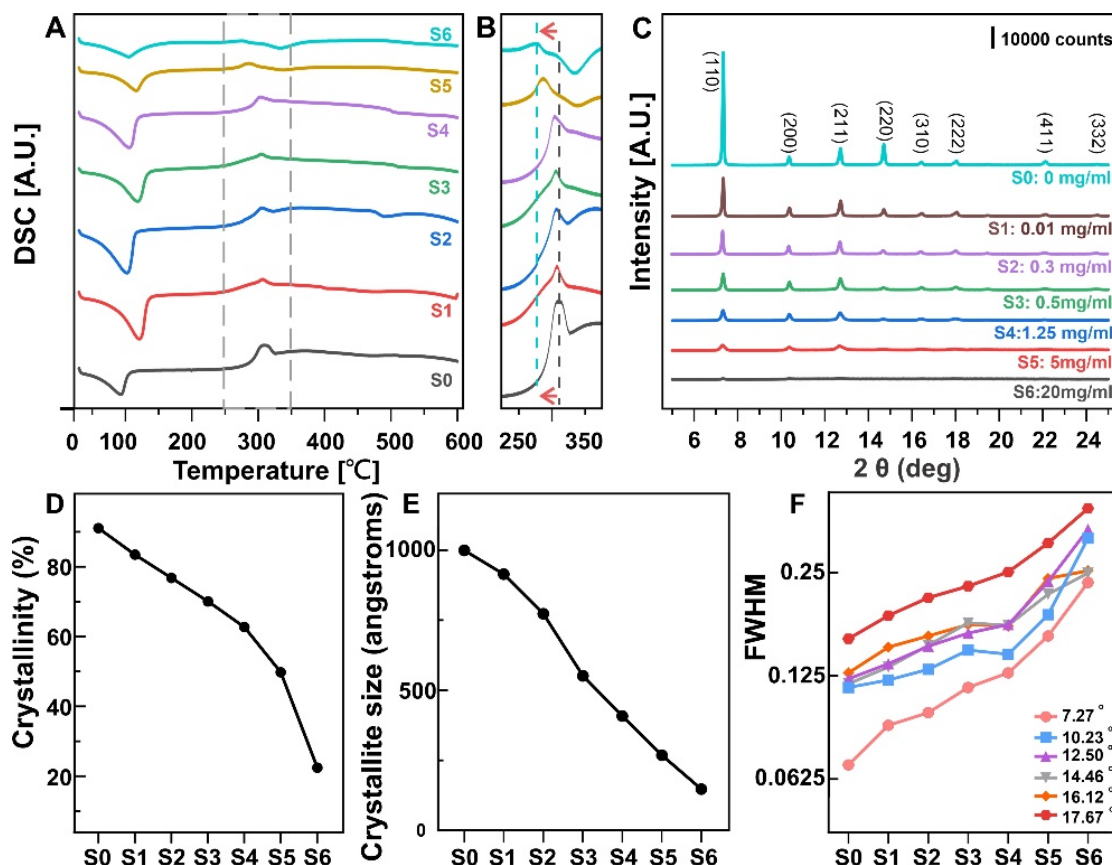


Figure 3. (A,B) DSC analysis of BSA-embedded ZIF-90 crystals with various BSA concentrations; (C) XRD analysis of BSA-embedded ZIF-90 crystals with various BSA concentrations; (D) Crystallinity; (E) and crystallite size analysis; (F) FWHM analysis.

Table 1. Vibrational frequency assignments of the MOF crystals and BSA.

Secondary Structure Assignment	Vibrational Frequency Range (cm^{-1})			
	Ref. [43]	Ref. [46]	Ref. [42]	This Work
MOF	-	-	-	1700–1680
β -Turns	1680–1663	1670–1662	1690–1660	1684–1662
α -Helix	1655–1650	1655–1650	1660–1650	1655–1648
Random coil	1646–1642	1645–1642	1648–1644	
Extended chains/ β -sheets/short-segment chains connecting the α -helical segment2	1639–1632	1638–1632	1640–1630	1639–1632
Extended chains/ β -sheets, Aggregated strands	1630–1620		1630–1620	1630–1620
Side chain moieties/ Intermolecular β -sheet	1616–1600	1620–1610	1620–1600	1616–1600

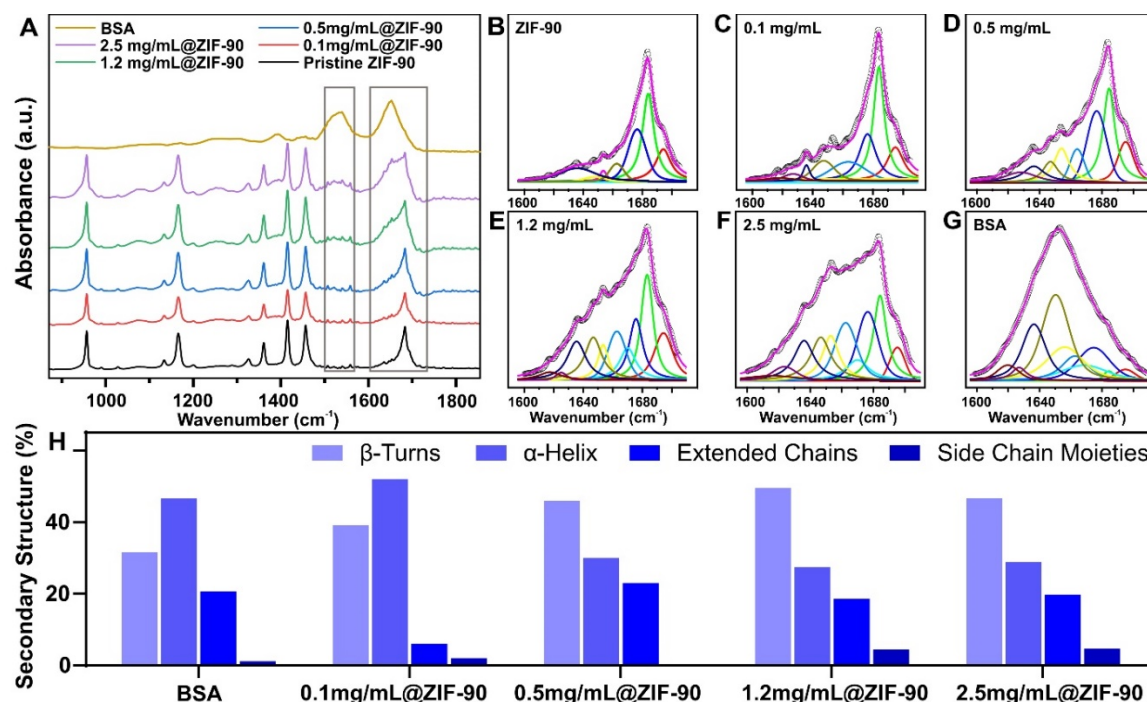


Figure 4. ATR-FTIR analysis of BSA-embedded ZIF-90 crystals with various BSA concentrations (A); deconvoluted ATR-FTIR spectra of the BSA-embedded ZIF-90 with BSA concentration of 0 mg/mL (B), 0.1 mg/mL (C), 0.5 mg/mL (D), 1.2 mg/mL (E), 2.5 mg/mL (F); Pristine BSA (G); Secondary structure analysis of BSA embedded in ZIF-90 crystals quantified by FTIR (H).

Lastly, we set out to evaluate the structure and biofunctionality of the biomolecules encapsulated in the biocomposites using HSA as a model protein. Samples were prepared by following the same protocol described above and analyzed using a commercial HSA enzyme-linked immunosorbent assay (ELISA) kit. The few BSA ELISA kits available commercially were not sufficiently sensitive. Hence, we have employed HSA as a model protein to investigate the loading density-dependent encapsulation and preservation. HSA and BSA have nearly 80% sequence homology, are similar structurally, and have similar binding pockets for various biomolecules [49]. To increase the sensitivity and dynamic range of the assay, we converted this commercial colorimetric assay to a plasmonic fluor-linked immunosorbent assay (p-FLISA) [10]. The amount of HSA quantified by p-FLISA accounts for various possible losses of protein, including encapsulated and retrieved protein with compromised secondary structure, unencapsulated protein with lost secondary structure, and finite loss that may occur in the encapsulation and retrieval process. The preservation efficacy, defined here as the recognition by antibodies, was found to be above 85% with HSA concentrations in the range of 0.1–1 mg/mL for 1 week stored at 55 °C (Figure 5A) and above 80% with HSA concentrations in the range of 0.1–0.5 mg/mL for 2 weeks stored at 55 °C (Figure 5B). For HSA concentration above 1 mg/mL, the preservation efficacy was below 75% for 1-week storage and below 55% for 2-week storage at 55 °C (Figure 5). Statistical analysis demonstrates significant differences in preservation efficacy between MOF-encapsulated HSA in the concentration range of 0.1–1 mg/mL and the negative control (without MOF encapsulation) (Figure 5). Additionally, within the concentration range of 0.1–1 mg/mL, no significant differences were observed in preservation efficacy across these concentrations after storage for 2 weeks at 55 °C. The resultant optimal concentration range for achieving high preservation efficacy was in good agreement with the range of maintaining well-defined crystal structures. In the optimal concentration range of protein (0.1–1 mg/mL), biomolecules serve as pre-nucleation sites for the MOF precursors and promote the fast formation of ZIF-90 crystals with a well-defined rhombic dodecahedron shape (Figures 1b,c and 2b,c) and well-defined structure preserve the structure and biofunctionality of biomolecules (Figures 4 and 5). The small but finite loss of protein during the encapsulation and release significantly lowers the measured preservation efficacy of MOFs at extremely low protein concentrations (Figure 5). On the other hand, at high protein loading densities, the ZIF-90 structure becomes partially disrupted due to increased defects in the crystals (Figures 1e,f and 2e,f). Under these conditions, ZIF-90 fails to provide tight encapsulation of the proteins, leading to a loss of secondary structure and functionality, including antibody recognition (Figure 5). In addition, excess protein can be adsorbed on the surface of the crystals or remain unencapsulated in the solution. The denaturation of the unencapsulated proteins at high temperatures decreases preservation efficacy.

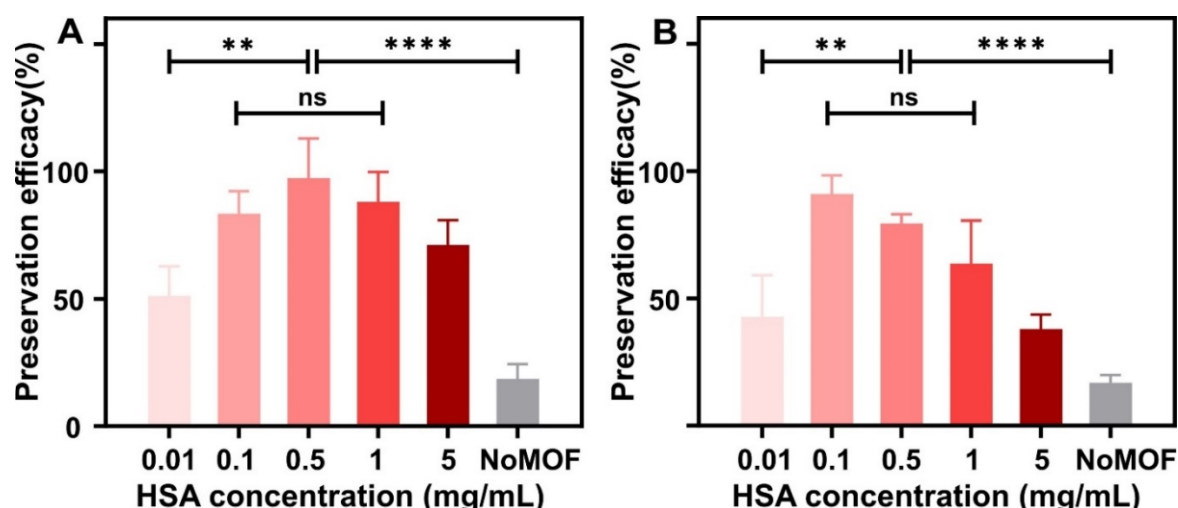


Figure 5. Preservation efficacy of HSA-embedded ZIF-90 particles stored at 55 °C for 1 week (A) and 2 weeks (B). (N = 3, ** $p < 0.01$, **** $p < 0.0001$, data represent mean \pm s.d.).

4. Conclusions

We systematically investigated the effect of protein loading on the morphology and structure properties of ZIF-90 crystals by synthesizing ZIF-90-based biocomposites using albumin as a model protein. We demonstrated that the morphology, crystallinity, thermal stability, and preservation efficacy of the MOF are total protein concentration-dependent. The structure of albumin-encapsulated MOF crystals was stable when the total protein concentration was below 0.5 mg/mL. The protein structure and immunologic functionality of albumin were well-preserved when the encapsulated protein concentration was around 0.1–1 mg/mL. While the optimal concentration range for individual proteins might slightly vary, we believe the dependence of the MOF structure and properties on the protein loading density will be similar for various globular proteins. Our results will inform and facilitate future research in the burgeoning area of MOF biocomposites for biopreservation, drug delivery, and diagnostics.

Supplementary Materials: The following supporting information can be downloaded at: <https://www.sciltp.com/journals/mi/2024/1/494/s1>, Figure S1: Nitrogen adsorption isotherms (A) and pore size distribution (B) of ZIF-90 and BSA-embedded ZIF-90 determined by Brunauer–Emmett–Teller (BET) and Barrett–Joyner–Halenda (BJH), respectively; Table S1: Specific surface area and pore dimensions of ZIF-90 and BSA embedded -ZIF-90; Video S1: MOF encapsulation with low protein concentration; Video S2: MOF encapsulation with high protein concentration.

Author Contributions: S.S., S.T. and Y.W. designed the project. S.S. and Y.W. designed the experiments. Y.W. synthesized MOF and MOF based biocomposites. Y.W. performed protein encapsulation, recovery and bioassays. Y.W. performed SEM, TEM, DSC, BET and FTIR measurements. H.B. performed XRD measurements. J.J.M. helped to design the HSA related experiments. S.S., J.J.M. and Y.W. wrote the paper. All authors reviewed and commented on the manuscript. All authors have read and agreed to the published version of the manuscript.

Funding: This work was supported by the National Cancer Institute-Innovative Molecular Analysis Technologies (R21CA236652) and the National Science Foundation (CBET-2224610 and CBET-2316285).

Acknowledgments: The authors thank the Institute for Materials Science and Engineering (IMSE) at Washington University in St. Louis for providing access to characterization facilities. The authors also thank Young-Shin Jun for providing access to the FTIR spectrometer and Katherine M. Flores for providing access to the differential scanning calorimeter. The content is solely the responsibility of the authors and does not necessarily represent the official view of the National Institutes of Health (NIH) or the National Science Foundation (NSF).

Conflicts of Interest: The authors declare the following competing financial interest(s): S.S. and J.J.M. are inventors on a pending patent related to plasmonic-fluor technology, and the technology has been licensed by the Office of Technology Management at Washington University in St. Louis to Auragent Bioscience LLC. S.S. and J.J.M. are co-founders/shareholders of Auragent Bioscience LLC. S.S. and J.J.M., along with Washington University, may have financial gain through Auragent Bioscience, LLC through this licensing agreement.

References

- Schrohl, A.S.; Würtz, S.; Kohn, E.; Banks, R.E.; Nielsen, H.J.; Sweep, F.C.; Brünner, N. Banking of biological fluids for studies of disease-associated protein biomarkers. *Mol. Cell. Proteom.* **2008**, *7*, 2061–2066. <https://doi.org/10.1074/mcp.R800010-MCP200>.
- Chaigneau, C.; Cabioch, T.; Beaumont, K.; Betsou, F. Serum biobank certification and the establishment of quality controls for biological fluids: Examples of serum biomarker stability after temperature variation. *Clin. Chem. Lab. Med.* **2007**, *45*, 1390–1395. <https://doi.org/10.1515/cclm.2007.160>.

3. Luan, J.; Seth, A.; Gupta, R.; Wang, Z.; Rath, P.; Cao, S.; Gholami Derami, H.; Tang, R.; Xu, B.; Achilefu, S.; et al. Ultrabright fluorescent nanoscale labels for the femtomolar detection of analytes with standard bioassays. *Nat. Biomed. Eng.* **2020**, *4*, 518–530. <https://doi.org/10.1038/s41551-020-0547-4>.
4. Livesey, J.H.; Ellis, M.J.; Evans, M.J. Pre-analytical requirements. *Clin. Biochem. Rev.* **2008**, *29*, S11–S15.
5. Evans, M.J.; Livesey, J.H.; Ellis, M.J.; Yandle, T.G. Effect of anticoagulants and storage temperatures on stability of plasma and serum hormones. *Clin. Biochem.* **2001**, *34*, 107–112. [https://doi.org/10.1016/s0009-9120\(01\)00196-5](https://doi.org/10.1016/s0009-9120(01)00196-5).
6. Zhang, J.; Pritchard, E.; Hu, X.; Valentin, T.; Panilaitis, B.; Omenetto, F.G.; Kaplan, D.L. Stabilization of vaccines and antibiotics in silk and eliminating the cold chain. **2012**, *109*, 11981–11986, doi:doi:10.1073/pnas.1206210109.
7. Liang, K.; Ricco, R.; Doherty, C.M.; Styles, M.J.; Bell, S.; Kirby, N.; Mudie, S.; Haylock, D.; Hill, A.J.; Doonan, C.J. Biomimetic mineralization of metal-organic frameworks as protective coatings for biomacromolecules. *Nat. Commun.* **2015**, *6*, 1–8.
8. Wijesundara, Y.H.; Herbert, F.C.; Trashi, O.; Trashi, I.; Brohlin, O.R.; Kumari, S.; Howlett, T.; Benjamin, C.E.; Shahrivarkevishahi, A.; Diwakara, S.D.; et al. Carrier gas triggered controlled biolistic delivery of DNA and protein therapeutics from metal–organic frameworks. *Chem. Sci.* **2022**, *13*, 13803–13814. <https://doi.org/10.1039/d2sc04982a>.
9. Wang, C.; Sun, H.; Luan, J.; Jiang, Q.; Tadepalli, S.; Morrissey, J.J.; Kharasch, E.D.; Singamaneni, S. Metal–Organic Framework Encapsulation for Biospecimen Preservation. *Chem. Mater.* **2018**, *30*, 1291–1300. <https://doi.org/10.1021/acs.chemmater.7b04713>.
10. Wang, Y.; Morrissey, J.J.; Gupta, P.; Chauhan, P.; Pachynski, R.K.; Harris, P.K.; Chaudhuri, A.; Singamaneni, S. Preservation of Proteins in Human Plasma through Metal–Organic Framework Encapsulation. *ACS Appl. Mater. Interfaces* **2023**, *15*, 18598–18607. <https://doi.org/10.1021/acsami.2c21192>.
11. Liang, W.; Wied, P.; Carraro, F.; Sumby, C.J.; Nidetzky, B.; Tsung, C.K.; Falcaro, P.; Doonan, C.J. Metal–Organic Framework-Based Enzyme Biocomposites. *Chem. Rev.* **2021**, *121*, 1077–1129. <https://doi.org/10.1021/acs.chemrev.0c01029>.
12. Wang, A.; Walden, M.; Ettlinger, R.; Kiessling, F.; Gassensmith, J.J.; Lammers, T.; Wuttke, S.; Peña, Q. Biomedical Metal–Organic Framework Materials: Perspectives and Challenges. *Adv. Funct. Mater.* **2023**, *34*, 2308589. <https://doi.org/10.1002/adfm.202308589>.
13. Furukawa, H.; Cordova, K.E.; O’Keeffe, M.; Yaghi, O.M. The chemistry and applications of metal-organic frameworks. *Science* **2013**, *341*, 1230444.
14. Morris, W.; Doonan, C.J.; Furukawa, H.; Banerjee, R.; Yaghi, O.M. Crystals as Molecules: Postsynthesis Covalent Functionalization of Zeolitic Imidazolate Frameworks. *J. Am. Chem. Soc.* **2008**, *130*, 12626–12627. <https://doi.org/10.1021/ja805222x>.
15. Gao, S.; Hou, J.; Deng, Z.; Wang, T.; Beyer, S.; Buzanich, A.G.; Richardson, J.J.; Rawal, A.; Seidel, R.; Zulkifli, M.Y.; et al. Improving the Acidic Stability of Zeolitic Imidazolate Frameworks by Biofunctional Molecules. *Chem* **2019**, *5*, 1597–1608. <https://doi.org/10.1016/j.chempr.2019.03.025>.
16. Wang, C.; Sudlow, G.; Wang, Z.; Cao, S.; Jiang, Q.; Neiner, A.; Morrissey, J.J.; Kharasch, E.D.; Achilefu, S.; Singamaneni, S. Metal–Organic Framework Encapsulation Preserves the Bioactivity of Protein Therapeutics. *Adv. Healthc. Mater.* **2018**, *7*, e1800950. <https://doi.org/10.1002/adhm.201800950>.
17. Kang, L.; Smith, S.; Wang, C. Metal–Organic Framework Preserves the Biorecognition of Antibodies on Nanoscale Surfaces Validated by Single-Molecule Force Spectroscopy. *ACS Appl. Mater. Interfaces* **2020**, *12*, 3011–3020. <https://doi.org/10.1021/acsami.9b19551>.
18. Liang, K.; Coghlan, C.J.; Bell, S.G.; Doonan, C.; Falcaro, P. Enzyme encapsulation in zeolitic imidazolate frameworks: A comparison between controlled co-precipitation and biomimetic mineralisation. *Chem. Commun.* **2016**, *52*, 473–476.
19. Liang, W.; Xu, H.; Carraro, F.; Maddigan, N.K.; Li, Q.; Bell, S.G.; Huang, D.M.; Tarzia, A.; Solomon, M.B.; Amenitsch, H.; et al. Enhanced Activity of Enzymes Encapsulated in Hydrophilic Metal–Organic Frameworks. *J. Am. Chem. Soc.* **2019**, *141*, 2348–2355. <https://doi.org/10.1021/jacs.8b10302>.
20. Luzuriaga, M.A.; Herbert, F.C.; Brohlin, O.R.; Gadhi, J.; Howlett, T.; Shahrivarkevishahi, A.; Wijesundara, Y.H.; Venkitapathi, S.; Veera, K.; Ehrman, R. Metal–Organic Framework Encapsulated Whole-Cell Vaccines Enhance Humoral Immunity against Bacterial Infection. *ACS Nano* **2021**, *15*, 17426–17438.
21. Luzuriaga, M.A.; Welch, R.P.; Dharmawardana, M.; Benjamin, C.E.; Li, S.; Shahrivarkevishahi, A.; Popal, S.; Tuong, L.H.; Creswell, C.T.; Gassensmith, J.J. Enhanced stability and controlled delivery of MOF-encapsulated vaccines and their immunogenic response in vivo. *ACS Appl. Mater. Interfaces* **2019**, *11*, 9740–9746.
22. Ehrman, R.N.; Brohlin, O.R.; Wijesundara, Y.H.; Kumari, S.; Trashi, O.; Howlett, T.S.; Trashi, I.; Herbert, F.C.; Raja, A.; Koirala, S.; et al. A scalable synthesis of adjuvanting antigen depots based on metal–organic frameworks. *Chem. Sci.* **2024**, *15*, 2731–2744. <https://doi.org/10.1039/d3sc06734c>.
23. Liang, K.; Richardson, J.J.; Cui, J.; Caruso, F.; Doonan, C.J.; Falcaro, P. Metal–organic framework coatings as cytoprotective exoskeletons for living cells. *Adv. Mater.* **2016**, *28*, 7910–7914.

24. Wang, C.; Tadepalli, S.; Luan, J.; Liu, K.K.; Morrissey, J.J.; Kharasch, E.D.; Naik, R.R.; Singamaneni, S. Metal-Organic Framework as a Protective Coating for Biodiagnostic Chips. *Adv. Mater.* **2017**, *29*, 1604433. <https://doi.org/10.1002/adma.201604433>.
25. Velásquez-Hernández, M.d.J.; Linares-Moreau, M.; Astria, E.; Carraro, F.; Alyami, M.Z.; Khashab, N.M.; Sumby, C.J.; Doonan, C.J.; Falcáro, P. Towards applications of bioentities@MOFs in biomedicine. *Coord. Chem. Rev.* **2021**, *429*, 213651. <https://doi.org/10.1016/j.ccr.2020.213651>.
26. Zhang, H.; Lv, Y.; Tan, T.; van der Spoel, D. Atomistic Simulation of Protein Encapsulation in Metal-Organic Frameworks. *J. Phys. Chem. B* **2016**, *120*, 477–484. <https://doi.org/10.1021/acs.jpcb.5b10437>.
27. Wang, Y.; Wang, Z.; Gupta, P.; Morrissey, J.J.; Naik, R.R.; Singamaneni, S. Enhancing the Stability of COVID-19 Serological Assay through Metal-Organic Framework Encapsulation. *Adv. Healthc. Mater.* **2021**, *10*, e2100410. <https://doi.org/10.1002/adhm.202100410>.
28. Ogata, A.F.; Rakowski, A.M.; Carpenter, B.P.; Fishman, D.A.; Merham, J.G.; Hurst, P.J.; Patterson, J.P. Direct Observation of Amorphous Precursor Phases in the Nucleation of Protein-Metal-Organic Frameworks. *J. Am. Chem. Soc.* **2020**, *142*, 1433–1442. <https://doi.org/10.1021/jacs.9b11371>.
29. Carraro, F.; Williams, J.D.; Linares-Moreau, M.; Parise, C.; Liang, W.; Amenitsch, H.; Doonan, C.; Kappe, C.O.; Falcáro, P. Continuous-Flow Synthesis of ZIF-8 Biocomposites with Tunable Particle Size. *Angew. Chem. Int. Ed. Engl.* **2020**, *59*, 8123–8127. <https://doi.org/10.1002/anie.202000678>.
30. Troyano, J.; Carne-Sanchez, A.; Avci, C.; Imaz, I.; MasPOCH, D. Colloidal metal-organic framework particles: The pioneering case of ZIF-8. *Chem. Soc. Rev.* **2019**, *48*, 5534–5546. <https://doi.org/10.1039/c9cs00472f>.
31. Carraro, F.; Velásquez-Hernández, M.d.J.; Astria, E.; Liang, W.; Twilight, L.; Parise, C.; Ge, M.; Huang, Z.; Ricco, R.; Zou, X.; et al. Phase dependent encapsulation and release profile of ZIF-based biocomposites. *Chem. Sci.* **2020**, *11*, 3397–3404. <https://doi.org/10.1039/C9SC05433B>.
32. Linares-Moreau, M.; Brandner, L.A.; Velasquez-Hernandez, M.J.; Fonseca, J.; Benseghir, Y.; Chin, J.M.; MasPOCH, D.; Doonan, C.; Falcáro, P. Fabrication of Oriented Polycrystalline MOF Superstructures. *Adv. Mater.* **2024**, *36*, e2309645. <https://doi.org/10.1002/adma.202309645>.
33. Lo, Y.; Lam, C.H.; Chang, C.-W.; Yang, A.-C.; Kang, D.-Y. Polymorphism/pseudopolymorphism of metal–organic frameworks composed of zinc(ii) and 2-methylimidazole: Synthesis, stability, and application in gas storage. *RSC Adv.* **2016**, *6*, 89148–89156. <https://doi.org/10.1039/c6ra19437k>.
34. Herbert, F.C.; Abeyrathna, S.S.; Abeyrathna, N.S.; Wijesundara, Y.H.; Brohlin, O.R.; Carraro, F.; Amenitsch, H.; Falcáro, P.; Luzuriaga, M.A.; Durand-Silva, A.; et al. Stabilization of supramolecular membrane protein-lipid bilayer assemblies through immobilization in a crystalline exoskeleton. *Nat. Commun.* **2021**, *12*, 2202. <https://doi.org/10.1038/s41467-021-22285-y>.
35. Tocco, D.; Chelazzi, D.; Mastrangelo, R.; Casini, A.; Salis, A.; Fratini, E.; Baglioni, P. Conformational changes and location of BSA upon immobilization on zeolitic imidazolate frameworks. *J. Colloid. Interface Sci.* **2023**, *641*, 685–694. <https://doi.org/10.1016/j.jcis.2023.03.107>.
36. Bakhshandeh, A.; Ardestani, F.; Ghorbani, H.R.; Darvish Ganji, M. Structural and molecular properties of complexes of biomolecules and metal-organic frameworks: Dispersion-corrected DFT treatment. *J. Mol. Model.* **2022**, *28*, 32. <https://doi.org/10.1007/s00894-021-04947-2>.
37. Mittal, A.; Gandhi, S.; Roy, I. Mechanistic interaction studies of synthesized ZIF-8 nanoparticles with bovine serum albumin using spectroscopic and molecular docking approaches. *Sci. Rep.* **2022**, *12*, 10331. <https://doi.org/10.1038/s41598-022-14630-y>.
38. Xu, Z.; Zhang, J.; Pan, T.; Li, H.; Huo, F.; Zheng, B.; Zhang, W. Encapsulation of Hydrophobic Guests within Metal–Organic Framework Capsules for Regulating Host–Guest Interaction. *Chem. Mater.* **2020**, *32*, 3553–3560. <https://doi.org/10.1021/acs.chemmater.0c00684>.
39. Marsh, C.; Shearer, G.C.; Knight, B.T.; Paul-Taylor, J.; Burrows, A.D. Supramolecular aspects of biomolecule interactions in metal–organic frameworks. *Coord. Chem. Rev.* **2021**, *439*, 213928. <https://doi.org/10.1016/j.ccr.2021.213928>.
40. Chen, G.; Huang, S.; Kou, X.; Zhu, F.; Ouyang, G. Embedding Functional Biomacromolecules within Peptide-Directed Metal-Organic Framework (MOF) Nanoarchitectures Enables Activity Enhancement. *Angew. Chem. Int. Ed. Engl.* **2020**, *59*, 13947–13954. <https://doi.org/10.1002/anie.202005529>.
41. Akhundzadeh Tezerjani, A.; Halladj, R.; Askari, S. Different view of solvent effect on the synthesis methods of zeolitic imidazolate framework-8 to tuning the crystal structure and properties. *RSC Adv.* **2021**, *11*, 19914–19923. <https://doi.org/10.1039/d1ra02856a>.
42. Schmidt, M.P.; Martinez, C.E. Kinetic and Conformational Insights of Protein Adsorption onto Montmorillonite Revealed Using in Situ ATR-FTIR/2D-COS. *Langmuir* **2016**, *32*, 7719–7729. <https://doi.org/10.1021/acs.langmuir.6b00786>.

43. Barreto, M.S.C.; Elzinga, E.J.; Alleoni, L.R.F. The molecular insights into protein adsorption on hematite surface disclosed by in-situ ATR-FTIR/2D-COS study. *Sci. Rep.* **2020**, *10*, 13441. <https://doi.org/10.1038/s41598-020-70201-z>.
44. Carpenter, B.P.; Talosig, A.R.; Mulvey, J.T.; Merham, J.G.; Esquivel, J.; Rose, B.; Ogata, A.F.; Fishman, D.A.; Patterson, J.P. Role of Molecular Modification and Protein Folding in the Nucleation and Growth of Protein-Metal-Organic Frameworks. *Chem. Mater.* **2022**, *34*, 8336–8344. <https://doi.org/10.1021/acs.chemmater.2c01903>.
45. Murty, R.; Bera, M.K.; Walton, I.M.; Whetzel, C.; Prausnitz, M.R.; Walton, K.S. Interrogating Encapsulated Protein Structure within Metal-Organic Frameworks at Elevated Temperature. *J. Am. Chem. Soc.* **2023**, *145*, 7323–7330. <https://doi.org/10.1021/jacs.2c13525>.
46. Lu, R.; Li, W.W.; Katzir, A.; Raichlin, Y.; Yu, H.Q.; Mizaikoff, B. Probing the secondary structure of bovine serum albumin during heat-induced denaturation using mid-infrared fiberoptic sensors. *Analyst* **2015**, *140*, 765–770. <https://doi.org/10.1039/c4an01495b>.
47. Ranjan, S.; Dasgupta, N.; Srivastava, P.; Ramalingam, C. A spectroscopic study on interaction between bovine serum albumin and titanium dioxide nanoparticle synthesized from microwave-assisted hybrid chemical approach. *J. Photochem. Photobiol. B* **2016**, *161*, 472–481. <https://doi.org/10.1016/j.jphotobiol.2016.06.015>.
48. Abrosimova, K.V.; Shulenina, O.V.; Paston, S.V. FTIR study of secondary structure of bovine serum albumin and ovalbumin. *J. Phys. Conf. Ser.* **2016**, *769*, 012016. <https://doi.org/10.1088/1742-6596/769/1/012016>.
49. Ketrat, S.; Japrun, D.; Pongprayoon, P. Exploring how structural and dynamic properties of bovine and canine serum albumins differ from human serum albumin. *J. Mol. Graph. Model.* **2020**, *98*, 107601. <https://doi.org/10.1016/j.jmgm.2020.107601>.

Article

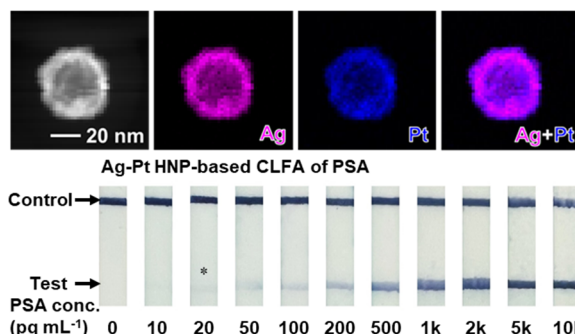
Silver-Platinum Hollow Nanoparticles as Labels for Colorimetric Lateral Flow Assay

Jinfeng Zhou¹, Shikuan Shao¹, Zhiyuan Wei¹, and Xiaohu Xia^{1,2,*}¹ Department of Chemistry, University of Central Florida, Orlando, FL 32816, USA² NanoScience Technology Center, University of Central Florida, Orlando, FL 32816, USA

* Correspondence: xiaohu.xia@ucf.edu

Received: 23 September 2024; Revised: 7 November; Accepted: 12 November 2024; Published: 18 November 2024

Abstract: Colorimetric lateral flow assay (CLFA) has been a widely recognized point-of-care testing technology over the past few decades. Driven by the increasing demand in various biomedical applications, it is urgently needed to develop CLFAs with high sensitivities and low costs. In this work, we report a type of CLFA that relies on unique colorimetric labels—silver-platinum hollow nanoparticles (Ag-Pt HNPs). The Ag-Pt HNPs possess intrinsic enzyme-like catalytic activities, providing the Ag-Pt HNP-based CLFA with strong color signal and thus a high sensitivity. Meanwhile, the Ag-Pt HNPs have hollow interiors and are mainly composed of less expensive silver, making the Ag-Pt HNP-based CLFA cost-effective. Using prostate-specific antigen (PSA) as a model disease biomarker, the Ag-Pt HNP-based CLFA achieved a high sensitivity with a detection limit at the low picogram-per-milliliter level. Potential application of the CLFA in clinical diagnosis was demonstrated by detecting PSA from human serum samples.



Keywords: hollow nanoparticles; lateral flow assay; catalysis; biomarker; detection

1. Introduction

Over the past few decades, lateral flow assays (LFAs) have been widely recognized and used as an accessible point-of-care (POC) technique due to their end-user-friendly, simple, rapid, and cost-effective natures [1,2]. Among various types of LFAs, colorimetric LFAs (CLFAs) stand out owing to their straightforward readouts, which provide visible test results without the need for additional equipment to stimulate or read signals [2]. This characteristic makes CLFAs particularly appealing for use in resource-limited settings [3]. Nevertheless, a significant drawback of CLFAs is their relatively low detection sensitivities compared to other laboratory tests. Conventional CLFAs typically use solid gold nanoparticles (Au NPs) with an overall spherical shape as labels (i.e., nanoscale particles pre-functionalized with bioreceptors that are responsible for specifically producing a visible signal in the test/control lines of a CLFA test strip) [1,4]. The color signal in conventional Au NP-based CLFAs originates from the plasmonic activities of Au NPs, which are intrinsically confined by the size of particles [5]. In general, small Au NPs generate limited colorimetric signals. Larger Au NPs or Au NP aggregates, however, can impede the mobility of the labels in the test strip [6]. Such a reduction of label mobility results in non-specific retention of labels in the membrane of test strip, leading to prolonged assay time and elevated background signals. In addition, bulky labels also cause steric hindrance that reduces the binding efficiency of the bioreceptors to analytes [7]. Because of the size effects, Au NPs of approximately 40 nm in diameter are widely used in conventional CLFAs [8–10].

To address these limitations, recent advancements have introduced a novel approach to substantially enhance the sensitivity of CLFAs. This approach employs platinum-group metal nanoparticles (PGM NPs) with peroxidase-like catalytic activities as labels, which are also known as “peroxidase mimics” or “artificial peroxidase” [11,12]. For example, in recent studies [8,13,14], conventional Au NPs were coated with Pt or Ir to form Au-Pt or Au-Ir



Copyright: © 2024 by the authors. This is an open access article under the terms and conditions of the Creative Commons Attribution (CC BY) license (<https://creativecommons.org/licenses/by/4.0/>).

Publisher's Note: Scilight stays neutral with regard to jurisdictional claims in published maps and institutional affiliations

core-shell NPs. The Pt or Ir shells endowed the nanoparticles with high peroxidase-like activities, which could generate intense color signals by catalyzing the oxidation of chromogenic substrates (e.g., 3,3',5,5'-tetramethylbenzidine (TMB) and 3,3'-diaminobenzidine (DAB) [15]) in the test region of CLFA. Through this catalytic process, these PGM NPs can generate a much stronger color signal than conventional Au NP-based labels that rely on intrinsic plasmonic activities, thereby significantly improving the sensitivity of CLFA. Despite their advantages, PGM NPs are precious and costly materials. Most of the reported PGM NPs used in CLFAs were solid particles [16], where only the surface layers contributed to catalytic activity [16,17]. In a sense, the underutilized PGM inside the solid particles causes extra materials costs.

In this work, we report a type of hollow PGM-based nanoparticles as labels for CLFA, namely silver-platinum hollow nanoparticles (Ag-Pt HNPs). The Ag-Pt HNPs were synthesized through galvanic replacement between silver nanoparticles (Ag NPs) and Pt^{2+} ions. The Ag-Pt HNPs possess hollow interiors and are mainly made of less expensive Ag, greatly reducing the materials cost of PGM. Using prostate-specific antigen (PSA) as a model analyte, we have demonstrated that the Ag-Pt HNP-based CLFA could offer a high sensitivity with a limit of detection (LOD) over 20-fold lower than the LOD of conventional Au NP-based CLFA. The design of labels in this work greatly enhances both the sensitivity and cost-effectiveness of CLFA, aligning with the Affordable, Sensitive, Specific, User-friendly, Rapid/Robust, Equipment-free, and Deliverable (ASSURED) criteria suggested by the World Health Organization (WHO) for POC diagnostics [18].

2. Materials and Methods

2.1. Materials and Reagents

Silver nitrate (AgNO_3 , $\geq 99.0\%$), gold(III) chloride trihydrate ($\text{HAuCl}_4 \cdot 3\text{H}_2\text{O}$, $\geq 99.9\%$), sodium citrate dihydrate ($\geq 99\%$), L-ascorbic acid ($\geq 99\%$), potassium tetrachloroplatinate(II) ($\text{K}_2\text{PtCl}_6 \cdot 6\text{H}_2\text{O}$, 98%), hydrogen peroxide solution (H_2O_2 , 30 wt % in H_2O), 3,3',5,5'-tetramethylbenzidine (TMB, $>99\%$), sodium acetate (NaOAc , $\geq 99\%$), acetic acid (HOAc , $\geq 99.7\%$), sodium borohydride (NaBH_4), prostate-specific antigen (PSA) from human semen, bovine serum albumin (BSA, $\geq 98\%$), potassium phosphate monobasic (KH_2PO_4 , $\geq 99\%$), sodium phosphate dibasic (Na_2HPO_4 , $\geq 99\%$), potassium chloride (KCl , $\geq 99\%$), sodium chloride (NaCl , $\geq 99.5\%$), sodium azide (NaN_3 , $\geq 99.5\%$), sodium carbonate (Na_2CO_3 , $\geq 99.5\%$), human serum (male AB plasma), TMB substrate solution for membranes, Tween 20, and NP 40 were all purchased from Sigma Aldrich (St. Louis, MS, USA). Monoclonal mouse anti-human PSA detection antibody (referred to as “anti-PSA DAb”) and polyclonal rabbit anti-human PSA capture antibody (referred to as “anti-PSA CAB”) were obtained from Abcam plc (Waltham, MA, USA). Polyclonal goat anti-mouse IgG antibody and Pierce protein concentrator (PES, 10K MWCO, 0.5 mL) were obtained from Thermo Fisher Scientific, Inc (Suwanee, GA, USA). The patient serum sample with PSA was purchased from Boca Biolistics LLC, Pompano Beach, Florida. Nitrocellulose (NC) membrane, glass fiber membrane, and absorbent pad were obtained from Cytiva. Polyvinyl chloride (PVC) backing card was obtained from DCN Diagnostics. All materials and reagents were used as received without further purifications and treatments. All aqueous solutions were prepared using deionized (DI) water with a resistivity of $18.2 \text{ M}\Omega \cdot \text{cm}$.

2.2. Instrumentations

The steady-state kinetic assays were recorded by an Agilent Cary 60 UV-vis spectrophotometer (Santa Clara, CA, USA). Transmission electron microscopy (TEM) images were taken using a JEOL 1011 microscope operated at 200 kV (Peabody, MA, USA). High-angle annular dark-field scanning TEM (HAADF-STEM) and energy dispersive X-ray (EDX) mapping images were taken using a FEI 200 kV Titan Themis scanning transmission electron microscope (Hillsboro, OR, USA). The concentrations of Au, Ag, and Pt ions (which were obtained from the digestion of nanoparticles by aqua regia) were determined using an inductively coupled plasma mass spectroscopy (ICP-MS, Thermo Scientific iCAP RQ, Waltham, MA, USA). These concentrations could be converted to the particle concentrations of Au NPs and Ag-Pt HNPs once the particle sizes and shapes had been resolved by TEM analyses. X-ray photoelectron spectroscopy (XPS) was performed on a Physical Electronics 5400 ESCA spectrometer system (Chanhassen, MN, USA). Fourier transform infrared spectroscopy (FT-IR) analyses were performed using a Shimadzu IRSpirit Infrared Spectrometer (Tampa, FL, USA). The lateral flow assay test strips were prepared by a ZX1000 Dispensing Platform and a CM4000 Guillotine Cutter (BioDot Inc., Irvine, CA, USA). The pH values of all buffer solutions were measured by an Oakton pH 700 benchtop meter. Photographs of strips were taken using a Canon EOS 80D digital camera (Huntington, NY, USA).

2.3. Synthesis of Ag NPs and Au NPs

The ~40 nm, citrate-capped Ag NPs (see Supplementary Figure S1) were synthesized using a two-step growth method [19]. First, the silver seed solution was prepared as follows: 12 mL of sodium citrate (SC) aqueous solution (0.25%, w/v) was added to a 50 mL round-bottom flask with a condenser and heated to boiling in an oil bath under magnetic stirring. Next, 270 μL of AgNO_3 (10 mg mL^{-1}) solution and 300 μL of freshly prepared NaBH_4 (1.0 mg mL^{-1}) solution were sequentially injected using a pipet. The reaction mixture was kept boiling and stirring for 30 min until the solution color became bright yellow. After that, the silver seed solution as the product was cooled to room temperature and stored in dark for future use. In the second step, the ~40 nm Ag NPs were synthesized using a seed-mediated growth with minor modifications [20]. Briefly, 1.0 mL of preformed silver seed solution was diluted to 35 mL with water in a 100 mL round-bottomed flask and heated to 80 °C in an oil bath under magnetic stirring. After 10 min, 256 μL of SC solution (1%, w/v), 256 μL of L-ascorbic acid solution (1%, w/v), and 256 μL of AgNO_3 solution (1%, w/v) were sequentially injected using a pipet with a time interval of ~1 min. The reaction was terminated after 30 min. The ~40 nm Ag NPs as final products were cooled to room temperature and stored in dark for future use.

The citrate-capped Au NPs with an average diameter of ~40 nm (see Supplementary Figure S2) were prepared according to our previously reported procedures [8].

2.4. Synthesis of Ag-Pt HNPs

The Ag-Pt HNPs were synthesized based on the galvanic replacement reaction between the above-mentioned ~40 nm Ag NPs as sacrificial templates and K_2PtCl_4 , according to published protocols with some modifications [21,22]. In a standard synthesis, 10 mL of ~40 nm Ag NPs was added to a 50 mL round-bottomed flask and preheated to 80 °C in an oil bath under magnetic stirring. Then, 160 μL of K_2PtCl_4 solution (0.005%, w/v) was injected into the flask at a rate of 8 $\mu\text{L min}^{-1}$ using a syringe pump. After completing injection of the K_2PtCl_4 solution, the reaction mixture was kept stirring at 80 °C for 10 min to allow reaction to complete. The Ag-Pt HNPs as final products were collected by centrifugation and eventually redispersed in 1.0 mL of water for future use.

2.5. Steady-State Kinetic Assays

All steady-state kinetic assays were performed at room temperature in cuvettes with a path length (l) of 1.0 cm using 0.2 M NaOAc/HOAc buffer (pH = 4.0) as the reaction buffer [23,24]. A final particle concentration at 8.6×10^{-13} M for Ag-Pt HNP suspension was used for all kinetic measurements. Note that the particle concentrations in this work were quantified using a combination of ICP-MS analysis and TEM imaging (see the Instrumentations section for details). After the addition of the nanoparticles to the reaction solution containing 2.0 M H_2O_2 and TMB of different concentrations, the absorbance of the reaction solution at 653 nm for each sample was immediately measured as a function of time using a UV-vis spectrophotometer for 1 min (interval = 3 s). The “absorbance vs. time” plots were then used to derive the slope at the initial point ($\text{Slope}_{\text{Initial}}$) of each reaction by performing the first derivation using Origin 2019 software. The initial reaction velocity (v) was calculated by $\text{Slope}_{\text{Initial}}/(\epsilon_{\text{oxTMB-653 nm}} \times l)$, where $\epsilon_{\text{oxTMB-653 nm}}$ is the molar extinction coefficient of oxidized TMB at 653 nm ($\epsilon_{\text{oxTMB-653 nm}} = 3.9 \times 10^4 \text{ M}^{-1} \text{ cm}^{-1}$) [23,24]. The plots of v against TMB concentrations were fitted using nonlinear regression of the Michaelis-Menten equation. The apparent kinetic parameters were calculated based on the Michaelis-Menten equation: $v = V_{\text{max}} \times [S]/(K_m + [S])$, where V_{max} is the maximal reaction velocity, $[S]$ represents the concentration of TMB substrate, and K_m is the Michaelis constant. V_{max} could be obtained from the double reciprocal plot (or Lineweaver-Burk plot) [25]. Finally, the catalytic constant (K_{cat} , which is defined as the maximum number of colored products generated per second per single nanoparticle) can be obtained from the equation: $K_{\text{cat}} = V_{\text{max}}/[E]$, where $[E]$ is the catalyst concentration (i.e., 8.6×10^{-13} M).

2.6. Conjugation of Antibodies to Nanoparticles

A non-covalent method was used to conjugate Ag-Pt HNPs to antibodies [8,16]. Specifically, 2 μL of anti-PSA DAb (2 mg mL^{-1}) was added to 100 μL of as-prepared Ag-Pt HNP suspension. After incubating at room temperature for 30 min, the mixture was put in a refrigerator overnight at 4 °C. Subsequently, 10 μL of blocking solution (10 mM phosphate buffered saline (PBS) buffer, pH 7.4, containing 10% BSA) was added to the mixture and incubated for 1 h. The final products (i.e., Ag-Pt HNP-anti-PSA DAb conjugates) were collected by centrifugation, washed twice by PBS, and redispersed in 100 μL of PBS solution containing 5% BSA, 0.5% NP40,

and 0.05% NaN_3 for future use. The same conjugation procedure was used for functionalizing Au NPs with anti-PSA DAb, which yielded Au NP-anti-PSA DAb conjugates as the final products.

2.7. Fabrication of CLFA Test Strips

The Ag-Pt HNP-based CLFA test strips were fabricated according to our previously reported protocol with minor modifications [8]. Specifically, a ZX1000 dispensing platform and a CM4000 Guillotine Cutter (BioDot Inc. Irvine, CA, USA) were used for the test strip fabrication. As shown in Figure 3A, a test strip comprises five main components: an absorbent pad, a PVC backing card, a nitrocellulose (NC) membrane with test and control lines, a sample pad, and a conjugate pad. The backing card and absorbent pad were used without pretreatment. The sample pad was prepared by immersing the glass fiber membrane in PBS solution containing 5% BSA, 0.5% NP40, and 0.05% NaN_3 , followed by drying at room temperature for 4 h. The conjugate pad was prepared by dispensing Ag-Pt HNP-anti-PSA DAb conjugates onto the glass fiber membrane at a rate of $25 \mu\text{L cm}^{-1}$ using the ZX1000 dispensing platform, followed by drying at room temperature for 2 h. The NC membrane with test and control lines was prepared by spotting anti-PSA CAb (1.1 mg mL^{-1} in PBS buffer containing 0.05% NaN_3 , which was pre-concentrated with a Pierce protein concentrator) at the test line region and anti-mouse IgG (1.2 mg mL^{-1} in PBS containing 0.05% NaN_3) at the control line region using a ZX1000 dispensing platform at the spray rate of $1.0 \mu\text{L cm}^{-1}$. The interval between the test and control lines was set to 8.0 mm. Finally, the sample pad, the conjugate pad, the NC membrane, and the absorbent pad were pasted to the PVC backing card with a 2 mm overlap between each component. The assembled sheets were then cut into 3 mm wide strips. The resultant Ag-Pt HNP-based CLFA strips were stored in refrigerator at -20°C under dry conditions for future use.

The procedure for preparing Au NP-based CLFA strips was the same as that for the Ag-Pt HNP-based CLFA strips, except that Ag-Pt HNP-anti-PSA DAb conjugates were substituted with the Au NP-anti-PSA DAb conjugates of the same particle concentration.

2.8. Detection of PSA by CLFA

The assay procedure of Ag-Pt HNP-based CLFA for PSA detection involves two steps: a sample loading step, which is a standard and routine procedure for CLFA, and a TMB substrate treatment step for color signal development [8,14]. Specifically, in the first step, $100 \mu\text{L}$ of PSA standard or human serum sample was loaded onto the sample pad of an Ag-Pt HNP-based CLFA strip using a pipet. Note, the serum samples were pre-diluted 2 folds by assay buffer (i.e., 1% BSA in PBS containing 0.05% Tween 20). The CLFA strip was then kept at room temperature for ~ 10 min until the liquid flow stopped. In the second step, a PBS solution containing 5% BSA, 0.5% NP40, and 0.05% NaN_3 was dropped to the sample pad using a pipet to wash away the excess Ag-Pt HNP-anti-PSA DAb conjugates in the NC membrane. Then, TMB substrate treatment process was applied according to the following procedure: the Ag-Pt HNP-based CLFA strip was immersed in a plastic centrifuge tube containing 1.5 mL of TMB substrate solution (i.e., a mixture containing 0.9 mL of TMB substrate solution for membrane, 0.3 mL of 1.0 M NaOAc/HOAc buffer, pH 4.0, and 0.3 mL of 1.0 M H_2O_2) at room temperature. After ~ 5 min of incubation, photograph of the CLFA strip was taken using a digital camera. For quantitative analysis, all photographs were imported into a computer and converted to 8-bit grayscale images using Adobe Photoshop software. The arithmetic mean of the pixel intensity in the test line region was measured as the color signal intensity [14].

The assay procedure for the Au NP-based CLFA of PSA was the same as the procedure for Ag-Pt HNP-based CLFA, except for the omission of TMB substrate treatment step.

3. Results and Discussion

3.1. Synthesis and Characterization of Ag-Pt HNPs

Ag-Pt HNPs were synthesized through galvanic replacement reaction between the ~ 40 nm Ag NPs as sacrificial templates and K_2PtCl_4 (see the Experimental section) [21]. Figure 1A,B shows typical transmission electron microscopy (TEM) images of the Ag-Pt HNPs at low- and high-magnifications, respectively. It can be observed that the Ag-Pt HNPs had good uniformities in terms of both shape and size. The Ag-Pt HNPs were of overall spherical shape with a hollow interior. By randomly analyzing 100 particles in the TEM images, the average outer diameter of the particles was measured to be 42.4 nm and their average wall thickness was measured to be 5.2 nm. In addition to morphology (i.e., size and/or shape), we also examined the elemental composition of these nanoparticles. The energy-dispersive X-ray (EDX) mapping images of an individual Ag-Pt HNP (see Figure 1C) revealed that elemental Ag and Pt co-exist in the particles in the form of Ag-Pt alloy, which is consistent with our

previous study [21]. The overall molar ratio of Ag to Pt in the Ag-Pt HNPs was quantified to be roughly 4:1 by inductively coupled plasma mass spectrometry (ICP-MS) analysis. This result suggests that the nanoparticles were primarily made of less expensive silver, ensuring a low material cost relative to those solid nanoparticles of pure PGMs.

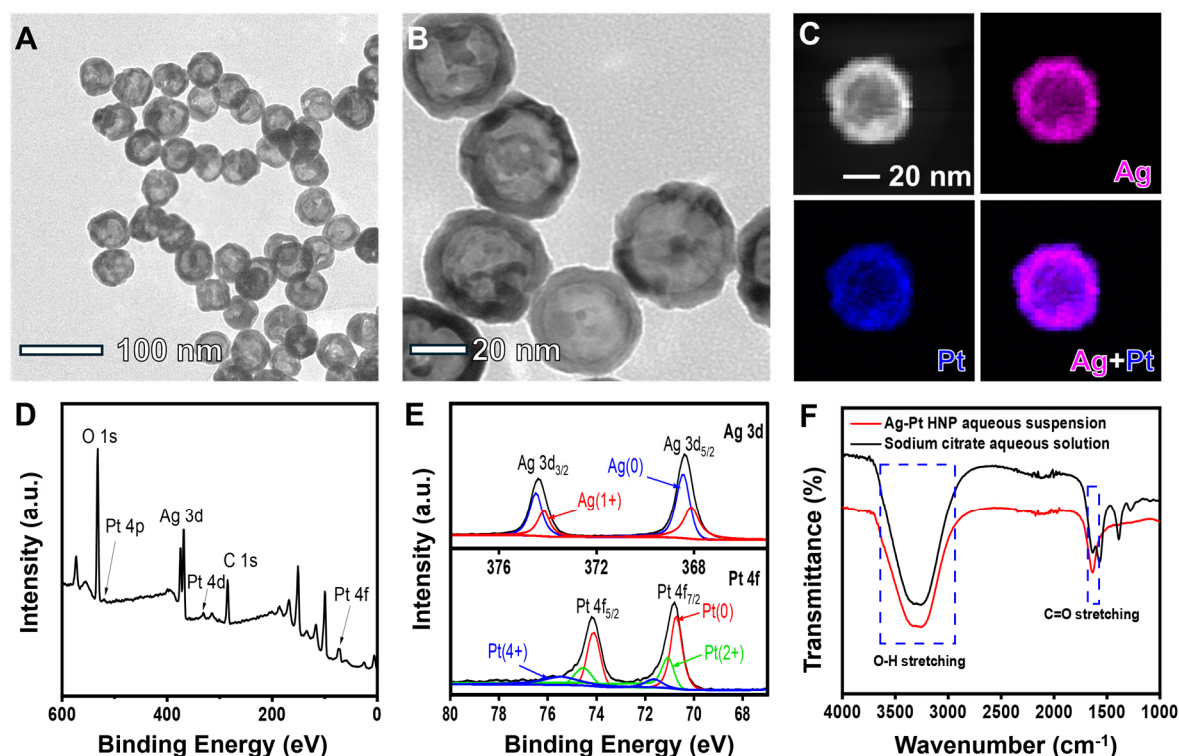


Figure 1. Morphological, structural, and compositional analyses of the Ag-Pt HNPs. (A,B) TEM images at low and high magnifications, respectively. (C) EDX mapping image of an individual particle (magenta = Ag, blue = Pt). (D) XPS survey spectrum. (E) High-resolution XPS spectra of the Ag 3d and Pt 4f regions shown in (D). (F) FT-IR spectra taken from an aqueous suspension of Ag-Pt HNPs and an aqueous solution of sodium citrate.

Surface chemistry of the Ag-Pt HNPs was characterized by X-ray photoelectron spectroscopy (XPS) and Fourier transform infrared spectroscopy (FT-IR). Figure 1D shows a full XPS spectral survey recorded from the Ag-Pt HNPs. The observation of peaks for Ag 3d, Pt 4p, Pt 3d, and Pt 4f confirmed that the nanoparticles were composed of Ag and Pt elements. The high-resolution XPS spectra of the Ag 3d and Pt 4f regions (Figure 1E) revealed that the Ag-Pt HNPs were mainly composed of zero-valent Ag(0) and Pt(0). The co-existence of relatively small amounts of oxidized metal atoms was presumably because of surface oxidations (e.g., by dissolved oxygen in nanoparticle suspensions) [26]. Notably, as shown by the full spectral scan (Figure 1D) and the high-resolution spectra (see Supplementary Figure S3), C 1s and O 1s peaks were observed, hinting at the adsorption of citrate on the surface of Ag-Pt HNPs. This assumption was confirmed by the FT-IR results (see the red spectrum in Figure 1F). Specifically, the peak observed at $\sim 1600\text{ cm}^{-1}$ was representative of the C=O stretch. The broad peak between 3100 and 3400 cm^{-1} was attributed to be from the O–H stretch. These characteristic peaks of citrate on nanoparticle surface were overall consistent with the peaks observed from pristine citrate (black spectrum in Figure 1F). These FT-IR analyses along with the XPS data confirmed the adsorption of citrate on the surface of Ag-Pt HNPs. Note that this result implies that the citrate acting as a colloidal stabilizer on initial Ag NP templates was retained on particle surface after the galvanic replacement reaction. The capping of citrate on particle surface allows for convenient conjugation of the Ag-Pt HNPs with antibodies through attractive electrostatic interactions [27,28].

It is worth noting that all these characterization data demonstrate that the Ag-Pt HNPs had a similar size and shape and the same surface ligand as the $\sim 40\text{ nm}$ citrate-capped Au NPs—a type of widely used label in the CLFA industry [9,29]. Such similarities facilitate a direct and reasonable comparison of the Ag-Pt HNPs and Au NPs in CLFA performance.

3.2. Catalytic Activities

The peroxidase-like catalytic activities of Ag-Pt HNPs were assessed using the oxidation of TMB (a typical peroxidase substrate) by H_2O_2 as a model catalytic reaction. This catalytic reaction yielded a blue product (i.e., oxidized TMB [30]) with maximal absorbance at ~ 653 nm, which could be easily tracked and quantified by a UV-vis spectrophotometer (see Supplementary Figure S4). It is worth noting that in addition to TMB, 2,2'-azino-bis(3-ethylbenzothiazoline-6-sulfonic acid) diammonium salt (ABTS), 3,3'-diaminobenzidine (DAB), and o-phenylenediamine (OPD) are commonly used peroxidase substrates that can yield blue/green-, brown-, and orange-colored products, respectively [31]. Nevertheless, in the context of application in CLFA, the catalytic products from the peroxidase substrates are preferred to meet the following expectations: (i) The color should be easily distinguished from that of the samples (e.g., red for whole blood samples); (ii) The products can be rendered to be insoluble by a precipitator to avoid being washed away by the liquid flow in the test strip; and (iii) the products exhibit minimal toxicities to human and environment. Taking all these into consideration, TMB is the optimal choice among all the peroxidase substrates.

To quantify the catalytic efficiency of Ag-Pt HNPs, an apparent steady-state kinetic assay was conducted, in which the particle concentration of Ag-Pt HNPs (E) was fixed at 8.6×10^{-13} M (details are provided in the Experimental section). Note that the catalytic efficiency is measured by a parameter—catalytic constant (K_{cat}) that is defined as the maximum number of colored molecules produced per second per catalyst [23,24]. Figure 2A shows the Michaelis-Menten curve, which was obtained by nonlinear fitting of the initial reaction velocity (v) at varying TMB concentrations. This curve was further transformed into a double reciprocal plot (Figure 2B), from which a maximum reaction rate (V_{max}) of 9.6×10^{-7} M s^{-1} was derived. Therefore, the catalytic constant K_{cat} was determined to be 1.1×10^6 s^{-1} , according to the equation $K_{\text{cat}} = V_{\text{max}}/[E]$. Notably, the K_{cat} of Ag-Pt HNPs as peroxidase mimics is several orders of magnitude higher than that of horseradish peroxidase (HRP, a typical natural peroxidase with a $K_{\text{cat}} = 4.0 \times 10^3$ s^{-1}) [24]. It is worth mentioning that the molar extinction coefficient of ~ 40 nm citrate-capped Au NPs is approximately at the level of 10^{10} $\text{M}^{-1} \text{cm}^{-1}$ as reported in previous studies [8,32]. In comparison, the equivalent molar extinction coefficient of the Ag-Pt HNPs (which is defined as the total light extinction of color products yielded at catalytic reaction time $t = 5$ min [8]) is estimated to be at the regime of 10^{13} $\text{M}^{-1} \text{cm}^{-1}$, based on their catalytic efficiency. In a sense, the color signal from the catalytic Ag-Pt HNPs (with a short reaction time of 5 min) is orders of magnitude stronger than that from conventional plasmonic Au NPs.

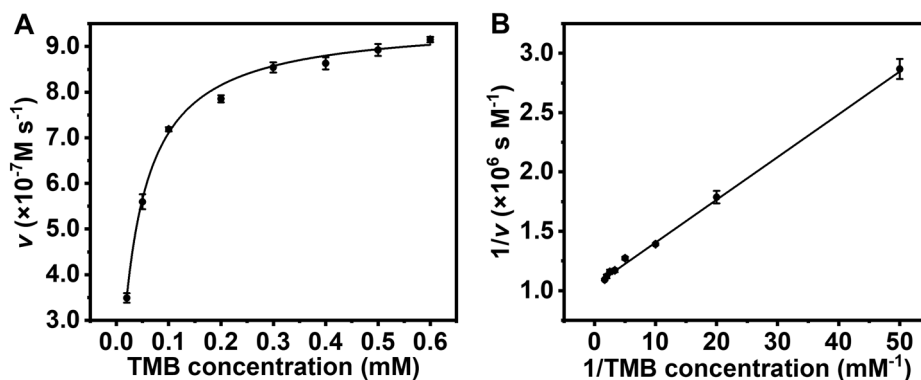


Figure 2. Kinetic assays of the Ag-Pt HNPs as catalysts for the oxidation of TMB by H_2O_2 . The initial reaction velocity (v) was measured from 0.2 M HOAc/NaOAc buffer solution (pH 4.0) containing 2.0 M H_2O_2 , 8.6×10^{-13} M Ag-Pt HNPs, and TMB of various concentrations at room temperature. (A) Plot of v against TMB concentration. (B) Double-reciprocal plot derived from the data in (A). Error bars denote the standard deviations of three independent measurements.

3.3. Application in CLFA

As illustrated in Figure 3A, the Ag-Pt HNPs were applied as labels to CLFA. Prostate-specific antigen (PSA, a biomarker for recurrence of prostate cancer [33]) was detected as a model disease biomarker to demonstrate the potential application of Ag-Pt HNP-based CLFA in medical diagnostics. After capturing the Ag-Pt HNP-antibody conjugates in the test and control line regions of the test strip, a simple TMB substrate treatment process was applied, which took only ~ 5 min and was operated at room temperature. Details of the CLFA assembly and assay procedures are provided in the Experimental section. It should be mentioned that instead of directly dropping the substrate solution onto the test and control lines as reported in previous studies [8,14], in this work we immersed the test strip in a substrate solution hosted in a plastic tube. Such a modification of the substrate treatment procedure

ensures good assay reproducibility and relatively low background at the expense of extra substrate solution, which is inexpensive [34]. Notably, the Ag-Pt HNPs display a visible color (gray) due to their plasmonic activities. Nevertheless, this color is significantly weaker than the color signal produced from the nanoparticles-mediated catalytic reaction [8]. Therefore, the color signal in the test and control lines of Ag-Pt HNP-based CLFA test strip is primarily from the catalytic reaction products (i.e., oxidized TMB). For comparison, conventional CLFA using ~40 nm citrate-capped Au NPs (see Supplementary Figure S2) as labels was fabricated using the same antibodies and materials as Ag-Pt HNP-based CLFA.

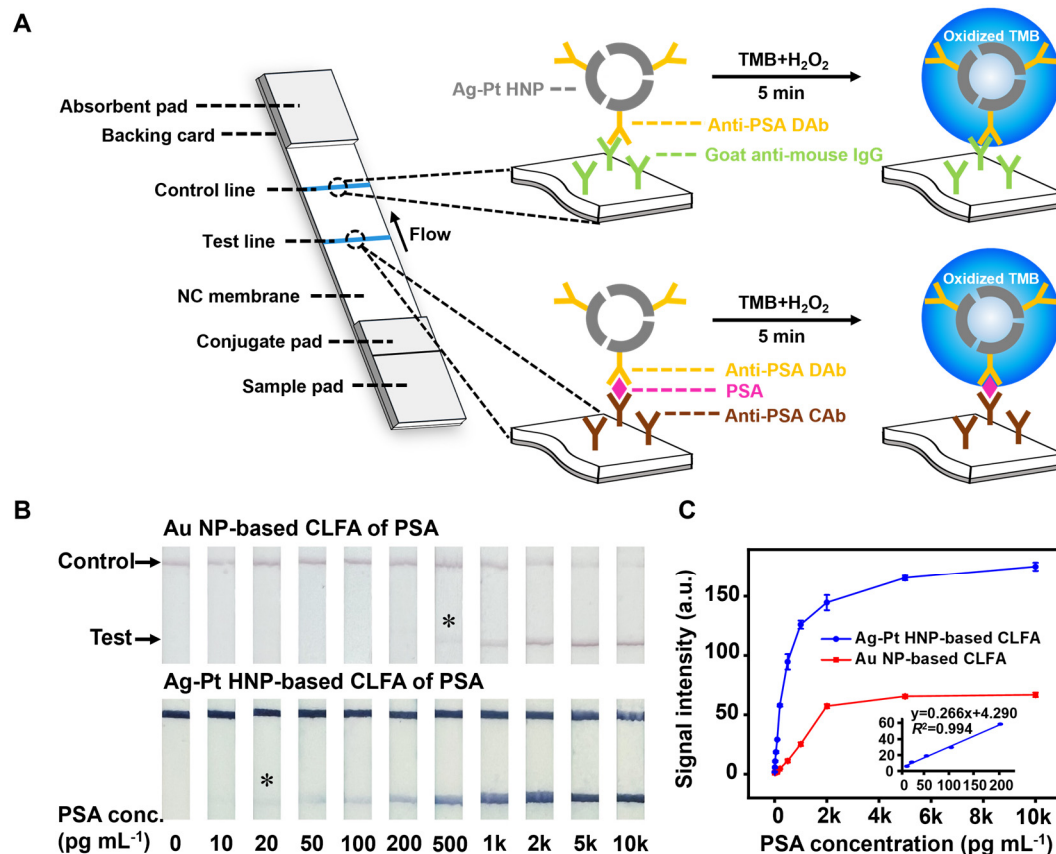


Figure 3. Ag-Pt HNP-based CLFA and conventional Au NP-based CLFA for detection of PSA. (A) Schematics illustrating the principle of Ag-Pt HNP-based CLFA. (B) Representative photographs of both CLFAs of PSA standards. Asterisks (*) indicate the detection limits by the naked eyes. (C) Corresponding calibration curves of the detection results shown in (B). Error bars denote standard deviations of six independent measurements. Inset shows linear range region of the Ag-Pt HNP-based CLFA.

PSA standards with concentrations ranging from 10 pg mL⁻¹ to 10 ng mL⁻¹ were detected by both the Ag-Pt HNP- and Au NP-based CLFAs. For quantitative analyses, the detection results were recorded with a digital camera (see Figure 3B). The color bands of the test line region were quantified using Adobe Photoshop software to generate the corresponding calibration curves (Figure 3C). For the Ag-Pt HNP-based CLFA, blue bands (originated from the oxidized TMB) at the test lines were visible to the naked eye at concentrations as low as 20 pg mL⁻¹. In contrast, the red bands (from the plasmonics of Au NPs) in Au NP-based CLFA could only be observed at PSA concentrations above 500 pg mL⁻¹. These results suggest the naked-eye detection limit of Ag-Pt HNP-based CLFA was about 25 times lower than that of Au NP-based CLFA. As shown by the calibration curves in Figure 3C, the Ag-Pt HNP-based CLFA exhibited a good linear correlation in 10–200 pg mL⁻¹ PSA with an R^2 of 0.994. The limit of detection (LOD, which is defined by the 3SD method [35,36]) of the Ag-Pt HNP-based CLFA was determined to be 3.07 pg mL⁻¹, which was ~27 times lower than the LOD of Au NP-based CLFA (82.64 pg mL⁻¹, which was calculated based on its calibration curve).

These results demonstrate that the Ag-Pt HNPs with peroxidase-like activities can lower the detection limit of conventional Au NP-based CLFA by more than 20 times. Such a substantial improvement in CLFA sensitivity is only paid by a simple substrate treatment process at room temperature. Remarkably, the hollow structure and composition of Ag-Pt HNPs significantly reduce the usage amount of previous noble metals in CLFA, making the

Ag-Pt HNP-based CLFA cost-effective. Taken together, the Ag-Pt HNP-based CLFA outperforms conventional Au NP-based CLFA from the aspects of both sensitivity and cost effectiveness.

3.4. Demonstration of Clinical Use

We first assessed the influence of biological matrices on the performance of Ag-Pt HNP-based CLFA. To this end, we applied the CLFA to quantify PSA from spiked human serum samples. Note, serum is one of the most common types of clinical samples in medical diagnostics [37–39]. All serum samples were diluted 2-fold by assay buffer prior to the loading of sample onto test strip. Four spiked samples with final PSA concentrations in 25–150 pg mL⁻¹ were prepared by spiking a PSA-free human serum sample (purchased from Sigma-Aldrich) with PSA standards. These samples were then detected by the Ag-Pt HNP-based CLFA. For quantitative analysis, the intensities of color signal at test lines of the CLFA strips were quantified and compared with the calibration curve shown in Supplementary Figure S5, from which the concentrations of PSA were determined. As summarized in Table 1, the analytical recoveries (which is defined as the PSA amount measured as a percentage of the PSA amount initially added to the serum) of the Ag-Pt HNP-based CLFA in detecting the four PSA-spiked serum samples were in the range of 94.81–102.92%. In addition, the coefficient of variation ($n = 6$) of all the spiked samples was $\leq 6.8\%$, indicating a good reproducibility of the CLFA test. These results demonstrated that the performance of Ag-Pt HNP-based CLFA was not significantly influenced by the biological matrices in human serum.

Table 1. Analytical recoveries of the Ag-Pt HNP-based CLFA in detection of PSA spiked human serum samples.

PSA Amount Spiked (pg mL ⁻¹)	PSA Amount Measured (pg mL ⁻¹)	Coefficient of Variations (%, $n = 6$)	Recovery (%)
25	24.00	4.37	96.00 \pm 4.20
50	51.46	3.31	102.92 \pm 3.19
100	97.88	5.51	97.88 \pm 4.99
150	142.22	6.80	94.81 \pm 6.45

Finally, to demonstrate the potential clinical use of Ag-Pt HNP-based CLFA, we used it for detecting PSA in a positive serum sample that was collected from a patient. This patient sample was purchased from Boca Biolistics (Pompano Beach, FL, USA, donor code #D106968). The sample was analyzed by a certified method (a commercial chemiluminescence immunoassay kit, Ortho-Clinical Diagnostics VITROS) to contain 0.5 ng mL⁻¹ of PSA. We intended to determine whether the PSA concentration measured by our Ag-Pt HNP-based CLFA agrees with the “known concentration” (i.e., 0.50 ng mL⁻¹) within experimental error. To this end, we analyzed the sample six times ($n = 6$) by our CLFA and measured the PSA concentrations. The measured values were 0.51, 0.40, 0.42, 0.49, 0.52, and 0.43 ng mL⁻¹ PSA, giving a mean of $\bar{x} = 0.46$ and a standard deviation of $s = 0.051$. Based on these results, we performed the *Student's t* test [40]. Specifically, for six measurements, there are 5 degrees of freedom and thus $t_{95\%} = 2.57$. The 95% confidence interval [which is expressed as $\bar{x} \pm ts/\sqrt{n}$] is calculated to be 0.46 ± 0.054 . The known concentration (0.50 ng mL⁻¹) is within the 95% confidence interval. Therefore, we can conclude that the detection result from our CLFA (0.46 ng mL⁻¹ PSA) agrees with the result from the commercial diagnostic kit (0.50 ng mL⁻¹ PSA) within experimental error at a 95% confidence level. These results demonstrated the potential application of the Ag-Pt HNP-based CLFA in clinical settings. A more comprehensive assessment of the clinical performance of the CLFA using large-scale samples will be the subject of our future study.

4. Conclusions

In summary, we have demonstrated a sensitive and cost-effective CLFA. The CLFA relies on Ag-Pt HNPs as colorimetric labels. The Ag-Pt HNPs possess strong peroxidase-like catalytic activities, allowing them to produce sensitive color signals through catalysis. Moreover, the Ag-Pt HNPs have hollow interiors and are primarily made of less expensive silver, which effectively reduces materials cost of previous noble metals in CLFA. The Ag-Pt HNP-based CLFA was successfully applied to the detection of a cancer biomarker PSA, of which sensitivity was much higher than conventional solid Au NP-based CLFA. We believe the CLFA presented in this work as a sensitive and cost-effective point-of-care technology has great potential for diagnostic applications, especially in resource-limited settings.

Supplementary Materials: The following supporting information can be downloaded at: <https://www.sciltp.com/journals/mi/2024/1/515/s1>, Figure 1: TEM image of citrate-capped silver nanoparticles (Ag NPs) with

an average diameter of 40.3 nm. These Ag NPs were used as sacrificial templates for the synthesis of Ag-Pt hollow nanoparticles (Ag-Pt HNPs) shown in Figure 1. Figure S2: Citrate-capped gold nanoparticles (Au NPs) with an average diameter of 40.8 nm. (A) A representative TEM image of the Au NPs. (B) An XPS spectrum recorded from the Au NPs. Figure S3: High-resolution XPS spectra of the C 1s and O 1s regions shown in Figure 1D. The peaks were analyzed and assigned according to the literature. Figure S4: UV-vis spectra recorded from 0.2 M NaOAc/HOAc buffer solution, pH 4.0, containing 0.8 mM TMB and 2.0 M H₂O₂ in the absence (#1) and presence (#2) of Ag-Pt HNPs (sample in Figure 1). Insets show the photographs of corresponding solutions. Figure S5: Calibration curve of the Ag-Pt HNP-based CLFA for detection of CEA standards in 1:1 (v/v) buffer/human serum mixture. Each data point in the plot represents an average of six independent measurements.

Author Contributions: J.Z.: conceptualization, methodology, data curation, writing-original draft preparation; S.S.: writing-reviewing and editing, validation; Z.W.: methodology; X.X.: supervision, conceptualization, writing-reviewing and editing. All authors have read and agreed to the published version of the manuscript.

Funding: This work was supported in part by the grants from the National Science Foundation (NSF) (DMR-2004546 and CBET-2234873) and U.S. Department of Agriculture (2020-67021-31257), and startup funds from the University of Central Florida (UCF).

Data Availability Statement: The data supporting this article have been included as part of the Supplementary Materials. Further data is available upon reasonable request from the authors.

Conflicts of Interest: There are no conflicts of interest to declare.

References

- Budd, J.; Miller, B.S.; Weckman, N.E.; Cherkaoui, D.; Huang, D.; Decruz, A.T.; Fongwen, N.; Hanet, G.-R.; Broto, M.; Estcourt, C.S.; et al. Lateral Flow Test Engineering and Lessons Learned from COVID-19. *Nat. Rev. Bioeng.* **2023**, *1*, 13–31.
- Liu, Y.; Zhan, L.; Qin, Z.; Sackrison, J.; Bischof, J.C. Ultrasensitive and Highly Specific Lateral Flow Assays for Point-of-Care Diagnosis. *ACS Nano* **2021**, *15*, 3593–3611.
- Jiang, N.; Tansukawat, N.D.; Gonzalez-Macia, L.; Ates, H.C.; Dincer, C.; Guder, F.; Tasoglu, S.; Yetisen, A.K. Low-Cost Optical Assays for Point-of-Care Diagnosis in Resource-Limited Settings. *ACS Sens.* **2021**, *6*, 2108–2124.
- Khlebtsov, B.N.; Tumskiy, R.S.; Burov, A.M.; Pylaev, T.E.; Khlebtsov, N.G. Quantifying the Numbers of Gold Nanoparticles in the Test Zone of Lateral Flow Immunoassay Strips. *ACS Appl. Nano Mater.* **2019**, *2*, 5020–5028.
- Dzhagan, V.; Kapush, O.; Plokhovska, S.; Buziashvili, A.; Pirko, Y.; Yeshchenko, O.; Yukhymchuk, V.; Yemets, A.; Zahn, D.R.T. Plasmonic Colloidal Au Nanoparticles in DMSO: A Facile Synthesis and Characterisation. *RSC Adv.* **2022**, *12*, 21591–21599.
- Yuan, Z.; Hu, C.C.; Chang, H.T.; Lu, C. Gold Nanoparticles as Sensitive Optical Probes. *Analyst* **2016**, *141*, 1611–1626.
- Cui, X.; Huang, Y.; Wang, J.; Zhang, L.; Rong, Y.; Lai, W.; Chen, T. A Remarkable Sensitivity Enhancement in a Gold Nanoparticle-Based Lateral Flow Immunoassay for the Detection of *Escherichia coli* O157:H7. *RSC Adv.* **2015**, *5*, 45092–45097.
- Gao, Z.; Ye, H.; Tang, D.; Tao, J.; Habibi, S.; Minerick, A.; Tang, D.; Xia, X. Platinum-Decorated Gold Nanoparticles with Dual Functionalities for Ultrasensitive Colorimetric In Vitro Diagnostics. *Nano Lett.* **2017**, *17*, 5572–5579.
- Zhan, L.; Guo, S.Z.; Song, F.; Gong, Y.; Xu, F.; Boulware, D.R.; McAlpine, M.C.; Chan, W.C.W.; Bischof, J.C. The Role of Nanoparticle Design in Determining Analytical Performance of Lateral Flow Immunoassays. *Nano Lett.* **2017**, *17*, 7207–7212.
- Ji, Y.; Ren, M.; Li, Y.; Huang, Z.; Shu, M.; Yang, H.; Xiong, Y.; Xu, Y. Detection of Aflatoxin B-1 with Immunochromatographic Test Strips: Enhanced Signal Sensitivity Using Gold Nanoflowers. *Talanta* **2015**, *142*, 206–212.
- Ge, C.; Wu, R.; Chong, Y.; Fang, G.; Jiang, X.; Pan, Y.; Chen, C.; Yin, J.J. Synthesis of Pt Hollow Nanodendrites with Enhanced Peroxidase-like Activity against Bacterial Infections: Implication for Wound Healing. *Adv. Funct. Mater.* **2018**, *28*, 1801484.
- Renzi, E.; Piper, A.; Natri, F.; Merkoçi, A.; Lombardi, A. An Artificial Miniaturized Peroxidase for Signal Amplification in Lateral Flow Immunoassays. *Small* **2023**, *19*, 2207949.
- Loynachan, C.N.; Thomas, M.R.; Gray, E.R.; Richards, D.A.; Kim, J.; Miller, B.S.; Brookes, J.C.; Agarwal, S.; Chudasama, V.; McKendry, R.A.; et al. Platinum Nanocatalyst Amplification: Redefining the Gold Standard for Lateral Flow Immunoassays with Ultrabroad Dynamic Range. *ACS Nano* **2018**, *12*, 279–288.
- Wei, Z.; Luciano, K.; Xia, X. Catalytic Gold-Iridium Nanoparticles as Labels for Sensitive Colorimetric Lateral Flow Assay. *ACS Nano* **2022**, *16*, 21609–21617.
- Jiang, B.; Duan, D.; Gao, L.; Zhou, M.; Fan, K.; Tang, Y.; Xi, J.; Bi, Y.; Tong, Z.; Gao, G.F.; et al. Standardized Assays for Determining the Catalytic Activity and Kinetics of Peroxidase-like Nanozymes. *Nat. Protoc.* **2018**, *13*, 1506–1520.

16. Gao, W.; Eastwood, H.; Xia, X. Peroxidase Mimics of Platinum-Group Metals for In Vitro Diagnostics: Opportunities and Challenges. *J. Mater. Chem. B* **2023**, *11*, 8404–8410.
17. Wei, Z.; Xi, Z.; Vlasov, S.; Ayala, J.; Xia, X. Nanocrystals of Platinum-Group Metals as Peroxidase Mimics for In Vitro Diagnostics. *Chem. Commun.* **2020**, *56*, 14962–14975.
18. Naseri, M.; Ziora, Z.M.; Simon, G.P.; Batchelor, W. ASSURED-Compliant Point-of-Care Diagnostics for the Detection of Human Viral Infections. *Rev. Med. Virol.* **2022**, *32*, e2263.
19. Bastús, N.G.; Merkoçi, F.; Piella, J.; Puentes, V. Synthesis of Highly Monodisperse Citrate-Stabilized Silver Nanoparticles of up to 200 nm: Kinetic Control and Catalytic Properties. *Chem. Mater.* **2014**, *26*, 2836–2846.
20. He, M.Q.; Ai, Y.; Hu, W.; Guan, L.; Ding, M.; Liang, Q. Recent Advances of Seed-Mediated Growth of Metal Nanoparticles: From Growth to Applications. *Adv. Mater.* **2023**, *35*, 2211915.
21. Gao, Z.; Ye, H.; Wang, Q.; Kim, M.J.; Tang, D.; Xi, Z.; Wei, Z.; Shao, S.; Xia, X. Template Regeneration in Galvanic Replacement: A Route to Highly Diverse Hollow Nanostructures. *ACS Nano* **2020**, *14*, 791–801.
22. Gao, Z.; Shao, S.; Gao, W.; Tang, D.; Tang, D.; Zou, S.; Kim, M.J.; Xia, X. Morphology-Invariant Metallic Nanoparticles with Tunable Plasmonic Properties. *ACS Nano* **2021**, *15*, 2428–2438.
23. Xia, X.; Zhang, J.; Lu, N.; Kim, M.J.; Ghale, K.; Xu, Y.; McKenzie, E.; Liu, J.; Ye, H. Pd-Ir Core-Shell Nanocubes: A Type of Highly Efficient and Versatile Peroxidase Mimic. *ACS Nano* **2015**, *9*, 9994–10004.
24. Gao, L.; Zhuang, J.; Nie, L.; Zhang, J.; Zhang, Y.; Gu, N.; Wang, T.; Feng, J.; Yang, D.; Perrett, S.; et al. Intrinsic Peroxidase-like Activity of Ferromagnetic Nanoparticles. *Nat. Nanotechnol.* **2007**, *2*, 577–583.
25. Lineweaver, H.; Burk, D. The Determination of Enzyme Dissociation Constants. *J. Am. Chem. Soc.* **1934**, *56*, 658–666.
26. Biby, A.; Crawford, H.; Xia, X. Platinum-Group Metal Nanoparticles as Peroxidase Mimics: Implications for Biosensing. *ACS Appl. Nano Mater.* **2022**, *5*, 17622–17631.
27. Lin, H.; Liu, Y.; Huo, J.; Zhang, A.; Pan, Y.; Bai, H.; Jiao, Z.; Fang, T.; Wang, X.; Cai, Y.; et al. Modified Enzyme-Linked Immunosorbent Assay Strategy Using Graphene Oxide Sheets and Gold Nanoparticles Functionalized with Different Antibody Types. *Anal. Chem.* **2013**, *85*, 6228–6232.
28. Glomm, W.R.; Halskau, Ø.; Hanneseth, A.-M.D.; Volden, S. Adsorption Behavior of Acidic and Basic Proteins onto Citrate-Coated Au Surfaces Correlated to Their Native Fold, Stability, and pI. *J. Phys. Chem. B* **2007**, *111*, 14329–14345.
29. Ye, H.; Xia, X. Enhancing the Sensitivity of Colorimetric Lateral Flow Assay (CLFA) through Signal Amplification Techniques. *J. Mater. Chem. B* **2018**, *6*, 7102–7111.
30. Josephy, P.D.; Eling, T.; Mason, R.P. The Horseradish Peroxidase-Catalyzed Oxidation of 3,5,3',5'-tetramethylbenzidine. Free Radical and Charge-Transfer Complex Intermediates. *J. Biol. Chem.* **1982**, *257*, 3669–3675.
31. Gao, W.; Sun, X.; Yishay, T.; Wei, Z.; Zhu, X.; Kim, M.J.; Xia, X. Iridium Nanoparticles as Highly Effective Peroxidase Mimics: Synthesis, Characterization, and Application in Biosensing. *ChemNanoMat* **2024**, *10*, e202300589.
32. Liu, X.; Atwater, M.; Wang, J.; Huo, Q. Extinction Coefficient of Gold Nanoparticles with Different Sizes and Different Capping Ligands. *Colloids Surf. B Biointerfaces* **2007**, *58*, 3–7.
33. Stamey, T.A.; Yang, N.; Hay, A.R.; McNeal, J.E.; Freiha, F.S.; Redwine, E. Prostate-Specific Antigen as a Serum Marker for Adenocarcinoma of the Prostate. *N. Engl. J. Med.* **1987**, *317*, 909–916.
34. Palladino, P.; Torrini, F.; Scarano, S.; Minunni, M. 3,3',5,5'-tetramethylbenzidine as Multi-Colorimetric Indicator of Chlorine in Water in Line with Health Guideline Values. *Anal. Bioanal. Chem.* **2020**, *412*, 7861–7869.
35. Armbruster, D.A.; Pry, T. Limit of Blank, Limit of Detection and Limit of Quantitation. *Clin. Biochem. Rev.* **2008**, *29*, S49–S52.
36. Armbruster, D.A.; Tillman, M.D.; Hubbs, L.M. Limit of Detection (LOD)/limit of Quantitation (LOQ): Comparison of the Empirical and the Statistical Methods Exemplified with GC-MS Assays of Abused Drugs. *Clin. Chem.* **1994**, *40*, 1233–1238.
37. Zerva, L.; Bourantas, K.; Mitka, S.; Kansouzidou, A.; Legakis, N.J. Serum is the Preferred Clinical Specimen for Diagnosis of Human Brucellosis by PCR. *J. Clin. Microbiol.* **2001**, *39*, 1661–1664.
38. Chen, X.; Ba, Y.; Ma, L.; Cai, X.; Yin, Y.; Wang, K.; Guo, J.; Zhang, Y.; Chen, J.; Guo, X. Characterization of MicroRNAs in Serum: A Novel Class of Biomarkers for Diagnosis of Cancer and Other Diseases. *Cell Res.* **2008**, *18*, 997–1006.
39. Wegner, K.D.; Jin, Z.; Linden, S.; Jennings, T.L.; Hildebrandt, N. Quantum-Dot-Based Förster Resonance Energy Transfer Immunoassay for Sensitive Clinical Diagnostics of Low-Volume Serum Samples. *ACS Nano* **2013**, *7*, 7411–7419.
40. Harris, D.C. *Quantitative Chemical Analysis*, 9th Ed.; W.H. Freeman & Company: New York, NY, USA, 2016.

Article

Piezocatalytic ZnS: Mn²⁺ Nanocrystals for Enhanced Organic Dye Degradation

Zhongxiang Wang¹, Elizaveta Tiukalova², Youyi Tai³, Miaofang Chi², Jin Nam^{3,*}, and Yadong Yin^{1,*}

¹ Department of Chemistry, University of California, Riverside, CA 92521, USA

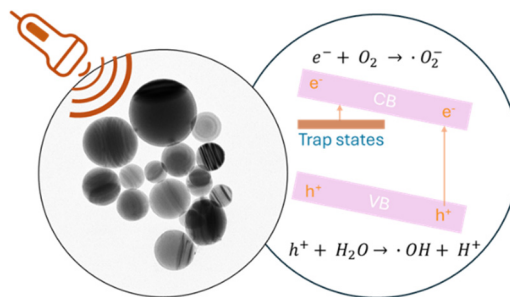
² Center for Nanophase Materials Sciences, Oak Ridge National Laboratory, Oak Ridge, TN 37831, USA

³ Department of Bioengineering, University of California, Riverside, CA 92521, USA

* Correspondence: jnam@engr.ucr.edu (J.N.); yadong.yin@ucr.edu (Y.Y.)

Received: 15 October 2024; Revised: 20 November; Accepted: 21 November 2024; Published: 22 November 2024

Abstract: Piezocatalysis, an emerging approach that harnesses mechanical energy to drive chemical reactions, has garnered significant attention due to its potential applications in diverse fields, particularly in environmental remediation. Its broader application, however, is often hindered by the low efficiency of existing piezocatalytic materials. Here, we report the synthesis of Mn²⁺-doped ZnS nanocrystals with improved piezoelectric properties using an emulsion-based colloidal assembly technique. Through well-controlled Mn²⁺ doping, these nanocrystals demonstrate high piezocatalytic activity for degrading organic dyes under ultrasonic vibration. The optimal performance is achieved with 3% Mn²⁺ doping, outperforming many existing piezocatalysts. Mechanistic studies reveal the generation of reactive oxygen species as the primary driving force for degradation. Notably, pre-excitation with UV light further boosts the piezocatalytic efficiency of these metal ion-doped ZnS nanocrystals by filling electron trap states, leading to improved overall performance. This research paves the way for developing high-performance piezocatalysts, expanding the potential of piezocatalysis for a wide range of applications.



Keywords: piezocatalysis; piezoelectricity; zinc sulfide; pollutant degradation; water decontamination

1. Introduction

The rapid industrial development has led to a surge in water-soluble organic pollutants, posing severe environmental and health concerns. Traditional water treatment methods often fall short of effectiveness in addressing these pollutants, necessitating the exploration of advanced oxidation processes (AOPs). Coupled with photocatalysis [1–3] electrocatalysis [4,5] and Fenton reactions [6–8] these methods have emerged as promising decontamination strategies due to their ability to generate reactive radicals for breaking down a wide range of organic molecules into less harmful substances. Photocatalysis utilizes light to activate semiconductor materials, creating electron-hole pairs to drive radical formation. Similarly, electrocatalysis applies an electrical current to induce redox processes, while Fenton reactions use iron-based catalysts to break down hydrogen peroxide into highly reactive hydroxyl radicals. Despite their effectiveness, these processes also face their own challenges, such as significant energy inputs or dependence on specific reagents, prompting the need for developing alternative catalytic strategies.

Recently, the piezoelectric effect has been explored to use mechanical energy to drive degradation reactions of organic pollutants [9,10], leading to the development of a new catalytic process termed piezocatalysis. Piezocatalysis distinguishes itself from traditional electrocatalysis and photocatalysis by utilizing charge separation in piezoelectric materials when subjected to mechanical vibrations [11,12]. This unique mechanism enables a range of chemical reactions, making piezocatalysis an attractive option for environmental remediation [13–17], energy sustainability [18–20], and biomedical applications [21–23]. Commonly studied piezocatalytic materials include ZnO and BaTiO₃, known for their non-centrosymmetric crystal structures and



Copyright: © 2024 by the authors. This is an open access article under the terms and conditions of the Creative Commons Attribution (CC BY) license (<https://creativecommons.org/licenses/by/4.0/>).

Publisher's Note: Scilight stays neutral with regard to jurisdictional claims in published maps and institutional affiliations

piezoelectric coefficients ranging between 20 and 100 pC/N [23,24]. However, these materials face limitations such as instability in acidic environments or potential ecological and cytotoxic concerns [25,26]. Alternatively, wurtzite-phase zinc sulfide (ZnS), another non-centrosymmetric piezoelectric material with good chemical stability and biocompatibility, has shown decent piezocatalytic performance in hydrogen generation from pure water [18]. Nonetheless, due to its lower piezoelectric coefficient than ZnO and BaTiO₃, ZnS has been less explored for piezocatalytic applications. Moreover, its transition from the stable zinc blende to the more piezoelectrically active wurtzite phase typically requires high-temperature calcination [27,28], which, however, increases its bulkiness, making it difficult to compete with nanoscale catalysts featuring extremely high specific surface area. Therefore, strategies to enhance the piezoelectric properties of ZnS nanocrystals and expand their use in piezocatalysis are of significant research interest.

In this study, we report the synthesis of manganese-doped ZnS (ZnS:Mn²⁺) nanocrystals from their quantum dot precursors using an emulsion-based assembly approach. The resulting nanocrystals exhibited exceptionally high piezoelectricity, with a piezoelectric coefficient of up to 23 pC/N, and outstanding piezocatalytic efficiency for the degradation of model organic pollutants, including methylene blue (MB) and rhodamine B (RhB), under ultrasound vibration. Our mechanistic studies revealed that the degradation process was driven by hydroxyl and superoxide radicals generated from charge carriers under sonication. Notably, UV pre-excitation of the catalysts significantly enhanced the piezocatalytic performance by filling the trap states and promoting charge separation during sonication. The enhanced piezoelectricity and piezocatalytic activity can be attributed to the synergistic effects of doping-induced point defects and assembly-caused stacking faults within the nanocrystals, with the former creating trap states that facilitate charge separation and the latter enhancing spontaneous polarization. These material characteristics promotes the generation and utilization of charge carriers under mechanical vibration, leading to improved catalytic performance. This innovative synthesis approach to develop high-performance piezocatalytic materials opens new avenues for sustainable environmental remediation and biomedical applications.

2. Results and Discussion

Figure 1a depicts the process of synthesizing wurtzite phase ZnS nanocrystals, using their zinc blende phase quantum dots (QD) as precursors. It begins with dispersing pre-synthesized QDs in droplets of an oil-in-water emulsion, allowing the QDs to form clusters as the solvent evaporates, and then coating the clusters with a layer of silica. Subsequent steps involve calcination of the core-shell particles, during which QD clusters transform into wurtzite nanocrystals and sinter into larger domains, followed by selective etching of the silica using sodium hydroxide (NaOH) to release the wurtzite nanocrystals. Specifically, pure ZnS QDs and ZnS:Mn²⁺ QDs were synthesized at a high temperature (300 °C) via a Lewis acid-base reaction between metal chlorides and elemental sulfur, with oleylamine as the solvent and capping ligand [29,30]. The synthesis produced QDs with a relatively narrow size distribution, as evidenced in the transmission electron microscopy (TEM, Thermo Fisher Scientific, Waltham, MA, USA) image in Figure S1a for a sample of 3% Mn²⁺-doped ZnS QDs with an average diameter of approximately 9.4 nm (Figure S1b). The Mn²⁺ doping level does not appear to affect the QD size, as indicated by the TEM images of undoped (Figure S1c) and 1% Mn²⁺-doped ZnS QDs (Figure S1d). Using cetyltrimethylammonium bromide (CTAB) as the surfactant, the QD solution in cyclohexane was dispersed in water to produce an oil-in-water emulsion. Subsequent evaporation of cyclohexane promoted the assembly of QDs into clusters [31]. The detailed procedures are provided in the Supporting Information. Figure 1b displays the TEM image of QD clusters with an average size of ~81 nm (size distribution shown in Figure S2). Since the as-prepared QDs are in the zinc blende phase [30], high-temperature calcination is required to induce the phase transition from zinc blende to wurtzite as the latter is more piezoelectrically active due to the lack of inversion symmetry. To prevent sintering between the clusters during calcination, they were coated with a silica layer using the Stöber method [32]. Figure 1c presents the TEM image of silica-coated clusters, which have an average coating thickness of ~11.5 nm, estimated based on 30 measurements (Figure S3). The silica-coated clusters were then calcined at 1050 °C for 90 min to convert them into larger nanocrystals (Figure 1d) and induce the zinc blende-to-wurtzite phase transition. After the silica layer was removed by NaOH etching, spherical nanocrystals in the wurtzite phase were obtained, as shown in Figures 1e and S4a. The average size of these nanocrystals was determined to be ~76 nm, based on the statistical size distribution presented in Figure S4b. These nanocrystals were further characterized using aberration-corrected scanning transmission electron microscopy (STEM, JEOL, Freising, Germany) equipped with energy-dispersive X-ray spectroscopy (EDS, JEOL, Freising, Germany). Figure 1f provides the high-angle annular dark-field (HAADF) STEM image of ZnS:3%Mn²⁺ nanocrystals, while

Figure 1g–i show that Mn^{2+} was successfully incorporated into the final nanocrystals through initial doping during QD synthesis, with Zn, S, and Mn elements uniformly distributed throughout the nanocrystals.

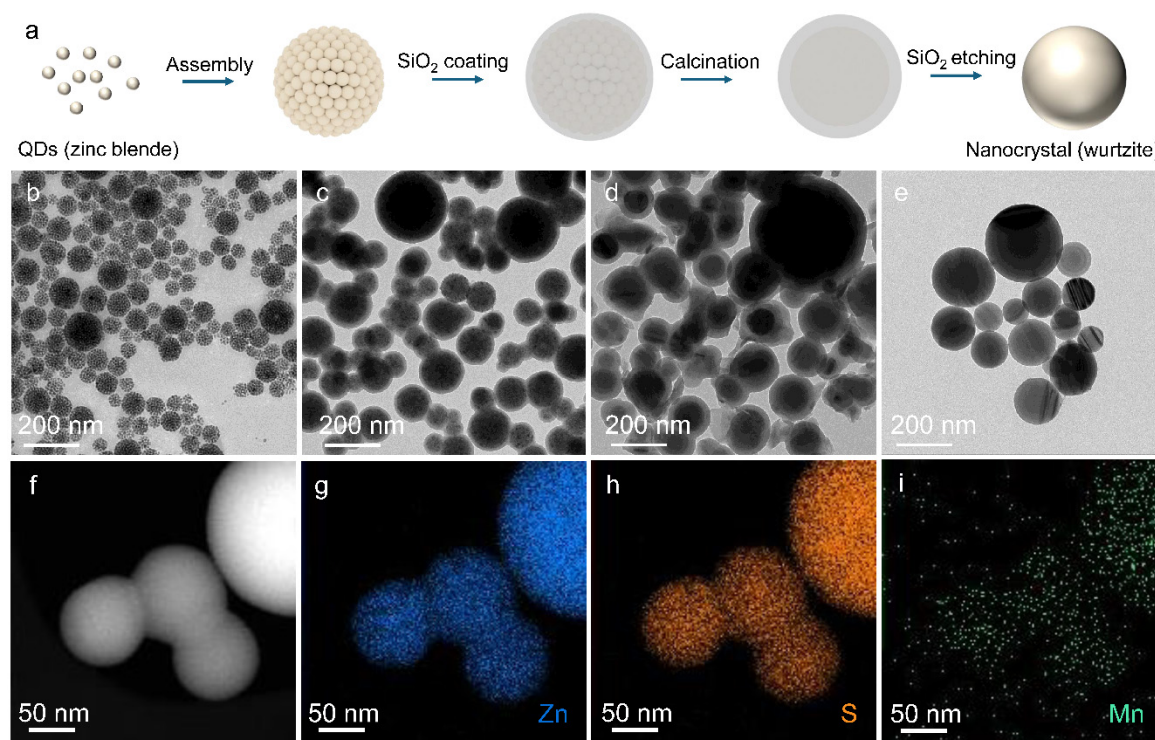


Figure 1. (a) Fabrication process of ZnS-based nanocrystals. (b–e) TEM images of clusters of ZnS:3%Mn²⁺ QDs (b), silica-coated clusters of ZnS:3%Mn²⁺ QDs (c), silica-coated ZnS:3%Mn²⁺ nanocrystals after calcination (d), and the released ZnS:3%Mn²⁺ nanocrystals after removing silica via base etching (e). (f) HAADF-STEM image of ZnS:3%Mn²⁺ nanocrystals. (g–i) EDS mapping of Zn (g), S (h), and Mn (i) in ZnS:3%Mn²⁺ nanocrystals.

Figure 2a shows the X-ray diffraction (XRD, PANalytical, Almelo, The Netherlands) patterns of the ZnS QD precursors and the ZnS nanocrystals doped with varying amounts of Mn^{2+} (0–4%). The ZnS QD precursors exhibit a zinc blende phase, displaying peaks consistent with the standard powder diffraction file (PDF#05-0566). After assembly and calcination, the nanocrystals transit to a wurtzite phase, as confirmed by comparing to the standard PDF#36-1450, regardless of the Mn^{2+} doping concentration. When the Mn^{2+} doping ratio exceeds 3%, a slight peak shift to lower angles is observed. This can be attributed to the larger ionic radius of Mn^{2+} (0.83 Å) compared to Zn^{2+} (0.74 Å) [33], which increases the lattice parameter and shifts the diffraction peaks to lower angles according to Bragg's Law. To investigate the piezoelectric properties, piezoresponse force microscopy (PFM, Asylum Research, Goleta, CA, USA) was performed on the ZnS:3%Mn²⁺ wurtzite nanocrystals. Figure S5 displays the response amplitude (A) of the nanocrystals under a voltage bias (B) of 3 V, resulting in a piezoelectric coefficient (d_{33}) of 23.3 pm/V, calculated using the equation $d_{33} = A \cdot f / (B \cdot Q_f)$, where f is the correction factor and Q_f is the quality factor ($Q_f = 150$) [28]. This high d_{33} value indicates strong piezoelectricity in the nanocrystals, significantly exceeding previously reported values for ZnS [34].

The piezoelectric ZnS-based nanocrystals were utilized as catalysts for dye degradation. The catalyst loading was maintained at 1 mg/mL, and the initial dye concentration was set to 10 ppm (or mg/L). The catalysts were stirred with the dyes in the dark to achieve adsorption-desorption equilibrium. Figure S6a shows the UV-Vis spectra of methylene blue (MB) during the stirring process with the catalysts for up to 60 min. The corresponding plot of C/C_0 over time, derived from Beer's Law (Figure S6b), indicates that 30 min of stirring is sufficient to establish adsorption-desorption equilibrium.

In the subsequent step, the mixture was exposed to UV light with emission centered at 365 nm for 1 min to fill the trap states within the bandgap of ZnS [35]. It was observed that exposure to UV light did not alter the dye concentration (Figure S7), confirming that no photocatalytic degradation occurred during this step. Subsequently, the mixture was subjected to ultrasound treatment at 40 kHz while maintaining a constant temperature of 22 °C. Aliquots were taken at specific time intervals, and the nanocrystals were separated by centrifugation. Figure 2b displays the UV-Vis spectra of MB degradation catalyzed by ZnS:3%Mn²⁺ nanocrystals. The MB was rapidly

degraded under sonication, achieving 95% degradation within just 20 min. The degradation ratio (D) was calculated by:

$$D = \left(1 - \frac{C}{C_0}\right) \times 100\% = \left(1 - \frac{A}{A_0}\right) \times 100\% \quad (1)$$

where C is the concentration at a given time during the reaction, C_0 is the initial concentration, A is the absorbance at a given time during the reaction, and A_0 is the initial absorbance value [16]. The inset photos in Figure 2b depict the color change of the MB solution during the piezocatalytic degradation process. The degradation of dyes follows a simplified Langmuir-Hinshelwood first-order kinetics model:

$$-\ln\left(\frac{C}{C_0}\right) = -\ln\left(\frac{A}{A_0}\right) = kt \quad (2)$$

where k represents the degradation rate constant.

ZnS nanocrystals with varying Mn^{2+} doping ratios were tested for their efficiencies in degrading MB. Figure S8 shows the UV-Vis spectra of MB degradation using ZnS nanocrystals doped with different Mn^{2+} ratios (0%, 0.5%, 1%, 2%, 3%, and 4%). The degradation rate constants, calculated using Equation (2), are summarized in Figure 2c. The ZnS nanocrystals doped with 3% Mn^{2+} exhibited the fastest degradation, with the highest rate constant of 0.1376 min^{-1} . To further confirm the piezocatalytic performance of the ZnS-based nanocrystals, Rhodamine B (RhB) with an initial concentration of 10 ppm was also used as a model organic dye. Figure 2d presents the UV-Vis spectra of RhB degradation catalyzed by ZnS:3% Mn^{2+} over 35 min, with the inset showing the color change of the RhB solution at various stages of degradation. The degradation ratio of RhB reached 95% after 30 min of sonication, as calculated using Equation (1).

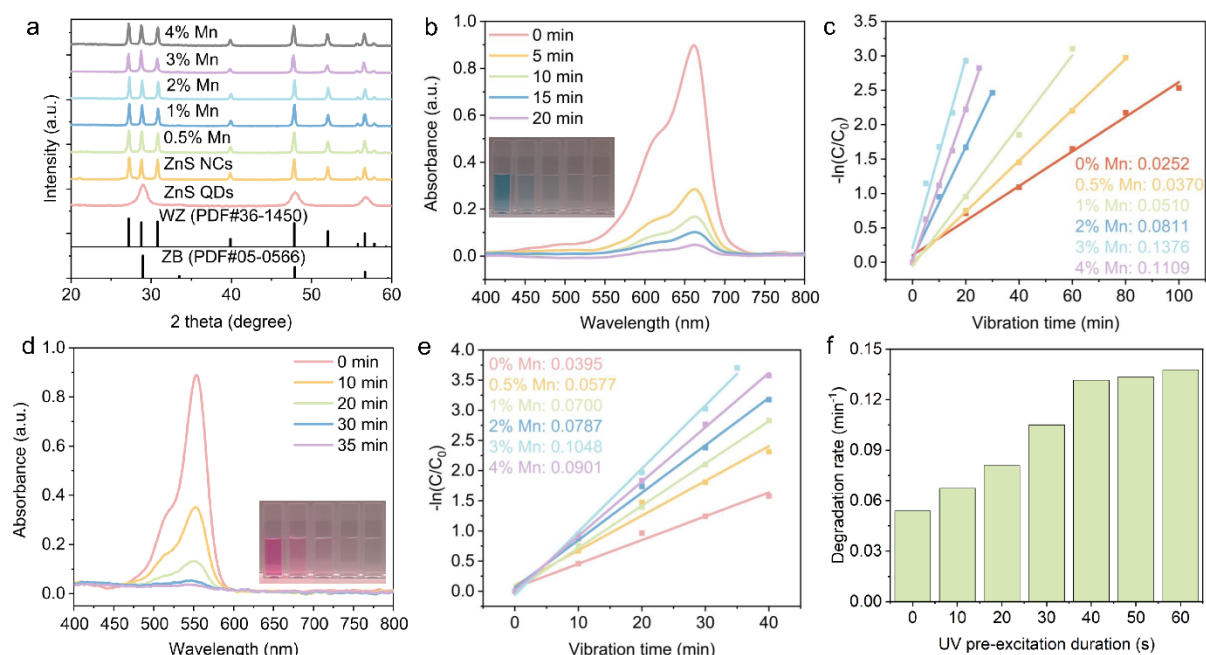


Figure 2. (a) XRD patterns of the ZnS QDs precursors and ZnS nanocrystals synthesized by calcination. The nanocrystals were doped with varying amounts of Mn^{2+} . (b,d) UV-Vis spectra of MB (b) and RhB (d) after piezocatalytic degradation by ZnS:3% Mn^{2+} nanocatalysts for varying periods. (c,e) Piezocatalytic performance of ZnS:Mn²⁺ nanocatalysts for degrading MB (c) and RhB (e). (f) Piezocatalytic degradation rates of MB using ZnS:3% Mn^{2+} nanocatalysts pre-excited under UV for varying durations.

Figure S9 shows the UV-Vis spectra of RhB degraded by ZnS:Mn²⁺ nanocrystals with doping ratios ranging from 0% to 4%. The degradation rate constants, determined using Equation (2), are summarized in Figure 2e. Again, the ZnS nanocrystals doped with 3% Mn^{2+} exhibited the highest degradation rate constant of 0.1048 min^{-1} . Control experiments were conducted by sonicating the organic dyes in the absence of catalysts. Figure S10a,b displays the UV-Vis spectra of MB and RhB during 40 min of sonication. The absorbances of both dyes showed no significant decrease, indicating that sonication alone is insufficient to degrade the dye molecules, and the observed degradation is primarily due to the catalytic activity of the ZnS-based nanocrystals.

The enhancement of piezocatalytic degradation efficiency by UV pre-excitation, a unique feature of our piezocatalysts, was further investigated using ZnS:3%Mn²⁺ nanocatalysts. The UV pre-excitation process involves exposing the dye/nanocatalyst mixture to UV light before initiating sonication, and it is believed to modify the electronic states of the nanocrystals. As illustrated in Figure S11, the degradation of MB was markedly slower when the pre-excitation step was omitted. Specifically, the MB degradation rate was calculated to be 0.0539 min⁻¹ without UV pre-excitation, compared to a significantly higher rate of 0.1397 min⁻¹ with UV pre-excitation of 1 min. These findings highlight the crucial role of UV pre-excitation in achieving efficient piezocatalytic degradation of organic dyes.

The observed enhancement in the degradation rate by UV pre-excitation can be attributed to the ability of UV light to excite electrons within the ZnS:Mn²⁺ nanocrystals, filling the trap states that are otherwise empty.²⁴ These trapped charge carriers can then be readily released under mechanical vibrations during the sonication process, participating in redox reactions that degrade the dye molecules. This mechanism underscores the importance of pre-activating the catalyst to maximize the utilization of charge carriers during the piezocatalytic process.

To further substantiate this hypothesis, we explored the effect of varying the UV pre-excitation time, ranging from 10 s to 1 min, on the degradation rates of MB. The results, presented in Figure 2f, demonstrate that the degradation rate initially increased with the duration of UV pre-excitation, reaching an optimal rate after 40 s. Beyond this point, the degradation rate plateaued, suggesting that the photoexcited electrons fully occupied the trap states, and additional UV exposure did not contribute to further improvements. The UV-Vis absorption spectra of MB degradation under different pre-excitation times are shown in Figure S12. The data clearly demonstrate that UV pre-excitation is essential for optimizing the piezocatalytic performance of the ZnS:Mn²⁺ nanocrystals. The lack of further noticeable enhancement in degradation rates beyond 40 s of pre-excitation likely indicates the saturation of electron trap states. This saturation behavior aligns with the hypothesis that UV pre-excitation maximizes the availability of reactive charge carriers, thereby boosting the overall efficiency of the piezocatalytic degradation process.

To elucidate the effect of Mn²⁺ doping ratios on piezocatalytic performance, electron paramagnetic resonance (EPR) spectroscopy was conducted on ZnS-based nanocrystals with varying Mn²⁺ doping levels, with the results shown in Figure 3a. The EPR signal intensities increase consistently with higher Mn²⁺ doping levels, indicating a rise in defect concentration as the Mn²⁺ content increases. At lower doping levels, Mn²⁺ ions predominantly occupy substitutional sites within the Zn-S lattice. However, Mn²⁺ ions are more likely to occupy interstitial sites at higher doping levels, leading to stronger Mn-Mn interactions. This is evidenced by the broadening of the EPR profiles at higher Mn²⁺ doping concentrations. While increasing Mn²⁺ doping enhances defect formation, excessive doping can destabilize the crystal lattice, ultimately diminishing piezocatalytic efficiency. As a result, the optimal piezocatalytic performance was observed at a 3% Mn²⁺ doping level.

To further elucidate the degradation mechanism, 5,5-Dimethyl-1-pyrroline N-oxide (DMPO) was employed as the spin trap to capture radicals produced within the reaction system. Figure 3b presents the EPR spectra of aqueous solutions containing DMPO and 1%, 3%, and 4% Mn²⁺-doped ZnS nanocrystals after sonication, showing a profile characteristic of ·OH radicals [36,37], and thus confirming their presence. Notably, the highest EPR signal intensity for ·OH radicals was observed in ZnS:3%Mn²⁺, consistent with its superior piezocatalytic performance. Figure 3c depicts the EPR spectra of the same Mn²⁺-doped ZnS nanocrystals/DMPO dispersions in dimethyl sulfoxide (DMSO), also after sonication. The EPR signals detected in this setup correspond to ·O₂⁻ radicals [38], with the highest intensity detected at 3% Mn²⁺ doping. These findings indicate the formation of reactive oxygen species (ROS), such as ·OH and ·O₂⁻, within the reaction environment. The proposed radical formation pathway during piezocatalysis is illustrated in Figure 3d. Upon sonication, the piezoelectric ZnS nanocrystals undergo tilting of band gap structure and charge separation, likely due to both electron detrapping from trap states and electron transition from the valence band to the conduction band, which drive the generation of these reactive species. Specifically, holes react with water molecules to produce hydroxyl radicals (·OH), while electrons combine with oxygen molecules to generate superoxide radicals (·O₂⁻).

The charge separation behavior of ZnS:Mn²⁺ nanocrystals under sonication was further confirmed by more in-depth studies, e.g., modifying the surface of ZnS:3%Mn²⁺ nanocrystals with Pluronic F-127, a hole scavenger. After pre-excitation with UV light, the nanocrystals were dispersed in degassed water and subjected to sonication. If charge separation occurred, the holes would be scavenged by Pluronic F-127, and the electrons would partially convert into hydrated electrons in the solution. These hydrated electrons are known to react with oxidative species, such as hydrogen peroxide (H₂O₂) and hydroxyl radicals (·OH). The concentration of these oxidative species can be quantified by reacting with molecules that can change their light absorbance, for example, potassium iodide (KI) for H₂O₂ and salicylic acid (SA) for ·OH. In the first experiment, the UV pre-excited nanocrystals were

combined with H_2O_2 and then sonicated. After centrifugation to remove nanocrystals, the supernatant was mixed with KI. UV-Vis spectroscopy was used to monitor the formation of triiodide (I_3^-), which followed these reactions: $\text{H}_2\text{O}_2 + 2\text{I}^- \rightarrow \text{I}_2 + 2\text{OH}^-$ and $\text{I}^- + \text{I}_2 \rightarrow \text{I}_3^-$. As shown in Figure 3e, the absorbance peak of I_3^- around 350 nm was significantly lower in the presence of ZnS:3\%Mn^{2+} nanocrystals (1 mg/mL) compared to the control experiment without nanocrystals, indicating the consumption of H_2O_2 by piezo-generated electrons and, therefore, reduced formation of I_3^- .

In the second experiment, the reaction between SA and $\cdot\text{OH}$ radicals was used to investigate charge carrier separation, as electrons can reduce hydroxyl radicals, leading to observable changes in the UV-Vis spectra. $\cdot\text{OH}$ was produced through a Fenton reaction involving ferrous sulfate and H_2O_2 and subsequently mixed with ZnS:3\%Mn^{2+} nanocrystals. The resulting oxidized product of SA, which appeared purple, exhibited an absorbance peak around 520 nm. Figure 3f shows that the absorbance decreased in the presence of ZnS:3\%Mn^{2+} nanocrystals, confirming the reaction of the $\cdot\text{OH}$ radicals with electrons generated from the nanocrystals. Moreover, the comparison of the absorbance with and without UV pre-excitation (Figure 3e,f) revealed that pre-excited samples had significantly lower absorbance for both I_3^- and oxidized SA. This result confirms that UV pre-excitation enhances electron generation during sonication by filling trap states within the ZnS:3\%Mn^{2+} nanocrystals. These findings are consistent with the piezocatalytic data discussed previously.

Control experiments were also performed to compare the absorbance of systems with and without sonication in the absence of nanocrystals. As illustrated in Figure 3e,f, sonication alone did not significantly decompose H_2O_2 or degrade $\cdot\text{OH}$, confirming that the observed effects were due to the presence and charge separation of the ZnS:3\%Mn^{2+} nanocrystals.

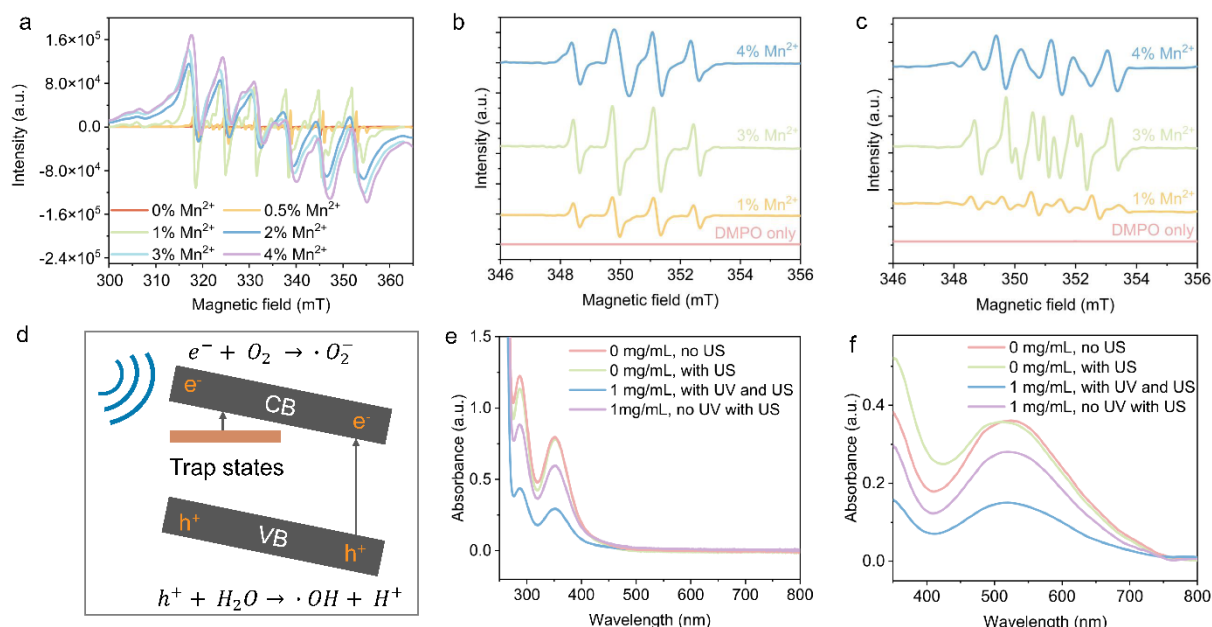


Figure 3. (a) EPR spectra of ZnS nanocrystals doped with different amounts of Mn^{2+} . (b) EPR spectra of DMPO-trapped hydroxyl radicals in water generated from sonication of water-dispersed ZnS:Mn^{2+} nanocrystals with 1%, 3%, and 4% doping, compared with DMPO/water solution. (c) EPR spectra of DMPO-trapped superoxide radicals in water generated from sonication of water-dispersed ZnS:Mn^{2+} nanocrystals with 1%, 3%, and 4% doping, compared with DMPO/water solution. (d) Scheme of charge separation for ZnS:Mn^{2+} nanocrystals under sonication. (e,f) UV-Vis spectra of I_3^- (e) and oxidized SA (f) generated during the reaction under various conditions including with or without ZnS:3\%Mn^{2+} catalyst (labeled with concentration), UV pre-excitation (labeled as “UV”), and (ultra)sonication (labeled as “US”).

The impact of the silica layer on the piezocatalytic performance of the nanocrystals was systematically investigated. Figure 4a shows the FTIR spectra of the ZnS:3\%Mn^{2+} nanocrystals before and after removing the silica coating. For the silica-coated samples, strong Si-O-Si vibrational peaks (highlighted in the pink region) appeared around 1060 and 1160 cm^{-1} . These peaks were significantly diminished after silica etching, suggesting effective removal of the silica layer. The adsorption of MB on ZnS:Mn^{2+} nanocrystals was further confirmed through FTIR analysis of the nanocrystal-MB mixture, collected after reaching adsorption-desorption equilibrium. The characteristic peaks at 1600 cm^{-1} (peak a, $\text{CH}=\text{N}$), 1388–1335 cm^{-1} (peak b,c, C-H), 1253 cm^{-1} (-C-N),

1153 cm^{-1} (C-N), and 1064 cm^{-1} (C-S-C) correspond to vibrations from MB, consistent with the FTIR spectrum of pure MB (Figure S13). The successful adsorption of these dyes on the nanocrystal surface is a critical factor contributing to the enhanced catalytic performance of the ZnS-based nanocatalysts.

The UV-Vis spectra of MB during piezocatalytic degradation using silica-coated ZnS:3%Mn²⁺ nanocrystals are shown in Figure S14. The degradation rate constant for silica-coated ZnS:3%Mn²⁺ was calculated to be 0.0597 min^{-1} , significantly lower than that for silica-etched nanocatalysts. This result suggests that the presence of a silica layer is detrimental to the piezocatalytic degradation of organic dyes. A plausible explanation is that after undergoing high-temperature calcination, the silica layer increased its crosslinking degree and reduced its porosity [39], inhibiting effective piezocatalysis.

We also measured the piezocatalytic degradation of a binary dye mixture of MB and RhB with the same initial concentration using ZnS:3%Mn²⁺ nanocrystals. Figure 4b shows the UV-Vis spectra of the dye mixture during sonication for 30 min, with measurements taken at 10-min intervals. Figure 4c presents the degradation rates for RhB (0.0765 min^{-1}) and MB (0.0582 min^{-1}), respectively, as derived from linear fitting. RhB degraded faster than MB in the dye mixture, likely due to their different molecular orbital energy levels, which may facilitate electron transfer from MB to RhB [28].

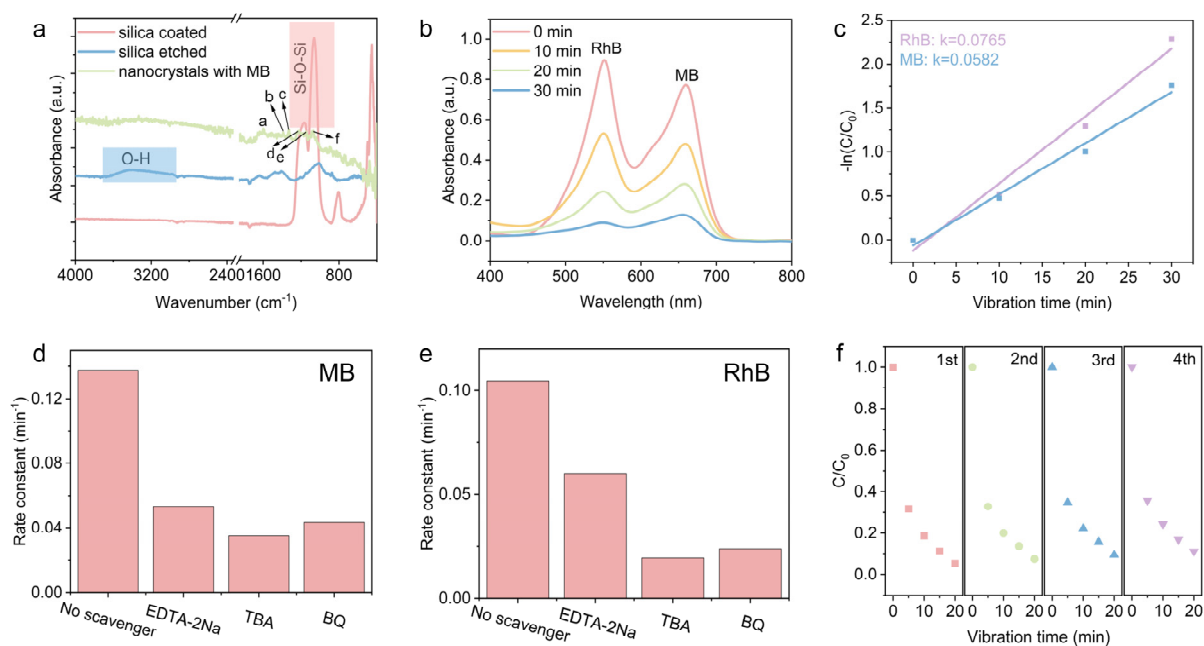


Figure 4. (a) FTIR spectra of silica-coated and silica-etched ZnS:3%Mn²⁺ nanocrystals. (b) The UV-Vis spectra of RhB and MB binary dye mixture during piezocatalytic degradation by ZnS:3%Mn²⁺. (c) The degradation rate for RhB and MB by linear fitting. (d) The kinetics of MB degradation with and without scavengers. (e) The kinetics of RhB degradation with and without scavengers. (f) The recyclability tests of ZnS:Mn²⁺ nanocrystal piezocatalysts.

To further verify the mechanism behind the piezocatalytic degradation of organic molecules, scavengers were introduced into the reaction system to assess their impact on the catalytic performance, including ethylenediaminetetraacetic acid disodium salt (EDTA-2Na) as a hole (h^+) scavenger, tert-butyl alcohol (TBA) as a $\cdot\text{OH}$ radical scavenger, and benzoquinone (BQ) as a $\cdot\text{O}_2^-$ radical scavenger. These scavengers were added to the reaction system containing ZnS:3%Mn²⁺ nanocrystals and organic dye molecules of MB or RhB. The UV-Vis spectra of MB during piezocatalytic degradation by ZnS:3%Mn²⁺ nanocrystals with EDTA-2Na, TBA, and BQ scavengers are shown in Figure S15a–c, respectively. The degradation kinetics were linearly fitted, yielding rate constants of 0.0533, 0.0351, and 0.0436 min^{-1} for EDTA-2Na, TBA, and BQ, respectively, as presented in Figure S15d–f. These kinetic values are summarized and compared in Figure 4d. Similarly, the UV-Vis spectra of RhB during piezocatalytic degradation in the presence of EDTA-2Na, TBA, and BQ are depicted in Figure S16a–c. The corresponding degradation rates were linearly fitted and found to be 0.0601, 0.0192, and 0.0239 min^{-1} for EDTA-2Na, TBA, and BQ, respectively, as illustrated in Figure S16d–f. These results are compared in Figure 4e. The significant reduction in degradation rates upon the addition of these scavengers supports the involvement of holes, hydroxyl radicals, and superoxide radicals in the piezocatalytic degradation process, further confirming the role of reactive oxygen species in the catalytic reaction.

The reusability of the Mn-doped ZnS piezocatalysts was evaluated through multiple catalytic cycles. As shown in Figure 4f, the relative concentration of MB (C/C_0) was monitored over four consecutive cycles using recycled ZnS:3%Mn²⁺ nanocrystals. Only slight decline in degradation efficiency was observed after four cycles, indicating high stability in catalytic activity, possibly due to the refillable trap states and stable crystal structure of the nanocrystals. Overall, the ZnS:3%Mn²⁺ nanocrystals exhibit substantial retention of their piezocatalytic performance, underscoring their potential for practical applications where catalyst reusability is essential.

The ZnS:3%Mn²⁺ nanocrystals synthesized in this study demonstrate exceptional piezocatalytic performance, outperforming many existing piezocatalysts such as BaTiO₃ [41], ZnO [42], metal dichalcogenides (MoS₂, WS₂, and WSe₂) [43] and BiFeO₃ [44,45], as shown in the comparison in Table 1. This enhanced performance can be primarily attributed to two key factors: the unique electron filling-detrapping mechanism enabled by UV pre-excitation and ultrasonic vibration, as well as the intrinsically high piezoelectricity of the nanocrystals. TEM images (Figures 1e and S4a) reveal a significant presence of stacking faults within the ZnS nanocrystals. These stacking faults are believed to greatly enhance the piezoelectric properties of the nanocrystals by inducing spontaneous polarization [46], consistent with the high piezoelectric coefficient (d_{33}) values measured via PFM. This piezoelectric enhancement is particularly advantageous for piezocatalysis, as it facilitates effective charge separation under mechanical vibrations, thereby generating more reactive radicals for the degradation of pollutants.

Table 1. Comparison of degradation rates for various piezocatalysts under ultrasonic vibrations.

Catalyst	Dye Species	Rate Constant (min ^{−1})	Reference
BaTiO ₃ nanowires	Methylene orange	~0.017	[41]
BaTiO ₃ nanocrystals	Methylene orange	0.019	[10]
	RhB	0.009	
	MB	~0.007	
(Ba,Sr)TiO ₃ nanowires	Methylene orange	0.0196	[15]
ZnO nanoparticles	MB	0.02487	[42]
MoS ₂			[43]
WS ₂	RhB	0.047	[43]
WSe ₂	RhB	0.023	[43]
BiFeO ₃	RhB	0.017	[44]
BiFeO ₃ /PVDF-TrFE	RhB	0.0143	[45]
ZnS:3%Mn ²⁺ (UV pre-excited)	MB	0.1376	This work
	RhB	0.1048	

We believe that the piezoelectric enhancement of ZnS:Mn²⁺ nanocrystals benefits from their dual-defect structure, which comprises both point defects resulting from Mn²⁺ doping and planar stacking faults generated during the sintering of the clusters. The point defects create numerous trap states within the bandgap, capable of storing photo-excited charge carriers that are essential for initiating subsequent piezocatalytic reactions. Meanwhile, the stacking faults likely enhance the piezoelectric effect by promoting spontaneous polarization and promote electron transport to the surface for chemical reactions [47,48]. These defects can efficiently inhibit charge carrier recombination, transforming ZnS:Mn²⁺ from a well-known luminescent material into active piezocatalysts [49–53]. We believe these two types of defects may work synergistically to not only maximize the generation of reactive oxygen species but also ensure a more sustainable and repeatable piezocatalytic process, making these nanocrystals highly promising for practical applications in environmental remediation and other catalytic fields.

3. Conclusion

We have successfully synthesized ZnS:Mn²⁺ nanocrystals with exceptional piezocatalytic performance for the degradation of organic pollutants. Our flexible synthesis method allows for precise tuning of the Mn²⁺ doping ratio, resulting in optimal piezocatalytic activity at 3% Mn²⁺ doping. This composition achieved a degradation rate of 0.1376 min^{−1} for methylene blue and 0.1048 min^{−1} for rhodamine B under ultrasonic vibrations. A distinctive advantage of this piezocatalyst is its significantly enhanced degradation efficiency when pre-excited with UV light prior to sonication. In-depth investigations revealed that the catalytic process is mediated by reactive oxygen species, including hydroxyl and superoxide radicals, generated under ultrasonic vibrations. The superior performance is attributed to the synergistic effects of two types of defects within the nanocrystals: Mn-induced point defects that facilitate efficient charge separation and stacking faults that enhance piezoelectricity. These

combined effects substantially boost piezocatalytic activity, positioning the doped-ZnS nanocrystals as promising catalysts for environmental remediation and broader catalytic applications.

Supplementary Materials: The Supplementary Materials can be downloaded at: <https://www.sciltp.com/journals/mi/2024/1/552/s1>, and accessed free of charge. Figure S1. (a) The TEM image of ZnS:3%Mn²⁺ QDs; (b) The particle size distribution of ZnS:3%Mn²⁺ QDs; (c) The TEM image of ZnS QDs; (d) The TEM image of ZnS:1%Mn²⁺ QDs. Figure S2. The size distribution of ZnS:3%Mn²⁺ QD assemblies. Figure S3. The thickness distribution of the silica layer around the QD assemblies. Figure S4. (a) The TEM image of silica-etched ZnS:3%Mn²⁺ nanocrystals; (b) The particle size distribution of silica-etched ZnS:3%Mn²⁺ nanocrystals. Figure S5. The PFM response amplitude of ZnS:3%Mn²⁺ nanocrystals under the voltage of 3 V. Figure S6. (a) The UV-Vis spectra of MB after stirring with ZnS:3%Mn²⁺ nanocrystals for different durations; (b) The concentration ratio (C/C₀) during the stirring. Figure S7. The UV-Vis spectra of MB solution before and after exposing the MB-nanocrystal mixture to 365-nm UV light for 1 min. Figure S8. The UV-Vis spectra of MB during piezocatalytic degradation using 0%Mn²⁺ (a), 0.5%Mn²⁺ (b), 1%Mn²⁺ (c), 2%Mn²⁺ (d), 4%Mn²⁺ (e). Figure S9. The UV-Vis spectra of RhB during piezocatalytic degradation using 0%Mn²⁺ (a), 0.5%Mn²⁺ (b), 1%Mn²⁺ (c), 2%Mn²⁺ (d), 4%Mn²⁺ (e). Figure S10. The UV-Vis spectra of MB (a) and RhB (b) during sonication for up to 40 min. Figure S11. (a) The UV-Vis spectra of MB during degradation without UV pre-excitation; (b) The corresponding linear fitting of -ln(C/C₀) vs. vibration time plot. Figure S12. The UV-Vis spectra of MB during piezocatalytic degradation with UV pre-excitation for different durations. Figure S13. The FTIR spectrum of pure MB. The peaks labeled as (a): 1600 cm⁻¹ (CH=N); (b,c): 1388–1335 cm⁻¹ (C-H); (d): 1253 cm⁻¹ (-C-N); (e): 1153 cm⁻¹ (C-N); (f): 1064 cm⁻¹ (C-S-C). Figure S14. The UV-Vis spectra of MB during piezocatalytic degradation with silica coating around the ZnS:3%Mn²⁺ nanocrystals. Figure S15. The UV-Vis spectra of MB during piezocatalytic degradation with the addition of scavengers: EDTA-2Na (a), TBA (b), BQ (c). The linear fitting of -ln(C/C₀) vs. vibration time plot for MB during piezocatalytic degradation with the addition of scavengers: EDTA-2Na (d), TBA (e), BQ (f). Figure S16. The UV-Vis spectra of RhB during piezocatalytic degradation with the addition of scavengers: EDTA-2Na (a), TBA (b), BQ (c). The linear fitting of -ln(C/C₀) vs. vibration time plot for RhB during piezocatalytic degradation with the addition of scavengers: EDTA-2Na (d), TBA (e), BQ (f).

Author Contributions: Z.W. and Y.Y. conceptualized the project. Y.Y. and J.N. supervised the project. Z.W., Y.T. and E.T. conducted the experiments. Z.W. drafted the manuscript, and all authors contributed to revising it. All authors have read and agreed to the published version of the manuscript.

Funding: Research reported in this publication was supported by the National Eye Institute of the National Institutes of Health under Award Number R21EY034806. The content is solely the responsibility of the authors and does not necessarily represent the official views of the National Institutes of Health. E. T. and M. C. would like to acknowledge the support from the U.S. DOE, Office of Science, Basic Energy Sciences, Materials Sciences, and Engineering Division. Microscopy was conducted at the Center for Nanophase Materials Sciences (CNMS), a US DOE, Office of Science User Facility at Oak Ridge National Laboratory.

Data Availability Statement: The data that support the findings of this study are available from the corresponding authors upon reasonable request.

Conflicts of Interest: The authors declare no conflict of financial interest.

References

1. Zhang, Q.; Lima, D.Q.; Lee, I.; Zaera, F.; Chi, M.; Yin, Y. A highly active titanium dioxide based visible-light photocatalyst with nonmetal doping and plasmonic metal decoration. *Angew. Chem. Int. Ed. Engl.* **2011**, *50*, 7088–7092.
2. Joo, J.B.; Zhang, Q.; Dahl, M.; Lee, I.; Goebel, J.; Zaera, F.; Yin, Y. Control of the nanoscale crystallinity in mesoporous TiO₂ shells for enhanced photocatalytic activity. *Energy Environ. Sci.* **2012**, *5*, 6321–6327.
3. Liu, H.; Joo, J.B.; Dahl, M.; Fu, L.; Zeng, Z.; Yin, Y. Crystallinity control of TiO₂ hollow shells through resin-protected calcination for enhanced photocatalytic activity. *Energy Environ. Sci.* **2015**, *8*, 286–296.
4. Berenguer, R.; Sieben, J.M.; Quijada, C.; Morallón, E. Electrocatalytic degradation of phenol on Pt- and Ru-doped Ti/SnO₂-Sb anodes in an alkaline medium. *Appl. Catal. B Environ.* **2016**, *199*, 394–404.
5. Du, X.; Oturan, M.A.; Zhou, M.; Belkessa, N.; Su, P.; Cai, J.; Trellu, C.; Mousset, E. Nanostructured electrodes for electrocatalytic advanced oxidation processes: From materials preparation to mechanisms understanding and wastewater treatment applications. *Appl. Catal. B Environ.* **2021**, *296*, 120332.
6. Yan, Q.; Zhang, J.; Xing, M. Cocatalytic Fenton Reaction for Pollutant Control. *Cell Rep. Phys. Sci.* **2020**, *1*, 100149.
7. Wang, Z.; Yin, Y. Upcycling sludge into high-performance catalysts. *Nat. Water* **2024**, *2*, 620–621.
8. Yan, Q.; Lian, C.; Huang, K.; Liang, L.; Yu, H.; Yin, P.; Zhang, J.; Xing, M. Constructing an Acidic Microenvironment by MoS₂ in Heterogeneous Fenton Reaction for Pollutant Control. *Angew. Chem. Int. Ed. Engl.* **2021**, *60*, 17155–17163.
9. Wu, J.M.; Chang, W.E.; Chang, Y.T.; Chang, C.K. Piezo-Catalytic Effect on the Enhancement of the Ultra-High Degradation Activity in the Dark by Single- and Few-Layers MoS₂ Nanoflowers. *Adv. Mater.* **2016**, *28*, 3718–3725.
10. Wu, J.; Xu, Q.; Lin, E.; Yuan, B.; Qin, N.; Thatikonda, S.K.; Bao, D. Insights into the Role of Ferroelectric Polarization in Piezocatalysis of Nanocrystalline BaTiO₃. *ACS Appl. Mater. Interfaces* **2018**, *10*, 17842–17849.
11. Tu, S.; Guo, Y.; Zhang, Y.; Hu, C.; Zhang, T.; Ma, T.; Huang, H. Piezocatalysis and Piezo-Photocatalysis: Catalysts Classification and Modification Strategy, Reaction Mechanism, and Practical Application. *Adv. Funct. Mater.* **2020**, *30*, 2005158.

12. Meng, N.; Liu, W.; Jiang, R.; Zhang, Y.; Dunn, S.; Wu, J.; Yan, H. Fundamentals, advances and perspectives of piezocatalysis: A marriage of solid-state physics and catalytic chemistry. *Progress. Mater. Sci.* **2023**, *138*, 101161.
13. Shi, H.; Liu, Y.; Bai, Y.; Lv, H.; Zhou, W.; Liu, Y.; Yu, D.-G. Progress in defect engineering strategies to enhance piezoelectric catalysis for efficient water treatment and energy regeneration. *Sep. Purif. Technol.* **2024**, *330*, 125247.
14. Tian, W.; Han, J.; Wan, L.; Li, N.; Chen, D.; Xu, Q.; Li, H.; Lu, J. Enhanced piezocatalytic activity in ion-doped SnS₂ via lattice distortion engineering for BPA degradation and hydrogen production. *Nano Energy* **2023**, *107*, 108165.
15. Yuan, B.; Wu, J.; Qin, N.; Lin, E.; Bao, D. Enhanced Piezocatalytic Performance of (Ba,Sr)TiO₃ Nanowires to Degrade Organic Pollutants. *ACS Appl. Nano Mater.* **2018**, *1*, 5119–5127.
16. Chen, L.; Jia, Y.; Zhao, J.; Ma, J.; Wu, Z.; Yuan, G.; Cui, X. Strong piezocatalysis in barium titanate/carbon hybrid nanocomposites for dye wastewater decomposition. *J. Colloid. Interface Sci.* **2021**, *586*, 758–765.
17. Kalhori, H.; Amaechi, I.C.; Youssef, A.H.; Ruediger, A.; Pignolet, A. Catalytic Activity of BaTiO₃ Nanoparticles for Wastewater Treatment: Piezo- or Sono-Driven? *ACS Appl. Nano Mater.* **2023**, *6*, 1686–1695.
18. Feng, W.; Yuan, J.; Zhang, L.; Hu, W.; Wu, Z.; Wang, X.; Huang, X.; Liu, P.; Zhang, S. Atomically thin ZnS nanosheets: Facile synthesis and superior piezocatalytic H₂ production from pure H₂O. *Appl. Catal. B: Environ.* **2020**, *277*, 119250.
19. Liu, W.; Fu, P.; Zhang, Y.; Xu, H.; Wang, H.; Xing, M. Efficient hydrogen production from wastewater remediation by piezoelectricity coupling advanced oxidation processes. *Proc. Natl. Acad. Sci. USA* **2023**, *120*, e2218813120.
20. Zhang, M.; Zhao, S.; Zhao, Z.; Li, S.; Wang, F. Piezocatalytic Effect Induced Hydrogen Production from Water over Non-noble Metal Ni Deposited Ultralong GaN Nanowires. *ACS Appl. Mater. Interfaces* **2021**, *13*, 10916–10924.
21. Chen, S.; Zhu, P.; Mao, L.; Wu, W.; Lin, H.; Xu, D.; Lu, X.; Shi, J. Piezocatalytic Medicine: An Emerging Frontier using Piezoelectric Materials for Biomedical Applications. *Adv. Mater.* **2023**, *35*, e2208256.
22. Wang, Y.; Wen, X.; Jia, Y.; Huang, M.; Wang, F.; Zhang, X.; Bai, Y.; Yuan, G.; Wang, Y. Piezo-catalysis for nondestructive tooth whitening. *Nat. Commun.* **2020**, *11*, 1328.
23. Wang, Y.; Zang, P.; Yang, D.; Zhang, R.; Gai, S.; Yang, P. The fundamentals and applications of piezoelectric materials for tumor therapy: Recent advances and outlook. *Mater. Horiz.* **2023**, *10*, 1140–1184.
24. Cafarelli, A.; Marino, A.; Vannozzi, L.; Puigmarti-Luis, J.; Pane, S.; Ciofani, G.; Ricotti, L. Piezoelectric Nanomaterials Activated by Ultrasound: The Pathway from Discovery to Future Clinical Adoption. *ACS Nano* **2021**, *15*, 11066–11086.
25. Polonini, H.C.; Brandao, H.M.; Raposo, N.R.; Mouton, L.; Yepremian, C.; Couto, A.; Brayner, R. Ecotoxicological studies of micro- and nanosized barium titanate on aquatic photosynthetic microorganisms. *Aquat. Toxicol.* **2014**, *154*, 58–70.
26. Ahamed, M.; Akhtar, M.J.; Khan, M.A.M.; Alhadlaq, H.A.; Alshamsan, A. Barium Titanate (BaTiO₃) Nanoparticles Exert Cytotoxicity through Oxidative Stress in Human Lung Carcinoma (A549) Cells. *Nanomater.* **2020**, *10*, 2309.
27. Wang, Z.; Tai, Y.; Nam, J.; Yin, Y. Calcination-Induced Transformation of ZnS:Mn²⁺ Nanorods to Microparticles for Enhanced Mechanoluminescence. *Chem. Mater.* **2023**, *35*, 6845–6852.
28. Wang, Z.; Tai, Y.; Ye, Z.; Nam, J.; Yin, Y. Integration of ZnS:Mn²⁺ Microparticles into Electrospun PVDF-Based Nanofibers for Enhanced Mechanoluminescence. *Adv. Funct. Mater.* **2024**, 2410358. <https://doi.org/10.1002/adfm.202410358>.
29. Kumara, C.; Armstrong, B.; Lyo, I.; Lee, H.W.; Qu, J. Organic-modified ZnS nanoparticles as a high-performance lubricant additive. *RSC Adv.* **2023**, *13*, 7009–7019.
30. Joo, J.; Na, H.B.; Yu, T.; Yu, J.H.; Kim, Y.W.; Wu, F.; Zhang, J.Z.; Hyeon, T. Generalized and Facile Synthesis of Semiconducting Metal Sulfide Nanocrystals. *J. Am. Chem. Soc.* **2003**, *125*, 11100–11105.
31. Bai, F.; Wang, D.; Huo, Z.; Chen, W.; Liu, L.; Liang, X.; Chen, C.; Wang, X.; Peng, Q.; Li, Y. A Versatile Bottom-up Assembly Approach to Colloidal Spheres from Nanocrystals. *Angew. Chem. Int. Ed.* **2007**, *119*, 6770–6773.
32. Stöber, W.; Fink, A.; Bohn, E. Controlled growth of monodisperse silica spheres in the micron size range. *J. Colloid. Interface Sci.* **1968**, *26*, 62–69.
33. Ma, L.; Amador, E.; Belev, G.S.; Gautam, C.; Zhou, W.; Liu, J.P.; Sammynaiken, R.; Chen, W. Tuning Ag⁺ and Mn²⁺ doping in ZnS:Ag,Mn embedded polymers for flexible white light emitting films. *Soft Sci.* **2024**, *4*, 10.
34. Mukhina, M.V.; Tresback, J.; Ondry, J.C.; Akey, A.; Alivisatos, A.P.; Kleckner, N. Single-Particle Studies Reveal a Nanoscale Mechanism for Elastic, Bright, and Repeatable ZnS:Mn Mechanoluminescence in a Low-Pressure Regime. *ACS Nano* **2021**, *15*, 4115–4133.
35. Wu, X.; Zhu, X.; Chong, P.; Liu, J.; Andre, L.N.; Ong, K.S.; Brinson, K. Jr.; Mahdi, A.I.; Li, J.; Fenno, L.E.; et al. Sono-optogenetics facilitated by a circulation-delivered rechargeable light source for minimally invasive optogenetics. *Proc. Natl. Acad. Sci. USA* **2019**, *116*, 26332–26342.
36. Zhang, Y.; Zhang, N.; Tang, Z.-R.; Xu, Y.-J. Transforming CdS into an efficient visible light photocatalyst for selective oxidation of saturated primary C–H bonds under ambient conditions. *Chem. Sci.* **2012**, *3*, 2812.
37. Zhao, D.; Sheng, G.; Chen, C.; Wang, X. Enhanced photocatalytic degradation of methylene blue under visible irradiation on graphene@TiO₂ dyade structure. *Appl. Catal. B Environ.* **2012**, *111–112*, 303–308.

38. Clément, J.-L.; Ferré, N.; Siri, D.; Karoui, H.; Rockenbauer, A.; Tordo, P. Assignment of the EPR Spectrum of 5,5-Dimethyl-1-pyrroline N-Oxide (DMPO) Superoxide Spin Adduct. *J. Org. Chem.* **2005**, *70*, 1198–1203.
39. Asgar, H.; Semeykina, V.; Hunt, M.; Mohammed, S.; Kuzmenko, I.; Zharov, I.; Gadikota, G. Thermally-Induced morphological evolution of spherical silica nanoparticles using in-operando X-ray scattering measurements. *Colloids Surf. A Physicochem. Eng. Asp.* **2020**, *586*, 124260.
40. Sharma, S.; Khare, N. Hierarchical Bi₂S₃ nanoflowers: A novel photocatalyst for enhanced photocatalytic degradation of binary mixture of Rhodamine B and Methylene blue dyes and degradation of mixture of p-nitrophenol and p-chlorophenol. *Adv. Powder Technol.* **2018**, *29*, 3336–3347.
41. Wu, J.; Qin, N.; Bao, D. Effective enhancement of piezocatalytic activity of BaTiO₃ nanowires under ultrasonic vibration. *Nano Energy* **2018**, *45*, 44–51.
42. Alshehri, A.A.; Malik, M.A. Biogenic fabrication of ZnO nanoparticles using *Trigonella foenum-graecum* (Fenugreek) for proficient photocatalytic degradation of methylene blue under UV irradiation. *J. Mater. Sci. Mater. Electron.* **2019**, *30*, 16156–16173.
43. Li, S.; Zhao, Z.; Yu, D.; Zhao, J.-Z.; Su, Y.; Liu, Y.; Lin, Y.; Liu, W.; Xu, H.; Zhang, Z. Few-layer transition metal dichalcogenides (MoS₂, WS₂, and WSe₂) for water splitting and degradation of organic pollutants: Understanding the piezocatalytic effect. *Nano Energy* **2019**, *66*, 104083.
44. Mushtaq, F.; Chen, X.; Hoop, M.; Torlakcik, H.; Pellicer, E.; Sort, J.; Gattinoni, C.; Nelson, B.J.; Pane, S. Piezoelectrically Enhanced Photocatalysis with BiFeO(3) Nanostructures for Efficient Water Remediation. *iScience* **2018**, *4*, 236–246.
45. Amdouni, W.; Fricaudet, M.; Otonicar, M.; Garcia, V.; Fusil, S.; Kreisel, J.; Maghraoui-Meherzi, H.; Dkhil, B. BiFeO(3) Nanoparticles: The “Holy-Grail” of Piezo-Photocatalysts? *Adv. Mater.* **2023**, *35*, e2301841.
46. Corfdir, P.; Hauswald, C.; Zettler, J.K.; Flissikowski, T.; Lähnemann, J.; Fernández-Garrido, S.; Geelhaar, L.; Grahn, H.T.; Brandt, O. Stacking faults as quantum wells in nanowires: Density of states, oscillator strength, and radiative efficiency. *Phys. Rev. B* **2014**, *90*, 195309.
47. Wang, Y.; Wang, T.; Arandiyán, H.; Song, G.; Sun, H.; Sabri, Y.; Zhao, C.; Shao, Z.; Kawi, S. Advancing Catalysts by Stacking Fault Defects for Enhanced Hydrogen Production: A Review. *Adv. Mater.* **2024**, *36*, e2313378.
48. Sebti, E.; Evans, H.A.; Chen, H.; Richardson, P.M.; White, K.M.; Giovine, R.; Koirala, K.P.; Xu, Y.; Gonzalez-Correa, E.; Wang, C.; et al. Stacking Faults Assist Lithium-Ion Conduction in a Halide-Based Superionic Conductor. *J. Am. Chem. Soc.* **2022**, *144*, 5795–5811.
49. Moreno, H.; Domingues, G.L.; Assis, M.; Ortega, P.P.; Mastelaro, V.R.; Ramirez, M.A.; Simoes, A.Z. The Relationship between Photoluminescence Emissions and Photocatalytic Activity of CeO(2) Nanocrystals. *Inorg. Chem.* **2023**, *62*, 4291–4303.
50. Pinatti, I.M.; Tello, A.C.M.; Pereira, P.F.S.; Trench, A.B.; Teodoro, M.D.; Rosa, I.L.V.; da Silva, A.B.F.; Longo, E.; Andres, J.; Simoes, A.Z. Towards a relationship between photoluminescence emissions and photocatalytic activity of Ag(2)SeO(4): Combining experimental data and theoretical insights. *Dalton Trans.* **2022**, *51*, 11346–11362.
51. Ang, E.H.; Zeng, J.; Subramanian, G.S.; Chellappan, V.; Sudhaharan, T.; Padmanabhan, P.; Gulyás, B.; Tamil Selvan, S. Silica-Coated Mn-Doped ZnS Nanocrystals for Cancer Theranostics. *ACS Appl. Nano Mater.* **2020**, *3*, 3088–3096.
52. Dai, L.; Strelow, C.; Kipp, T.; Mews, A.; Benkenstein, I.; Eifler, D.; Vuong, T.H.; Rabeah, J.; McGettrick, J.; Lesyuk, R.; et al. Colloidal Manganese-Doped ZnS Nanoplatelets and Their Optical Properties. *Chem. Mater.* **2020**, *33*, 275–284.
53. Liu, H.; Zheng, Y.; Liu, S.; Zhao, J.; Song, Z.; Peng, D.; Liu, Q. Realizing Red Mechanoluminescence of ZnS:Mn²⁺ Through Ferromagnetic Coupling. *Adv. Funct. Mater.* **2024**, *34*, 2314422.

Article

Cathodic Corrosion-Induced Structural Evolution of CuNi Electrocatalysts for Enhanced CO₂ Reduction

Wenjin Sun ^{1,†}, Bokki Min ^{2,†}, Maoyu Wang ³, Xue Han ⁴, Qiang Gao ¹, Sooyeon Hwang ⁵, Hua Zhou ³, and Huiyuan Zhu ^{1,2,*}

¹ Department of Chemistry, University of Virginia, Charlottesville, VA 22904, USA

² Department of Chemical Engineering, University of Virginia, Charlottesville, VA 22904, USA

³ Advanced Photon Source, Argonne National Laboratory, Lemont, IL 60439, USA

⁴ Department of Chemical Engineering, Virginia Polytechnic Institute and State University, Blacksburg, VA 24061, USA

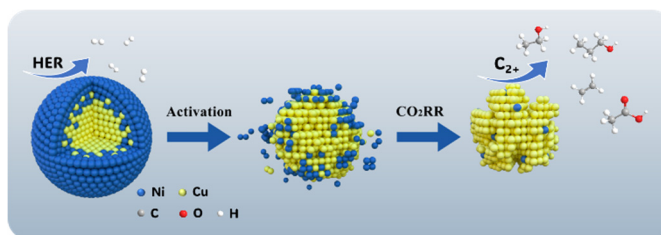
⁵ Center for Functional Nanomaterials, Brookhaven National Laboratory, Upton, NY 11973, USA

* Correspondence: kks8js@virginia.com

† These authors contributed equally to this work.

Received: 22 October 2024; Revised: 25 November 2024; Accepted: 27 November 2024; Published: 4 December 2024

Abstract: The electrochemical CO₂ reduction reaction (CO₂RR) has attracted significant attention as a promising strategy for storing intermittent energy in chemical bonds while sustainably producing value-added chemicals and fuels. Copper-based bimetallic catalysts are particularly appealing for CO₂RR due to their unique ability to generate multi-carbon products. While substantial effort has been devoted to developing new catalysts, the evolution of bimetallic systems under operational conditions remains underexplored. In this work, we synthesized a series of Cu_xNi_{1-x} nanoparticles and investigated their structural evolution during CO₂RR. Due to the higher oxophilicity of Ni compared to Cu, the particles tend to become Ni-enriched at the surface upon air exposure, promoting the competing hydrogen evolution reaction (HER). At negative activation potentials, cathodic corrosion has been observed in Cu_xNi_{1-x} nanoparticles, leading to the significant Ni loss and the formation of irregularly shaped Cu nanoparticles with increased defects. This structural evolution, driven by cathodic corrosion, shifts the electrolysis from HER toward CO₂ reduction, significantly enhancing the Faradaic efficiency of multi-carbon products (C₂₊).



Keywords: electrochemical CO₂ reduction; bimetallic; nanoparticles; cathodic corrosion; structural evolution

1. Introduction

With the rapid rise in CO₂ emissions and growing global energy demand, the electrochemical CO₂ reduction reaction (CO₂RR) has attracted widespread interest as a promising strategy to close the carbon cycle by converting CO₂ into valuable chemicals and fuels [1–3]. Extensive research has been devoted to CO₂RR catalysts in recent years, particularly Cu-based catalysts, which exhibit a unique ability to convert CO₂ into multi-carbon products, such as C₂H₄, C₂H₅OH, and C₃H₇OH. These multi-carbon products offer higher energy density and greater market value compared to single-carbon products [4–8]. This unique property is closely associated with the moderate *CO adsorption energy on Cu, which balances the activation of CO₂ and the subsequent hydrogenation of *CO intermediate [5,9]. However, Cu still faces challenges such as poor selectivity, high overpotential, and competition from the hydrogen evolution reaction (HER) [10,11]. To overcome these limitations, various strategies—such as alloying [12–14], tuning the oxidation state [15,16], and surface/interface modification [17,18]—have been explored to modulate the physicochemical properties of Cu.

Constructing bimetallic catalysts has emerged as an effective strategy for improving CO₂RR performance by harnessing the synergistic effects between Cu and a secondary metal [13,19,20]. For instance, AgCu bimetallic catalysts employ a tandem catalysis strategy, where the reaction is partitioned into distinct steps, each facilitated by different catalytic sites [21,22]. Additionally, the compressive strain exerted on Cu by the CuAg surface alloy exemplifies the bimetallic synergistic effect in CO₂RR. This strain reduces the surface coverage of adsorbed



Copyright: © 2024 by the authors. This is an open access article under the terms and conditions of the Creative Commons Attribution (CC BY) license (<https://creativecommons.org/licenses/by/4.0/>).

Publisher's Note: Scilight stays neutral with regard to jurisdictional claims in published maps and institutional affiliations

hydrogen (*H) and decreases oxophilicity, thereby improving catalytic performance [23]. Alloying can also refine catalytic performance. The Cu-Ni alloy, for instance, exhibits synergistic Cu-Ni active sites that increase *H coverage, facilitating the hydrogenation of adsorbed *CO into C₁ products. This leads to a gradual shift from the production of CO and C₂ species toward an increased formation of CH₄ and HCOO[−] [14].

While numerous Cu-based bimetallic catalysts have been studied, maintaining their structural stability under CO₂RR conditions remains a significant challenge [24,25]. The application of potential bias, along with exposure to electrolytes, CO₂, and reaction intermediates, can induce substantial changes in catalyst structures. These changes, often involving atomic rearrangement or alterations in chemical states [26], ultimately lead to the reconstruction of active sites [9,27,28], which can significantly impact catalytic performance. Unfortunately, the dynamic evolution of bimetallic systems is often overlooked, resulting in a limited fundamental understanding of the true nature of the active sites. For example, polycrystalline Cu electrodes undergo facet evolution through stepwise surface reconstruction, initially forming Cu (111) within the first 30 min, followed by a transition to Cu (100) after an additional 30 min [29]. Cu is also prone to spontaneous oxidation in air and reduction under cathodic potential. The presence of Cu⁺ and subsurface oxygen atoms is believed to contribute to the enhanced catalytic performance of oxide-derived (OD)-Cu [30]. Subsurface oxygen can improve *CO adsorption and promote subsequent C-C coupling; however, the precise nature and dynamic evolution of the true active sites remains elusive [16]. Using in-situ and *operando* techniques, Vavra et al. observed that during the startup phase, dissolution and redeposition occur on the surface of Cu, resulting in an increase in particle size and changes in morphology, with Cu oxides playing a crucial role in this process [31]. Beyond redox reactions, Cu's high mobility under working conditions can result in leaching from electrodes. Chen et al. synthesized intermixed and phase-segregated AgCu nanoparticles (NPs) and found that both types evolved into structures with two distinct phases due to Cu's high mobility and poor Ag-Cu compatibility [32]. Another example is the Cu-Zn system, where cationic Zn species are reduced during the reaction, forming a CuZn alloy, which shifts selectivity from CH₄ (over Cu-ZnO) to CO (over the CuZn alloy) [33]. Overall, the dynamic evolution of Cu-based bimetallic catalysts is anticipated to be more complex than that of pure metals, involving morphological changes, structural reconstruction, and variations in chemical state. This complexity arises from the competitive and coexisting processes of redox reactions, dissolution, and redeposition of multiple metal species.

In this work, we investigated the structural evolution of bimetallic Cu_xNi_{1−x} NPs with tunable composition under CO₂RR operating conditions. Our results reveal that these bimetallic catalysts undergo cathodic corrosion in CO₂RR, shifting selectivity from H₂ evolution to CO₂ reduction. Prior to cathodic activation, these catalysts exhibited a Ni-enriched surface due to Ni's high oxophilicity, resulting in over 90% Faradaic efficiency (FE) for H₂. Upon cathodic activation, the catalysts underwent surface reconstruction and changes in oxidation state, with Ni leaching out due to cathodic corrosion at working potentials, while Cu was simultaneously reduced. This process results in a roughened surface that exposed more metallic Cu active sites (Figure 1a), significantly enhancing the selectivity for multi-carbon products. By tuning the Cu and Ni composition and optimizing the cathodic activation steps, we found that Cu_xNi_{1−x} with a precursor ratio of Cu_{0.71}Ni_{0.29} achieved the highest C₂₊ FE of 42.5% at −1.4 V_{RHE} (reversible hydrogen electrode, RHE), compared to 24.1% for pristine Cu at the same potential.

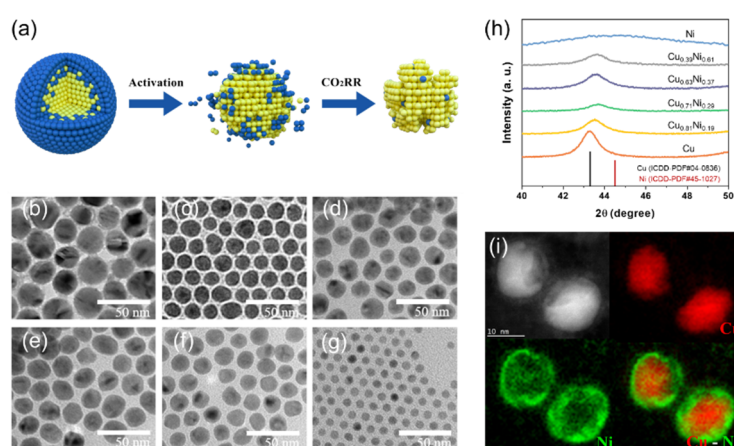


Figure 1. (a) Scheme of evolution behavior of Cu_xNi_{1−x} NPs upon cathodic corrosion and CO₂RR. TEM images of Cu_xNi_{1−x} NPs: (b) pure Cu, (c) Cu_{0.81}Ni_{0.19}, (d) Cu_{0.71}Ni_{0.29}, (e) Cu_{0.63}Ni_{0.37}, (f) Cu_{0.39}Ni_{0.61}, (g) pure Ni. (h) XRD patterns of Cu_xNi_{1−x} NPs. (i) The HAADF-STEM image and corresponding STEM-EELS elemental maps of Cu_{0.71}Ni_{0.29}.

2. Result and Discussion

2.1. Synthesis and Characterization of $\text{Cu}_x\text{Ni}_{1-x}$

A series of $\text{Cu}_x\text{Ni}_{1-x}$ NPs with varying Cu and Ni compositions were synthesized using a modified method [34], by adjusting the Ni precursor content (details provided in the Supporting Information). For comparison, pure Cu and Ni NPs were also synthesized using the same method. The composition of the as-synthesized $\text{Cu}_x\text{Ni}_{1-x}$ NPs was confirmed by inductively coupled plasma optical emission spectroscopy (ICP-OES) on a SPECTRO GENESIS ICP spectrometer (SPECTRO Analytical Instruments GmbH, Kleve, North Rhine-Westphalia, Germany) and designated as Cu, $\text{Cu}_{0.81}\text{Ni}_{0.19}$, $\text{Cu}_{0.71}\text{Ni}_{0.29}$, $\text{Cu}_{0.63}\text{Ni}_{0.37}$, $\text{Cu}_{0.39}\text{Ni}_{0.61}$, and Ni, respectively. Transmission electron microscope (TEM, Thermo Fisher Scientific, Waltham, MA, US) images (Figure 1b–g) reveal that the $\text{Cu}_x\text{Ni}_{1-x}$ exhibit a spherical shape and uniform morphology, with average sizes ranging from 15 nm to 25 nm. Pure Cu has the largest size (25.4 ± 6.0 nm), while Ni displays the smallest diameter (7.4 ± 1.3 nm). Particle size generally decreases with increasing Ni content (Figure S1 and Table S1). The X-ray Diffraction (XRD, Philips Analytical, Westborough, MA, US) patterns of all the samples are presented in Figure S2. As shown in the magnified region (Figure 1h), the Cu (111) peak in $\text{Cu}_x\text{Ni}_{1-x}$ gradually shifts from 43.3° to 44.5° with the incorporation of Ni, indicating a reduction in Cu lattice spacing [35]. The peak also broadens with increasing Ni content, consistent with the TEM results. Notably, due to Ni's higher oxophilicity compared to Cu, the $\text{Cu}_x\text{Ni}_{1-x}$ NPs tend to develop a Ni-enriched surface when stored under ambient conditions, as evidenced by the high-angle annular dark-field (HAADF) scanning transmission electron microscopy combined with electron energy loss spectroscopy (STEM-EELS, Hitachi, Tokyo, Japan) images and element mappings of $\text{Cu}_{0.71}\text{Ni}_{0.29}$ (Figure 1i).

2.2. Cathodic Activation of $\text{Cu}_x\text{Ni}_{1-x}$

Electrochemical experiments were conducted on all samples to assess their CO_2RR performance, with detailed procedures provided in the SI. Prior to CO_2RR , cathodic pre-treatment was employed to activate the working electrodes loaded with the as-synthesized NPs. Half of the electrodes were activated for 2 h at their optimal activation potential, while the untreated electrodes served as the control group. The difference in the CO_2RR between the activated and control groups was used to evaluate the impact of activation on catalytic performance. Cathodic activation was performed at various potentials in a conventional H-cell, with a Pt foil serving as the anode and Ag/AgCl as the reference electrode, while CO_2 was continuously bubbled at a rate of 10 sccm. Cyclic voltammetry (CV) was initially performed in Ar-saturated and subsequently in CO_2 -saturated solutions, with scans between $-1.4 \text{ V}_{\text{RHE}}$ and 0 V_{RHE} for 20 cycles at a scan rate of 20 mV/s to clean the surface of the electrocatalysts. For instance, CV cycles were performed on pure Cu electrode, and then the electrode activated at $-1.0 \text{ V}_{\text{RHE}}$ for 2 h under continuous CO_2 flow (10 sccm). After activation, CV was performed again in both Ar-saturated and CO_2 -saturated solutions. The treated electrode was then used for CO_2RR at potentials from $-1.0 \text{ V}_{\text{RHE}}$ to $-1.4 \text{ V}_{\text{RHE}}$, in 0.1 V intervals, with each potential step maintained for 1 h. This process was repeated for different activation potentials of $-1.1 \text{ V}_{\text{RHE}}$, $-1.2 \text{ V}_{\text{RHE}}$, and $-1.3 \text{ V}_{\text{RHE}}$ (Figure S3). Figure 2a,b illustrate the product distribution and corresponding FEs for pure Cu before and after activation at $-1.1 \text{ V}_{\text{RHE}}$ for 2 h. Notably, there is no substantial change in product distribution before and after activation. At the applied potential of $-1.0 \text{ V}_{\text{RHE}}$, the primary products of CO_2RR on pure Cu before activation are formate, H_2 , and CO, with FEs of 50.3%, 37.7%, and 4.8%, respectively (Figure 2a). At the same potential after activation, the FEs of these products are 51.4%, 41.8% and 5.2%, which are close to those observed prior activation. This indicates that cathodic activation had minimal effect on the catalytic performance of pure Cu. The C_{2+} FE summarized in Figure 2c further confirms the negligible effect of the activation treatment on pure Cu, with only a slight increase in C_{2+} FE from 20.0% to 24.1% at $-1.4 \text{ V}_{\text{RHE}}$ after activation, while the FEs of other products remain largely unchanged.

In contrast, $\text{Cu}_{0.71}\text{Ni}_{0.29}$ exhibits a high H_2 FE of over 90% at $-1.0 \text{ V}_{\text{RHE}}$ before activation, which can be attributed to surface enrichment with Ni, leading to a notably low FE for CO_2RR products (Figure 2d). Electrodes loaded with $\text{Cu}_{0.71}\text{Ni}_{0.29}$ were then activated at $-1.2 \text{ V}_{\text{RHE}}$, $-1.3 \text{ V}_{\text{RHE}}$, $-1.4 \text{ V}_{\text{RHE}}$, respectively. Taking the $-1.3 \text{ V}_{\text{RHE}}$ activation as an example, the HER after activation was significantly suppressed, with the FE decreasing to 67.4% at $-1.0 \text{ V}_{\text{RHE}}$ (Figure 2e). Products distribution shifts remarkably after activation, as evidenced by a substantial increase in CO_2RR efficiency. For instance, the formate FE rose from 5.8% to 29.4% at $-1.0 \text{ V}_{\text{RHE}}$, and the CO FE increased from 7.9% to 21.1% at $-1.2 \text{ V}_{\text{RHE}}$. As shown in Figure 2f and Table S4, after activation at $-1.3 \text{ V}_{\text{RHE}}$, the C_{2+} FE at $-1.4 \text{ V}_{\text{RHE}}$ increased to 42.5%, the highest among all trials, establishing $-1.3 \text{ V}_{\text{RHE}}$ as the optimal activation potential for $\text{Cu}_{0.71}\text{Ni}_{0.29}$. Additionally, a new liquid product, 1-propanol (1-PrOH), was detected with a FE of 12.6% at $-1.4 \text{ V}_{\text{RHE}}$. These results indicate that cathodic activation of $\text{Cu}_{0.71}\text{Ni}_{0.29}$ effectively suppressed the HER while promoting the formation of C_{2+} product. A similar trend is observed for other $\text{Cu}_x\text{Ni}_{1-x}$

catalysts (Figures S4–S7). Based on these findings, we hypothesize that cathodic activation induces surface evolution or reconstruction in $\text{Cu}_x\text{Ni}_{1-x}$, enhancing CO_2RR selectivity. In addition, the suppressed HER after activation suggests a plausible mechanism in which surface Ni atoms leach from catalysts, creating more surface defects under cathodic potentials.

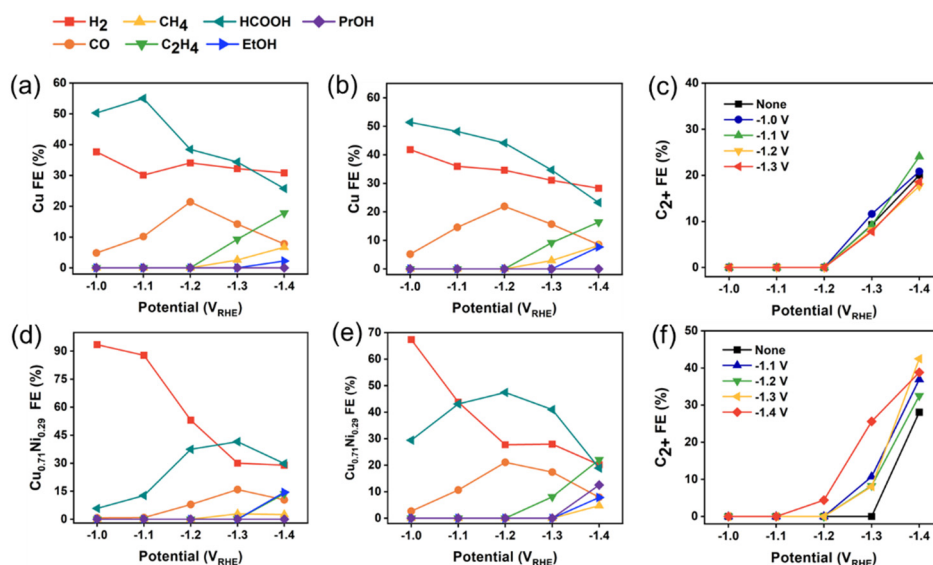


Figure 2. FEs of CO_2RR on pure Cu before activation (a), and after activation (b) at $-1.1 V_{\text{RHE}}$ for 2 h. (c) C_2^+ FEs on pure Cu after activation at different potentials. FEs of CO_2RR on $\text{Cu}_{0.71}\text{Ni}_{0.29}$ before activation (d), and after activation (e) at $-1.3 V_{\text{RHE}}$ for 2 h. (f) C_2^+ FEs on $\text{Cu}_{0.71}\text{Ni}_{0.29}$ after activation at different potentials.

2.3. CO_2RR Performance

To comprehensively evaluate the composition effect, Figures 3, S8 and S9 summarize the activity and selectivity towards H_2 , C_1 and C_2^+ of $\text{Cu}_x\text{Ni}_{1-x}$ under different conditions. It is important to note that each catalyst was activated at its optimized activation potential. Notably, differences in product distribution were observed with changes in catalysts composition, applied potential, and the activation status. As shown in Figures 3a and S8, the $\text{Cu}_x\text{Ni}_{1-x}$ catalysts generally exhibit higher geometric surface area-normalized total current density (j_{total}) and partial current density for C_2^+ ($j_{\text{C}_2^+}$) than pure Cu. The $j_{\text{C}_2^+}$ increases with Cu content, highlighting the intrinsic activity of Cu for C_2^+ formation and the advantage of the bimetallic NPs over pure Cu. $\text{Cu}_{0.81}\text{Ni}_{0.19}$ exhibits the highest $j_{\text{C}_2^+}$ as well as the highest FE before activation. After activation, $\text{Cu}_{0.71}\text{Ni}_{0.29}$ achieved the highest C_2^+ FE of 42.5%, compared to 24.1% of pure Cu at $-1.4 V_{\text{RHE}}$, and the largest current density ratio of $j_{\text{C}_2^+}/j_{\text{H}_2}$ of 2.1 (Figure 3b). By reducing Ni content and increasing applied potential, CO_2RR selectivity was enhanced, while HER was greatly suppressed both in pre-activated and after activated conditions (Figure S9). For instance, for pre-activated $\text{Cu}_{0.63}\text{Ni}_{0.37}$, as the potential shifts from $-1.0 V_{\text{RHE}}$ to $-1.4 V_{\text{RHE}}$, the H_2 FE drops from 95.8% to 35.4%, while the C_1 FE increases from 2.0% to 32.6% and the C_2^+ FE rises from 0 to 28.6%. Regarding the C_2^+ , cathodic activation enhances the FE for all $\text{Cu}_x\text{Ni}_{1-x}$ compositions (Figure 3c). For example, for $\text{Cu}_{0.71}\text{Ni}_{0.29}$, after activation at $-1.3 V_{\text{RHE}}$, the H_2 FE decreases from 87.7% to 43.8% at $-1.1 V_{\text{RHE}}$ and from 28.9% to 20.2% at $-1.4 V_{\text{RHE}}$, while the C_2^+ FE increases from 28.1% to 42.5% at $-1.4 V_{\text{RHE}}$. 1-PrOH was detected on $\text{Cu}_{0.63}\text{Ni}_{0.37}$, $\text{Cu}_{0.71}\text{Ni}_{0.29}$, and $\text{Cu}_{0.81}\text{Ni}_{0.19}$ (Figure 3d). The optimization of detailed activation and reaction conditions in Figure 3d were listed in Tables S2–S6. These results suggest that the $\text{Cu}_x\text{Ni}_{1-x}$ NPs with higher Cu content exhibit greater C_2^+ activity and selectivity after activation, and the cathodic activation positively influence CO_2RR . In the following discussion, we focus on the evolution behavior of $\text{Cu}_{0.71}\text{Ni}_{0.29}$ NPs.

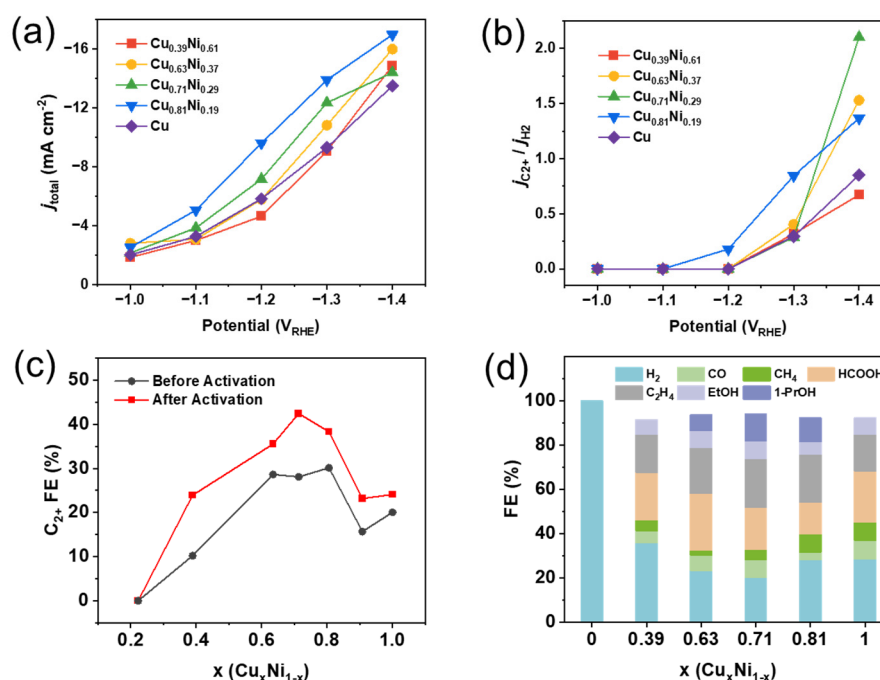


Figure 3. (a) The geometric surface area-normalized total current density (j_{total}) at different applied potentials. (b) Partial current density ratio $j_{\text{C2+}}/j_{\text{H2}}$. (c) C_{2+} FE of $\text{Cu}_x\text{Ni}_{1-x}$. (d) Products distribution after activation under the condition highlighted in Tables S2–S6.

2.4. In-Situ and Ex-Situ Characterization of the Structural Evolution of $\text{Cu}_x\text{Ni}_{1-x}$.

To elucidate the mechanisms driving the shift in selectivity, we employed *in-situ* and *ex-situ* techniques to investigate the structural evolution under working conditions. Figure 4 presents the STEM-EELS data, clearly showing a Ni-enriched surface (green) with a Cu core (red). According to the EELS data in Table S7, after 2 h of activation, both Ni and O content in $\text{Cu}_{0.71}\text{Ni}_{0.29}$ decrease, with Ni dropping from 24.9% to 13.7%, while the Cu ratio increasing from 52.0% to 76.0%. This compositional change is further corroborated by ICP-OES results (Figure S10), which indicates that as the activation potential becomes more cathodic, the Ni loss of the electrode increases, while the Cu content rises. When the activation is performed at $-1.4 V_{\text{RHE}}$, the Ni content loss reaches 90%. In addition, the change in morphology and composition persists during the subsequent reaction and become increasingly pronounced as the reaction progresses. After 5 h of CO_2RR , nearly all Ni leaches off, resulting in an approximate absolute loss of 100% and the formation of a rougher surface with more defects. The morphology of NPs undergoes a significant transformation, adopting an irregular shape (Figures 4k–m), similar to the morphological changes observed in the pure Cu (Figure S11). Regarding the observed cathodic corrosion and dissolution, recent studies suggest that pure Cu can form dissolvable ternary hydrides under CO_2RR conditions at extremely negative potentials, aided by alkali cations [36]. Another possible mechanism for Cu's structural evolution involves the formation of transient Cu-carbonyls and Cu-oxalates [27]. Our observations indicate that $\text{Cu}_x\text{Ni}_{1-x}$ catalysts with a Ni-enriched surface predominantly produce H_2 via the HER in the absence of electrochemical activation. Given that Ni is more susceptible to corrosion in CuNi solid solutions, as indicated by the Pourbaix diagram [37], it is plausible that Ni undergoes an H_2 -induced and/or ternary hydride pathway [38], leading to its dissolution into the electrolytes. Notably, unlike Cu, which tends to redeposit onto the parent material [31,32], Ni remains in the electrolyte without re-deposition onto the electrode (Figure S10) [39].

In-situ X-ray absorption spectroscopy (XAS) was performed to monitor the evolution of the chemical state of $\text{Cu}_{0.71}\text{Ni}_{0.29}$ and pure Cu at relevant potentials. Figures 5 and S12–S18 present the normalized Cu and Ni K-edge spectra from X-ray absorption near-edge spectroscopy (XANES) and Fourier-transformed extended X-ray absorption fine structure (EXAFS) spectra, along with fitting results. The XANES spectra show that the absorption edges of both $\text{Cu}_{0.71}\text{Ni}_{0.29}$ and pure Cu shift to higher energy direction compared to Cu foil, with $\text{Cu}_{0.71}\text{Ni}_{0.29}$ being closer to Cu foil (Figure 5a,b), indicating that Cu in $\text{Cu}_{0.71}\text{Ni}_{0.29}$ is less oxidized than that in pure Cu. Under activation conditions, the edge positions shift to lower energy direction, approaching that of Cu foil, which suggests reduction upon activation. In the R space (Figures 5c,d and S12), two distinct peaks at 1.5 Å and 2.2 Å correspond to Cu–O and Cu–Cu/Ni coordination, respectively [40]. Due to the similar atomic radius of Cu and Ni (2.552 Å and 2.488 Å, respectively), it is challenging to distinguish between Cu–Ni and Cu–Cu coordination. While

no significant peak shifts are observed, the increased intensity of the Cu-Cu/Ni coordination and the diminished Cu-O signal confirms a transition from the oxidized to metallic state upon cathodic activation. Additionally, the difference in R space between pure Cu and Cu_{0.71}Ni_{0.29} further confirms the higher oxidation state of pure Cu (Figure S12). EXAFS fitting (Figure S14–S18, Table S8–S10) provides quantitative insights into the coordination environment of Cu and Ni. At open circuit potential (OCP), the coordination numbers (CNs) of Cu-Cu/Ni for Cu_{0.71}Ni_{0.29} and pure Cu are 9.28 and 5.54 (Figure 5e), respectively, indicating that a predominantly metallic Cu state in Cu_{0.71}Ni_{0.29}. After activation, the CNs increase to over 10 for both catalysts and remain stable throughout reaction process, with Cu_{0.71}Ni_{0.29} exhibiting slightly higher CNs than pure Cu. In the zoomed R space (Figure 5f), a slight peak shift in Cu-O and Cu-Cu/Ni is observed for Cu_{0.71}Ni_{0.29} compared to pure Cu and Cu foil. The peak positions for pure Cu are close to those of Cu foil, while those of Cu_{0.71}Ni_{0.29} shift to shorter radial distances, indicating the presence of residual Ni after activation and reaction under the most cathodic potential, as shown in ICP results (Figure S10). Compared to the pre-activated Cu_{0.71}Ni_{0.29} catalysts, this extremely low concentration of Ni residue, along with the structural defects and roughened Cu surface, may play a role in promoting CO₂ adsorption and reduction during the CO₂RR. For Ni, the shift of the absorption edge to higher energy at OCP followed by a subsequent shift to lower energy after activation (Figure S13) suggests the presence of Ni oxides and their subsequent reduction. As the potential becomes more negative, Ni transitions into a more metallic state, as evidenced by the increase in Ni-Cu peak intensity in R space and Ni-Ni/Cu CN. Collectively, the Cu in Cu_{0.71}Ni_{0.29} is largely protected from oxidation by Ni-enriched surface. During activation, Ni leaches from the catalyst surface due to cathodic corrosion, allowing Cu to be reduced to its metallic state. This process creates structural defects and roughness on the Cu surface, potentially enhancing CO₂ adsorption and catalytic activity. The residual Ni likely stabilizes the metallic Cu state and provides additional active sites [41].

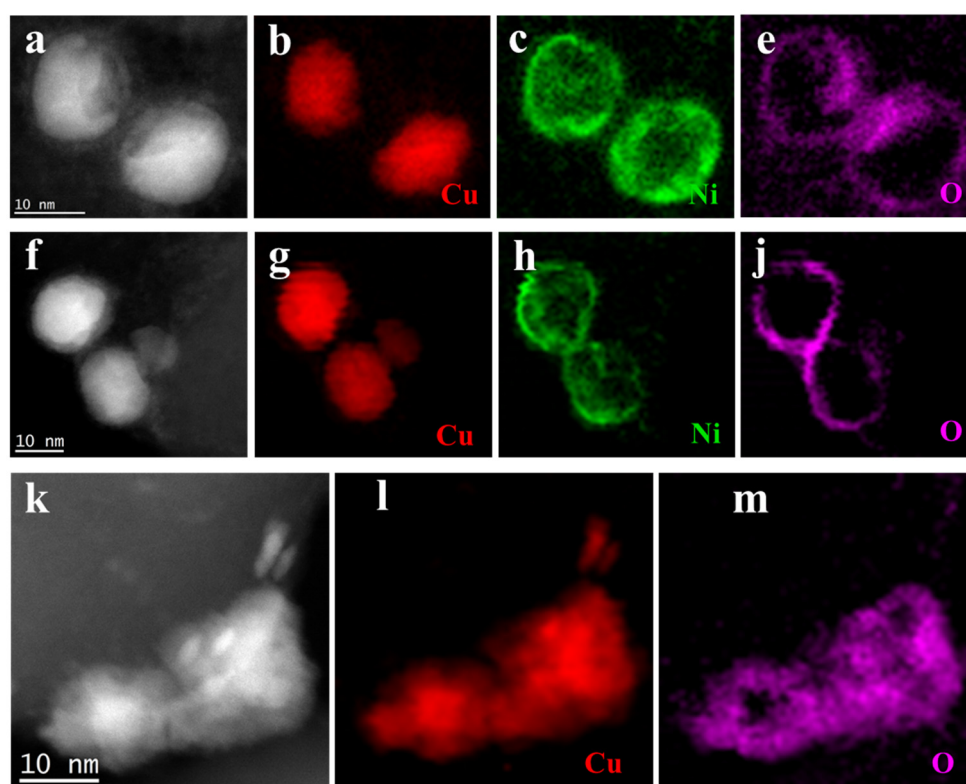


Figure 4. Structural evolution of Cu_{0.71}Ni_{0.29} catalysts during activation and CO₂RR. HAADF-STEM and corresponding STEM-EELS elemental maps of pristine Cu_{0.71}Ni_{0.29} (a–e), Cu_{0.71}Ni_{0.29} after activation for 2 h at −1.3 V_{RHE} (f–j), and Cu_{0.71}Ni_{0.29} after CO₂RR for 5 h (k–m).

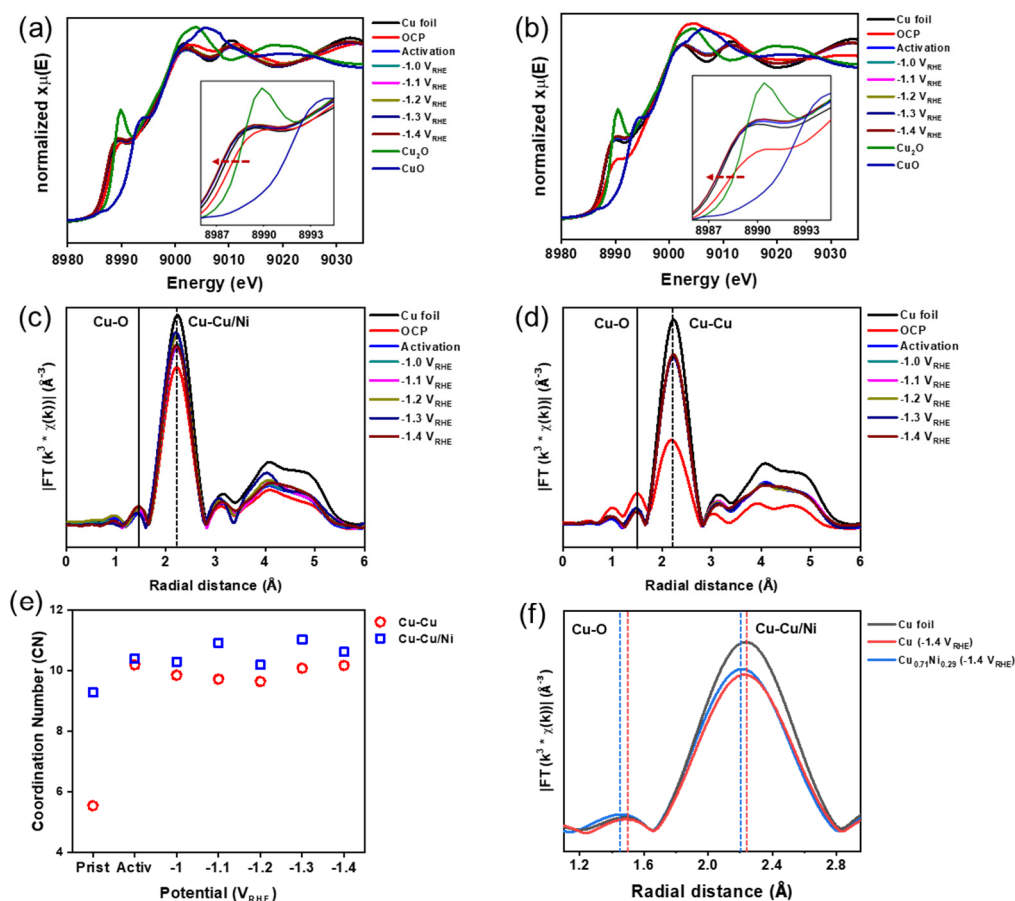


Figure 5. (a) Cu K-edge XANES of $\text{Cu}_{0.71}\text{Ni}_{0.29}$ under different potentials and standard references of Cu foil, Cu_2O and CuO, with a zoomed view of the Cu K-edge as inset. (b) Cu K-edge XANES of pure Cu under different potentials and references, with a zoomed view of the Cu K-edge as inset. (c) k^3 -Weighted Cu K-edge *in-situ* EXAFS spectra of $\text{Cu}_{0.71}\text{Ni}_{0.29}$ and standard samples. (d) k^3 -Weighted Cu K-edge *in-situ* EXAFS spectra of pure Cu and standard samples. (e) CNs of Cu-metal for $\text{Cu}_{0.71}\text{Ni}_{0.29}$ (blue) and pure Cu (red). (f) k^3 -Weighted Cu K-edge *in-situ* EXAFS of Cu foil, pure Cu and $\text{Cu}_{0.71}\text{Ni}_{0.29}$ after CO_2 reduction condition.

3. Conclusion

In summary, we report the cathodic corrosion-induced structural evolution and enhanced catalytic performance of bimetallic $\text{Cu}_x\text{Ni}_{1-x}$ NPs for CO_2RR . The incorporation of Ni, due to its higher oxophilicity, results in surface enrichment that favors the HER prior to activation. Upon cathodic activation, Ni undergoes corrosion, resulting in Ni leaching, Cu exposure, and the formation of a roughened, defect-rich surface. This structural evolution significantly enhances both CO_2RR activity and C_{2+} selectivity, with $\text{Cu}_{0.71}\text{Ni}_{0.29}$ achieving a $j_{\text{C}_{2+}}/j_{\text{H}_2}$ ratio of 2.1 and a FE of 42.5% for C_{2+} products at $-1.4 \text{ V}_{\text{RHE}}$, compared to just 24.1% for pure Cu NPs. *In-situ* and *ex-situ* structural analyses reveal that the Cu in $\text{Cu}_{0.71}\text{Ni}_{0.29}$ is less oxidized than in pure Cu and is fully reduced upon activation, confirming Ni's protective effect. Changes in Cu morphology and coordination environment suggest that cathodic corrosion optimizes catalyst performance through the synergistic effects of Ni leaching, Cu reduction, and trace amounts of Ni residue.

Supplementary Materials: The Supplementary Materials can be downloaded at: <https://www.sciltp.com/journals/mi/2024/1/562/s1>. Figure S1. TEM images and size distribution of (a,b) Cu; (c,d) $\text{Cu}_{0.81}\text{Ni}_{0.19}$; (e,f) $\text{Cu}_{0.71}\text{Ni}_{0.29}$; (g,h) $\text{Cu}_{0.63}\text{Ni}_{0.37}$; (i,j) $\text{Cu}_{0.39}\text{Ni}_{0.61}$ and (k,l) Ni NPs. Figure S2. XRD patterns from 30 to 80 degree of $\text{Cu}_x\text{Ni}_{1-x}$ with Cu and Ni references. Figure S3. Optimization of the activation step for pure Cu. (a) No activation step. (b) Activation at $-1.0 \text{ V}_{\text{RHE}}$. (c) Activation at $-1.1 \text{ V}_{\text{RHE}}$. (d) Activation at $-1.2 \text{ V}_{\text{RHE}}$. (e) C_{2+} products FE. Figure S4. Optimization of the Activation step for $\text{Cu}_{0.81}\text{Ni}_{0.19}$. (a) No activation step. (b) Activation at $-1.2 \text{ V}_{\text{RHE}}$. (c) Activation at $-1.3 \text{ V}_{\text{RHE}}$. (d) Activation at $-1.4 \text{ V}_{\text{RHE}}$. (e) C_{2+} products FE. Figure S5. Optimization of the Activation step for $\text{Cu}_{0.71}\text{Ni}_{0.29}$. (a) No activation step. (b) Activation at $-1.2 \text{ V}_{\text{RHE}}$. (c) Activation at $-1.3 \text{ V}_{\text{RHE}}$. (d) Activation at $-1.4 \text{ V}_{\text{RHE}}$. (e) C_{2+} products FE. Figure S6. Optimization of the Activation step for $\text{Cu}_{0.63}\text{Ni}_{0.37}$. (a) No activation step. (b) Activation at $-1.0 \text{ V}_{\text{RHE}}$. (c) Activation at $-1.1 \text{ V}_{\text{RHE}}$. (d) Activation at $-1.2 \text{ V}_{\text{RHE}}$. (e) C_{2+} products FE. Figure S7. Optimization of the Activation step for $\text{Cu}_{0.39}\text{Ni}_{0.61}$. (a) No activation step. (b) Activation at $-1.1 \text{ V}_{\text{RHE}}$. (c) Activation at $-1.2 \text{ V}_{\text{RHE}}$. (d) Activation at $-1.3 \text{ V}_{\text{RHE}}$. (e) C_{2+} products FE. Figure S8. Geometric surface area-normalized current density of $\text{Cu}_x\text{Ni}_{1-x}$ during CO_2RR . (a) Partial current density of C_{2+} products ($j_{\text{C}_{2+}}$) at different applied potential. (b) Partial current density of H_2 (j_{H_2}) at different applied potential. Figure S9. FEs of H_2 , C_1 and

C₂₊ for Cu_xNi_{1-x} before (top) and after (bottom) activation at optimized potential. Figure S10. Composition change and Ni leaching percentage of Cu_{0.71}Ni_{0.29} under different activation potentials. (The black and blue line are the composition change of Cu and Ni, respectively; the red line is the Ni leaching percentage). Figure S11. HAADF-STEM and corresponding STEM-EELS elemental maps of pure Cu. (a–c) Before activation. (d,e) After activation for 2 h. (g–i) After CO₂RR for 5 h. Figure S12. Comparison in *k*³-Weighted Cu K-edge *in-situ* EXAFS spectra of pure Cu and Cu_{0.71}Ni_{0.29} at OCP and after activation at their optimized activation potential. Figure S13. (a) XANES of Cu_{0.71}Ni_{0.29}, Ni scan. (b) Fourier Transformed EXAFS of Cu_{0.71}Ni_{0.29}, Ni scan. (c) CN of Cu_{0.71}Ni_{0.29}, Ni scan. Figure S14. (a–h) Fourier Transformed EXAFS fitting of Cu_{0.71}Ni_{0.29} at different activation potential, and Cu foil. Figure S15. Fourier Transformed EXAFS fitting of pure Cu at different activation potentials. Figure S16. Fourier Transformed EXAFS fitting of Cu_{0.71}Ni_{0.29}, Ni scan and Ni foil. Figure S17. EXAFS oscillation functions at the Cu K-edge of Cu_{0.71}Ni_{0.29} at different conditions and Cu foil reference. Figure S18. EXAFS oscillation functions at the Cu K-edge of pure Cu at different conditions and Cu foil reference. Table S1. Sizes of Cu_xNi_{1-x} NPs. Table S2. C₂₊ FE in the optimization of the activation step for pure Cu (the optimized condition is highlighted). Table S3. C₂₊ FE in the optimization of the activation step for pure Cu_{0.81}Ni_{0.19} (the optimized condition is highlighted). Table S4. C₂₊ FE in the optimization of the activation step for pure Cu_{0.71}Ni_{0.29} (the optimized condition is highlighted). Table S5. C₂₊ FE in the optimization of the activation step for pure Cu_{0.63}Ni_{0.37} (the optimized condition is highlighted). Table S6. C₂₊ FE in the optimization of the activation step for pure Cu_{0.39}Ni_{0.61} (the optimized condition is highlighted). Table S7. Atomic composition of Figures 4 and S11. Table S8. Fitting parameters of Cu_{0.71}Ni_{0.29}, Cu scan. Table S9. Fitting parameter of pure Cu, Cu scan. Table S10. Fitting parameters of Cu_{0.71}Ni_{0.29}, Ni scan.

Author Contributions: W.S.: data curation, investigation, writing, and revising draft. B.M.: data curation, investigation, methodology. M.W.: investigation. X.H.: visualization. Q.G.: methodology. S.H.: methodology, investigation. H.Z. (Hua Zhou): methodology. H.Z. (Huiyuan Zhu): conceptualization and supervision. All authors have read and agreed to the published version of the manuscript.

Funding: This work was supported by the US National Science Foundation (CHE-2332802).

Data Availability Statement: The authors declare that the data supporting the findings of this study are available from the corresponding author, H. Zhu, upon reasonable request.

Acknowledgements: This research used Electron Microscopy facility of the Center for Functional Nanomaterials (CFN), which is a U.S. Department of Energy Office of Science User Facility, at Brookhaven National Laboratory under Contract No. DE-SC0012704. XAS was done at 12BM. This research used resources of the Advanced Photon Source; a U.S. Department of Energy (DOE) Office of Science User Facility operated for the DOE Office of Science by Argonne National Laboratory under Contract No. DE-AC02-06CH11357.

Conflicts of Interest: The authors declare no conflict of financial interest.

References

1. Wu, J.; Huang, Y.; Ye, W.; Li, Y. CO₂ reduction: From the electrochemical to photochemical approach. *Adv. Sci.* **2017**, *4*, 1700194.
2. Zhang, L.; Zhao, Z.J.; Gong, J. Nanostructured materials for heterogeneous electrocatalytic CO₂ reduction and their related reaction mechanisms. *Angew. Chem. Int. Ed.* **2017**, *56*, 11326–11353.
3. Bushuyev, O.S.; De Luna, P.; Dinh, C.T.; Tao, L.; Saur, G.; van de Lagemaat, J.; Kelley, S.O.; Sargent, E.H. What should we make with CO₂ and how can we make it? *Joule* **2018**, *2*, 825–832.
4. Garza, A.J.; Bell, A.T.; Head-Gordon, M. Mechanism of CO₂ reduction at copper surfaces: Pathways to C₂ products. *ACS. Catal.* **2018**, *8*, 1490–1499.
5. Nitopi, S.; Bertheussen, E.; Scott, S.B.; Liu, X.; Engstfeld, A.K.; Horch, S.; Seger, B.; Stephens, I.E.L.; Chan, K.; Hahn, C.; et al. Progress and perspectives of electrochemical CO₂ reduction on copper in aqueous electrolyte. *Chem. Rev.* **2019**, *119*, 7610–7672.
6. Kuhl, K.P.; Hatsukade, T.; Cave, E.R.; Abram, D.N.; Kibsgaard, J.; Jaramillo, T.F. Electrocatalytic conversion of carbon dioxide to methane and methanol on transition metal surfaces. *J. Am. Chem. Soc.* **2014**, *136*, 14107–14113.
7. Bagger, A.; Ju, W.; Varela, A.S.; Strasser, P.; Rossmeisl, J. Electrochemical CO₂ reduction: A classification problem. *Chemphyschem* **2017**, *18*, 3266–3273.
8. Gao, D.; Arán-Ais, R.M.; Jeon, H.S.; Roldan Cuenya, B. Rational catalyst and electrolyte design for CO₂ electroreduction towards multicarbon products. *Nat. Catal.* **2019**, *2*, 198–210.
9. Zhao, J.; Xue, S.; Barber, J.; Zhou, Y.; Meng, J.; Ke, X. An overview of Cu-based heterogeneous electrocatalysts for CO₂ reduction. *J. Mater. Chem. A* **2020**, *8*, 4700–4734.
10. Kuhl, K.P.; Cave, E.R.; Abram, D.N.; Jaramillo, T.F. New insights into the electrochemical reduction of carbon dioxide on metallic copper surfaces. *Energy Environ. Sci.* **2012**, *5*, 7050–7059.
11. Zheng, Y.; Vasileff, A.; Zhou, X.; Jiao, Y.; Jaroniec, M.; Qiao, S.Z. Understanding the roadmap for electrochemical reduction of CO₂ to multi-carbon oxygenates and hydrocarbons on copper-based catalysts. *J. Am. Chem. Soc.* **2019**, *141*, 7646–7659.
12. Zhao, R.; Ding, P.; Wei, P.; Zhang, L.; Liu, Q.; Luo, Y.; Li, T.; Lu, S.; Shi, X.; Gao, S.; et al. Recent progress in electrocatalytic methanation of CO₂ at ambient conditions. *Adv. Funct. Mater.* **2021**, *31*, 2009449.

13. Okatenko, V.; Loiudice, A.; Newton, M.A.; Stoian, D.C.; Blokhina, A.; Chen, A.N.; Rossi, K.; Buonsanti, R. Alloying as a strategy to boost the stability of copper nanocatalysts during the electrochemical CO₂ reduction reaction. *J. Am. Chem. Soc.* **2023**, *145*, 5370–5383.
14. Song, H.; Tan, Y.C.; Kim, B.; Ringe, S.; Oh, J. Tunable product selectivity in electrochemical CO₂ reduction on well-mixed Ni-Cu alloys. *ACS Appl. Mater. Interfaces* **2021**, *13*, 55272–55280.
15. Wu, Z.-Z.; Gao, F.-Y.; Gao, M.-R. Regulating the oxidation state of nanomaterials for electrocatalytic CO₂ reduction. *Energy Environ. Sci.* **2021**, *14*, 1121–1139.
16. Favaro, M.; Xiao, H.; Cheng, T.; Goddard, W.A., 3rd; Yano, J.; Crumlin, E.J. Subsurface oxide plays a critical role in CO₂ activation by Cu(111) surfaces to form chemisorbed CO₂, the first step in reduction of CO₂. *Proc. Natl. Acad. Sci. USA* **2017**, *114*, 6706–6711.
17. Gu, Z.; Shen, H.; Chen, Z.; Yang, Y.; Yang, C.; Ji, Y.; Wang, Y.; Zhu, C.; Liu, J.; Li, J.; et al. Efficient electrocatalytic CO₂ reduction to C₂+ alcohols at defect-site-rich Cu surface. *Joule* **2021**, *5*, 429–440.
18. Vasileff, A.; Xu, C.; Jiao, Y.; Zheng, Y.; Qiao, S.-Z. Surface and interface engineering in copper-based bimetallic materials for selective CO₂ electroreduction. *Chem.* **2018**, *4*, 1809–1831.
19. Du, C.; Mills, J.P.; Yohannes, A.G.; Wei, W.; Wang, L.; Lu, S.; Lian, J.X.; Wang, M.; Guo, T.; Wang, X.; et al. Cascade electrocatalysis via AgCu single-atom alloy and Ag nanoparticles in CO₂ electroreduction toward multicarbon products. *Nat. Commun.* **2023**, *14*, 6142.
20. Kim, D.; Resasco, J.; Yu, Y.; Asiri, A.M.; Yang, P. Synergistic geometric and electronic effects for electrochemical reduction of carbon dioxide using gold-copper bimetallic nanoparticles. *Nat. Commun.* **2014**, *5*, 4948.
21. Chen, C.; Li, Y.; Yu, S.; Louisia, S.; Jin, J.; Li, M.; Ross, M.B.; Yang, P. Cu-Ag tandem catalysts for high-rate CO₂ electrolysis toward multicarbons. *Joule* **2020**, *4*, 1688–1699.
22. Iyengar, P.; Kolb, M.J.; Pankhurst, J.R.; Calle-Vallejo, F.; Buonsanti, R. Elucidating the facet-dependent selectivity for CO₂ electroreduction to ethanol of Cu–Ag tandem catalysts. *ACS Catal.* **2021**, *11*, 4456–4463.
23. Clark, E.L.; Hahn, C.; Jaramillo, T.F.; Bell, A.T. Electrochemical CO₂ reduction over compressively strained CuAg surface alloys with enhanced multi-carbon oxygenate selectivity. *J. Am. Chem. Soc.* **2017**, *139*, 15848–15857.
24. Chang, C.J.; Lin, S.C.; Chen, H.C.; Wang, J.; Zheng, K.J.; Zhu, Y.; Chen, H.M. Dynamic reoxidation/reduction-driven atomic interdiffusion for highly selective CO₂ reduction toward methane. *J. Am. Chem. Soc.* **2020**, *142*, 12119–12132.
25. Huang, J.; Hormann, N.; Oveisi, E.; Loiudice, A.; De Gregorio, G.L.; Andreussi, O.; Marzari, N.; Buonsanti, R. Potential-induced nanoclustering of metallic catalysts during electrochemical CO₂ reduction. *Nat. Commun.* **2018**, *9*, 3117.
26. Lai, W.; Ma, Z.; Zhang, J.; Yuan, Y.; Qiao, Y.; Huang, H. Dynamic evolution of active sites in electrocatalytic CO₂ reduction reaction: Fundamental understanding and recent progress. *Adv. Funct. Mater.* **2022**, *32*, 2111193.
27. Vavra, J.; Ramona, G.P.L.; Dattila, F.; Kormányos, A.; Priamushko, T.; Albertini, P.P.; Loiudice, A.; Cherevko, S.; Lopéz, N.; Buonsanti, R. Solution-based Cu⁺ transient species mediate the reconstruction of copper electrocatalysts for CO₂ reduction. *Nat. Catal.* **2024**, *7*, 89–97.
28. Lee, S.H.; Lin, J.C.; Farmand, M.; Landers, A.T.; Feaster, J.T.; Aviles Acosta, J.E.; Beeman, J.W.; Ye, Y.; Yano, J.; Mehta, A.; et al. Oxidation state and surface reconstruction of Cu under CO₂ reduction conditions from in situ X-ray characterization. *J. Am. Chem. Soc.* **2021**, *143*, 588–592.
29. Kim, Y.G.; Baricuatro, J.H.; Javier, A.; Gregoire, J.M.; Soriaga, M.P. The evolution of the polycrystalline copper surface, first to Cu(111) and then to Cu(100), at a fixed CO₂RR potential: A study by operando EC-STM. *Langmuir* **2014**, *30*, 15053–15056.
30. Delmo, E.P.; Wang, Y.; Song, Y.; Zhu, S.; Zhang, H.; Xu, H.; Li, T.; Jang, J.; Kwon, Y.; Wang, Y.; et al. In Situ infrared spectroscopic evidence of enhanced electrochemical CO₂ reduction and C-C coupling on oxide-derived copper. *J. Am. Chem. Soc.* **2024**, *146*, 1935–1945.
31. Vavra, J.; Shen, T.H.; Stoian, D.; Tileli, V.; Buonsanti, R. Real-time monitoring reveals dissolution/redeposition mechanism in copper nanocatalysts during the initial stages of the CO₂ reduction reaction. *Angew. Chem. Int. Ed.* **2021**, *60*, 1347–1354.
32. Chen, P.C.; Chen, C.; Yang, Y.; Maulana, A.L.; Jin, J.; Feijoo, J.; Yang, P. Chemical and structural evolution of AgCu catalysts in electrochemical CO₂ reduction. *J. Am. Chem. Soc.* **2023**, *145*, 10116–10125.
33. Jeon, H.S.; Timoshenko, J.; Scholten, F.; Sinev, I.; Herzog, A.; Haase, F.T.; Roldan Cuenya, B. Operando insight into the correlation between the structure and composition of CuZn nanoparticles and their selectivity for the electrochemical CO₂ reduction. *J. Am. Chem. Soc.* **2019**, *141*, 19879–19887.
34. Gao, Q.; Ju, Y.M.; An, D.; Gao, M.R.; Cui, C.H.; Liu, J.W.; Cong, H.P.; Yu, S.H. Shape-controlled synthesis of monodisperse PdCu nanocubes and their electrocatalytic properties. *ChemSusChem* **2013**, *6*, 1878–1882.
35. Wang, Y.; Xu, A.; Wang, Z.; Huang, L.; Li, J.; Li, F.; Wicks, J.; Luo, M.; Nam, D.H.; Tan, C.S.; et al. Enhanced nitrate-to-ammonia activity on copper-nickel alloys via tuning of intermediate adsorption. *J. Am. Chem. Soc.* **2020**, *142*, 5702–5708.

36. Liu, S.; Li, Y.; Wang, D.; Xi, S.; Xu, H.; Wang, Y.; Li, X.; Zang, W.; Liu, W.; Su, M.; et al. Alkali cation-induced cathodic corrosion in Cu electrocatalysts. *Nat. Commun.* **2024**, *15*, 5080.
37. McCafferty, E. *Introduction to Corrosion Science*; Springer: New York, NY, USA, 2010; pp. 111–112.
38. Hersbach, T.J.P.; Koper, M.T.M. Cathodic corrosion: 21st century insights into a 19th century phenomenon. *Curr. Opin. Electrochem.* **2021**, *26*, 100653.
39. Nong, H.N.; Reier, T.; Oh, H.-S.; Gliech, M.; Paciok, P.; Vu, T.H.T.; Teschner, D.; Heggen, M.; Petkov, V.; Schlögl, R.; et al. A unique oxygen ligand environment facilitates water oxidation in hole-doped IrNiOx core-shell electrocatalysts. *Nat. Catal.* **2018**, *1*, 841–851.
40. Lin, S.C.; Chang, C.C.; Chiu, S.Y.; Pai, H.T.; Liao, T.Y.; Hsu, C.S.; Chiang, W.H.; Tsai, M.K.; Chen, H.M. Operando time-resolved X-ray absorption spectroscopy reveals the chemical nature enabling highly selective CO₂ reduction. *Nat. Commun.* **2020**, *11*, 3525.
41. Pan, H.; Barile, C.J. Bifunctional nickel and copper electrocatalysts for CO₂ reduction and the oxygen evolution reaction. *J. Mater. Chem. A* **2020**, *8*, 1741–1748.

Article

Controlled Polymerization of Aniline against Templating Oxide Nanostructures

Matas Simukaitis¹, Grace Purnell¹, Zachary Zander², Danielle Kuhn², and Yugang Sun^{1,*}

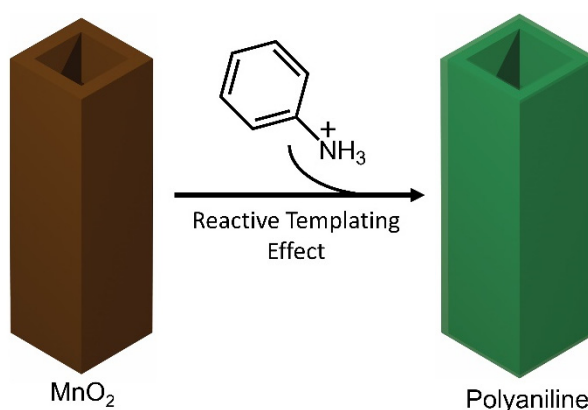
¹ Department of Chemistry, Temple University, 1901 North 13th Street, Philadelphia, PA 19122, USA

² U.S. Army DEVCOM Chemical Biological Center, Research & Technology Directorate, Aberdeen Proving Ground, MD 21010, USA

* Correspondence: ygsun@temple.edu

Received: 6 November 2024; Revised: 30 November 2024; Accepted: 3 December 2024; Published: 4 December 2024

Abstract: Conducting polyaniline (PANI) nanotubes with strong broadband optical absorption have been synthesized using single-crystalline MnO₂ nanotubes as a solid-state oxidant that can oxidize aniline to induce polymerization in acidic solutions. The smooth surfaces and high crystalline integrity of the MnO₂ nanotubes provide the appropriate reactive solid/liquid interface and templating effect to enable the transformation of the MnO₂ nanotubes into PANI nanotubes. Such templated chemical transformation can be extended to silica-coated MnO₂ nanotubes, allowing the synthesis of silica-coated PANI nanotubes, which are challenging to be synthesized through direct coating silica on PANI nanotubes due to the low wettability between PANI and silica. The versatile chemistry of the outer silica shells opens the possibility of modifying the as-synthesized PANI nanotubes, which usually inconveniently graft other interesting motifs.



Keywords: templated redox reaction synthesis; conducting polymer nanotubes; inorganic-polymer core-shell nanotubes; broadband optical absorption composite nanomaterials

1. Introduction

Polyaniline (PANI), a widely studied conducting polymer, has shown great promise in many fields, such as sensing, energy storage, and medicine, owing to its favorable physical properties, tunable electrical conductivity, ease of processing, and stability [1–5]. While polymerization of aniline monomer is a simple process initiated in the presence of an appropriate oxidant [6,7], shape-controlled synthesis of PANI nanostructures is still challenging. For example, the widely adopted approach is using ammonium persulfate (APS), a soluble oxidant salt with a redox potential of 2.01 V (vs. SHE or standard hydrogen electrode), to enable the polymerization of aniline (with a redox potential of 1.10 V) [8]. Persulfate ions oxidize aniline monomer rapidly in solution, leading to difficulty in controlling the morphology of PANI. Emerging strategies for controlling the shape of PANI nanostructures include confined polymerization in micelles [9,10], self-assembly micro/nanotubes [11], and polymerization on inert nanoparticle surfaces followed by post-processing [12]. Alternatively, a solid-state oxidant that relies on the exposed surface to react with aniline could provide controllability over reaction kinetics to enable a controlled growth of PANI nanostructures. When the solid-state oxidant is a nanostructure with a desirable shape, it oxidizes aniline to initiate a polymerization reaction, forming a PANI nanoparticle with a shape determined by the oxidant nanostructure. The solid-state oxidant nanostructure provides the important solid-liquid interface to restrict the reaction kinetics and confine the polymerization adjacent to the nanostructure surface, in which the oxidant nanostructure behaves as a reactive transient template. For instance, nanostructures of manganese oxides [13–19] and cerium dioxides (ceria) [20] have been reported to react with aniline and guide polymerization of aniline, forming PANI nanostructures with inheritance of the geometries of the oxide nanostructures. Reproducing the



Copyright: © 2024 by the authors. This is an open access article under the terms and conditions of the Creative Commons Attribution (CC BY) license (<https://creativecommons.org/licenses/by/4.0/>).

Publisher's Note: Scilight stays neutral with regard to jurisdictional claims in published maps and institutional affiliations

reported recipes showed that some oxide nanostructures (e.g., MnO₂ nanorods and nanotubes) gave successful production of PANI nanostructures with controlled shapes, but some oxide nanostructures (e.g., ceria nanoparticles, MnO₂ flowers, MnO₂ spheres) failed to produce the well-shaped PANI nanostructures. Such inconsistent reproducibility motivated us to investigate the critical parameters of the oxide nanostructures to determine the success of producing well-shaped PANI nanostructures.

In this work, we compare the use of CeO₂ nanoparticles, desert rose-like δ -MnO₂ flowers, and single-crystalline α -MnO₂ nanotubes in reaction with aniline and analyze whether the geometries of the oxide nanostructures are preserved in the resulting PANI nanostructures. Conducting PANI nanotubes are successfully synthesized by using the α -MnO₂ nanotubes as the reactive template to oxidize aniline and facilitate polymerization reaction in a controlled manner, without the appearance of randomly formed PANI. The standard reduction potential of MnO₂/Mn²⁺ pair is 1.23 V, which is high enough to oxidize aniline under appropriate conditions, for example, a high acidity of the reaction solution that allows the solid MnO₂ is reduced to soluble Mn²⁺ ions. Reducing MnO₂ nanotubes to soluble ions is essential to continuously expose reactive MnO₂ surfaces to oxidize aniline and drive polymerization reaction. In addition, the single crystallinity of the MnO₂ nanotubes prevents them from being shattered during the redox reaction, facilitating the formation of PANI nanotubes due to the templating effect. In contrast, the polycrystalline δ -MnO₂ flowers made of intertwined thin nanoflakes and polycrystalline MnCO₃@MnO₂ spherical particles with rough surfaces react with aniline to form entangled PANI nanofibers without inheriting the MnO₂ geometries. The stark difference indicates that high crystallinity and smooth surfaces of the reactive template oxide nanostructures are crucial to forming integral PANI nanostructures with the preservation of oxide geometries. The evolution of PANI nanotubes has been examined to understand the shape preservation of the single-crystalline MnO₂ nanotubes during the templated redox reaction.

2. Materials and Methods

2.1. Synthesis of MnO₂ Nanotubes

Single-crystalline MnO₂ nanotubes were synthesized through a hydrothermal method. In a typical synthesis, 112.5 mg of KMnO₄ (Acros Organics, ACS Reagent, 99%+, Fair Lawn, NJ, USA) was dissolved in 10 mL of DI H₂O. To this solution was added 0.250 mL of concentrated HCl (Fisher Chemical, ACS Plus Reagent, 37% w/w, Fair Lawn, NJ, USA) under magnetic stirring, and the solution was allowed to stir for 30 min. The solution was transferred to a Teflon-lined stainless steel hydrothermal reactor, which was then placed in an oven set at 120 °C for 12 h. The reactor was allowed to cool completely to room temperature before opening. The solid product was washed three times with DI H₂O and one time with ethanol (Pharmco, 190 proof, Brookfield, CT, USA) before drying in an oven set at 60 °C overnight.

2.2. Synthesis of PANI Nanotubes

In a synthesis, 15 mg of the as-prepared MnO₂ nanotubes were dispersed in 5 mL of DI H₂O. To this dispersion was added 0.2 mL of 0.6 M H₂SO₄ (Fisher Chemical, Certified ACS Plus, 95% w/w, Fair Lawn, NJ, USA). The dispersion was ultrasonicated for 30 min. A separate solution containing 18 mL of aniline (Acros Organics, ACS Reagent, 99%, Fair Lawn, NJ, USA) in 1 mL of DI H₂O was prepared. Following the 30-min ultrasonication period, the aniline solution was added to the dispersion of MnO₂ nanotubes to trigger the redox and polymerization reactions. The reaction was performed at room temperature and ambient air atmosphere. The PANI product was washed three times with DI H₂O before being dispersed in 5 mL of ethanol for storage.

2.3. Synthesis of PANI@silica Nanotubes

The as-synthesized MnO₂ nanotubes were first coated with silica with an appropriate thickness through a sol-gel process. For example, 15 mg of MnO₂ nanotubes were dispersed in a solution containing 2.5 mL DI H₂O and 0.5 mL NH₄OH with the assistance of ultrasonication. While magnetic stirring, to the MnO₂ dispersion 12 mL of 0.03 M cetyltrimethylammonium bromide (CTAB) (CHEM-IMPEX INT'L INC., 99.52%, Wood Dale, IL, USA) solution in H₂O/ethanol (v/v = 2:1) was added dropwise and the magnetical stirring continued for additional 30 min. A solution containing the appropriate amount of tetraethyl orthosilicate (TEOS) (Acros Organics, 98%, Fair Lawn, NJ, USA) in 0.5 mL of pure ethanol was then added dropwise to the dispersion, followed with continuous stirring at room temperature overnight. The solution was centrifuged and washed with DI H₂O and ethanol to remove excess CTAB. The MnO₂@silica nanotubes were dried in an oven set at 60 °C before use. Transforming the MnO₂ nanotubes to PANI nanotubes inside the silica coating followed the same procedure described above.

2.4. XRD Characterization

The XRD characterization was performed using a Bruker D8 Advance diffractometer (Billerica, MA, USA). The as-synthesized MnO₂ product powder was loaded to a sample holder made of Poly(Methyl Methacrylate) (PMMA). The X-ray beam was generated using Cu K_α emission with wavelength of 1.5418 Å. The total power of the instrument was set at 1600 W. The measurement was recorded at a rate of 1 s per increment of 0.0204°.

2.5. TEM Characterization

The transmission electron microscopy (TEM) images were recorded using a JEOL JEM-1400 electron microscope equipped with a LaB₆ filament (Tokyo, Japan). For sample preparation, the PANI dispersion in ethanol was diluted by a factor of 4 with additional ethanol before a 20-μL aliquot was drop cast on a Formvar/carbon 200 mesh copper TEM grid (Ted Pella Inc. Redding, CA, USA). The solvent vaporized in a fume hood to dry the sample. All images were collected at an accelerating voltage of 120 kV with the beam current between 85–100 μA.

2.6. SEM/EDS Characterization

The scanning electron microscopy (SEM) images were recorded using a FEI Quanta 450FEG electron microscope (Hillsboro, OR, USA), which was equipped with an Oxford Instruments X-Max^N 50 detector for energy dispersive x-ray spectroscopy (EDS) characterization (High Wycombe, UK). For sample preparation, the PANI dispersion in ethanol was directly used and a 20-μL aliquot was drop-cast on a silicon chip. The solvent vaporized in a fume hood to dry the sample. All images were collected at an accelerating voltage of 10 kV. All EDS characterization and analysis was conducted using the AZtec software (Oxford Instruments, High Wycombe, UK).

2.7. UV-Visible Absorption/Extinction Spectroscopy

The UV-visible optical absorption/extinction spectroscopy was studied using a Thermo Scientific Evolution 220 UV-Visible spectrophotometer (Madison, WI, USA). For the study of reaction evolution, a 0.1-mL aliquot of the reaction solution was sampled at a specific time and dispersed in 1 mL of DI H₂O. The quartz cuvette was rinsed twice with DI H₂O between samples. The spectral scans were conducted at a rate of 3000 nm/min with an integration time of 30 milliseconds and a scan interval of 1.5 nm.

3. Results and Discussion

When a MnO₂ nanotube is immersed in acidic aniline solution, aniline molecules are in direct contact with the outer side surfaces and end surfaces of the nanotube to react and initiate polymerization to form a thin PANI layer on these surfaces (step i, Figure 1). Because of the small diameter of the nanotube, the diffusion of aniline into the tube cavity is significantly restricted, making it difficult to form a PANI layer against the inner surfaces of the MnO₂ nanotube. The thin PANI layer is still permeable to aniline monomer, allowing the continuous redox reaction between aniline and MnO₂ to grow the PANI layer. The outer side surfaces of the single-crystalline α-MnO₂ nanotube are smooth and terminated by the low-index {100} facets, while its end surfaces are rough (or curved) and terminated by the higher-index facets [21]. The crystallographic differences between the side and end surfaces lead to different reactivity: the end surfaces are more reactive than the outer side surfaces. As a result, the continuous reaction will consume MnO₂ along the longitudinal direction faster than the transverse direction. Such anisotropic reactivity results in a PANI nanotube with a shortened MnO₂ nanotube in the middle (step ii, Figure 1). The end portions of the PANI nanotube (with complete consumption of MnO₂) become thicker to reach the thickness determined by the reaction stoichiometry. Meanwhile, the PANI layer outside the remaining MnO₂ also slightly thickens even though the reaction along the transverse direction is slow. The further reaction will ultimately consume the MnO₂ nanotube to form a pure PANI nanotube with uniform thickness (step iii, Figure 1). The redox reaction and polymerization occurring against the MnO₂ surfaces ensures the resulting PANI to adopt the tubular morphology of the MnO₂ nanotube.

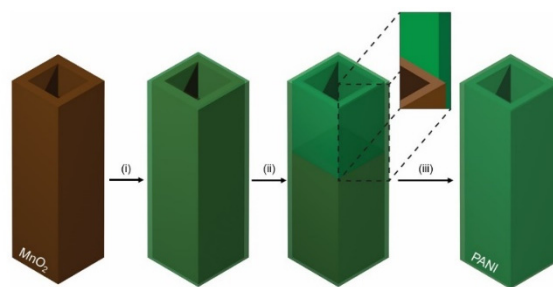


Figure 1. Schematic illustration of the major steps involved in the evolution of single-crystalline α -MnO₂ nanotube during the reaction with aniline, which results in a PANI nanotube.

PANI exists in three oxidation states: fully reduced leucoemeraldine, fully oxidized pernigraniline, and partially oxidized emeraldine phase. The former two forms exhibit negligible electric conductivity, while the latter emeraldine phase is highly conductive and represents the most studied PANI phase [7]. The conductivity and optical properties of PANI can be modulated by the concentration of doped protons along the polymer backbone, allowing delocalization of the trapped electron states. Therefore, strong acidity (or low pH) of reaction solutions is necessary to synthesize highly conductive PANI nanostructures. The polymerization reaction using APS yields H₂SO₄ as a byproduct, providing sufficient proton dopant to produce conductive PANI. In contrast, the polymerization reaction with MnO₂ consumes protons (Figure S1, ESI), preventing the formation of the conductive emeraldine phase. A high concentration of acid must be added to the reaction solution to maintain a sufficiently acidic condition for producing conductive PANI when using MnO₂ as a solid-state oxidant.

Single-crystalline α -MnO₂ nanotubes were synthesized using a hydrothermal method reported elsewhere [22]. The X-ray diffraction (XRD) pattern exhibits only a group of peaks consistent with the α -phase of MnO₂ (Figure S2). The electron microscopy images show their tubular geometry with smooth surfaces and square cross-sections. Each nanotube is straight with a uniform lateral dimension of 105 nm on average (Figure S3). In a typical reaction with aniline, 15 mg of the synthesized MnO₂ nanotubes were dispersed in 5 mL of deionized (DI) H₂O under ultrasonication. The pH of the aqueous dispersion was adjusted using 0.5 M H₂SO₄ aqueous solution to a value of 1.5 (or any value below 1.5, condition optimization in Table S1, ESI). A mixture of 0.013 mL of aniline and 1 mL of DI H₂O was then added to the acidified dispersion of MnO₂ nanotubes under vigorous magnetic stirring. The mixing promoted the redox reaction between aniline and the MnO₂ nanotubes, producing aniline radicals followed by polymerization into PANI. The dispersion was under constant stirring at room temperature to complete the reaction. Centrifuging the dispersion collects the PANI product, which was washed three times with DI H₂O and then dispersed in ethanol for further use.

The morphological and compositional evolution of the MnO₂ nanotubes during reaction with aniline in the acidic solution was studied by sampling the reaction solution at different times. The solid nanostructures in each aliquot were immediately collected through centrifugation and washing with DI H₂O. Figure 2 compares the TEM images of the typical individual nanotubes sampled at different reaction times. Each α -MnO₂ nanotube exhibits smooth side surfaces, open ends with curved end surfaces, and slightly tapered walls at the ends (Figure 2a). The line-scan energy-dispersive X-ray spectroscopy (EDS) across the nanotube shows a typical bell-curve profile of Mn with the presence of C that is common due to environment contamination (Figure 3a). The larger surface curvatures of the end surfaces are responsible for the higher reactivity than the side surfaces. The initial reaction of the MnO₂ nanotubes with aniline (i.e., for 1 min) formed a thin layer of PANI covering both the outer side surfaces and the end surfaces of the MnO₂ nanotubes (Figure 2b). The line scan EDS across the nanotube for both Mn and C exhibit the same profile with an increase of C signal relative to Mn (Figure 3b), confirming the occurrence of redox reaction that consumes MnO₂ and produces PANI. The PANI on the end surfaces is much thicker than on the side surfaces, which could be partially attributed to the different reactivity of the MnO₂ surfaces at different locations. In addition, the diffusion of aniline to the MnO₂ surfaces influences the redox reaction kinetics at the solid/liquid interface. The diffusion cross section for the end MnO₂ surfaces, which is close to a three-dimensional (3D) point diffusion model, is much larger than that for the side MnO₂ surfaces, which is equivalent to a two-dimension (2D) planar diffusion model (dashed curve vs. dashed line, Figure 2b). The difference in diffusion also contribute to the fast reaction on the end surfaces of the MnO₂ nanotubes, leading to the anisotropic shrink of the MnO₂ nanotubes along their longitudinal direction. Continuous reaction for 5 min shortens the MnO₂ nanotubes, forming composite nanotubes with multiple segments—pure PANI for the end sections and PANI/MnO₂ for the central section (Figure 2c). The compositional difference at different segments is evaluated with the line-scan EDS analysis (Figure 3c). The line-scan EDS profiles for both C and Mn at the

central section are similar, confirming the incomplete consumption of MnO_2 . The C intensity relative to Mn increases compared to the sample formed at 1 min, indicating that the redox reaction on the side surfaces of the MnO_2 nanotubes (i.e., along the transverse direction) still occurs, although the reaction rate is slower than that along the longitudinal direction. Another possibility of the redox reaction could be similar to the formation of hollow metal nanoparticles through the galvanic replacement reaction of silver nanoparticles with chloroauric acid [23]. Aniline molecules give out electrons on the outer surface, being oxidized to polymerize and thicken the PANI shells. The electrons migrate across the conductive PANI layer to inject into the MnO_2 nanotubes, reducing MnO_2 into soluble Mn^{2+} ions. In contrast, the line-scan EDS profiles at the end section show the absence of Mn, indicating that MnO_2 is completely consumed, and this section is composed of pure PANI. The apparent diameter of the end section is $\sim 75\%$ of that of the central section, implying the mechanical flexibility of the PANI nanotube. Without the support of the rigid MnO_2 nanotube, the PANI nanotube tends to shrink, possibly due to capillary force during drying. Reaction for a longer time (e.g., 10 min) completely consumes MnO_2 , producing pure PANI nanotubes (Figures 2d and S4). The long PANI nanotubes in electron microscopy images exhibit bent geometries (Figure S5), different from the straight geometry of the MnO_2 nanotubes, confirming the mechanical flexibility of PANI.

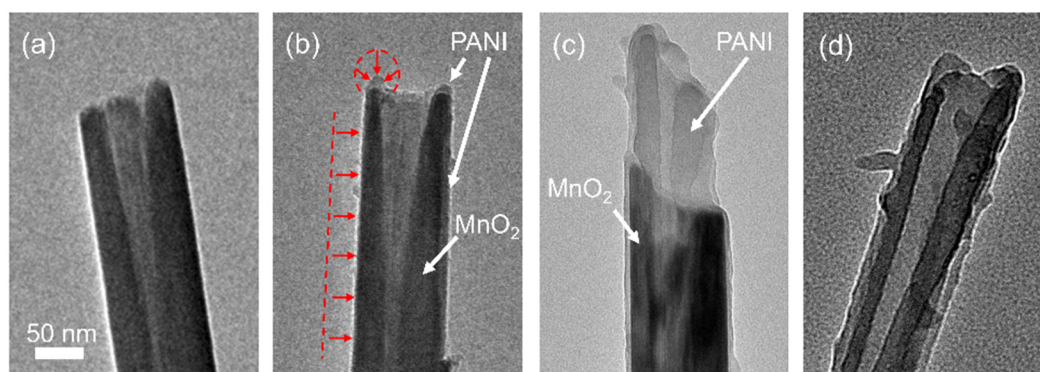


Figure 2. Typical TEM images of representative $\alpha\text{-MnO}_2$ nanotube (a) and (b–d) after reaction with aniline for different times: (b) 1 min, (c) 5 min, and (d) 10 min. The dotted curve and line in (b) indicate the diffusion cross-sections of aniline toward the end and side surface, respectively. The red arrows indicate the diffusion direction of aniline.

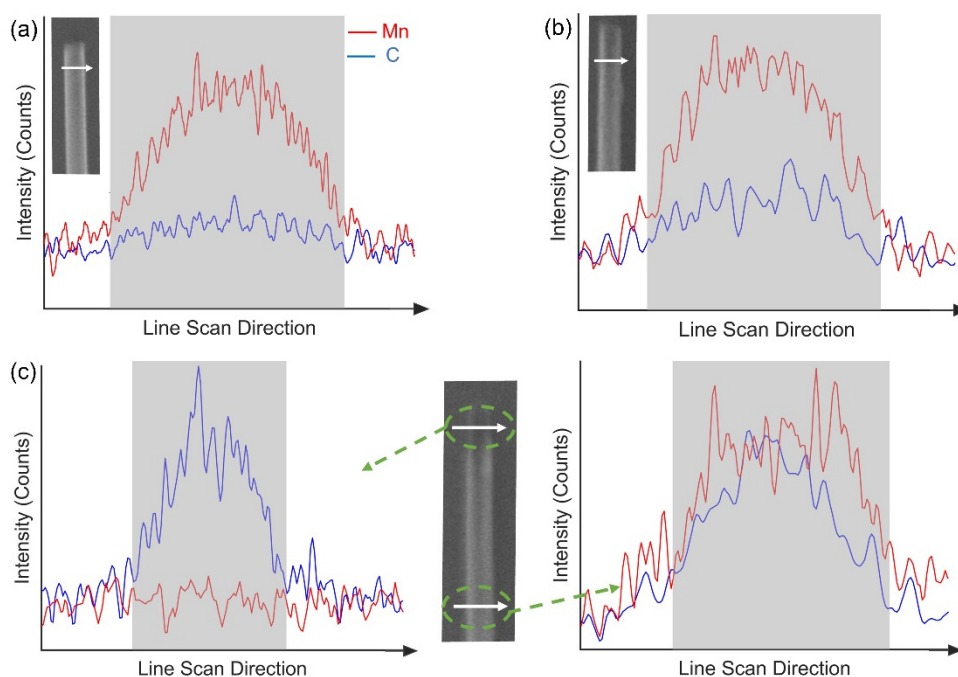


Figure 3. Line-scan EDS profiles of Mn and C along individual nanotubes before (a) and after (b,c) the $\alpha\text{-MnO}_2$ nanotubes react with aniline for different times: (b) 1min. and (c) 10 min. The insets are the nanotubes that have

been studied. The arrows highlight the positions for EDS analysis and line-scan directions. The grey boxes highlight the edges of the studied nanotubes, which determine their lateral dimensions.

The Fourier transform infrared (FTIR) spectrum of the as-synthesized nanotubes exhibits characteristic peaks of PANI (Figure S6). The two peaks located at 1583 cm^{-1} and 1498 cm^{-1} are attributed to quinonoid and benzenoid ring stretching respectively [24]. The weak peak at 1384 cm^{-1} appears as a result of C-N stretching of alternating quinonoid-benzenoid-quinonoid rings within the PANI structure [25]. The peak at 1315 cm^{-1} represents the C-N vibrational mode of secondary aromatic amines [26] while the peak at 1267 cm^{-1} is attributed to the polaron lattice C-N stretching mode [27]. The broad peak at 1142 cm^{-1} is associated with positively charged -NH^+ stretching modes within the polymer arising from the high degree of polymer backbone protonation while the peak at 699 cm^{-1} represents -NH wagging in secondary amines. The peak at 824 cm^{-1} corresponds to the out of plane C-H stretching modes of para-disubstituted benzene rings arising from the end to end monomer coupling during the polymerization reaction [25].

The color evolution of the solution during the conversion of MnO_2 nanotubes to PANI nanotubes allows using ultraviolet (UV)-visible absorption spectroscopy to follow the redox/polymerization reactions on MnO_2 surfaces. The emeraldine PANI phase has three characteristic absorption bands in the UV-visible spectral range. According to the previous studies on emeraldine PANI films [28], the absorption band around 4 eV (or 310 nm) originates from the $\pi\text{-}\pi^*$ transition, owing to the excitation of benzenoid rings within the polymer chain. This transition is present in both aniline monomer and PANI of all phases. The emeraldine base has an absorption band at $\sim 2.1\text{ eV}$ (or 590 nm) due to the localized benzenoid HOMO (highest occupied molecular orbital) to quinoid LUMO (lowest unoccupied molecular orbital) excitation. Protonation of the emeraldine base leads to the formation of bipolarons, in which the two N atoms connecting to the quinoid rings are protonated with positive charges. Such localized protonation could elevate the quinoid LUMO position and blueshift the absorption band. The internal redox reaction of bipolarons transforms quinoids into benzenoid rings, forming polarons. The following polaron separation spreads the polarons to form a polaronic lattice with alternated cations ($\text{-}\dot{\text{N}}\text{H}^+\text{-}$) along the polymer chains. The polymer chain with high-density polarons possesses a polaron band that is half occupied with electrons. Excitation of electrons from the fully occupied lower-energy band to the polaron band becomes possible, shifting the HOMO-LUMO absorption peak to the red around 1.5 eV (or 825 nm). The polaron band transition usually gives an intense and broad absorption peak. Further protonation increases the density of polarons to exhibit polaron bications that are neighboring polarons. Such breaking of the polaron lattice makes the emeraldine PANI more metallic, extending its absorption further to the near-infrared region [28,29].

Figure 4 plots the time-dependent UV-visible extinction spectra of an acidic dispersion of MnO_2 nanotubes before and after the reaction with aniline for different times. The extinction spectrum of the MnO_2 nanotubes shows a shallow and broad peak at 610 nm (black curve, Figure 4a). The significant baseline offset is attributed to the strong scattering of the MnO_2 nanotubes due to their longitudinal dimensions comparable to or larger than the light wavelength. The dispersion of the MnO_2 nanotubes is opaque (inset, Figure S3), confirming the strong scattering of the nanotubes. Once the reaction with aniline starts, a strong absorption peak at 530 nm and a weak shoulder peak at 700 nm emerge simultaneously (see the spectrum at 15 s), indicating the formation of protonated emeraldine PANI dominated by bipolarons. The absorption peak of MnO_2 is too weak to display and be embedded in the strong absorption of PANI. The absorption of resulting Mn^{2+} cations is also very weak compared to PANI (Figure S7). Therefore, the peaks observed in the extinction spectra are dominated by the absorption of emeraldine PANI. As the reaction continues, the peak at the shorter wavelength slightly increases and redshifts. The peak at the longer wavelength significantly increases in intensity, but its position remains unchanged. The evolution of these two absorption peaks indicates that thicker PANI favors the formation of polaron lattice at longer reaction times. For example, the PANI nanotubes formed at 10 min after complete consumption of MnO_2 essentially exhibit one peak at 700 nm (yellow curve, Figure 4a), indicating the freshly produced PANI nanotubes are composed of polymer chains primarily with polaron lattices. This extinction spectrum still shows a large offset baseline without the MnO_2 nanotubes, indicating that the resulting PANI nanotubes have strong scattering. The strong scattering makes the dispersion of PANI nanotubes opaque (inset, Figure S5). In contrast, the PANI dispersion synthesized using APS exhibits an extinction spectrum with a smaller offset (Figure S8), indicating that the lateral dimensions of the PANI nanostructures are smaller compared to the PANI nanotubes. The PANI product is dominated by wavy and entangled nanofibers with thin diameters, which could be easily swollen with solvent to minimize the difference in dielectric constant between the PANI nanofibers and solvent. Both the small lateral dimensions and swelling of the PANI nanofibers lower their optical scattering. The PANI synthesized from reaction with polycrystalline MnO_2 shells with rough surfaces [19] gives a transparent solution even though the spherical MnO_2 shells have sizes over $2\text{ }\mu\text{m}$ (Figure S9). The lack of strong light scattering implies that the resulting PANI cannot

inherit the geometry and dimension from the polycrystalline MnO_2 shells but form fragments. The differences in PANI products formed from the reactions with the single-crystalline MnO_2 nanotubes and the polycrystalline MnO_2 shells confirm the importance of single crystallinity, which prevents the reactive MnO_2 from falling apart during reaction with aniline, and smooth surface, which provides the solid/liquid interface favoring the localized polymerization and growth of PANI against the MnO_2 surface, in synthesizing PANI nanotubes that can inherit the geometry and dimensions of the MnO_2 nanotubes.

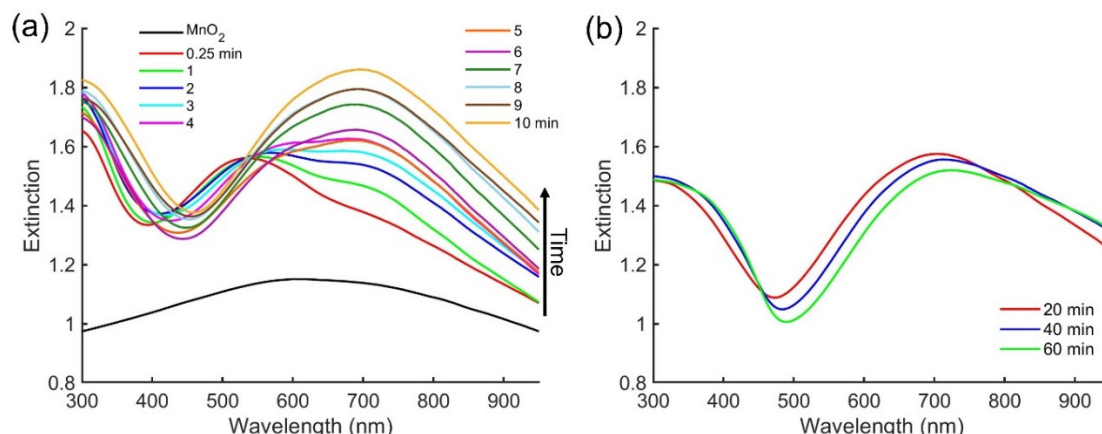


Figure 4. Time-dependent UV-Visible extinction spectra of the dispersion of MnO_2 nanotubes before (black curve) and after reaction with aniline for different times: (a) 15 s–10 min and (b) 20 min–60 min. Note: The first spectrum (red curve) in (a) was recorded at 15 s (i.e., 0.25 min), the second spectrum (green curve) was recorded at 1 min, and the following spectra were collected at an interval of 1 min. The units of the legends in (a) are the same as min.

Since the absorption peaks at 530 nm and 700 nm originated from the emeraldine PANI, it is feasible to use their intensity to roughly estimate the extent of polymerization, which is approximately proportional to the absorbance [30]. The integrated area by using the line connecting the peak valley around 400 nm and the data point at the longest wavelength (i.e., 980 nm) as the baseline is used to evaluate the polymerization kinetics during the reaction of aniline with the MnO_2 nanotubes (Figure S10). The integrated area exhibits a linear dependence on the reaction time at the middle stage of the reaction (i.e., 2–7 min), indicating that the polymerization follows a quasi-zeroth reaction order and is independent of concentrations of both aniline and MnO_2 nanotubes. Such concentration independence indicates that the exposed MnO_2 surfaces (i.e., the end surfaces with an almost constant value) primarily determine the reaction kinetics when the diffusion of aniline does not limit the reaction. The polymerization becomes slower at the late stage (Figure S10), where the concentration of aniline is so low that diffusion starts limiting the reaction. After the complete redox and polymerization reaction, incubating the PANI nanotubes in the acidic reaction solution leads to a slight decrease in peak intensity at 700 nm and an overall broadband increase in the near-infrared region (Figure 4b). The soaking allows deep protonation of the polaron lattices (alternated polaron distribution along polymer chains) to polymer chains with high-density polarons (i.e., forming neighboring polaron bications), making PANI more metallic (or conductive) to extend its optical absorption to even longer wavelength, i.e., near-infrared region [31].

The transformation of transient template MnO_2 nanotubes to PANI nanotubes through an interfacial redox reaction provides a possibility to form PANI nanotubes coated with an inorganic layer, which is difficult to deposit on PANI directly. For example, the conventional sol-gel process cannot grow a silica coating on PANI nanostructures through controlled hydrolysis of tetraethyl orthosilicate (TEOS) in the presence of the PANI nanostructures in a solution due to the chemical non-wettability between silica and PANI. In contrast, it is convenient to grow a silica layer on MnO_2 nanotubes, forming MnO_2 @silica core-shell nanotubes, through the sol-gel process [32]. When the silica coating is thin enough (<20 nm), the intrinsic porosity of the thin silica layer still allows the diffusion of aniline molecules to react with MnO_2 nanotubes and outward diffusion of Mn^{2+} ions, resulting in the transformation of the MnO_2 nanotubes into PANI ones inside the silica shells (Figure 5). The FTIR spectrum of the resulting composite nanotubes exhibits the same characteristic peaks of the PANI nanotubes shown in Figure 2d, confirming the conversion of MnO_2 to PANI (Figure S6). The formation of PANI nanotubes inside the silica shells indicates the diffusion of aniline monomer across the silica layer. The EDS linescan profiles of Si (corresponding to silica shell) and C (corresponding to PANI tube) of a single composite tube (Figure S11) show that the signal of Si is wider than the signal of C, highlight the PANI@silica core-shell structure. The lack of Mn signal and strong C signal indicate the complete reaction of MnO_2 with aniline monomers to yielding soluble

Mn²⁺ ions and PANI core tubes. Due to the versatile chemistry of silica, the presence of silica layer outside the PANI nanotubes enables the feasibility to modify or graft interesting components onto the composite nanotubes, adding appropriate properties/functionalities to the PANI nanotubes.

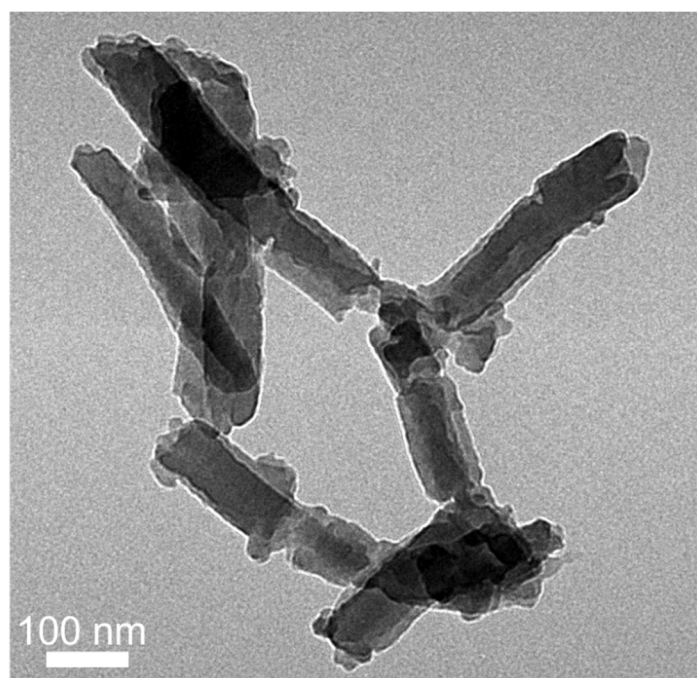


Figure 5. Typical TEM image of representative PANI@silica nanotubes.

4. Conclusion

Single-crystalline α -phase MnO₂ nanotubes have been used as a new class of solid-state oxidant to oxidize aniline and promote polymerization of emeraldine PANI in the appropriate acidic solutions. The MnO₂ nanotubes with smooth surfaces also serve as transient templates to confine the polymerization against the MnO₂ surfaces, forming pure PANI nanotubes with dimensions determined by the MnO₂ nanotubes and reaction stoichiometry. The reduction of MnO₂ into soluble Mn²⁺ ions is also crucial for hollow PANI nanostructures, which inherit the geometry of MnO₂ nanostructures. The reaction of aniline with CeO₂ nanoparticles failed to produce hollow PANI shells because Ce₂O₃ (i.e., the product of reduced CeO₂) is not soluble. After the initial reaction, the presence of thin Ce₂O₃ coating on CeO₂ prevents the contact between aniline and CeO₂, thus ceasing the continuous redox reaction. This work shed light on using highly crystalline reactive oxide nanostructures as transient templates to synthesize shape-controlled conducting polymer nanostructures through oxidation-induced polymerization.

Supplementary Materials: The following supporting information can be downloaded at: <https://www.sciltp.com/journals/mi/2024/1/578/s1>. Figure S1. Change of solution pH value as aniline added to the dispersion of MnO₂ nanostructures at 30, 90, 180, 270 s. The jump of pH value indicates the consumption of protons as aniline being oxidized by MnO₂. Figure S2. XRD pattern of the synthesized MnO₂ nanotubes. Figure S3. (a) Scanning electron microscopy (SEM) image of the synthesized MnO₂ nanotubes. The nanotubes standing out-of-substrate show the square cross sections and hollow interiors. The inset is a photo of an aqueous dispersion of the MnO₂ nanotubes. (b) Statistic histogram of the lateral dimensions of individual MnO₂ nanotubes. Figure S4. Line-scan EDS profiles across a PANI nanotube (formed from 10-minute reaction as shown in Figure 2d) at different locations. The near-zero signals of Mn regardless of position confirm the complete consumption of MnO₂ throughout the entire nanotube. The gray boxes highlight the boundaries of the nanotube along the scan traces. Figure S5. Transmission electron microscopy (TEM) image of the synthesized PANI nanotubes. The bended curves along their longitudinal directions indicate their mechanical flexibility. Figure S6. FTIR spectrum of the as-synthesized PANI nanotubes as shown in Figure 2d and PANI@silica nanotubes as shown in Figure 5. Figure S7. Absorption spectrum of the supernatant after complete reaction of the MnO₂ nanotubes. The absorbance beyond 500 nm, where optical absorption of the emeraldine PANI locates, is lower than 0.01, which is less than 2% of the peak absorption of the PANI nanotube dispersion. Therefore, it is reasonable to ignore the influence of resulting Mn²⁺ on the extinction spectra during the reaction. Figure S8. (a) TEM image of PANI synthesized using APS. The inset is the photo of the PANI dispersion. (b) Extinction spectrum of the PANI dispersion. The concentration of aniline units is same as that used in the synthesis of PANI nanotubes. Figure S9. (a) SEM image of MnO₂ spherical shells with rough surfaces. (b) TEM image of PANI synthesized from reaction with the MnO₂ shells. The inset is the photo of the PANI dispersion. (c) Extinction spectrum of the PANI dispersion. The concentration of aniline units is same as that used in the synthesis of PANI nanotubes. Figure S10. Time-dependent integrated area of the absorption beyond the valley points in Figure 4a. The integration was processed using the line connecting the valley point around 400 nm and the data point at the longest wavelength (i.e., 980 nm) in each spectrum. Figure S11. Line-scan EDS profiles

of a synthesized PANI@silica core-shell nanotube. The inset represents the SEM image of the PANI@silica nanotube, with an arrow highlighting the scan position and direction. The grey box represents the outer boundary of the nanotube along the scan traces. Table S1: Reactivity of MnO₂ nanotubes and the resulting PANI phase at different pH of reaction solution.

Author Contributions: D.K. and Y.S. conceptualized the project. Z.Z., D.K. and Y.S. supervised the project. M.S. and G.P. conducted the experiment. All authors discussed and analyzed the results. M.S. drafted the manuscript, and all authors contributed to revising it. All authors have read and agreed to the published version of manuscript.

Funding: This work was supported through the subcontract No. SciTech 22-22-F-0037-02 funded by US Army DEVCOM Chemical Biological Center. Materials characterization was partially performed at Temple Materials Institute.

Data Availability Statement: The data that support the findings of this study are available from the corresponding authors upon reasonable request.

Conflicts of Interest: The authors declare no conflict of financial interest.

References

- McQuade, D.T.; Pullen, A.E.; Swager, T.M. Conjugated Polymer-Based Chemical Sensors. *Chem. Rev.* **2000**, *100*, 2537–2574. <https://doi.org/10.1021/cr9801014>.
- Yang, D.; Wang, J.; Cao, Y.; Tong, X.; Hua, T.; Qin, R.; Shao, Y. Polyaniline-Based Biological and Chemical Sensors: Sensing Mechanism, Configuration Design, and Perspective. *ACS Appl. Electron. Mater.* **2023**, *5*, 593–611. <https://doi.org/10.1021/acsaelm.2c01405>.
- Novák, P.; Müller, K.; Santhanam, K.S.V.; Haas, O. Electrochemically Active Polymers for Rechargeable Batteries. *Chem. Rev.* **1997**, *97*, 207–282. <https://doi.org/10.1021/cr941181o>.
- Wang, K.; Wu, H.; Meng, Y.; Wei, Z. Conducting Polymer Nanowire Arrays for High Performance Supercapacitors. *Small* **2014**, *10*, 14–31. <https://doi.org/10.1002/sml.201301991>.
- Zare, E.N.; Makvandi, P.; Ashtari, B.; Rossi, F.; Motahari, A.; Perale, G. Progress in Conductive Polyaniline-Based Nanocomposites for Biomedical Applications: A Review. *J. Med. Chem.* **2020**, *63*, 1–22. <https://doi.org/10.1021/acs.jmedchem.9b00803>.
- Tran, H.D.; D’Arcy, J.M.; Wang, Y.; Beltramo, P.J.; Strong, V.A.; Kaner, R.B. The Oxidation of Aniline to Produce “Polyaniline”: A Process Yielding Many Different Nanoscale Structures. *J. Mater. Chem.* **2011**, *21*, 3534–3550. <https://doi.org/10.1039/C0JM02699A>.
- Sapurina, I.; Stejskal, J. The Mechanism of the Oxidative Polymerization of Aniline and the Formation of Supramolecular Polyaniline Structures. *Polym. Int.* **2008**, *57*, 1295–1325. <https://doi.org/10.1002/pi.2476>.
- Pavitt, A.S.; Bylaska, E.J.; Tratnyek, P.G. Oxidation Potentials of Phenols and Anilines: Correlation Analysis of Electrochemical and Theoretical Values. *Environ. Sci. Process. Impacts* **2017**, *19*, 339–349. <https://doi.org/10.1039/C6EM00694A>.
- Zhang, X.; Manohar, S.K. Polyaniline Nanofibers: Chemical Synthesis Using Surfactants. *Chem. Commun.* **2004**, *20*, 2360. <https://doi.org/10.1039/b409309g>.
- Kim, B.-J.; Oh, S.-G.; Han, M.-G.; Im, S.-S. Preparation of Polyaniline Nanoparticles in Micellar Solutions as Polymerization Medium. *Langmuir* **2000**, *16*, 5841–5845. <https://doi.org/10.1021/la9915320>.
- Wei, Z.; Zhang, Z.; Wan, M. Formation Mechanism of Self-Assembled Polyaniline Micro/Nanotubes. *Langmuir* **2002**, *18*, 917–921. <https://doi.org/10.1021/la0155799>.
- Wu, C.-G.; Bein, T. Conducting Polyaniline Filaments in a Mesoporous Channel Host. *Science* **1994**, *264*, 1757–1759. <https://doi.org/10.1126/science.264.5166.1757>.
- Pan, L.J.; Pu, L.; Shi, Y.; Song, S.Y.; Xu, Z.; Zhang, R.; Zheng, Y.D. Synthesis of Polyaniline Nanotubes with a Reactive Template of Manganese Oxide. *Adv. Mater.* **2007**, *19*, 461–464. <https://doi.org/10.1002/adma.200602073>.
- Han, J.; Wang, M.; Cao, S.; Fang, P.; Lu, S.; Chen, R.; Guo, R. Reactive Template Strategy for Fabrication of MnO₂/Polyaniline Coaxial Nanocables and Their Catalytic Application in the Oxidative Decolorization of Rhodamine B. *J. Mater. Chem. A* **2013**, *1*, 13197–13202. <https://doi.org/10.1039/C3TA12545A>.
- Ren, L.; Zhang, G.; Wang, J.; Kang, L.; Lei, Z.; Liu, Z.; Liu, Z.; Hao, Z.; Liu, Z. Adsorption–Template Preparation of Polyanilines with Different Morphologies and Their Capacitance. *Electrochim. Acta* **2014**, *145*, 99–108. <https://doi.org/10.1016/j.electacta.2014.08.088>.
- Tian, Y.; Li, H.; Liu, Y.; Cui, G.; Sun, Z.; Yan, S. Morphology-Dependent Enhancement of Template-Guided Tunable Polyaniline Nanostructures for the Removal of Cr(VI). *RSC Adv.* **2016**, *6*, 10478–10486. <https://doi.org/10.1039/C5RA25630E>.
- Han, J.; Li, L.; Fang, P.; Guo, R. Ultrathin MnO₂ Nanorods on Conducting Polymer Nanofibers as a New Class of Hierarchical Nanostructures for High-Performance Supercapacitors. *J. Phys. Chem. C* **2012**, *116*, 15900–15907. <https://doi.org/10.1021/jp303324x>.
- Feng, X.; Zhang, Y.; Yan, Z.; Chen, N.; Ma, Y.; Liu, X.; Yang, X.; Hou, W. Self-Degradable Template Synthesis of Polyaniline Nanotubes and Their High Performance in the Detection of Dopamine. *J. Mater. Chem. A* **2013**, *1*, 9775–9780. <https://doi.org/10.1039/C3TA11856H>.

19. Fei, J.; Cui, Y.; Yan, X.; Yang, Y.; Wang, K.; Li, J. Controlled Fabrication of Polyaniline Spherical and Cubic Shells with Hierarchical Nanostructures. *ACS Nano* **2009**, *3*, 3714–3718. <https://doi.org/10.1021/nn900921v>.
20. Li, X.; Liu, X.; Qiao, X.; Xing, S. Confining the Polymerization of Aniline to Generate Yolk–Shell polyaniline@SiO₂ Nanostructures. *RSC Adv.* **2015**, *5*, 79172–79177. <https://doi.org/10.1039/C5RA15065E>.
21. Truong, T.T.; Liu, Y.; Ren, Y.; Trahey, L.; Sun, Y. Morphological and Crystalline Evolution of Nanostructured MnO₂ and Its Application in Lithium–Air Batteries. *ACS Nano* **2012**, *6*, 8067–8077. <https://doi.org/10.1021/nn302654p>.
22. Xiao, W.; Wang, D.; Lou, X.W. Shape-Controlled Synthesis of MnO₂ Nanostructures with Enhanced Electrocatalytic Activity for Oxygen Reduction. *J. Phys. Chem. C* **2010**, *114*, 1694–1700. <https://doi.org/10.1021/jp909386d>.
23. Sun, Y.; Xia, Y. Mechanistic Study on the Replacement Reaction between Silver Nanostructures and Chloroauric Acid in Aqueous Medium. *J. Am. Chem. Soc.* **2004**, *126*, 3892–3901. <https://doi.org/10.1021/ja039734c>.
24. Furukawa, Y.; Ueda, F.; Hyodo, Y.; Harada, I.; Nakajima, T.; Kawagoe, T. Vibrational Spectra and Structure of Polyaniline. *Macromolecules* **1988**, *21*, 1297–1305. <https://doi.org/10.1021/ma00183a020>.
25. Trchová, M.; Stejskal, J. Polyaniline: The Infrared Spectroscopy of Conducting Polymer Nanotubes (IUPAC Technical Report). *Pure Appl. Chem.* **2011**, *83*, 1803–1817. <https://doi.org/10.1351/PAC-REP-10-02-01>.
26. Boyer, M.-I.; Quillard, S.; Rebourt, E.; Louarn, G.; Buisson, J.P.; Monkman, A.; Lefrant, S. Vibrational Analysis of Polyaniline: A Model Compound Approach. *J. Phys. Chem. B* **1998**, *102*, 7382–7392. <https://doi.org/10.1021/jp972652o>.
27. Boyer, M.I.; Quillard, S.; Louarn, G.; Froyer, G.; Lefrant, S. Vibrational Study of the FeCl₃-Doped Dimer of Polyaniline; A Good Model Compound of Emeraldine Salt. *J. Phys. Chem. B* **2000**, *104*, 8952–8961. <https://doi.org/10.1021/jp000946v>.
28. Huang, W.S.; MacDiarmid, A.G. Optical Properties of Polyaniline. *Polymer* **1993**, *34*, 1833–1845. [https://doi.org/10.1016/0032-3861\(93\)90424-9](https://doi.org/10.1016/0032-3861(93)90424-9).
29. Stafström, S.; Brédas, J.L.; Epstein, A.J.; Woo, H.S.; Tanner, D.B.; Huang, W.S.; MacDiarmid, A.G. Polaron Lattice in Highly Conducting Polyaniline: Theoretical and Optical Studies. *Phys. Rev. Lett.* **1987**, *59*, 1464–1467. <https://doi.org/10.1103/PhysRevLett.59.1464>.
30. Neoh, K.G.; Kang, E.T.; Tan, K.L. Evolution of Polyaniline Structure during Synthesis. *Polymer* **1993**, *34*, 3921–3928. [https://doi.org/10.1016/0032-3861\(93\)90521-B](https://doi.org/10.1016/0032-3861(93)90521-B).
31. Canales, M.; Torras, J.; Fabregat, G.; Meneguzzi, A.; Alemán, C. Polyaniline Emeraldine Salt in the Amorphous Solid State: Polaron versus Bipolaron. *J. Phys. Chem. B* **2014**, *118*, 11552–11562. <https://doi.org/10.1021/jp5067583>.
32. Shi, X.; Cao, M.; Fang, X. β -MnO₂/SiO₂ Core–Shell Nanorods: Synthesis and Dielectric Properties. *J. Nanosci. Nanotechnol.* **2011**, *11*, 6953–6958. <https://doi.org/10.1166/jnn.2011.4252>.